Universidad de La Laguna
Oficina de Sede Electrónica
Entrada
Nº registro: 2018/37907
Nº reg. oficina: OF002/2018/33824
Fecha: 29/06/2018 18:42:13

DEPARTAMENTO DE ASTROFÍSICA

Universidad de La Laguna

Analysis of the magnetic and dynamic structure of solar filaments

Thesis submitted by
D. Carlos José Díaz Baso
as a requirement for the degree of
Doctor by University of La Laguna.

Director: Dr. María Jesús Martínez González
Co-director: Dr. Andrés Asensio Ramos
Tutor: Dr. Basilio Ruiz Cobo

INSTITUTO Ð ASTROFISICA Ð CANARIAS
September 2018

Examination date: September, 2018
Thesis supervisors:
Dr. María Jesús Martínez González & Dr. Andrés Asensio Ramos

Part of the material included in this document have been already published in *The Astrophysical Journal*.

Agradecimientos

Me gustaría dar las gracias en primer lugar, al Instituto de Astrofísica de Canarias por haber podido disfrutar del programa de Astrofísico Residente “La Caixa”–Severo Ochoa, y a la Fundación la Caixa por financiarlo, apostando así por los jóvenes investigadores. También reconocer la labor de todas las instituciones detrás de las grandes instalaciones que han posibilitado esta tesis como son el telescopio GREGOR y la Torre Solar Sueca. De igual modo, a aquellas personas de la comunidad científico/informática, y en particular a la de python, que han generado una infraestructura de librerías que me han permitido llegar tan lejos en el análisis de datos.

Quiero agradecer a mis directores, María Jesús Martínez González y Andrés Asensio Ramos, la gran labor que han hecho guiándome durante el desarrollo de esta tesis. Ha sido un placer trabajar con ellos, tanto a nivel científico como personal.

Estoy muy agradecido con Basilio Ruiz Cobo y Manolo Collados Vera por sus valiosas lecciones que fueron de gran ayuda durante años anteriores y para este trabajo. Asimismo, me siento afortunado de haber disfrutado de importantes conversaciones con otros compañeros, entre ellos Ivan Milić, Iker Requerey, Andrii Sukhorukou y Carlos Quintero.

Quiero dar las gracias especialmente a Nazaret Bello González por la primera escuela de CASSDA que me introdujo por primera vez en la comunidad de físicos solares. También quiero agradecer a Jaime de la Cruz Rodríguez y a todo el equipo del Instituto de Física Solar en Estocolmo por su ayuda y hospitalidad durante mi estancia.

Valoro mucho la inestimable ayuda de Lourdes González y de Eva Bejarano durante mi tiempo en el IAC. También estoy agradecido a toda la gente del CAU y en particular a Antonio Dorta, que me echaron una mano siempre que hizo falta. Doy gracias a todos los compañeros del Instituto de Astrofísica de Canarias con los que he pasado grandes momentos durante estos años, al grupo de física solar y sobre todo a la gente de mi despacho, sin duda la mejor.

Por supuesto, no hubiese llegado aquí sin el cariño y apoyo de mi familia: mis padres Juan José Díaz de León y América Baso Armas, y mi hermano Raúl Díaz Baso. Soy consciente de la suerte que tengo por tenerlos.

A mi chica, mi pareja, y ahora mi mujer, María del Buen Paso Bethencourt Mesa, que ha sido sin lugar a dudas mi pilar durante estos años.

Por último me gustaría terminar, con la memoria de alguien que siempre echaré de menos y que me ha acompañado durante todo el proceso. Alguien que siempre estaba tanto dispuesta a escuchar como a compartir, y que me ha enseñado a ser la persona que soy. ¡Gracias Abuela Carmen!

Resumen

Los filamentos y protuberancias solares han sido el foco de muchos estudios desde hace más de 200 años por ser uno de los fenómenos más fascinantes del Sol. Sin embargo, no es hasta ahora, con la instrumentación actual, nuestra potencia de cálculo y una consolidada teoría de generación y transporte de radiación polarizada que podemos estudiar estas estructuras con mayor precisión.

Las protuberancias aparecen como condensaciones de plasma frío suspendidas a gran altura, con una estructura filamentosa. En lugar de caer a la superficie debido a la aceleración gravitatoria, pueden permanecer varias semanas sin apenas cambios. El campo magnético es el que parece sostener estas estructuras y a pesar de ser un ingrediente fundamental, el conocimiento sobre su topología exacta y su conectividad con la fotosfera es escaso hoy día. Después de todos estos años de estudio, los filamentos continúan presentando un desafío para el análisis observacional. La razón principal es la dificultad para obtener datos espectropolarimétricos con una precisión que haga posible estudiar las señales de polarización débiles que generan e inferir su campo magnético a partir de ellas.

Dado que en este trabajo no estudiamos los filamentos como eventos aislados sino también su conexión con el medio, presentamos desde el comienzo de esta tesis una descripción general de la estructura del Sol y de los fenómenos característicos de cada capa. Esto nos permite entender la relación entre los filamentos y su entorno. También revisamos los aspectos más relevantes de los filamentos y su naturaleza magnética.

El objetivo principal de este trabajo radica en la inferencia del campo magnético en filamentos a través de las señales de polarización de las líneas espectrales. Para ello hacemos una pequeña introducción sobre las ideas básicas de transporte radiativo y cómo utilizar el potencial de las líneas espectrales para inferir las propiedades del plasma. Además, discutimos en profundidad las propiedades de las líneas espectrales usadas en este trabajo: el multiplete He I 10830 Å y la línea Ca II 8542 Å; así como la instrumentación y los métodos utilizados para lograr los resultados de este trabajo.

Para hacernos una idea de cómo se genera la polarización y hacer una correcta interpretación física de las observaciones, sintetizamos los parámetros de Stokes de algunos escenarios interesantes y estudiamos las señales del triplete He I 10830 Å. En concreto, analizamos cómo cambian las señales si tenemos varias estructuras en la línea de visión, un fenómeno común cuando observamos el “césped” de espículas en el limbo donde cada una contribuye a la polarización observada. Este efecto también es importante en observaciones en el disco donde estructuras (como los filamentos) están iluminadas desde abajo por una superficie solar que tiene, en principio, propiedades diferentes.

Hasta la fecha, las señales de polarización provenientes de los filamentos en regiones activas se analizaban como si procedieran directamente de él, asignando valores de campo muy superiores ($\sim$700 G) a los esperados de similares filamentos en zonas de Sol en calma ($\sim$20 G). Basándonos en la idea de que un filamento iluminado por una región activa muy magnetizada podría generar una interpretación errónea, proponemos un modelo de dos componentes atmosféricas en la misma línea de visión. Este modelo permite además explicar de forma mucho más natural las señales de polarización observada. La conclusión importante de este experimento sugiere que los filamentos son transparentes a la radiación que proviene de la superficie. Consecuentemente, los valores altos de campo magnético podrían pertenecer al campo magnético producido por la cromosfera activa debajo del filamento y no al filamento en sí, cuestionando las intensidades exactas del campo magnético de estas estructuras medidas anteriormente.

A continuación, estudiamos la topología magnética de un filamento de región activa mediante observaciones espectropolarimétricas adquiridas con el instrumento *GREGOR Infrared Spectrograph* en el telescopio solar GREGOR. Su rango espectral nos permite mapear simultáneamente la cromosfera con la línea de He I 10830 Å y la fotosfera con la línea de Si I 10827 Å. Empezamos usando un modelo de

una sola componente para inferir las propiedades magnéticas del filamento. Dado que el filamento se encuentra sobre la granulación, uno no esperaría una fuerte contaminación desde abajo. Sin embargo, hemos encontrado evidencias observacionales de la necesidad de modelos más complejos para explicar las observaciones. Con esto demostramos de nuevo que el filamento es transparente incluso a la polarización circular generada por una cromosfera de apenas unos 200 G. Finalmente, en un esfuerzo por estudiar la viabilidad de las inversiones de dos componentes, mostramos que el modelo es demasiado flexible y puede reproducir las observaciones con un alto número de configuraciones de campos magnéticos, lo que hace la interpretación mucho más compleja.

Hasta ahora, el estudio magnético de filamentos y protuberancias se ha realizado usando los multipletes de He I en 10830 Å y 5876 Å. En la última parte de la tesis exploramos el potencial de la línea de Ca II en 8542 Å para el estudio de las propiedades magnéticas y dinámicas de filamentos solares. Para ello hemos utilizado el *Swedish Solar Telescope*, que consigue imágenes de una resolución espacial excelente y nos permite realizar mediciones espectropolarimétricas de la línea Ca II 8542 Å con el instrumento *CRisp Imaging SpectroPolarimeter*. Inferimos las propiedades de un filamento solar observado con este telescopio y discutimos la validez de los resultados debido a la suposición de equilibrio hidrostático usualmente incluida en los códigos de inversión. Para estudiar la dinámica global de la región y la evolución del filamento hemos utilizado otros telescopios como el *Chromospheric Telescope* y el *Solar Dynamics Observatory*. Mostramos que los métodos comúnmente usados en la fotosfera, como el *Local Correlation Tracking*, pueden no ser adecuados para estudiar el movimiento del plasma en la cromosfera. Finalmente, mostramos cómo un filamento solar a diferentes alturas puede generar perfiles de intensidad similares, demostrando que su altura no puede ser inferida a partir de inversiones espectroscópicas.

Finalmente, contextualizamos los resultados de este trabajo con la idea de buscar nuevas estrategias de observación que ayuden a determinar el campo magnético de los filamentos solares de una manera más fiable en el futuro.

Abstract

Solar filaments and prominences have been the focus of many studies for more than 200 years as they are one of the most fascinating phenomena of the Sun. However, only now, with the current instrumentation, computing power, and a consolidated theory of generation and transfer of polarized radiation can we study these structures with higher precision.

Prominences appear as cold plasma condensations suspended at high altitudes above the solar surface, with a filamentary structure. Instead of falling to the surface due to gravitational acceleration, they can remain suspended several weeks with little changes. The magnetic field is what seems to support these structures and, despite being such a fundamental ingredient, the knowledge about their exact topology and connectivity with the photosphere is currently poor. After all these years of study, filaments continue to present a challenge for observational analysis. The main reason is the difficulty of obtaining spectropolarimetric data with enough precision to study the weak polarization signals they generate and properly infer their magnetic field.

Since in this work we do not study filaments as isolated events, but also their connection with the environment, we present in the beginning of this thesis a general description of the structure of the Sun and the characteristic phenomena of each atmospheric layer. This allows us to understand the relationship between filaments and their environment. We also review the most relevant aspects of filaments and their magnetic nature.

The main objective of this work lies in the inference of the magnetic field in filaments from the polarization signals of spectral lines. To this end we make a short introduction about the basic ideas of radiative transfer that we apply in this thesis and how to use the polarization of spectral lines to infer the plasma properties. In addition, we discuss in depth the properties of the spectral lines used in this work, the He I 10830 Å multiplet and the Ca II line at 8542 Å, as well as the instrumentation and methods used to achieve the results of this work.

To gain some intuition on how the polarization is generated and to do a correct physical interpretation of the observations, we synthesize and study the polarization signals of the He I 10830 Å triplet for some interesting scenarios. In particular, we also analyze how the spectropolarimetric signals change when we have several structures in the line of sight, a common phenomenon when we observe the “grass” of spicules at the limb and each one contributes to the observed polarization. This effect is also important in observations on the disk where structures (such as filaments) are illuminated from below by a solar surface that has different magnetic properties with respect to such structures.

Up to now, the polarization signals received from active region filaments were analyzed as if they came directly from them, i.e., the signals were generated inside the filament, assigning magnetic field values much higher ($\sim$700 G) than those expected in similar structures on quiet areas ($\sim$20 G). Based on the idea that a filament illuminated by a highly magnetized active region could generate this misinterpretation, we propose a model with two atmospheric components in the same line of sight. This model makes it possible to explain observed polarization signals much more naturally. We conclude with this experiment that filaments are transparent to radiation coming from the solar surface. Consequently, the large magnetic field values may belong to the active chromosphere below the filament and not to the filament itself, questioning previous magnetic field inferences of these structures.

In the following, we study the magnetic topology of an active region filament from spectropolarimetric observations acquired with the instrument *GREGOR Infrared Spectrograph* installed at the GREGOR telescope. Its spectral range allows us to simultaneously map the chromosphere with the He I 10830 Å multiplet and the photosphere with the Si I 10827 Å line. We started using only one single component

model to infer the magnetic properties of the filament. Since the filament was above granulation, one would not expect strong contamination from below. However, we find observational evidences of the need for more complex models to explain the observations. This demonstrates again that the filament is transparent even to the circular polarization generated by a chromosphere of only about 200 G. Finally, in an effort to study the feasibility of two-component inversions, we show that the model contains too much freedom and it can reproduce the observations with a high number of magnetic configurations, making the interpretation very complex.

Until now, the magnetic study of filaments and prominences has been carried out using the multiplets of He I at 10830 Å and 5876 Å. In the last part of the thesis we explore the potential of the chromospheric Ca II line at 8542 Å for the study of the magnetic and dynamic properties of solar filaments. We have used the *Swedish Solar Telescope*, which obtains images of a remarkable spatial resolution and allows us to carry out spectropolarimetric measurements of the Ca II 8542 Å line with the *CRisp Imaging SpectroPolarimeter* instrument. We infer the properties of an observed solar filament and discuss the validity of the results due to the assumption of hydrostatic equilibrium to support the structure, usually included in inversion codes. To study the global dynamics of the region and the evolution of the filament, we have used other telescopes such as the *Chromospheric Telescope* and the *Solar Dynamics Observatory*. We show that commonly used methods in photospheric diagnostics, such as *Local Correlation Tracking*, may not be suitable for studying plasma motions in the chromosphere. In the last part we show how a filament at different heights above the solar surface can generate a similar intensity profile, demonstrating that its height cannot be inferred from spectroscopic inversions.

Finally, we put the results of this work in context with the idea of looking for new observation strategies that will help in the future to determine the magnetic field of solar filaments in a more reliable way.

Contents

1

Introduction

This thesis deals with the study of solar filaments and their connection with their environment. Here, we present a general description of the structure of the solar atmosphere and the characteristic phenomena of each atmospheric layer. This allows us to understand the environment of filaments and their relationship. The following section reviews the most relevant aspects of filaments and their magnetic nature. Finally, the structure and motivation of this work is indicated and will be developed in the following chapters.

1.1 Solar atmosphere

The energy produced inside the Sun by nuclear fusion is mainly transported to the outer atmosphere radiatively (or convection in a thin layer close and below the surface). The amount of solar energy that reaches the Earth is highly controlled by magnetic activity which generates phenomena at different scales: from sizes that are almost invisible to our largest telescopes to spectacular large scale high energy eruptions.

Any reliable prediction of space weather (see e.g. Bobra & Ilonidis, 2016, and references therein), important to avoid any damage to satellites in orbit around Earth or any disturbance in our technological society, requires an understanding of how energy is stored, transported and released into the magnetized solar atmosphere. A robust determination of the solar magnetic field in all atmospheric layers is thus mandatory. Therefore, studying the radiation emitted by the Sun and, in particular, the spectral lines that are sensitive to different atmospheric parameters (temperature, density, etc.), allows us to map the stratification of the solar atmosphere (see e.g. de la Cruz Rodríguez et al., 2016a, and references therein).

1.1.1 Photosphere

The photosphere is the layer in the solar atmosphere from where most of the photons escape in the optical continuum. This is mainly because the density decreases so fast that photons can travel almost freely to the Earth. The photosphere is a layer of about 500 km deep, with a temperature of about 6000 K. When the Sun is observed in the optical continuum or in photospheric spectral lines, the granulation pattern becomes evident. This pattern emerges as a result of convective motions that transport energy from the interior, resulting in bright granules where the plasma rises up, surrounded by darker, narrower intergranular lanes in which the plasma flows downward (Nordlund et al., 2009).

The most visible consequences of the magnetic field in the photosphere are bright magnetic points, pores, and sunspots (such as the one showed in panel a of Fig. 1.1). Recent studies have shown that there are not only strong concentrations of magnetic field at large spatial scales, but there also is a background magnetic field of about 100 G that permeates the entire surface, with concentrations of kG in tiny areas and small-scale magnetic loops (see Sánchez Almeida & Martínez González, 2011, for a review).

An important quantity when studying the solar atmosphere is the plasma-β parameter, which is defined as the ratio between the gas pressure and the magnetic pressure ($\beta = P_{\rm gas}/P_{\rm mag}$). This parameter informs us whether the evolution of plasma is dominated by convective motions or by magnetic forces. The photosphere has a high plasma-β with high densities in which collisions govern the formation of spectral lines and, therefore, the local thermodynamic equilibrium approximation (LTE) can be used (such as the Fe I 5434 Å displayed in panel a of Fig. 1.1).

1.1.2 Chromosphere

Following the radial direction outwards, the chromosphere is the layer above the photosphere, with higher temperatures of around 10^4 K. In the chromosphere, the pressure decreases by several orders of magnitude, so the plasma has a low β value and the magnetic force dominates the dynamics. Therefore, magnetic fields play a crucial role in the physics of the chromosphere and the corona. Among other phenomena, the magnetic field is the origin of the formation and evolution of various chromospheric structures such as solar prominences or filaments (focus of our study) and spicules. An example can be seen in panels c–e of Fig. 1.1, where in "a huge field of fiery grass" (Nagy, 2015), a compact filament appears at the bottom part of the area.

To understand these objects it is essential to compare the magnetic field vector inferred from the observations with the one derived from theoretical studies. Advances in this field of research have been hampered by several aspects of the chromosphere itself. First, the decrease of gas pressure leads to an expansion and subsequent attenuation of the magnetic field. Weak fields and low densities require spectropolarimetric measurements of even higher sensitivity than the ones for photospheric lines. Second, while typical velocities in the photosphere are of about $5\,\mathrm{km\,s^{-1}}$, in the chromosphere they can easily be an order of magnitude higher (due to the conservation of kinetic energy, $\rho v^2 =$const). Shocks can appear if the speed is above the sonic propagation speed c_s (Centeno et al., 2009; de la Cruz Rodríguez et al., 2013a). As a result, the exposure time to freeze the solar evolution for a large aperture solar telescope has to be very short (Lagg et al., 2017). To achieve these objectives, highly photon efficient instrumentation on large aperture solar telescopes such as the *Daniel K. Inouye Solar Telescope* (DKIST; Tritschler et al., 2015), or the *European Solar Telescope* (EST; Collados et al., 2013) is under development. Finally, the chromosphere is typically observed in the core of strong lines of the solar spectrum, such as Ca II 8542 Å (panel c of Fig. 1.1) or Hα 6563 Å (panel d of Fig. 1.1) lines. These spectral lines have such large opacities that the photons of the line core escape from the chromosphere while the photons of the line wing escape from the photosphere (e.g., panel b of Fig. 1.1 taken in the wing of the Ca II 8542 Åline). Due to the low density, collisional rates are lower, so the LTE approach is typically invalid for chromospheric lines, which is a challenge for the modelling of these lines (see de la Cruz Rodríguez & van Noort, 2017, for a review).

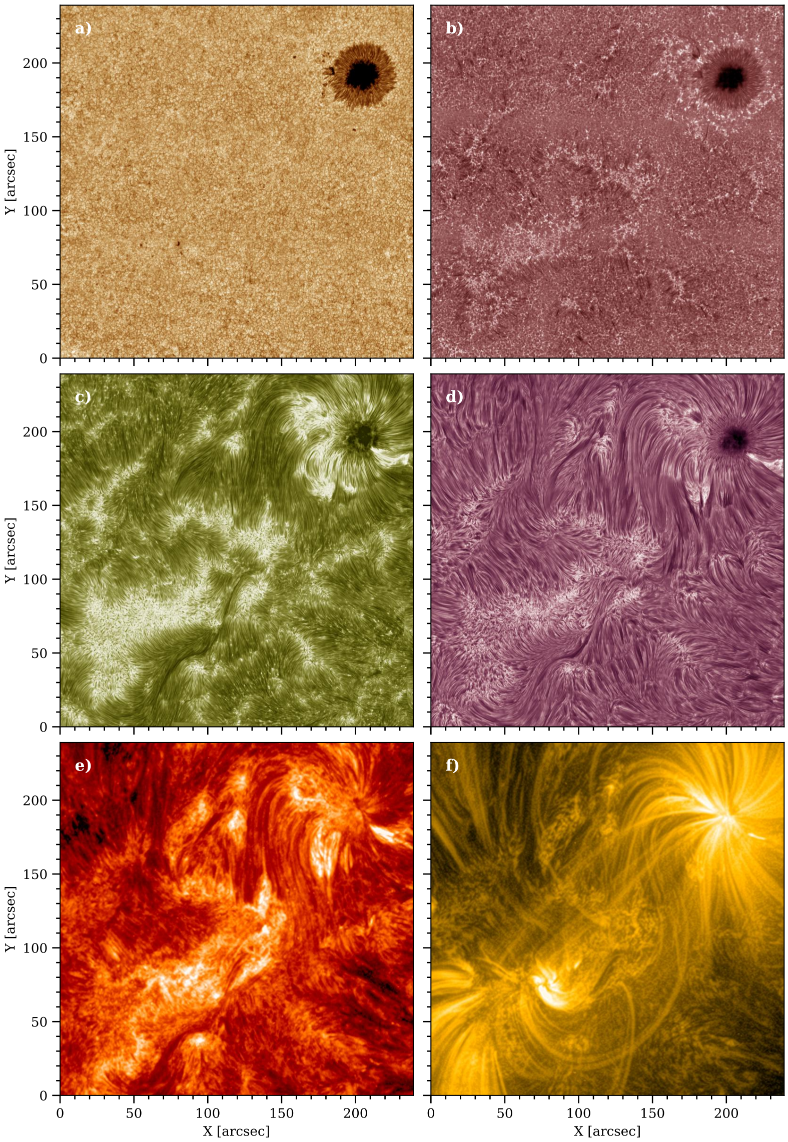

Figure 1.1 – Maps of the solar atmosphere from the photosphere to the corona from filtergram images at the following wavelengths: a) Fe I 5434 Å, b) Ca II 8542 Å wing, c) Ca II 8542 Å core, d) Hα 6563 Å, e) AIA 304 Å, and f) AIA 171 Å. Figure adapted from (Cauzzi & Reardon, 2012) and processed with the enhanced Multi-Scale Gaussian Normalization (MGN) algorithm (Morgan & Druckmüller, 2014).

1.1.3 Corona

The corona is the outer layer of the solar atmosphere and reaches temperatures of millions of degrees ($\sim 10^6$ K). The corona is located on top of the chromosphere with a thickness of a few solar radii, with a thin transition of about 200 km between these two layers, the so-called Transition Region (TR).

In the hot TR and corona all hydrogen (and helium) is ionized. Other ionized species, such as the Si IV and O IV, are the main diagnostic tools for many studies of the TR using data from the *Interface Region Imaging Spectrograph* (IRIS, De Pontieu et al., 2014). The hot corona is studied through spectral lines of highly ionized species such as Fe IX 171 Å (shown in panel f of Fig. 1.1) with space instruments such as the *Atmospheric Imaging Assembly* (AIA, Lemen et al., 2012) on board the *Solar Dynamics Observatory* (SDO, Pesnell et al., 2012). In these images, observable features of the corona are, for example, large-scale magnetic loops above active regions that are bright due to heating and density concentrations.

The reason why the chromosphere and the corona have such high temperatures is still under discussion today, a problem known as the coronal (and chromosphere) heating problem (for recent revisions, see, e.g., Parnell & De Moortel 2012; Klimchuk 2015). It seems evident that magnetic Alfvén waves can reach the corona while they are transporting energy that is dissipated in the plasma of the chromosphere and/or corona by other mechanisms. But additional sources of magnetic heating are also needed, for example, small-scale reconnection events. Even though most of these models seem plausible, none has been able to produce a quantitative measure of the energy produced without relying on parameters that were, at best, uncertain. Then, a combination of MHD modelling, radiative transfer modelling, and high-resolution observations of the chromosphere and the transition region is needed to advance on this problem and to gain a better understanding of the solar atmosphere.

1.2 Solar prominences

1.2.1 Introduction

In this section we discuss the actual focus of our research: solar filaments and prominences. They are fascinating, *large arch-shaped* magnetic structures on the Sun. They were first observed at the solar limb during total solar eclipses and recognized in terms of *lunar clouds* (Tandberg-Hanssen, 1998). In recent years, filaments have become an interesting topic of research in solar physics. However, they continue to be a puzzling subject, as their polarization signals are challenging to measure. Even more challenging is to infer the magnetic field that supports their material. For a more in-depth review of filament and prominence observations we recommend Parenti (2014), among others.

Filaments appear as dark thready structures seen on the disk as absorption in the core of some strong chromospheric lines (such as the above-mentioned Hα or Ca II lines), some weaker chromospheric lines such as the He I multiplets at 10830 Å and 5876 Å (D_3), and in the extreme ultraviolet (EUV) continua. They are called prominences when they are seen as diffuse bright clouds at the limb, as they scatter light from the underlying disk. These two terms are often used interchangeably in the literature since they refer, in principle, to the same phenomenon from different points of view. To clarify these concepts, Fig. 1.2 displays the typical body of an off-limb and on-disk filament in panel a and b, respectively.

From the thermodynamic point of view, they are cool chromospheric plasma over-densities embedded in the extremely hot and less dense corona, confined by magnetic fields anchored in the photosphere (Tandberg-Hanssen, 1998). Their body mainly consists of three structural components: a spine, barbs and two ends (Mackay et al., 2010; Panesar, 2014). The main long and horizontal body of the filament is known as the spine and it lies above a magnetic polarity inversion line (PIL; defined as the line that

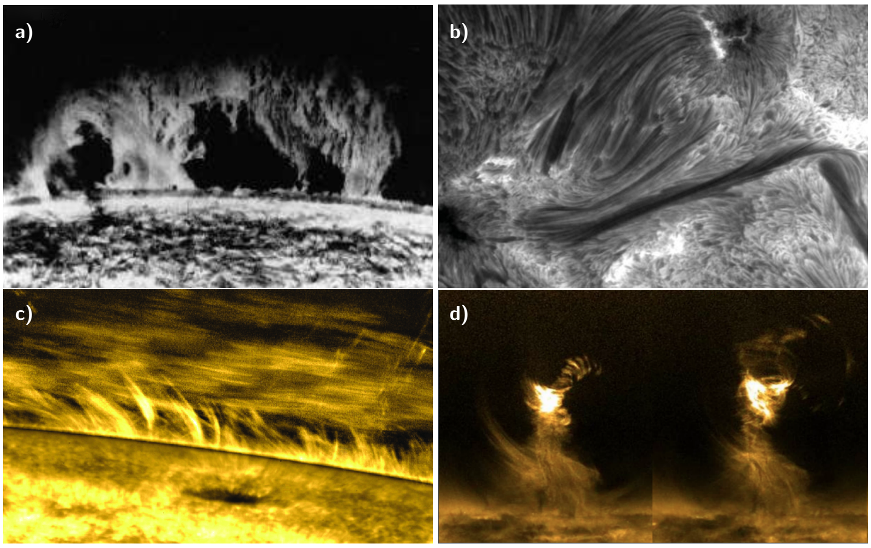

Figure 1.2 – a) Hα image of a prominence observed at *Big Bear Solar Observatory* obtained on 1995 November 22 (van Ballegooijen & Cranmer, 2010); b) an active region filament seen in Hα on disk, obtained from the *Swedish Solar Telescope* on 2003 August 22, (Lin et al., 2007); c) an active region prominence seen in Ca II H, obtained with *Hinode* on 2006 November 9 (Okamoto et al., 2007); d) a huge tornado-like feature captured by SDO in the channel AIA 171 Å on 2011 September 25 (Li et al., 2012).

delineates magnetic fields of opposite polarity, where the polarity is typically measured with the sign of the circular polarization). Barbs protrude from the sides of the spine toward both sides and they appear to be rooted in the photosphere as the legs of the filament. Sometimes the spine is not clearly visible, only the barbs can be seen as vertical dense pillars (Merenda et al., 2006; Martínez González et al., 2015). Finally, the beginning and end points of the filaments are known as ends or legs.

Prominences are often seen to be associated with coronal cavities. They are the upper coronal parts of filament channels. They appear darker than the surrounding corona, with a comparable temperature but less dense than the surroundings as it can be seen in Fig. 1.3. They can be observed in EUV images, above the PIL, with or without filament material, and are difficult to study because they are not always visible, depending on the orientation of the filament (Panesar, 2014).

The overall filament structure changes little with time, preserving its more o less homogeneous shape. However, locally they consist of fine plasma structures, known as threads, that evolve continuously. They can be detected with high resolution observations as they have a width of ~200 km (Heinzel, 2007) and they can be seen in the panels of Fig. 1.4. Space- and ground-based studies have estimated the thermodynamic properties of filaments using the above-mentioned spectral lines (Tziotziou et al., 2001; Stellmacher et al., 2003; Stellmacher & Wiehr, 2005; Tziotziou, 2007; Panesar, 2014; Mackay et al., 2010), finding temperatures in the range 6000–14000 K, a gas pressure of 0.1–1.0 dyn cm^{-2}, unresolved bulk velocities of ~5 km s^{-1} , and electron density values of 10^9–10^{11} cm^{-3}. From space they can be observed in the EUV as an enhanced hot layer surrounding the body of the structure known as prominence-corona transition region (PCTR) (Soler et al., 2007). In other lower chromospheric lines such as the Na I 5890Å D$_2$, filaments are very difficult to detect (Kuckein et al., 2016).

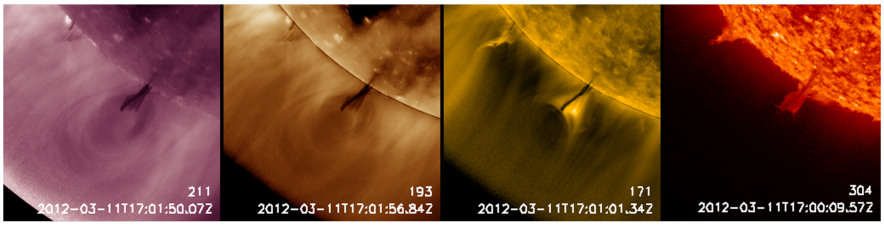

Figure 1.3 – Multi-wavelength images taken by SDO/AIA at 17:00 UT on 2012 March 11. Picture taken from Su et al. (2015). In this image, we can see the filament as a vertical structure surrounded by a dark cavity, easily detected in the coronal channels 211 Å, 193 Å and 171 Å.

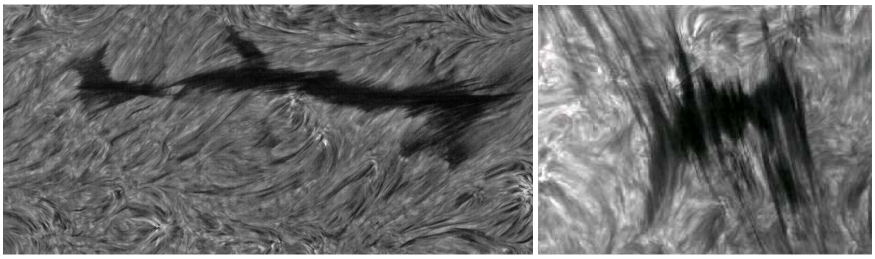

Figure 1.4 – High-resolution Hα filtrogram of two filaments. The fine-structure fibrils are clearly visible. Images taken from Lin et al. (2007) and Heinzel & Anzer (2006).

1.2.2 Filament classification

Filaments can be categorized by where they appear on the Sun. Depending on their location, they are generally considered to have different magnetic structures and formation processes. They differ in the amount of activity they display throughout their lifetime and the magnetic flux density found around them (Kilper et al., 2009). They range from *quiescent* (QS), when the filament has a stable size with a lifetime of up to a few months (i.e. several solar rotations) and a size of hundreds of Mm of length, to *active region* (AR) filaments, when they are formed on active regions or sunspots, develop at lower heights in the solar atmosphere ($<$10 Mm, Aulanier & Démoulin, 2003; Lites, 2005), have small lifetimes (hours to days), short lengths (over 10 Mm) and have magnetic fields superior to QS filaments (of severals tens of G). They are also very dynamic, mostly associated with flares and coronal eruptions. Sometimes the term *intermediate filaments* is used when no clear classification into quiescent or AR is possible (Mackay et al., 2010). Another subclass of QS filament is used when they are formed close to the solar poles and are called *polar crown prominences*.

QS filaments are easily detected at the limb with heights up to 200 Mm, but AR are hardly seen as prominences because they probably lie lower in the atmosphere (Mackay et al., 2010), and are hidden by a background of spicules of 6 Mm of height. Although the average length of filaments is around several tens of Mm, larger filaments exist ($>$600 Mm) but they are scarce (Kuckein et al., 2016).

Also, depending on the shape, we can distinguish between *hedgerow prominences*, which consist of thin vertical threads (van Ballegooijen & Cranmer, 2010), and prominences with horizontal threads such as those observed by Okamoto et al. (2016) (see panel c in Fig. 1.2). Another interesting type is the *tornado-*

like prominence[1] which appears as vertical spiral structure on the solar limb. The term solar tornado was introduced by Pettit (1932) and nowadays they are frequently observed because of the availability of both temporal and spatial high-resolution observations from the Solar Dynamic Observatory (SDO). With them, a controversy has arisen regarding whether the magnetic field is forming vertical, helical or predominantly horizontal structures. Concerning their dynamics, we still do not know if tornadoes are really rotating or the Doppler shifts are just a consequence of plasma oscillations or flows (Su et al., 2014; Schmieder et al., 2015; Martínez González et al., 2016).

1.2.3 Filament models

In this section we summarize some of the most important filament models. These models try to answer some of the basic questions about their formation and balance, such as how cold plasma rises to these heights or how do they live for so long. In all prominence models, the solar magnetic field plays a fundamental role in the formation, support, and eruption of these structures. The topology of the magnetic field is a key ingredient because the magnetic force can balance the solar gravitational force and support the plasma in places where the fields are upward-curved, forming dips. Although it is such a fundamental ingredient, the details of the topology of the magnetic field in the filaments are not well known.

Generally, in the literature (Gilbert et al., 2002; Kuckein et al., 2012a) models are divided into twisted and non-twisted field scenarios. However, due to the great variety of models, we think it makes sense to discuss about them according to two characteristics: the different magnetic topologies and formation, and the mechanism for filling the filament channel with material.

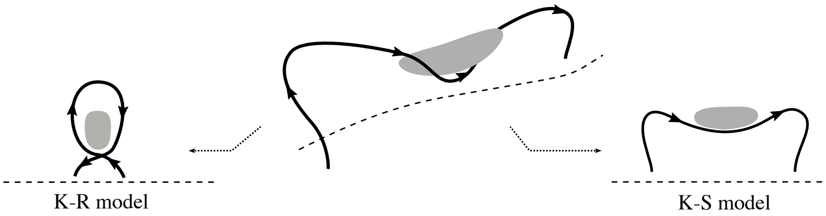

Figure 1.5 – Scheme of a 3D slightly twisted sheared arcade interpreted from two different views as two different 2D models. Figure adapted from one Lecture courtesy of Dr. Magara Tetsuya (`http://web.khu.ac.kr/~magara`).

Magnetic models and formation

The first theoretical models were developed to explain how to support the material and to understand the magnetic topology of the filament with respect to the photospheric magnetic field. The field configuration is called normal polarity (NP) if the field lines of the filament follow the same direction as the photospheric field lines, and if it is opposite it is called inverse polarity (IP) configuration. Two important and opposite simple 2D models emerged: the K-S model (Kippenhahn & Schlüter, 1957) which has NP configuration, and the K-R model (Kuperus & Raadu, 1974) which has an IP configuration. However, even being remarkable and precise models to explain the support of the material, they only represent different 2D aspects[2] of the three-dimensional magnetic structure of a filament as we can see from Fig. 1.5.

---

[1] This terminology should be used to describe the barbs of the prominence. However it is used for the whole structure when there is not material in the filament channel.

[2] The model on the left of the figure does not have an inverse polarity as the real K-R model, but is enough to represent the complexity of 2D vs 3D interpretations.

Since then, more complex 3D models have emerged. For example, the *sheared arcade model* (Antiochos et al., 1994) (see panel a of Fig. 1.6) is generated due to a shear motion of the footpoints in opposite directions, that causes the rise up of the field, generating an arcade (or dip) whose horizontal component is capable of supporting the plasma. The dipped lines are free of twist or slightly twisted and Aulanier et al. (2002) showed that IP and NP configurations can be found in the same filament. A similar scenario is known as *flux linkage model* (Martens & Zwaan, 2001) where a shear produces, by reconnection of several magnetic fields, a new and longer body (such as the one detected on polar crown prominences).

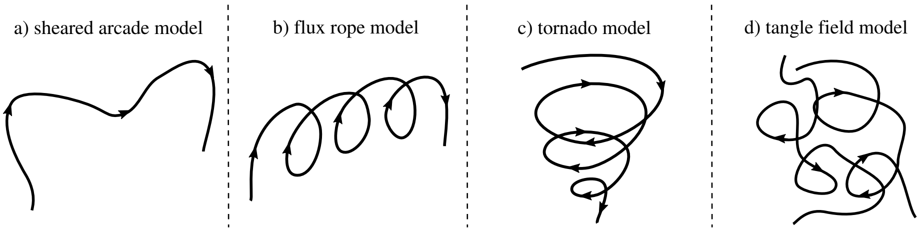

Figure 1.6 – Scheme of the magnetic topology of some of the most relevant 3D models. The details of each one are explained in the text.

Another important 3D model is the *flux rope model* (see panel b of Fig. 1.6) that is believed to be responsible for plasma support especially in AR filaments. It is defined as a group of helical flux tubes which carry the prominence material in their local dips. According to van Ballegooijen & Martens (1989), a flux rope can be formed by shearing motions along the PIL and eventually reconnecting with other sheared field lines to form a flux rope. This topology usually has an inverse polarity with respect to the photosphere, but Demoulin et al. (1989) found that it is also possible to generate different configurations in flux ropes: NP at the top of the helix if another dip is present and IP at the bottom (see also Xu et al. 2012 for an observational interpretation).

It is also possible to generate a flux rope by emergence from the photosphere below (Lites, 2005). This latest model has been supported by numerous recent studies such as Xu et al. (2012); Okamoto et al. (2016), detecting evidences of the emergence of the structure or helical topologies (Martínez González et al., 2015). Another example of the complexity of these models is the possibility of coexisting flux rope and dipped arcade sections along the same solar filament (Guo et al., 2010).

Finally, a new topology has also been proposed to explain the tornado-like prominences. In this *tornado model* (see panel c of Fig. 1.6) the Lorentz force can indeed support the plasma if the magnetic structure is sufficiently twisted and/or significant poloidal flows are present (Luna et al., 2015). In the same way, a *tangled magnetic field model* (see panel d of Fig. 1.6) with many dips (van Ballegooijen & Cranmer, 2010) has been proposed to explain the support of hedgerow prominences, with the observed vertical threads being the result of the Rayleigh-Taylor instability (Khomenko et al., 2014).

Therefore, neither the polarity with respect to the photosphere, nor their photospheric motions, are characteristics that can distinguish among models. On the contrary, these features are compatible with several models and magnetic reconnection can even transform one model into another. This topology controversy is also connected with the dynamics of the filament. For example, Zirker et al. (1998) identified streaming and counter-streaming flows in a filament in both spines and barbs. After that, the same "pattern" has been observed by other authors (Lin et al., 2003; Diercke et al., 2018) and it is interpreted as plasma flows along not dipped magnetic flux tubes. On the other hand, authors such as Heinzel (2007), insist on that any analysis of 2D images can lead to misinterpretations just because of the lack of a fully 3D dynamical pattern and the counter-streaming could be explained with oscillations rather than flows along threads. For this reason, it is very important to study the magnetic field topology from spectropolarimetric observations and check between the large variety of existent models.

Origin of the filament material

For more than 30 years, we have known that the large masses that hold the prominences should come from the chromosphere because there is not enough plasma in the corona to fill them (Saito & Tandberg-Hanssen, 1973). Then, to provide material to the filament channel we can mainly distinguish three mechanisms: injection, levitation, and evaporation-condensation (Mackay et al., 2010).

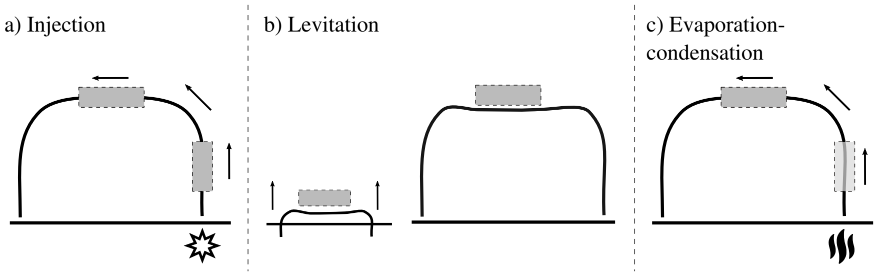

Figure 1.7 – Scheme of the three main mechanism which provide material to the filament channel. The details of each one are explained in the text.

On the one hand, in the *injection model* (panel a of Fig. 1.7), the cold plasma is forced upwards, by reconnection in the lower solar atmosphere, with sufficient speed to reach the heights of the filament channel. This mechanism could be associated with AR filaments as they are low lying and reconnection events are more frequent in active regions (Chae, 2003). On the other hand, in the *levitation model* (panel b of Fig. 1.7) the plasma is lifted by rising magnetic fields at the PIL. This levitation of material could be happening when a highly twisted flux rope emerges from the photosphere (Rust & Kumar, 1994) or when U-shaped field lines are generated by reconnection (Welsch et al., 2005). Finally, *evaporation-condensation models* (panel c of Fig. 1.7) are based on the fact that concentrated heating near the footpoints of the loop should produce a cool condensation at the apex. As the radiative losses increase with the density, the material reaches a critical point and it condensates catastrophically by this thermal instability (Antiochos et al., 1994). This process does not require the presence of dipped field lines (although it facilitates the retention of the plasma), as they are formed by the material itself (Keppens & Xia, 2014). This mechanism is associated with QS filaments since it shows (when it is analyzed in simulations) characteristics such as lifetime and size achieved similar to the observed ones. Moreover, this process can be cyclic, i.e., the prominence mass is not static but maintained by condensation at a high rate, comparable to the drainage rate of the prominence. Therefore, a macroscopic QS prominence can be microscopically dynamic in the sense of a continuous mass feed that counteracts mass drainage along the threads (Tandberg-Hanssen, 1998; Liu et al., 2012).

Consequently, for the study of prominences it is necessary not only to use 3D models of such structures, but also realistic MHD simulations including thermal conduction and radiative losses effects (Keppens & Xia, 2014). They can also be used for generating synthetic spectropolarimetric observations, trying to distinguish between the mechanisms mentioned above.

Magnetic field measurements

All these theoretical models must be constrained by the empirical determination of magnetic fields in prominences. Many works have studied prominences with the aim of determining magnetic fields using spectro-polarimetry. However, the magnetic field vector is very difficult to constrain observationally since it requires high precision spectropolarimetric measurements and the interpretation of signals coming from the joint action of scattering polarization and the Hanle and Zeeman effects[3].

The magnetic field has been studied since the 1970s and early 1980s. The first measurements[4] were done by Leroy et al. (1977, 1983) with coronographs in the Pic du Midi observatory (France) and Sacramento Peak observatory (USA) with very limited spatial resolution. In their prominences they measured a magnetic field strength within 3-15 G using the He I 5876 Å (D$_3$) multiplet, almost horizontal and with a small azimuthal angle ($\sim$30°) with respect to the long axis of the structure. After these first daring efforts and using other telescopes such as THEMIS at the Observatorio del Teide, Paletou et al. (2001) also reported full-Stokes observations of a limb prominence in He D$_3$, and derived magnetic field strengths of 30-45 G. Later, Casini et al. (2003) published the first vector-field map of a QS prominence with an horizontal magnetic field of 10-20 G and with the magnetic vector pointing 20-30° off the prominence axis. Barbs were also interpreted as a series of local horizontal dips sustaining plasma at different heights (López Ariste et al., 2006).

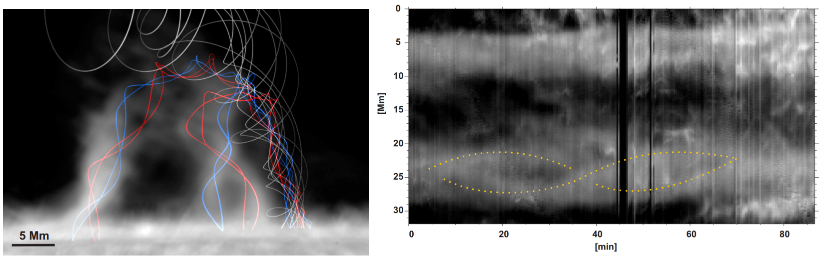

Figure 1.8 – Left: Artistic representation of the 3D magnetic field recovered from the observations with the intensity in the He I 10830 Å as a background image. Right: Space-time variations of Hα intensity for an artificial slit parallel to the limb across the helical structure. Dotted yellow lines trace the periodic movement of the two fibrils in the double-helix. Figures taken from Martínez González et al. (2015).

In contrast, vertical fields have been also diagnosed in prominences. Merenda et al. (2006) observed in He I 10830 Å a polar crown prominence above the limb and found evidence for fields of about 30 G oriented just 25° from the vertical direction. Recent studies have tried to break the controversy of whether the magnetic field is vertical or horizontal, but a vertical or horizontal magnetic field generate similar polarimetric signals under these conditions. Only some studies have achieved this goal by using additional physical constrains, such as Martínez González et al. (2015), by taking into account the stability of the structure. An example is shown in Fig. 1.8.

All these studies have created a "picture" of what we know about QS solar prominences, always with magnetic fields strengths of the order of a few tens of G (Casini et al., 2003; Merenda et al., 2006; Orozco Suárez et al., 2014; Martínez González et al., 2015). However, there are fewer studies about on-disk filaments (e.g., Lin et al., 1998; Collados et al., 2003; Merenda et al., 2007; Kuckein et al., 2009; Sasso

---

[3] These concepts will be explained in detail in the next chapter.

[4] In this section, the term measurement refers to the inference of the magnetic field from remote sensing instruments by interpreting signals directly influenced by the solar magnetic field, as it cannot be measured in situ.

et al., 2011). Most of these measurements are restricted to a single view and this makes difficult to link between what we measure at the limb (prominences) and what we measure on the disk (filaments).

Moreover, AR filaments lie lower in the atmosphere and cannot be observed at the limb because they can be confused with spicules. This, combined with the fact that they have been found under a higher variety of conditions, generates a debate about the characteristics of these structures. For example, Kuckein et al. (2009) studied the magnetic field vector of an active region filament above a strongly magnetized region and found the highest field strengths measured in filaments to date, with values around 600−700 G. After that, Sasso et al. (2007, 2011) studied an active region filament during its phase of increased activity, finding values for the magnetic field strength in the range 100−250 G. Also, Xu et al. (2012), who studied the same filament as Sasso et al. (2011), but before the eruption, found a section of the filament above the granulation with weak inferred magnetic fields ($\sim$100 G) and a second section above a strongly magnetized area, which returned much higher magnetic fields ($\sim$700 G).

Therefore, the question that we will discuss in the following chapters is whether this variety is intrinsic to AR filaments or, on the contrary, there is a bias in the interpretation of the spectro-polarimetric observations.

Prominence seismology

Analyzing spectropolarimetric observations is not the only way to study the magnetic field of solar filaments. When the filaments are perturbed by solar energetic events such as distant or nearby flares, jets, and eruptions, these triggers produce large amplitude oscillations (LAOs) which involve motions with velocities above 20 $\mathrm{km\,s^{-1}}$ (Oliver & Ballester, 2002) and large portions of the filament move in phase, reflecting global characteristics of its plasma and magnetic field structure. These oscillations (see right panel of Fig. 1.9) offer a new method for estimating the magnetic field of the prominence by combining observations and theoretical modeling through a technique known as *prominence seismology*. Several studies have started to obtain impressive results (Luna & Karpen, 2012; Bi et al., 2014; Zhang et al., 2017; Luna et al., 2017). In the future it would be also interesting to improve the estimation of the magnetic field inferred from spectropolarimetric observations with the values obtained through this technique. This is a wide new topic that is beyond this work, but we recommend the review of Arregui et al. (2012) if more information is needed.

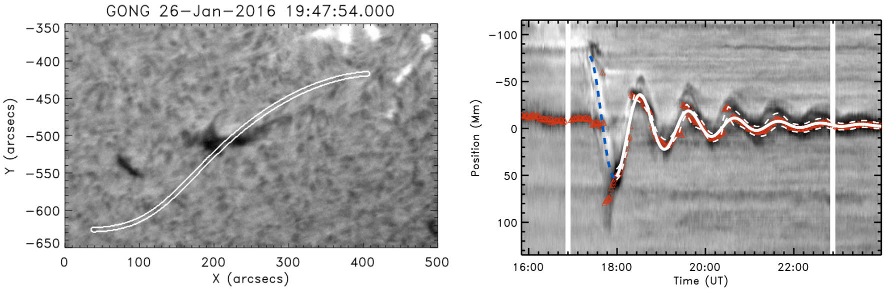

Figure 1.9 – A plot of the Hα data after the eruption of a filament is displayed in the left panel. The white contour shows the artificial curved slit used to construct the time-distance diagram in the right panel. Images adapted form Luna et al. (2017).

Neutrals and ions

Another important characteristic of filaments is their composition. The cold filament material is mainly composed of hydrogen and helium, partially ionized due to the relatively low temperature. A clear example of the presence of these neutral atoms is the observation of filaments in spectral lines such as Hα, He I 10830 Å, or Ca I 4227 Å (Nikol'Skii & Khetsuriani, 1970; Gilbert et al., 2002)

In previous sections we explored several different magnetic models to explain how cool, dense plasma can be supported. However, the neutral component of the plasma is not affected by the restoring magnetic forces. In the past, it has been proposed that the frictional coupling between ions and neutrals is the main mechanism that produces the support for the neutral species. Gilbert et al. (2002) showed that the draining effect for a hydrogen–helium plasma is rather small. They found that the drainage timescale for the neutral hydrogen is 20 times longer than for the neutral helium, in agreement with the differences detected in comparisons between Hα and He I images. Besides elastic ion–neutral collisions, another mechanism to consider is the charge exchange process where a proton captures the electron of a neutral. Terradas et al. (2015) used a multi-fluid approach implementing both effects finding that the charge exchange mechanism is about three times more efficient at sustaining neutrals than elastic scattering between ions and neutrals.

The conclusion of these experiments is that while the ions are supported by the magnetic field against gravity and are essentially static, neutrals have a very small downflow velocity. The existence of these drifts between species is thus a direct consequence of the partial ionization, and reflects that the coupling between the fluids is not strong enough for them to behave as a single fluid. To detect these effects, it is then necessary to measure as accurately as possible the velocity of different species simultaneously at the same spatial position. For instance, Khomenko et al. (2016) analyzed a prominence which was oscillating (see left panel of Fig. 1.10) with spectra of the ionized Ca II 8542 Å line and the neutral He I 10830 Å line. The drift velocity between them showed patches of non-zero drift velocity with a typical size of about 2″ and with lifetimes of about 1 minute (right panel of the same figure).

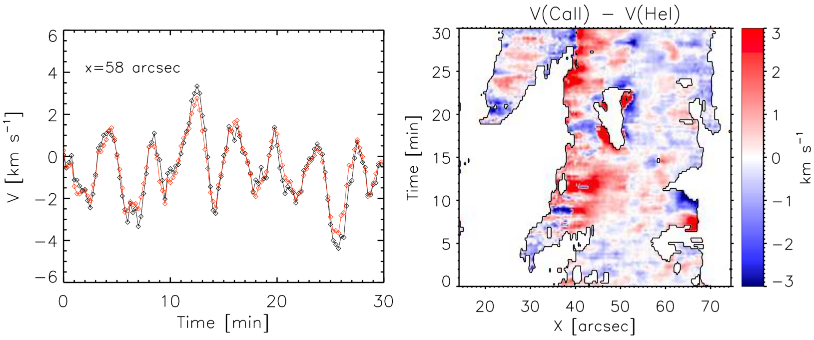

Figure 1.10 – Left: time series of velocity variations for a fixed position along the slit where black lines are Ca II velocities and red lines are He I velocities. Right: drift velocity as a function of time and distance along the slit. Both figures are taken from Khomenko et al. (2016).

Filament eruption

When prominences become unstable, the whole energy stored in their magnetic field is suddenly released leading to an eruption[5]. The material can be ejected resulting in a *coronal mass ejection* (CME) or returned back to the surface. Several studies have focused on determining the mechanism which drives filament eruptions such as the twist of the field lines, the speed of the event, the size of the cavity, the height of the filament, or their mass composition (e.g., Filippov & Den, 2000, 2001; Guo et al., 2013; Gibson, 2015). An example, taken by the *Transition Region and Coronal Explorer* telescope (TRACE, Strong et al., 1994), is displayed in Fig. 1.11. If the twist of a flux rope filament is increased, there is a critical point (helical kink instability) where the filament becomes unstable. Nevertheless, emerging flows, as well as shearing motions close to the PIL, are also responsible for the destabilization of the filaments. As the present study is not focused on the filament eruption, we will not go into deeper details. However, understanding these processes requires precise measurements of the magnetic field both in filaments and their environment, as well as the dynamics of the region which surrounds the filament, the two main ingredients of the topic of this work.

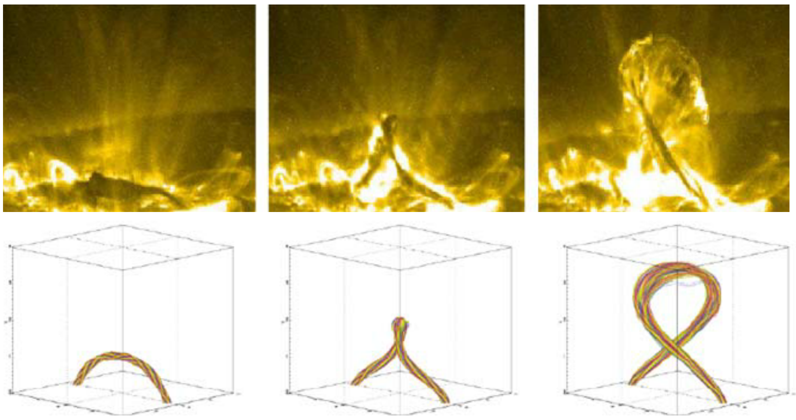

Figure 1.11 – Upper row: TRACE 195 Å images of the confined filament eruption on 2002 May 27. Lower row: magnetic field simulation of a kink–unstable flux rope. Images adapted from (Török & Kliem, 2005)

1.3 Motivation and overview

Throughout this first chapter we have explained how magnetic fields govern plasma dynamics in the outer layers of the solar atmosphere. The same magnetic field supports and determines the evolution of solar filaments. Therefore, the measurement of the magnetic field is essential to identify the precise topology of these structures. Many theoretical models have been proposed to understand their characteristics, but only in recent years have we been able to approach the problem with new high-resolution and very sensitive polarimetric observations. Thus, this work opens the door to a better understanding of this common but complex solar phenomenon.

---

[5] Movie sequences of quiescent and erupting prominences can be found at the STEREO Web site `https://stereo.gsfc.nasa.gov/gallery/selects.shtml`

Throughout Chapter 2, we summarize some theoretical concepts of radiative transfer and spectral line formation used in this work. We also present the general characteristics of the two studied spectral lines: He I 10830 Å and Ca II 8542 Å, as well as the characteristics of the telescopes and instruments for the observations and the methods of data reduction and post-processing. In Chapter 3 we introduce the models used for the interpretation of polarimetric signals. Later, in Chapter 4 we present the analysis of an active region filament measured on the He I 10830 Å line and the limitations of using single component models for its study. Chapter 5 is dedicated to the analysis of a second filament measured on the Ca II 8542 Å line and the problem of using the hydrostatic equilibrium approach during its investigation. Finally, Chapter 6 outlines the main conclusions and presents the perspective for future works.

2

Diagnostic techniques

In this chapter we start describing the basic ideas of radiative transfer needed in this thesis and how to use the polarization of the spectral lines to infer the properties of an astrophysical plasma. We continue discussing the properties of the spectral lines used in this work: the He I 10830 Å multiplet and the Ca II line at 8542 Å. Finally, we present in detail the instrumentation and the methods used to achieve the results of this work.

2.1 Spectral line polarization

In the previous chapter we have shown the complexity of the solar atmosphere, and how in order to study it we need precise and powerful diagnostic tools. Since our main source of information is the light that reaches us from the Sun, our goal is to extract the encoded information in this radiation field. For this purpose, we have to study all the properties of the radiation, i.e., not only the intensity of the radiation as a function of wavelength (spectroscopy), but also its state of polarization, which contains information about the preferred direction of the electric and magnetic field vibrations carried by the electromagnetic wave. The plane which contains these vibrations, is orthogonal to the direction of propagation of the light, and the phase relationship between the two orthogonal components of the electric field vector in this plane defines the state of polarization. For example, if these components vibrate in phase there is only a direction of vibration and the light is described as linearly polarized. Circularly polarized light occurs if this phase is $\pm\pi/2$ (and the amplitude of these component is the same) since the vibration describes a circular motion, and depending on its sign it can rotate clockwise or anti-clockwise. For a general case, the light is elliptically polarized since the end-point of the electric field vector traces out an ellipse. Finally, if the phase changes randomly with time, the light is called unpolarized.

These privileged directions of vibration contain information about the medium where the light was emitted, such as, the magnetic fields we want to analyze. These electromagnetic properties can be efficiently described with only 4 observables (which we will explain later in Sec. 2.1.1), and by studying them for different spectral lines of the spectrum, we can map different regions of the solar atmosphere at several heights, as each line is formed under different atmospheric conditions. For this reason spectral line polarization is so useful for astrophysical plasmas diagnostics. Understanding the mechanisms that generate this polarization (such as the Zeeman effect, scattering processes, and the Hanle effect) is the purpose of the following sections (we recommend Degl'innocenti & Landolfi 2004 for a detailed review).

2.1.1 Stokes parameters

The state of polarization can be conveniently described using four measurable quantities. These observables are the four Stokes parameters (I, Q, U, V) whose definition is schematically shown in Fig. 2.1. The Stokes $I(\lambda)$ profile represents the intensity as a function of wavelength. Given a reference direction, Stokes $Q(\lambda)$ is the difference between linear polarization at $+0°$ and $+90°$. Stokes $U(\lambda)$ is the difference between linear polarization at $+45°$ and $-45°$. Finally, Stokes $V(\lambda)$ is the difference between the right- and left-handed circular polarization. Note that the definition of Stokes Q and U requires choosing a reference direction for $Q > 0$ in the plane perpendicular to the propagation direction. To measure these quantities, there are optical devices such as linear polarizers, which allow the transmission of the component of the electric field that oscillates along a given direction (transmission axis) while the perpendicular component is filtered out, and retarders, which modify the phase of the orthogonal components of the electric field. Through a smart configuration of these devices, all four Stokes parameters can be measured almost simultaneously. From these parameters, we can infer quantitative information about the magnetic field (among other aspects) by analyzing the fingerprint generated by each physical mechanism.

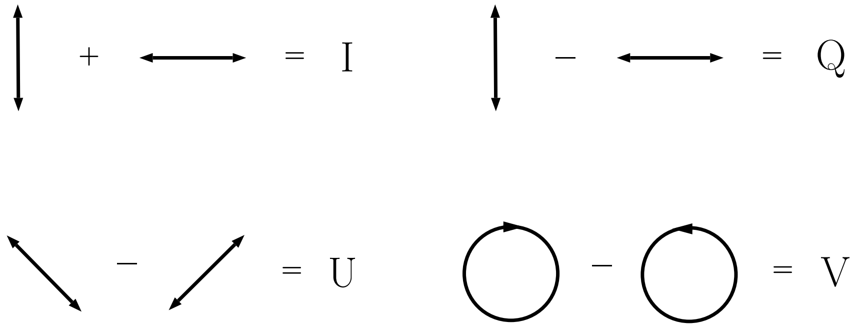

Figure 2.1 – Schematic representation of the definition of the four Stokes parameters, for which the vertical direction has been taken as the direction for positive Stokes Q. The observer is assumed to be facing the radiation source. Figure adapted from Degl'innocenti & Landolfi (2004). The arrows represent the pictorial definition of the intensities differences mentioned in the text. In fact, the Stokes I parameter can be defined in the same way as Stokes Q, U or V but with a '$+$' sign instead of a '$-$' sign.

2.2 Radiative transfer equation

The radiation from the Sun has traveled throughout the solar atmosphere to reach our detectors. Therefore, it is not only important to know how these signals are generated, but also how they evolve and interact with the environment they traverse. This requires calculating the excitation state of the atoms within the plasma, as well as their interaction with the light generated in the atmosphere under certain magnetic and thermodynamic conditions.

The calculation of the emergent radiation field in any astrophysical plasma requires the solution of the *radiative transfer equation* (RTE) of the full Stokes vector $\mathbf{I} = (I, Q, U, V)^{\dagger}$ (with the superscript † denoting the transpose) that depends on the frequency ν and the direction of propagation of the ray $\boldsymbol{\Omega}$. The RTE describes how the radiation (and its polarization) propagates through the medium. This set of equations is written in a vectorial form as:

$$\mathrm{d}\mathbf{I}/\mathrm{ds} = \boldsymbol{\epsilon} - \mathbf{K}\mathbf{I} \tag{2.1}$$

where s is the geometrical distance along the ray under consideration along the direction $\boldsymbol{\Omega}$, $\boldsymbol{\epsilon} = (\epsilon_I, \epsilon_Q, \epsilon_U, \epsilon_V)^{\dagger}$ is the emission vector that accounts for the contribution of the spontaneous emission process and $\mathbf{K}$ is the 4×4 propagation matrix. The expanded form of the RTE equation is as follows:

$$\frac{d}{ds}\begin{pmatrix} I \\ Q \\ U \\ V \end{pmatrix} = \begin{pmatrix} \epsilon_I \\ \epsilon_Q \\ \epsilon_U \\ \epsilon_V \end{pmatrix} - \begin{pmatrix} \eta_I & \eta_Q & \eta_U & \eta_V \\ \eta_Q & \eta_I & \rho_V & -\rho_U \\ \eta_U & -\rho_V & \eta_I & \rho_Q \\ \eta_V & \rho_U & -\rho_Q & \eta_I \end{pmatrix} \begin{pmatrix} I \\ Q \\ U \\ V \end{pmatrix}, \tag{2.2}$$

The propagation matrix contains two contributions $\mathbf{K} = \mathbf{K}^{\mathrm{A}} - \mathbf{K}^{\mathrm{S}}$, where $\mathbf{K}^{\mathrm{A}}$ results from transitions from the lower-level towards the upper-level (absorption), while $\mathbf{K}^{\mathrm{S}}$ is the contribution caused by the stimulated emission process. The stimulated emission is written as a negative absorption as it depends on the radiation field as does the absorption. The matrix $\mathbf{K}^{\mathrm{A}}$ (or $\mathbf{K}^{\mathrm{S}}$) can be decomposed into three different contributions: the diagonal (η_I) which is the attenuation (or amplification) of the radiation beam irrespective of its polarization state; the dichroism, which takes into account the effect of a selective absorption (or amplification) of different polarization states (η_{QUV}), and the dispersion which describes the attenuated (or amplified) dephasing between different polarization states (ρ_{QUV}). The general expressions of the emission vector and propagation matrix components are very complicated and will not be reproduced here (see section 7.6 of Degl'innocenti & Landolfi, 2004, for the explicit expressions for a multi-term atomic model). However, some simplified cases will be shown to understand the polarization generated in some cases of interest. Since this section is a brief introduction to this field, we recommend the following references to the reader if more information is needed: Trujillo Bueno (2003); del Toro Iniesta (2003); Degl'innocenti & Landolfi (2004).

2.2.1 Zeeman effect

A spectral line is the result of a radiative transition between two different atomic levels characterized by the quantum numbers S, L, and J (at least in LS coupling) with the consequent absorption or emission of a photon. These quantum numbers describe the total spin, the orbital angular momentum, and the total angular momentum of the electronic configuration, respectively. Each energy level (S, L, J) has $(2J + 1)$ sublevels characterized by their magnetic quantum number $M = +J, ..., -J$. The polarization induced by means of the energy separation of the atomic energy levels into different magnetic sublevels caused by the presence of a magnetic field is known as Zeeman effect. As a result, a spectral line between a lower energy level with (J_l) and an upper level with (J_u) is composed of several individual components, usually referred as Zeeman components, from a sublevel (J_l, M_l) to another (J_u, M_u) sublevel. These new components are shifted in wavelength with respect to the original transition because the magnetic field modifies the energy of the sublevels. This splitting in wavelength (and energy, $\Delta\lambda = hc/\Delta E$) $\Delta\lambda_{B[M_u,M_l]}$ depends on the magnetic field strength B and the wavelength λ_0 of the transition:

$$\Delta\lambda_{B[M_u,M_l]} = \frac{\lambda_0^2 eB}{4\pi m_e c^2}(g_l M_l - g_u M_u). \tag{2.3}$$

The symbols g_l and g_u are the Landé factors (g_J) of the involved levels and they are calculated by a simple expression which only depends on the level quantum numbers (S, L, J). This theory and expressions assumes spin-orbit coupling (LS coupling), which is valid when the electrostatic interaction between the individuals electrons is stronger than the individual spin-orbit interaction (see section 3.1 of Degl'innocenti & Landolfi, 2004, for a better description). In this expression e, m_e and c are the charge and mass of the electron, and the speed of light, respectively. For an electric dipole transition, the selection rules allow only transitions with $\Delta L = \pm 1$, $\Delta S = 0$, $\Delta M = M_u - M_l = \pm 1, 0$, and $\Delta J = J_u - J_l = \pm 1, 0$ (except $J_u = 0 \rightarrow J_l = 0$). The transitions are classified in π ($\Delta M = 0$), σ_b (blue component, $\Delta M = +1$), and σ_r (red component, $\Delta M = -1$). In general, the fine structure of the Zeeman pattern (individual transitions with the same ΔM value) cannot be spectrally resolved, and they are treated as equivalent Zeeman triplets having an unshifted π component and two symmetrical σ component shifted by:

$$\Delta\lambda = \frac{\lambda_0^2 eB}{4\pi m_e c^2}\bar{g}B. \tag{2.4}$$

where $(\bar{g})$ describes the sensitivity of the circular polarization of the transition to the magnetic field by a single number called the effective Landé factor, which is calculated as a combination of those of each atomic level:

$$\bar{g} = \frac{1}{2}\,(g_l + g_u) + \frac{1}{4}\,(g_l - g_u)[J_l(J_l+1) - J_u(J_u+1)]\ . \tag{2.5}$$

The Zeeman effect is usually more sensitive to the circular polarization[1, 2], quantified by the Stokes V parameter. The Zeeman-induced polarization sensitive to the line-of-sight component of the magnetic field, is known as *longitudinal Zeeman effect* and has an antisymmetric spectral shape. The shape of Stokes V comes from the sign and the splitting of the red and blue components and can be understood with the expression of the emissivity in Stokes V given by:

$$\epsilon_V = \frac{h\nu}{4\pi} N_u A_{ul} \frac{1}{2}[\phi_r - \phi_b]\cos\Theta_B\ , \tag{2.6}$$

where Θ_B is the angle between the magnetic field vector and the LOS, A_{ul} is the Einstein coefficient for the spontaneous emission processes, N_u the number of atoms per unit of volume of the upper level, and ϕ_r and ϕ_b are the superposition of all the individuals Voigt (H) profiles of the σ_r and σ_b components respectively, which are displaced to the red or blue side of the central wavelength λ_0. The later can be written as $\phi = \sum_i s_i H(\lambda - \lambda_0 - \Delta\lambda_{B_i})$, where the sum extends to those transitions with the same ΔM value. From dependence on the angle of inclination in the previous equation we see that a magnetic field pointing towards and away from the observer produces signals of opposite signs. Then, if we have a turbulent magnetic field with both polarities within the same resolution element, we would observe null circular polarization.

The Zeeman-induced polarization to the transverse field relative to the line of sight, is referred to as the *transverse Zeeman effect* and generates linear polarization (quantified by Stokes Q & U parameters).

---

[1] This is true when the magnetic field is not highly inclined with respect to the LOS as it will produce a weak circular polarization signal

Linear polarization signals are usually weaker than circular polarization signals[2]. Linear polarization signals have a three-lobe spectral shape that can be understood as the combination of two symmetrically shifted σ components and an unshifted π component with opposite sign. It can be seen from the Stokes Q and U components of the emission vector:

$$\epsilon_Q = \frac{h\nu}{4\pi} N_u A_{ul} \frac{1}{2} \left[\phi_\pi - \frac{\phi_r + \phi_b}{2} \right] \sin^2 \Theta_B \cos 2\Phi_B \ , \tag{2.7}$$

$$\epsilon_U = \frac{h\nu}{4\pi} N_u A_{ul} \frac{1}{2} \left[\phi_\pi - \frac{\phi_r + \phi_b}{2} \right] \sin^2 \Theta_B \sin 2\Phi_B \ , \tag{2.8}$$

where Φ_B is the angle between the projection of the magnetic field vector on the plane perpendicular to the line-of-sight and the reference direction for $Q > 0$. Panel A of Fig. 2.2 illustrates the typical shape of a Zeeman linear polarization profile and the π and σ components in a transition with $J_l = 0$ and $J_u = 1$. As the populations of the three sublevels are assumed to be the same, the positions of each component, drawn as dashed lines, generate the 3-lobed profile of the figure: the π component at the center and the σ components at each side.

2.2.2 Paschen-Back effect

The above-mentioned theory of the Zeeman effect is valid under the LS coupling. However, for strong enough magnetic fields, the spin S and the orbital angular momentum L are decoupled. In this case the energy separation between the magnetic sublevels (M_J) of the same J-level is comparable to the energy separation of different J-levels and there is level crossing. In the He I 10830 Å multiplet, the transition between the Zeeman and the Paschen-Back regimes lies between 400 G and 1500 G (Socas-Navarro et al., 2004). This transition is also known as *incomplete* Paschen-Back regime. If this effect is not taken into account in the inference of the magnetic field, the magnetic field strength could be underestimated by more than 20% (Sasso et al., 2006) since mainly the amplitudes of the Zeeman components are strongly reduced in the Paschen-Back effect.

2.2.3 Atomic level polarization

In the absence of a magnetic field, there is no Zeeman splitting and in the polarization all the Zeeman components cancel out because there is no wavelength shift between them. This can be seen in panel B of Fig. 2.2, where we have drawn the product $\rho_X \phi_X$ (with $_X$ the π, r and b components) in dashed lines. This cancellation takes place because the contributions of the σ and π components to the emissivity have opposite signs, as we showed in Eq. 2.7.

However, this is only true if the population of each sublevel is identical. If this is not the case, there is not a complete cancellation and we can generate polarization without magnetic field (zero Zeeman splitting). This can happen simply because, for example, the strength of the σ transitions is larger than that of the π transition due to the difference in populations (see panel C and D of Fig. 2.2). This can be understood from the Stokes Q & U components of the emissivity for a $J_u = 1 \rightarrow J_l = 0$ transition, given by:

$$\epsilon_Q = \frac{h\nu}{4\pi} 3A_{ul} \frac{1}{2} \left[\rho_\pi \phi_\pi - \frac{\rho_r \phi_r + \rho_b \phi_b}{2} \right] \sin^2 \theta \cos 2\chi \ , \tag{2.9}$$

---

[2] This is understood when we solve the RTE through a Taylor expansion of the Stokes parameters and circular polarization appears at the first order, while linear polarization appears at the second order. This is valid in the weak field approximation which considers that the Zeeman splitting is much smaller than the typical width of the line without magnetic field (see Sec. 9.6 of Degl'innocenti & Landolfi, 2004, for more details).

$$\epsilon_U = \frac{h\nu}{4\pi} 3 A_{ul} \frac{1}{2} \left[\rho_\pi \phi_\pi - \frac{\rho_r \phi_r + \rho_b \phi_b}{2} \right] \sin^2\theta \sin 2\chi \, , \tag{2.10}$$

where θ is the angle between the solar radius vector of the observed point and the line of sight, χ is the angle from the $Q > 0$ reference direction, and ρ is the population of each upper-level sublevel. Then, we can generate polarization if at least one of the levels (upper or lower) can develop population imbalances among the sublevels. If it is in the lower level, the process is called *selective absorption* (Trujillo Bueno et al., 2002) and if it is the upper level it is called *selective emission*. This phenomenon is known as *atomic level polarization* (e.g., Stenflo, 1994; Degl'innocenti & Landolfi, 2004). We want to note that the lower levels are usually long-lived and elastic collisions can eliminate the atomic polarization. However, the lower-level atomic polarization is relevant in several solar cases (Trujillo Bueno et al., 2002), in particular for the magnetic study of filaments because for absorption structures is the mechanism which generates polarization in the blue component of the He I 10830 Å.

The most important types of atomic level polarization are two: alignment and orientation. We have atomic alignment when the population imbalances occur between the Zeeman substates of a level with different absolute values of the magnetic quantum number $|M|$ (see panel C of Fig. 2.2); and atomic orientation between substates of equal absolute M (see panel D of Fig. 2.2). Moreover, the concept of atomic polarization includes also the possibility of quantum interference (or coherence) among the magnetic sublevels of each J-level, and even among those belonging to different J-levels (Stenflo & Keller, 1997). Therefore, there more types of atomic level polarization, but they do not have any special designation.

As a graphical summary, Fig. 2.2 displays the typical linear polarization profiles generated by different mechanisms for a transition between a lower level $J_l = 0$ and an upper level $J_u = 1$. Atomic polarization can also generate circular polarization introducing imbalance between the σ components. However, the mechanism for generating atomic orientation and hence circular polarization is less common in the Sun.

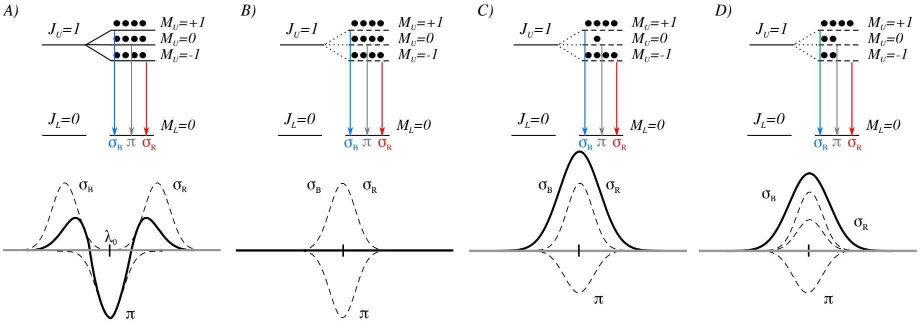

B≠0, Zeeman effect
Stokes Q&U

B=0, No polarization
Stokes Q&U

B=0, Atomic polarization
(alignment)
Stokes Q&U

B=0, Atomic polarization
(orientation & alignment)
Stokes Q&U

Figure 2.2 – Illustration of the Stokes Q and U parameters generated in an emission process by several mechanisms. From left to right: A) the Zeeman effect has three lobes in the linear polarization due to the energy splitting; B) without magnetic field and equally populated sublevels, there is no polarization; C) with population imbalances among the $|M|$ sublevels (atomic alignment); D) with population imbalances among the M sublevels (atomic orientation). Here, the σ_X symbols represent the product of $\rho_X \phi_X$ for each component and they are drawn as dashed lines. The combinations of components according to equations 2.7-2.10 give the profile drawn as a solid line.

2.2.4 Anisotropic radiation pumping

The main mechanism which induce population imbalances in the solar atmosphere is the anisotropic illumination. While in the Sun's interior an ensemble of atoms is isotropically illuminated, in the outer atmospheric layers of the Sun the outgoing radiation is larger than the incoming radiation. This effect is enhanced by the center-to-limb variation of the radiation field[3]. Then, this "degree of anisotropy" is a fundamental quantity in scattering polarization and is quantified by $A = J^2_0/J^0_0$ where J^0_0 is the *mean intensity* and J^2_0 is the *anisotropy* given by:

$$J^0_0 = \frac{1}{4\pi}\int \mathrm{d}\nu \oint \mathrm{d}\mathbf{\Omega}\; \phi_\nu\, I_{\nu,\mathbf{\Omega}}\;, \tag{2.11}$$

$$J^2_0 \approx \frac{1}{4\pi}\int \mathrm{d}\nu \oint \mathrm{d}\mathbf{\Omega}\; \frac{1}{2\sqrt{2}}\,(3\mu^2-1)\,\phi_\nu\, I_{\nu,\mathbf{\Omega}}\;, \tag{2.12}$$

with $I_{\nu,\mathbf{\Omega}}$ the Stokes I as a function of frequency and direction $\mathbf{\Omega}$, $\mu = \cos\theta$, with θ the polar angle with respect to the local vertical axis and ϕ_ν the absorption line shape. The anisotropy J^2_0 can be understood as follows: predominantly vertical rays, i.e. with $\mu > 1/\sqrt{3}$ make a positive contribution, while predominantly horizontal rays, i.e. those with $\mu < 1/\sqrt{3}$ make a negative contribution. The angle corresponding to $\mu = 1/\sqrt{3}$ ($\theta \approx 54.7°$) is known as Van Vleck's angle and separates both contributions. As a consequence, J^2_0 is a competition between predominantly vertical and predominantly horizontal intensities. The integral of J^2_0 has also another term related with a linear polarized illumination which is often neglected as it is smaller than the intensity term (Trujillo Bueno, 2006) or a unpolarized illumination is considered (Asensio Ramos et al., 2008).

It is important to point out that the larger A, the larger the induced atomic polarization. The anisotropy factor, defined as $W = \sqrt{2}A$ (Trujillo Bueno, 2006), can vary between $W = -1/2$ for a pure horizontal radiation field and $W = 1$ for a pure unidirectional and vertical illumination. As J^0_0 is always positive (see Eq. 2.11), then W (or A) reflects the sign of J^2_0. In general, the anisotropy increases with the height in the atmosphere (as it is displayed in the left panel of Fig. 2.3) as the illumination cone which is illuminating the ensemble of atoms is narrower as we move away from the surface.

After showing that the radiation received by a high-altitude ensemble of atoms is almost unidirectional from below, we will now see how we generate population imbalances. To understand the importance of this anisotropic pumping we present the simple case of a pure unidirectional unpolarized light beam that illuminates a gas of two-level atoms with $J_l = 1$ and $J_u = 0$ (Trujillo Bueno, 2003). Since these atoms can only absorb ± 1 units of angular momentum from the light beam, only $\Delta M_l = \pm 1$ are effective transitions and no transitions occur from the $M_l = 0$ sublevel to the upper level. Thus, after the spontaneous relaxation, the atomic system have a higher population with $M_l = 0$. Figure 2.3 displays a scheme of this situation in the right panel. This selective absorption process due to the illumination of the light coming from the underlying atmosphere has a preferred direction and the scattered radiation will have this polarization imprint.

For unpolarized illumination without any azimuthal dependence only J^0_0 and J^2_0 are needed to characterize the radiation field. However, in the most general case all spherical tensor components J^K_Q (with $K = 0, 1, 2$ and $-K \leq Q \leq K$) are needed to quantify the radiation field. Their explicit form are described for example in Sec. 5.11 of (Degl'innocenti & Landolfi, 2004).

---

[3] Depending on the spectral line and its formation height, the center-to-limb variation can be different because of the increase of the temperature in the outer atmosphere, and the anisotropy can be produced by the limb-darkening or by the limb-brightening.

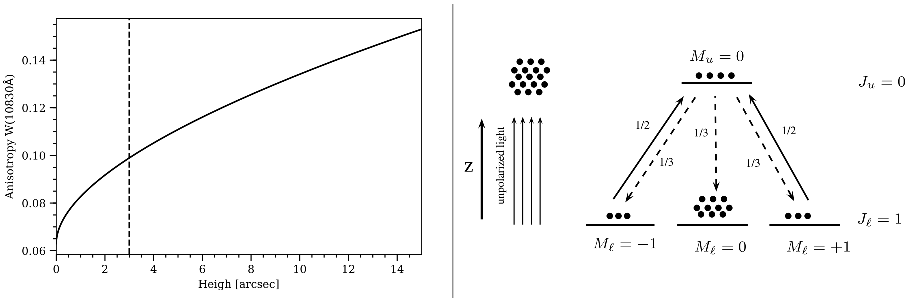

Figure 2.3 – Left panel: it shows how the anisotropy factor increases with the height at 10830 Å. A dashed line at 3″ is drawn indicating the typical height of chromospheric structures. Right panel: sketch of the radiation pumping mechanism which generates population imbalances between different $|M|$ sublevels.

We describe the explicit form of the spherical tensor J_0^1 due to its importance and relation to the following chapters:

$$J_0^1 = \frac{1}{4\pi} \int \mathrm{d}\nu \oint \mathrm{d}\boldsymbol{\Omega} \, \sqrt{\frac{3}{2}} \, \mu \, \phi_\nu V_{\nu,\boldsymbol{\Omega}} \tag{2.13}$$

with $V_{\nu,\boldsymbol{\Omega}}$ being the Stokes V as a function of frequency and direction $\boldsymbol{\Omega}$. This tensor generates net circular polarization through atomic orientation and, as we see from Eq. 2.13, to be a non-zero quantity it requires a circularly polarized illumination.

2.2.5 Hanle effect

The Hanle effect is the modification of the atomic polarization caused by the action of a magnetic field inclined with respect to the symmetry axis of the pumping radiation field. With respect to the zero magnetic field case, the Hanle effect changes the amplitude and rotates the pre-existent atomic polarization. Depending on the scattering geometry and on the topology of the magnetic field, the Hanle effect can either destroy or create linear polarization in spectral lines (see e.g., Degl'innocenti & Landolfi, 2004; Trujillo Bueno, 2001, 2006, for a review).

The reason why this effect is important in solar filaments (the focus of our work) is that since they are located at a considerable height, the radiation which illuminates anisotropically the structure coming from the solar surface produces atomic polarization and then the presence of a magnetic field inside the filament changes this expected polarization.

The magnetic field produces a measurable change in the atomic polarization via the Hanle effect when its strength produces a Zeeman splitting of the order of the natural width of the spectral line. This critical Hanle field intensity (B_H) can be calculated as (in gauss):

$$B_H = 1.137 \times 10^{-7} / (t_{\text{life}} g_J) \ , \tag{2.14}$$

where g_J and t_{life} are the Landé factor and the lifetime of the level (in seconds), respectively. Since the lifetime of upper levels are usually much smaller than those of the lower levels for the most of the relevant transitions (as they usually are a ground or a metastable[4] level), diagnostic techniques based on the lower-level Hanle effect are sensitive to much weaker fields.

---

[4] A metastable level is a level whose radiative transition (under the selection rules of a electric dipole) to a lower level is forbidden. As a consequence its lifetime is very large.

The application of Eq. 2.14 to typical spectral lines shows that the Hanle effect allow us to diagnose magnetic fields with strengths between milligauss to hundreds[5] of gauss, i.e., a parameter domain that is very hard to study via the Zeeman effect in the chromosphere. Therefore, the Hanle effect will be the main diagnostic tool for detecting the weak magnetic fields of solar filaments.

The Hanle effect has a more complex dependence with the magnetic field than the Zeeman effect. For example, there is a range of magnetic field strengths with $B \gtrsim 10B_H$ (called saturation regime) where the emergent linear polarization only depend on the orientation of the magnetic field vector. In this regime, the dependence of the Stokes profiles on the field geometry is similar to the Zeeman regime. The main difference is the role of the local vertical, associated to the scattering. We can see this in the expression of the linear polarization (for a $J_l = 0 \rightarrow J_u = 1$ transition in the saturation regime for the Hanle effect):

$$\epsilon_Q = q_0(3\cos^2\theta_B - 1)\sin^2\Theta_B\cos 2\Phi_B\ , \tag{2.15}$$

$$\epsilon_U = q_0(3\cos^2\theta_B - 1)\sin^2\Theta_B\sin 2\Phi_B\ , \tag{2.16}$$

where q_0 contains the dependence on the scattering geometry in absence of a magnetic field (Martínez González et al., 2015). This expression depends on both the angle between the local vertical and the magnetic field θ_B and the one between the line of sight and the magnetic field Θ_B.

The Zeeman and Hanle effects are highly complementary because they are sensitive to different magnetic field regimes, allowing the Zeeman effect to measure large field strengths by Zeeman splitting, or via the Hanle effect to very weak fields when such splitting is comparable to the inverse of the lifetime of the atom (Trujillo Bueno et al., 2004). In conclusion, depending on the spectral line and the magnetic field, the mechanisms involved in the formation of the polarization change as it is well illustrated in the Fig. 2.4.

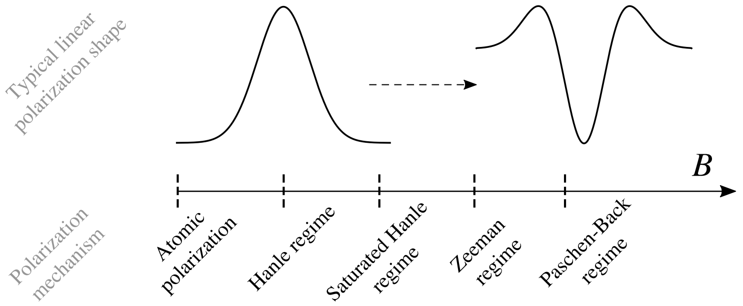

Figure 2.4 – Scheme of the mechanisms and polarization shapes involved at different magnetic field strengths.

2.2.6 Magnetic ambiguities

In both the Zeeman and Hanle regimes, there are magnetic configurations which generate similar or even identical polarimetric signals. A brief description is given here and a detailed study of them is done in the next chapters during the analysis of the observations (Chapter 4).

From Eq. 2.3 for the Zeeman effect we see that we can modify the azimuth Φ_B in the form $\Phi_B \pm 180^\circ$ and the solution remains the same because of the term $\cos 2\Phi_B$. This is known as the fundamental Zeeman

---

[5] Note that some spectral lines can have even a higher critical magnetic field strength, being sensitive to thousand of gauss, such as the the He II line at 304 Å which has a critical field of $B_H \sim 850\,$G.

180 ambiguity. The Hanle effect introduces additional potential ambiguities with the term $(3\cos^2\theta_B - 1)$ of the Eq. 2.15 as we can now modify also the magnetic inclination in the local θ_B and sky frame Θ_B. They are known as the 90 Van Vleck ambiguities. Then, in the Hanle saturation regime we have the following potential ambiguities: Φ_B, $\Phi_B + 180$, $\Phi_B + 90$, $\Phi_B - 90$ and the corresponding inclination can be calculated with the strategy presented in Martínez González et al. (2015). If the polarity of the field is not measured by the detection of Stokes V signals, the number of potential ambiguous solutions can increase up to eight (also increases up to four in the Zeeman case).

These ambiguities can be solved with additional constraints. For example, for a sunspot (Schad et al., 2013; Joshi et al., 2016) we can impose that the expected magnetic field must be radial. However, the field solutions in filaments and prominences are very difficult to disambiguate. A good example of this is found in Martínez González et al. (2015), where they imposed some physical constrains on the stability of the structure to reject some of the inferred ambiguous configurations.

2.2.7 Statistical equilibrium equation

From the beginning we have shown the importance of atomic populations $\rho_J(M,M)$ and their imbalances for generating polarization signals. Due to the quantum nature of the atom, the energy sublevels can be also coupled. The quantum coherence between different magnetic sublevels M and M' pertaining a given J-level is expressed as $\rho_J(M,M')$. A matricial representation to take into account all these quantities is used, called *atomic density matrix*. As we have seen (in a simplified manner), the elements of the emission vector $\boldsymbol{\epsilon}$ and and the propagation matrix $\mathbf{K}$ are given in terms of the density matrix elements.

Usually, the density matrix is better described in the irreducible spherical tensor representation, which provides a more compact and intuitive description. This representation is also useful to take advantage of symmetries of the problem. In this basis, the components ρ^K_Q, are linear combinations of the density matrix elements shown before, where $K = 0, \ldots, 2J$ and $-K \leq Q \leq K$. All the explicit equations of these terms can be found in Sec. 3.7 of Degl'innocenti & Landolfi (2004). For instance, ρ^0_0 is proportional to the total population, ρ^1_0 the atomic orientation, and ρ^2_0 the atomic alignment. To obtain the ρ^K_Q values, one can solve the *statistical equilibrium equations* (SEE) assuming these quantities do not change with time (approximation due to the timescales in our problems):

$$\frac{\mathrm{d}\rho^K_Q(J)}{\mathrm{dt}} = \left[\frac{\mathrm{d}\rho^K_Q(J)}{\mathrm{dt}}\right]_{\mathrm{mag}} + \left[\frac{\mathrm{d}\rho^K_Q(J)}{\mathrm{dt}}\right]_{\mathrm{coll}} + \left[\frac{\mathrm{d}\rho^K_Q(J)}{\mathrm{dt}}\right]_{\mathrm{rad}} = 0 \tag{2.17}$$

which we have split into three terms according to its contribution to the change of the populations (del Pino Alemán, 2015), i.e., these ρ^K_Q elements are determined by the atmospheric conditions: the magnetic field, the plasma thermodynamics (collisions), and the radiation field. Note that each ρ^K_Q value of a $J-$level is strongly coupled with the other multipole components of the same level and with the other energy level of the transition. Therefore, Eq. 2.17 is strictly a system of equations which describes the interactions between the two (or more) energy levels.

In the solar photosphere, densities are high such that the level populations are controlled by inelastic collisions and can be accurately described by the approximation of *local thermodynamic equilibrium* (LTE). Then, it is not necessary to solve the statistical equilibrium equations as the collisions depolarize the atomic sublevels, destroying population imbalances and coherences, and as a result there can be no atomic level polarization. The total population can be quantified by the Saha-Boltzmann equations, being the term ρ^0_0 the only non zero. In conclusion, the radiation in LTE can only be polarized by magnetic fields via Zeeman effect.

As the density diminishes in the upper solar atmosphere, the collisional rates decrease while the photon mean free path increases. The level populations start to decouple from LTE as the radiative rates start to control the equilibrium, allowing the generation of atomic polarization. If we add a magnetic field, it will reduce and dephase the coherence between the sublevels via Hanle effect. Then, chromospheric lines are formed under non-LTE (NLTE) conditions and the computational effort to calculate the emergent Stokes parameters is larger than with LTE-lines as we have to solve the whole SEE.

As the populations depend also on the radiation field, and to solve the RTE we need the populations, these quantities are coupled and this process has to be solved iteratively. Therefore, we need to find the self consistent ρ^K_Q values by solving iteratively the non-local and non-linear system of equations of the elements of the atomic density matrix and the Stokes-vector transfer equations.

This procedure is usually started by assuming a first estimation of the ρ^K_Q values (for example, LTE populations) and then solving the RTE (Eq. 2.2) to obtain new J^K_Q values which can be used to calculate again the ρ^K_Q values (Eq. 2.17). This cycle is repeated until convergence, in which the solution does not vary significantly between iterations. Once the ρ^K_Q values are known at each point within the medium, it is possible to formally solve the RTE to obtain the emergent Stokes profiles.

2.3 Chromospheric spectral lines

To infer the physical conditions of the solar chromosphere, we need to use spectral lines that are sensitive to this layer. Unfortunately, there are only a few spectral lines with sufficient opacity to sample this layer and their modeling is usually complex. Therefore, which line to use as a diagnostic tool is a compromise between the modeling effort of the line and the sensitivity required to measure the polarization signals (see de la Cruz Rodríguez & van Noort 2017 for more information).

The selection of lines observable from Earth is even smaller because ground based observations are limited to visible and infrared wavelengths where the Earth atmosphere is transparent to the radiation. The most common chromospheric diagnostics are perhaps the Ca II H & K lines (3934 Å & 3968 Å), the H I 6563 Å line (Hα), the Ca II infrared triplet lines (IR, 8489 Å, 8542 Å & 8662 Å), the Ca I 4227 Å, and the He I 5876 Å (D$_3$) and 10830 Å lines. There are also other strong ultra-violet chromospheric lines but they have to be observed from space and their diagnostic capabilities have been less explored: the H I 1216 Å line (Lyα), Mg II h & k lines (2796 Å & 2804 Å), the He II 304 Å line, and more. To get some insight on the formation height of each line in the solar atmosphere, Fig. 2.5 illustrates the surface $\tau = 1$ at the line center of some of them as computed from a 3D MHD simulation (de la Cruz Rodríguez & van Noort, 2017).

For instance, the pair of lines Ca II H (3969 Å) and Ca II K (3933 Å) are formed in the middle-upper chromosphere and they constitute the strongest lines in the visible spectrum. Other chromospheric lines such as Mg II h & k, H I Lyα forms below the TR, and are also influenced by 3D radiative transfer effects as well as partial-coherent scattering, also known as *partial frequency redistribution* (PRD)[6]. Some studies (Sukhorukov & Leenaarts, 2017; Bjørgen et al., 2017) have included both effects only in intensity and have shown their importance for accurate diagnostics motivated by observations in Mg II h & k from IRIS (De Pontieu et al., 2014), measurements in H I Lyα obtained by CLASP (Kubo et al., 2014), and Ca II H & K from CHROMIS observations at the Swedish 1-m Solar Telescope. Recently, de la Cruz Rodríguez et al.

---

[6] PRD includes the fact that there is a correlation between absorbed and emitted photons in frequency (being the most extreme case the coherent scattering). The atomic levels of the line transition are weakly perturbed by elastic collisions to be able to retain information about the last absorption process. This is true in low density layers of the solar atmosphere such as the chromosphere. Including this effect is very computationally intensive.

(2016a) have implemented a NLTE inversion code taking into account PRD (not in 3D) in these lines with impressive results.

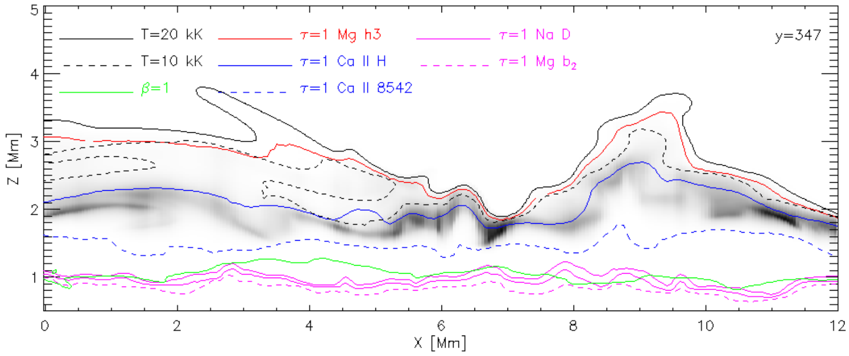

Figure 2.5 – Slice from a 3D MHD simulation indicating the $\tau = 1$ surface at line center for Mg II h3 & b2, Ca II H & 8542 Å, and Na I D. The contribution function of the He I 10830 Å triplet is rendered in grey-scale because it is optically thin. Figure courtesy of M. Carlsson (Institute for theoretical astrophysics, University of Oslo) taken from de la Cruz Rodríguez & van Noort (2017).

Hα (6563 Å) is one of the most popular lines to study the solar chromosphere, as its core is formed in the middle chromosphere. The crucial ingredient to obtain a reliable intensity profile is the full 3D geometry in the radiative transfer calculations as the source function decouples from the local temperature and mainly depend on the radiation emitted from below. This line can be safely modeled in *complete frequency redistribution* (CRD)[7] with some approximations Leenaarts et al. (2012). However, this line is not well suited for implementations of non-LTE inversions because the RTE problem has to be computed in 3D in order to reproduce the observed intensities, something that is not affordable in terms of computing time.

The Ca I 4227 Å line is the one with the largest linear polarization signals in the solar limb visible spectrum produced by scattering processes. It is a very broad line and its core is formed in the low chromosphere. At such heights and densities, PRD effects are essential and create complex and strong polarization signals in the wings of the spectral line. Motivated by recent spectropolarimetric observations, several studies have been carried out (Bianda et al., 2011; Anusha et al., 2011; Carlin & Bianda, 2017; Alsina Ballester et al., 2018) investigating the potential of the Hanle and Zeeman effects in this spectral line to infer the weak magnetic fields of the chromosphere.

Finally, in the infrared region there are the two spectral lines used in this work and arguably the most suitable to infer thermodynamic and magnetic chromospheric properties: the Ca II at 8542 Å and He I triplet at 10830 Å. Both can be modelled assuming CRD and statistical-equilibrium, which greatly simplifies the modeling.

---

[7] The CRD is an approximation in which during line scattering there is no correlation between the absorbed and the emitted photons. CRD requires the atomic levels of the line transition to be strongly perturbed by elastic collisions with other atoms. This is true in dense layers of the atmosphere such as the photosphere or low chromosphere. The CRD approximation strongly simplifies analytical and numerical solutions of the radiative transfer problem in such lines.

2.3.1 He I 10830 Å

The He I 10830 Å multiplet occurs between the atomic levels 2^3S_1 and $2^3P_{2,1,0}$[8]. It comprises a "blue" transition at 10829.09 Å with $J_l = 1$ and $J_u = 0$, and two "red" transitions at 10830.25 Å with $J_l = 1$ and $J_u = 1$ and at 10830.34 Å with $J_l = 1$ and $J_u = 2$, which are blended at temperatures typical of the solar atmosphere. A Grotrian diagram for He I is displayed in the left panel of Fig. 2.6 with the fine structure diagram shown in the right panel. The three transitions within the 10830 Å multiplet have been colored according to their classification in the right panel of the same figure.

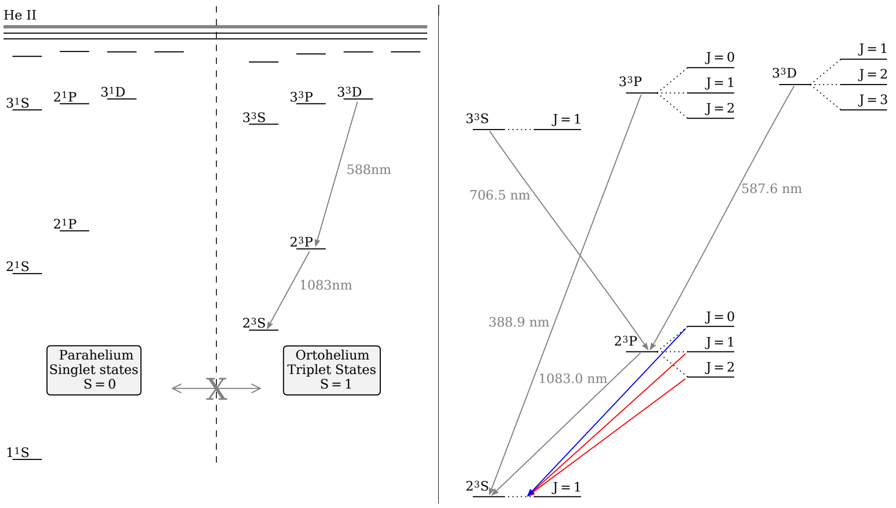

Figure 2.6 – Grotrian diagram for the helium atom. *Left panel:* Global scheme of the helium singlet and triplet states. *Right panel:* zoom of the triplet states and description of the model atom used in this investigation with their J-levels. The three transitions within the 10830 multiplet have been colored according to their classification.

This multiplet has gained attention mainly due to two major breakthroughs: developments in detector technology have allowed for spectropolarimetric observations with signal-to-noise ratios as large as 10^4, and the theoretical understanding of how the polarized light arises from selective absorption and emission processes (e.g. Trujillo Bueno et al., 2002, and references therein). Since then, this multiplet have been increasingly used to infer the magnetic field vector in the solar chromosphere. Another advantage of this spectral window is that this line is blended with the red wing of the nearby strong Si I 10827.1 Å line that can be used to infer the photospheric thermodynamic and magnetic ($\bar{g} = 1.5$) conditions simultaneously. It is also important to mention the He I triplet D_3 at 5876 Å whose lower level is the upper one of the 10830 Å (see Fig. 2.6). Both lines have similar characteristics but D_3 is less used due to its lower absorption. To understand the formation of these lines it is necessary to explain the atomic structure of the helium atom because the formation process is significantly different than those spectral lines of the previous sections.

The fundamental state of helium has two electrons 1s. In an excited state, one electron is in the ground state 1s and the second can be in a higher state with opposite spin (with total momentum $S = 0$, called singlet, and para-helium in this atom) or parallel to the other electron (where the total momentum is $S = 1$,

---

[8] We are using the standard terminology $n^{2S+1}L_J$, where n is the principal quantum number, S the total spin, L the angular quantum number ($S = 0, P = 1, D = 2, ...$) and J the total angular momentum

called triplet or ortho-helium). The ground state of the atom is a singlet level, but the D_3 and the 10830 transitions take place between two levels of the triplet system (see left panel of Fig. 2.6). Since transitions between the para- and the ortho- levels are forbidden by the electric dipole selection rules and collisional rates in the chromosphere are very low (to produce this excitation by collisional processes), the main mechanism to populate the ortho-levels is through photo-ionization from the para-helium system followed by a recombination into the ortho-system. This mechanism is known as photoionization-recombination or PR process (Avrett et al., 1994). A scheme of this process is shown in Fig. 2.7.

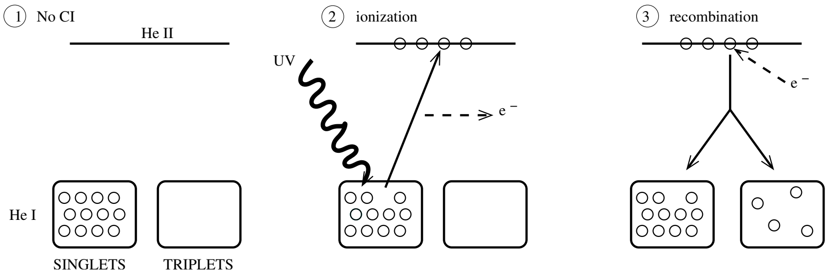

Figure 2.7 – Ionization-recombination scheme for the He I atom triggered by the EUV coronal irradiance. In the absence of coronal illumination (CI; left panel) almost all the population of He I is in the ground state of the singlet system. The photoionization-recombination process (middle and right panels) is able to populate the triplet system significantly. Figure extracted from Centeno et al. (2008).

Consequently, the electrons cascade down to the ground meta-stable level of the ortho-helium system. The ionization potential of the para-system is 24.6 eV, which means that the photo-ionization of the He I atom can only be effectively achieved by UV photons with wavelengths $<$ 504 Å (energy necessary to remove the first electron). Such radiation can only originate in the solar corona, which makes these lines particularly interesting because they are sensitive to both chromospheric and coronal physical conditions (Centeno et al., 2008; Golding et al., 2014; Leenaarts et al., 2016).

Figure 2.8 shows how the He I 10830 Å triplet is enhanced close to active regions where the coronal EUV incident radiation is larger. We can see the correlation between a coronal image (middle panel) and the absorption detected in an image taken at the He I 10830 Å line (left panel). Filaments are also highly visible in this spectral line while in coronal hole areas there is a lack of absorption as compared to the average quiet Sun. These images are taken with the telescope *Chromospheric Helium line Imaging Photometer* (CHIP, Kopp et al., 1997) telescope at the He I 10830 Å triplet (left panel) and from the SOHO's *Extreme ultraviolet Imaging Telescope* (EIT) at the Fe XII channel at 195 Å that shows the corona at a temperature of 1.5 MK (middle panel). Both images are taken on 2004/03/16 and we have reversed the color palette of the coronal image to easily see this correlation. In the right panel of the same figure, we show the intensity profiles of the He I 10830 Å triplet and Si I 10827.1 Å from different regions. The line centers are indicated above each one with colors. Three intensity profiles (extracted from observations) show the very different absorptions of quiet Sun, active region and, filaments. The filament absorption can be down to $0.4 I_c$ while in active regions it is around $0.85 I_c$, and $0.95 I_c$ in quiet-Sun areas.

Since UV photons can only penetrate a thin layer of the chromosphere before they being absorbed, the He I lines are assumed to form in a relatively thin and localized range of heights. Consequently, the constant slab or Milne-Eddington descriptions can be applicable (Leroy et al., 1977; Sahal-Brechot et al., 1977; Lagg et al., 2004; Trujillo Bueno & Asensio Ramos, 2007; Asensio Ramos et al., 2008). While in typical QS conditions the multiplet is formed in the chromosphere, above 1500 km above the solar surface

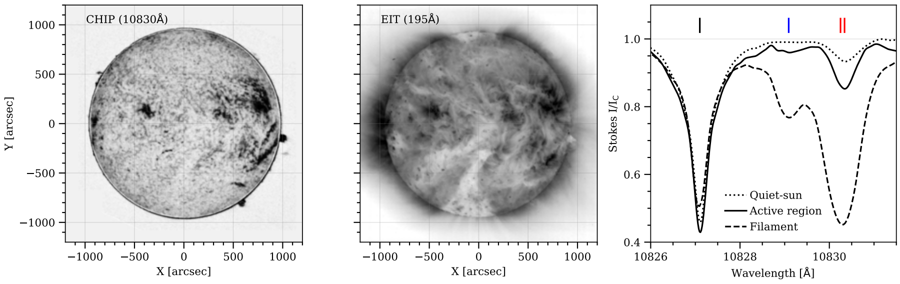

Figure 2.8 – Left panel: image taken by CHIP at the He I 10830 Å triplet. Middle panel: image taken by EIT at the Fe XII 195 Å channel. Note the correlation between the coronal radiation and the higher absorption of the He I. Right panel: typical Stokes profiles from different locations. Above each absorption feature a small line indicates the central wavelengths of the silicon and the blue and red components of the helium line. This panel has been generated from observations showed in this work.

(see Fig. 2.5, where its formation height is indicated with a grey scale), it can be also found in high filaments or coronal loops as other mechanisms have elevated this cool material to heights of several megameters (such as the ones mentioned in Sec. 1.2.3).

This spectral line is very sensitive to the magnetic field in a wide range from dG to kG thanks to the joint action of the scattering polarization, and the Hanle and Zeeman effects. According to Eq. 2.14, the He I 10830 Å multiplet has a critical field of $B_H \sim 0.8$ G, denoting that the Hanle effect mainly operates between 0.01$<B<$100 G. However, Trujillo Bueno & Asensio Ramos (2007) demonstrated that the emergent linear polarization has some influence of scattering polarization and Hanle effect even for magnetic fields as large as 1000 G . For more magnetized plasmas, the observed signals are dominated by the Zeeman effect (Schad et al., 2013) characterized by the effective Landé factors 2.0, 1.75, and 1.25 for the transitions with $J_u = 0, 1$, and 2, respectively.

The He I 10830 Å multiplet (and D$_3$) has been showing us a *new rich world* (Solanki et al., 2006) as it has allowed to infer the full magnetic vector in the upper chromosphere, to reveal the structure of magnetic loops (Solanki et al., 2003; Xu et al., 2010), supersonic downflows, the chromosphere above sunspots (Schad et al., 2013; Joshi et al., 2016), flares (Sasso et al., 2011; Kuckein et al., 2015; Judge et al., 2015b), study of abundances (Mauas et al., 2005), spicules (López Ariste & Casini, 2005; Trujillo Bueno et al., 2005; Centeno et al., 2008, 2010; Martínez González et al., 2012a; Orozco Suárez et al., 2015), prominences (Bommier et al., 1981; Casini et al., 2003; Merenda et al., 2006; Orozco Suárez et al., 2014; Martínez González et al., 2015) and filaments (Xu et al., 2012; Kuckein et al., 2012a), and so on.

2.3.2 Ca II IR triplet

Another example of good spectral lines for chromospheric diagnostics are the Ca II infrared triplet (8498 Å, 8542 Å, and 8662 Å) which constitute a good compromise of modeling efforts, polarimetric sensitivity, and observational requirements (Quintero Noda et al., 2016, 2017a). As shown in the left panel of Fig. 2.9 this multiplet shares their upper levels with the K and H lines, but has different lower states compared to K and H lines.

The Ca II IR triplet is formed by three wide and deep spectral lines with relatively low effective Landé factors ($\bar{g}_{8498}$=1.07, $\bar{g}_{8542}$=1.10, and $\bar{g}_{8662}$=0.87). An example of the typical spectral shape of the Ca II 8542 Å line in quiet-Sun regions is displayed in the right panel of Fig. 2.9. Although they are not

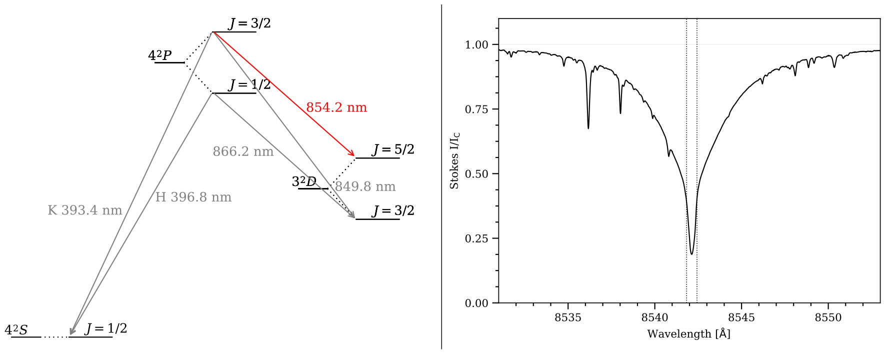

Figure 2.9 – Left panel: Grotrian diagram of the calcium atom highlighting the transition used in this work. Right panel: the typical shape of the Ca II 8542 Å line in quiet-Sun regions. Spectral range taken from the FTS at disk center (Neckel & Labs, 1984). The line is sensitive to the chromospheric conditions in the spectral range between the two dotted lines at ±0.3 Å of the central wavelength.

especially sensitive to the magnetic field, they can be observed in the entire solar disk (as opposed to the He I 10830 Å triplet, whose opacity in the quiet Sun is extremely small) and we can use them to extract information about the plasma temperature (Socas-Navarro et al., 2000). This triplet is formed under non-LTE conditions as it is usual with chromospheric lines. This line is usually modelled assuming CRD, as PRD effects are negligible for this triplet (Uitenbroek, 1989). Also the assumption of the statistical equilibrium is valid, and a constant ionization fraction can be supposed during the observation, because under typical chromospheric conditions almost the whole calcium is in the single ionized state (Wedemeyer-Böhm & Carlsson, 2011).

Of the three lines of the triplet, the Ca II 8542 Å is the one that has been more extensively used in previous works. The reason is that it has the largest Landé factor of the three and does not have blends with other spectral lines like the Ca II 8498 Å. This line turns out to be very sensitive to the temperature stratification of the atmosphere and can be used to infer it even when 3D effects are neglected (de la Cruz Rodríguez et al., 2012). It also encodes information about velocity gradients and the magnetic field which can be reliably recovered (through the Zeeman effect) even under the LTE approach. The horizontal component of the magnetic field typical of quiet-Sun areas can be inferred only if the noise level is below $3 \cdot 10^{-4}$ in units of continuum intensity (de la Cruz Rodríguez et al., 2012). For that reason, the spectropolarimetric studies are mainly carried out oriented towards the analysis of active regions where the magnetic field is high and the polarization signals are higher (Socas-Navarro et al., 2000; de la Cruz Rodríguez et al., 2013a; Asensio Ramos et al., 2017). Another reason for this limited use is that including the Hanle effect (Carlin et al., 2013; Štěpán & Trujillo Bueno, 2016) in this spectral line is very time-consuming in terms of computation. To compare with the He I 10830 Å line, the Ca I 8542 Å has a Hanle regime between 0.001<B<0.1 G and a Hanle saturation regime for B>10 G (Manso Sainz & Trujillo Bueno, 2010). Above 100 G we are again sensitive to the magnetic field vector through the Zeeman effect.

Recently, Leenaarts et al. (2014) showed that the effect of isotopic splitting must be included in the diagnostic to properly retrieve the velocity stratification. Moreover, Quintero Noda et al. (2016) indicated that the Ca II 8542 Å line is mostly sensitive to the solar layers in the range $\log(\tau) = [0, -5.5]$, with τ the continuum optical depth at 5000 Å. The chromospheric sensitivity is encoded in the core, as it is shown in the left panel of Fig. 2.9 with two dotted lines at ±0.3 Å of the center. Due to this wide range of formation, it has been also used to study flare evolutions (Kuridze et al., 2017; Kuckein et al., 2017b). This line has very low sensitivity to the temperature around $\log(\tau) = -4.5$ and others spectral lines, such as the K I D_1 7698 Å line, have been proposed to complement the Ca II 8542 Å analysis (Quintero Noda et al., 2018).

2.4 Inversion codes

The magnetic field –as the rest of thermodynamic properties of the plasma– is not an observable quantity; it has to be inferred from the observed polarized light. To this end we use inversion codes, that carry out this task in a semi-automatic way. The interpretation of any spectropolarimetric observation is thus done assuming a specific generative model, which has the ability to generate a synthetic spectrum that is used to explain the observed Stokes parameters for a given set of wavelengths.

Inversion codes have an automated minimization engine which is used to find the model that best reproduces the measured Stokes vector. In this process we compare the observed spectrum $\mathbf{S}^{\mathbf{obs}}(\lambda)$ with the synthetic spectrum $\mathbf{S}^{\mathbf{syn}}(\lambda, \mathbf{x})$, being $\mathbf{x}$ the set of M free parameters of the model. This comparison is done with a merit function that measures the goodness of the fit (see e.g., Ruiz Cobo & del Toro Iniesta, 1992). In the case of uncorrelated Gaussian noise the merit function can be defined by:

$$\chi^2 \equiv \frac{1}{N-M} \sum_{i=1}^{4} \sum_{j=1}^{N} \left[\frac{S_i^{obs}(\lambda_j) - S_i^{syn}(\lambda_j, \mathbf{x})}{\sigma_j} \right]^2 w_i^2 \, , \tag{2.18}$$

where N is the number of measured wavelength points λ_j with uncertainty σ_j. From Eq. 2.18 we obtain a value close to 1 with a good fit (only when $w_i = 1$). A weight factor w_i is often introduced to balance the goodness of the fit for each Stokes parameter as they differ by some orders of magnitude. Changing this weight is equivalent to modify the σ of each Stokes parameter.

In the following, we will explain how a typical inversion code works. In general, an inversion code can be characterized by the physical ingredients of the generative model (temperature, magnetic field, approximations used, ...) and the optimization techniques used to fit the generative model to the observations.

Minimizing Eq. 2.18 is a typical optimization problem where one wants to minimize the distance (l_2 norm) between the synthetic and observed profile. Several optimization methods have been implemented in the literature depending on the kind of study or computational requirements. For an extensive review of this topic we recommend del Toro Iniesta & Ruiz Cobo (2016). Current inversion codes are based on gradient–descent type algorithms (GD, or similar as the Levenberg–Marquard algorithm, LM), Bayesian techniques, genetic algorithms (e.g. PIKAIA or another search method such as DIRECT), or on look-up tables, like the Principal Component Analysis (PCA, Rees et al., 2000) inversion codes.

The simplest (and fastest) method is the one based on look-up tables and PCA, which tries to find the profile in a database that better fits the observed profile. However, the size of the database quickly grows with the complexity of the atmosphere (also known as curse of dimensionality) and it severely limits its applicability. On the other hand, global minimization algorithms such PIKAIA (Charbonneau, 1995; Lagg et al., 2004) or DIRECT (Jones et al., 1993; Asensio Ramos et al., 2008) are more robust in finding global minima than LM, but they are more time consuming because they need an elevated number of evaluations of the merit function. Bayesian techniques allow us also to extract reliable uncertainties and degeneracies between the parameters, option which will be used in next chapters where a detailed explanation is also included.

Finally the most widespread methods are based on the use of derivates of the merit function χ^2 with respect to the parameters $\mathbf{x}$ to drive the solution in the direction of the minimum. From Eq. 2.18, and following the chain rule, the gradient of the χ^2 with respect to a parameter x_k is given by:

$$\frac{\partial \chi^2}{\partial x_k} = \frac{2}{N-M} \sum_{i=1}^{4} \sum_{j=1}^{N} \left[\frac{S_i^{obs}(\lambda_j) - S_i^{syn}(\lambda_j, \mathbf{x})}{\sigma_j} \right] w_i^2 \cdot \underbrace{\frac{\partial S_i^{syn}(\lambda_j, \mathbf{x})}{\partial x_k}} , \tag{2.19}$$

where the term marked with a curly bracket is known as *response function* (Ruiz Cobo & del Toro Iniesta, 1992) and encodes the relationship between the emergent spectrum and the model parameters. The most common algorithm currently in use is the Levenberg–Marquard (Levenberg, 1944; Marquardt, 1963) whose convergence is very fast as it gradually combines the GD and the Newton method that includes second order information through the Hessian matrix (for more details see del Toro Iniesta & Ruiz Cobo, 2016).

The synthetic Stokes parameters emerge from a solar atmosphere which is modeled with a discrete set of points. This representation can be more or less sophisticated depending on the information of the spectral line, i.e., the formation range and the sensitivity to gradients in the physical quantities. Thus, this grid can have only one point like in a Milne-Eddington (ME) atmosphere (Harvey & Hall, 1971; Auer et al., 1977), or more than 50 points that spawn from the photosphere to the chromosphere, like the FAL-C model (Fontenla et al., 1993).

In order to reduce the number of parameters, the depth stratification of a physical magnitude of the atmosphere (e.g. the temperature) is controlled by a few *nodes* that have to be smartly located[9]. The rest of the depth points are interpolated using the values at the nodes. Consequently, the number of nodes controls the degree of complexity of the perturbations of the free parameters of our atmosphere from the initial state, i.e., one node modifies the stratification with a constant, two nodes cause a linear perturbation, etc. Another way to control the approach to the solution, or convergence, of the initial model is through *cycles*, which is just a way to divide the total convergence process into several steps by modifying the flexibility (increasing the number of parameters or nodes) ensuring a smooth and more realistic solution. There is not an established rule for selecting the number of nodes or cycles. However, a more simple model (less freedom) is preferred because it is easier to interpret. Another reason is that more degrees of freedom does not mean more accuracy, since one can fits details that are produced just by the noise of the observations. An initial model is used from which the minimization algorithm can start. In the literature, one can find some models of the solar atmosphere, built to reproduce the observations of certain solar phenomena that can be used as initial guesses (e.g. Fontenla et al., 1993). Finally, the success of a good inversion lies also in the scientist experience as some degeneration problems can appear during the process (where different parameters or nodes produce similar results), and they have to be diminished by means of previous knowledge or other more quantitative criteria (Asensio Ramos et al., 2012).

To visualize the previous concepts, Fig. 2.10 shows an example of the inversion of the Stokes profiles of a simulated Sunrise/IMaX observation (Martínez Pillet et al., 2011) of the Fe I line at 5250.2 Å (del Toro Iniesta & Ruiz Cobo, 2016). A first cycle (green lines) is used with only one node in the LOS velocity and the magnetic field vector to have a first approximation of the atmosphere, roughly reproducing the Stokes amplitudes. In a second cycle (red lines), two nodes are used allowing for gradients of these physical quantities and thus reproducing the asymmetries of the profiles. At this point the Stokes vector is perfectly reproduced with the model atmosphere resulting from the inversion.

---

[9] In the extreme case that the nodes are placed in a region of the atmosphere where the spectral line is not sensitive, we will not be able to correctly reproduce the line profile.

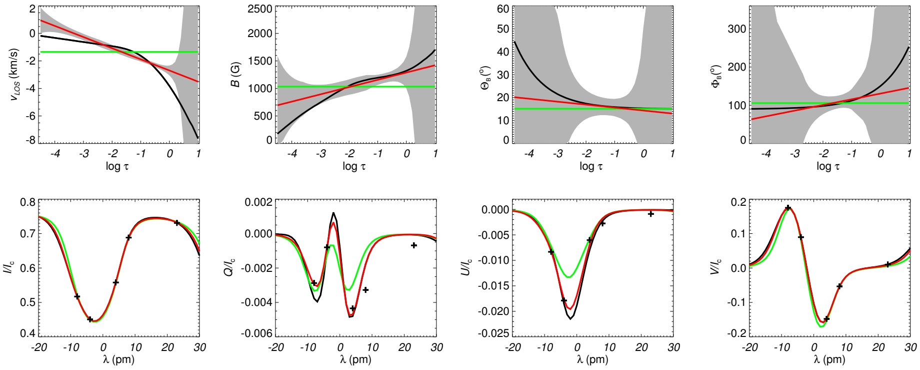

Figure 2.10 – Upper panels: atmospheric stratification with continuum optical depth at 5000 Å of the LOS velocity and the magnetic field vector (strength, inclination and azimuth) for the original model atmosphere (black lines) and for the resulting models from the cycle 1 (green lines) and cycle 2 (red lines) runs of SIR. Gray shaded areas cover the uncertainty region of the last cycle solution. Lower panel: synthetic Stokes parameters for the same colored atmospheres. Figure adapted from (del Toro Iniesta & Ruiz Cobo, 2016).

In addition, in this figure we also see the importance of using more complex models that can extract more information from observations, such as gradients along the LOS. However, it is crucial to control the level of complexity because, if it is too large, the inversion problem is highly ill-posed and a huge number of solutions can be found. For example, any stratification inside the gray areas of Fig. 2.10 is compatible with the Stokes profiles. Recently, a new generation of methods has appeared (Asensio Ramos & de la Cruz Rodríguez, 2015) that reduce the freedom of the inversion process introducing the information of the surrounding pixels of the field of view.

Finally, it should be noted that the major drawback of more sophisticated inversion approaches that include more realistic physics is the required computational effort. A ME inversion of several thousand profiles can be done in a few minutes, LTE codes commonly need a few seconds per profile to be inverted, while NLTE codes can require up to a few minutes per profile. This has hindered the regular application of inversion codes to most chromospheric observations. In the following, we will explain some of the inversion codes used in this work and their physical ingredients.

2.4.1 SIR code

The *Stokes Inversion based on Response functions* code[10] (SIR; Ruiz Cobo & del Toro Iniesta, 1992) allows us to synthesize and invert spectral lines formed in LTE conditions in stratified atmospheres, allowing gradients along the LOS. It will be used to extract information at the photospheric level, using the Si I 10827 Å line.

SIR is a versatile, fast, and widely used inversion code. In LTE conditions, the source function is the Planck function at the local temperature $B_\nu(T)$ and the population levels are calculated using the Saha-Boltzmann equations. It assumes a magnetic field in the Zeeman regime, the atomic polarization is neglected, and uses the approximation of complete frequency redistribution. The magnitudes that SIR can infer with depth stratification are: temperature, electron pressure, line-of-sight velocity v_{LOS},

---

[10] The latest version is hosted at `https://github.com/BasilioRuiz/SIR-code`.

microturbulent velocity, and the magnetic field vector (B, Θ_B, Φ_B). The rest of magnitudes are constant: macroscopic velocity, stray-light, and filling factor.

2.4.2 NICOLE code

The LTE approximation breaks down in the upper solar atmosphere and a non-LTE code is necessary. Only the *Non-LTE Inversion COde using the Lorien Engine*[11] (NICOLE; Socas-Navarro et al., 2000, 2015) is able to compute the full Stokes vector and perform inversions of the Stokes profiles under non-LTE conditions. It will be used to extract information about the solar stratification from the Ca II 8542 Å line. Under NLTE conditions we cannot use the Saha-Boltzmann equations to calculate the atomic populations because they depend on the radiation field. They are calculated instead in statistical equilibrium, i.e. atomic populations are computed assuming instantaneous balance between all transitions going to and out of each atomic level.

This code only takes into account the polarization induced by the Zeeman effect. This means that atomic polarization is not considered and all Zeeman sublevels are equally populated, what limits the analysis of polarization signals in regions with weak magnetic field strengths. Hence, the code is more suitable for inferring fields in regions of moderate magnetic field like network patches in the quiet Sun or active regions.

Finally, although the code can work with 3D data cubes, each column is treated independently, and the NLTE atomic populations are solved assuming a plane-parallel atmosphere (also known as 1.5D approximation). This approximation works well in LTE conditions and for some strong NLTE lines where the 3D radiation field does not play an important role for the computed population densities. In the case of the Ca II infrared lines, this assumption is fairly accurate[12] (de la Cruz Rodríguez et al., 2012, 2013a).

2.4.3 HAZEL code

The *HAnle and ZEeman Light* code[13] (HAZEL, Asensio Ramos et al., 2008) is the only diagnostic tool that allows us to synthesize and invert Stokes profiles taking into account the joint action of atomic polarization, Hanle and Zeeman effects assuming a slab model. It was developed to extract information from the He I 10830 Å and He I 5876 Å multiplets, but it can be used with other spectral lines. It will be used to extract information at chromospheric levels and, in particular, to infer the magnetic field from the spectropolarimetric signals of a filament in the He I 10830 Å.

HAZEL assumes that we have a layer (slab) of atoms at a height h above the solar surface, permeated by a magnetic field, and illuminated by the solar photospheric continuum (with its center-to-limb variation) assuming axial symmetry. The effect of a magnetic field on the energy levels is computed in the general incomplete Paschen–Back regimen (see Sec. 2.2.2). In inversion mode, HAZEL minimizes a merit function like the Eq. 2.18 with the following free parameters: the magnetic field vector (B, θ_B, ϕ_B), Doppler width (Δv_D), LOS velocity of the plasma (v_LOS), optical depth of the line (τ_red), and the line damping parameter (a).

In the process of minimization, HAZEL uses a procedure with several cycles with two different algorithms. To reduce the computation time of the minimization, it explores the space of parameters with the DIRECT algorithm. This method efficiently reduces the space where the minimum is located. From this first estimation, a Levenberg-Marquardt algorithm is applied to refine the solution. A scheme of two DIRECT+LM cycles is recommended (Asensio Ramos et al., 2008). In the first two, the algorithm tries

---

[11] The latest version is hosted at `https://github.com/hsocasnavarro/NICOLE`.

[12] However, see Štěpán & Trujillo Bueno (2016) to understand the limits of this conclusion.

[13] The latest version is hosted at `https://github.com/aasensio/hazel`.

to infer the thermodynamic parameters by fitting only Stokes I. In the last two cycles, the magnetic parameters are inferred from Stokes Q, U, and V.

2.5 Instrumentation

Large diameter solar telescopes, such as the 1.5m–GREGOR or the 1m–Swedish Solar Telescope (SST), are necessary for two important reasons: (1) to have a sufficient photon flux to allow for high sensitivity polarization measurements, hence high quality measurements of magnetic fields, and (2) to have high spatial resolution in order to resolve small concentrations of magnetic flux or, in our case, the fine structure of the chromosphere. In the following, we present the instrumentation used to obtain spectropolarimetric measurements of the He I 10830 Å line (at the GREGOR telescope) and of the Ca II 8542 Å line (at the SST telescope).

2.5.1 GRIS at GREGOR

From the first chapter we have mentioned the very weak polarization signals expected for the magnetic field in the chromosphere and, in particular, in solar filaments. We have used data from GRIS at GREGOR that ensure a very high polarimetric sensitivity while keeping a moderate spatial resolution.

Telescope structure and optical design

The GREGOR telescope (Volkmer et al., 2010; Schmidt et al., 2012a,b) is located at the *Observatorio del Teide* in Tenerife, Spain. It replaced the older Gregory-Coudé Telescope (GCT) with 40 cm of aperture, using the same infrastructure, and it was inaugurated on May 21, 2012. It was built by a German consortium under the leadership of the Kiepenheuer-Institut für Sonnenphysik in Freiburg, with the participation of the Leibniz-Institut für Astrophysik Potsdam, the Max-Planck-Institut für Sonnensystemforschung in Katlenburg/Lindau, the Institut für Astrophysik Göttingen, the Astronomical Institute of the Academy of Sciences of the Czech Republic, and the Instituto de Astrofísica de Canarias. With 1.5 m of aperture, it is the third-largest solar telescope in the world at the time of writing. The diffraction limited resolution with this diameter at 5000 Å is 0.08″, and around 0.2″ at 10830 Å. The telescope has an "open-air" design where the classic dome is replaced by a retractable dome which allows wind circulation and avoids the heating of the structure and the gas turbulence above the mirrors. The internal structure is also refrigerated.

To understand its optical design in Fig. 2.11 we will follow the light path from the Sun to the detector. GREGOR is a double Gregory system with three imaging mirrors (Soltau et al., 2012). The primary mirror M1 has a diameter of 1.5 m and a focal length of 2.5 m. In the primary focal plane, an image of the solar disk is formed, with a total power of about 2000 W. For this reason, a water-cooled field stop is located in the primary focus, which deflects most of the sunlight out of the telescope, and transmits only a circular field-of-view with a diameter of 150″ through a central hole. The secondary mirror M2, located after the primary focus, forms a secondary image near the intersection of the optical and the elevation axis of the telescope (see F2 in the figure). At this position, the GREGOR Polarization calibration Unit (GPU, Hofmann et al., 2012) is located, which, with two sets of polarizers and retarders, allows us to calibrate the polarization induced by the reflections on the mirrors of the telescope. The beam continues to propagate to the mirror M3, which forms the final image in the focal plane F3 (after M11). The mirror M4 directs the beam into the elevation axis and, following an evacuated optical path, and M5 directs the beam to the observing laboratory, which is one floor below the telescope platform. A second calibration unit (GPU2 in the figure) is at the exit window of the telescope and assures high precision polarimetric observations.

Since the alt-azimuth mount delivers a rotating solar image at F3, there is an image derotator between the exit window and F3. After M11, the light continues through the adaptive optics system (AO). It is integrated in the optical path for distortions of the light wavefront introduced by the terrestrial atmospheric turbulence (Berkefeld et al., 2012) with a deformable mirror (DM, M14 in the figure) with 256 actuators and a tip-tilt mirror (TT, M13 in the figure). Their movements are controlled by the wavefront sensor (WFS) that has 156 subapertures which measure the wavefront deformation. After that, the light is distributed to the different post-focus instruments.

Instrumentation

The light is split with a dichroic beamsplitter in two spectral ranges: above (red arm) and below (blue arm) 8700 Å. It allows multi-instrument observations:

- *GREGOR Infrared Spectrograph* (GRIS, Collados et al., 2012) is the grating spectrograph designed, built, and installed at the GREGOR telescope under the responsibility of the Instituto de Astrofísica de Canarias. It has polarimetric capabilities when attached to the *Tenerife Infrared Polarimeter II* (TIP-II, Collados et al., 2007). Although nothing prevents its use at visible wavelengths, the spectrograph is used in combination with the infrared detector TIP-II. A slit scanner allows to explore and measure 2D areas in the Sun. The slit length corresponds to 65″, with 0.14″ wide. It operates in the range 1.0–2.3 μm with a theoretical resolving power of R=525000 at 1.1μm.

- *GREGOR Fabry-Pérot Interferometer* (GFPI, Puschmann et al., 2012) comprises two tunable etalons in collimated mounting in the blue arm, which provide a spectral resolution of R=250000. The field-of-view (FOV) is $50'' \times 38''$ in the spectroscopic observing mode. The polarimetric mode is not available at this time. The coatings of the etalons are optimized for the wavelength range 5300 Å–8700 Å.

- *High-resolution Fast Imager* (HiFi, Kuckein et al., 2017a) is the new instrumentation in the blue imaging channel of the GFPI (3900–5300 Å) since 2016, which can be used independently from the GFPI and GRIS as a context image during the observations (Denker et al., 2018). Two cameras acquire images strictly simultaneously to the GFPI in the narrow- and broad-band channels to facilitate post-facto image restoration including simple destretching, speckle masking imaging, and deconvolution.

GRIS: Data acquisition and reduction

GRIS is located in the red arm and covers two of the most widely used spectral regions for spectropolarimetric observations, the 10830 Å and the 15650 Å regions. The FOV surrounding the slit is reflected back and used as a slit-jaw image. The next device is the polarimeter. It is formed by two ferroelectric liquid crystals (LCs) and a polarizing beamsplitter (PBS) (see Fig. 2.12). Two pairs of LCs are available, one is optimized for 15648 Å, where a neutral iron line with a Zeeman-splitting factor of 3.0 is present, and the other pair is centered on the helium line at 10830 Å. The ferroelectric crystals act as retarders and are used to modulate the light in four different linear combinations of the Stokes parameters at each slit position by changing the voltage applied to each crystal. The beamsplitter is used to separate the beam in orthogonal polarization states. This configuration with two beams reduces the crosstalk induced by intensity fluctuations (Collados, 1999). The two beams are then redirected to the grating, which is the same of the previous GCT, and it has a ruling density of 316 lines mm^{-1} with a blaze angle of 63.4°. After

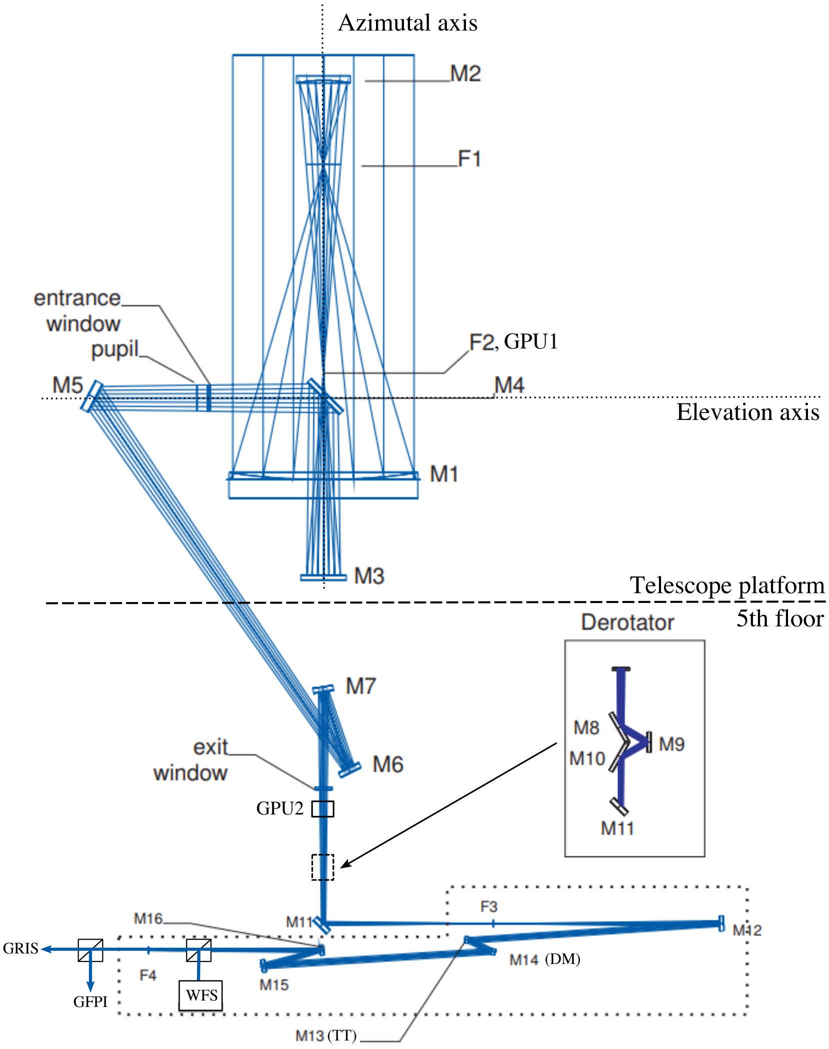

Figure 2.11 – Sketch of the optical layout for the GREGOR telescope. It shows the optical light path including the image derotator, an adaptive optics system, and dichroic beamsplitters, which distribute the light to the wavefront sensor and post-focus instruments. Figure adapted from (Soltau et al., 2012). The optical path continues in Fig. 2.12.

the dispersion several mirrors guide the two beams to the detector. As any IR detector, it is placed inside a container that is cooled with liquid nitrogen (lower part of Fig. 2.12).

For each slit position the data is acquired by four sequential images, which correspond to four different linear combinations of the Stokes parameters (*modulation*). In vectorial form, this may be written as $\mathbf{N} = \mathbf{MI}$ where $\mathbf{N} = (N_1, ..., N_N)^\dagger$ is a vector containing the N intensity measurements, $\mathbf{I} = (I, Q, U, V)^\dagger$

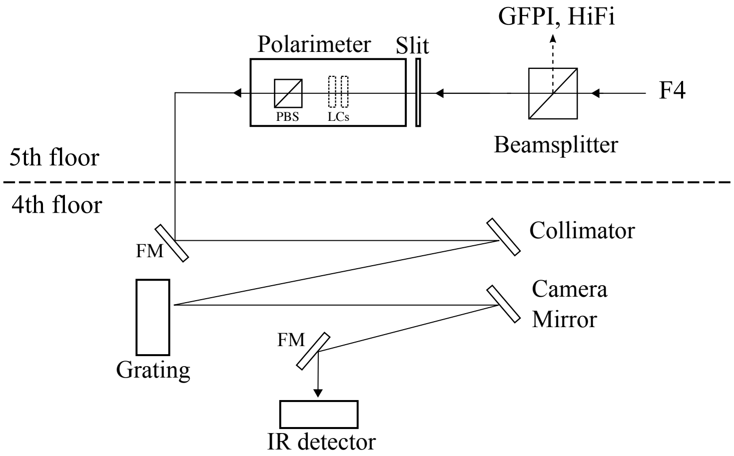

Figure 2.12 – Sketch of the optical layout for the GRIS instrument. FM: fold mirror. The detector optimized for the infrared is inside a cryostat.

is the input Stokes vector, and $\mathbf{M}$ is the matrix of coefficients that depend on the properties of the polarimeter and the whole optical system of the telescope (usually referred to as modulation matrix), and the symbol † represent matrix transposition. If the system of equations is square ($n = 4$) and all the combinations are linearly independent, the inverse matrix ($\mathbf{D} = \mathbf{M}^{-1}$, demodulation matrix) exists, and the input Stokes vector can be recovered from the measured intensities as $\mathbf{I} = \mathbf{DN}$. It is important to have a reliable estimation of the $\mathbf{M}$ matrix. Some parts of the telescope are daily calibrated while other parts are modeled.

The instrument includes a software for the data reduction, which processes the raw data to end up with a product that is ready to analyze. This software addresses the dark current subtraction, the flat-fielding correction, bad-pixels removal, and the demodulation of the data. The software includes a routine to correct the residual cross-talk between the different Stokes parameters, that is, a small fraction of the signals that does not belong to the analyzed Stokes parameter due to an errors in the demodulation process. The correction is only applied for the cross-talk of Stokes I to Q, U, and V, and it is estimated from the non-zero continuum value of Stokes Q, U, and V.

Under the assumption of unpolarized continuum, the deviations from zero are assumed to come from Stokes I. Hence Stokes Q, U, and V are corrected subtracting the amount of Stokes I needed to settle the polarimetric continuums at zero level. For the crosstalk of Stokes V to Q and U we have verified that there is almost no correlation between circular and linear polarization (Schlichenmaier & Collados, 2002).

The next step is to correct the fringes that persist after the standard reduction process. These fringes are produced by interferences due to multiple reflections on flat surfaces in the optical path. These fringes are often corrected using Fourier filtering, but this standard procedure does not achieve our requirements. The long-period fringes are corrected by comparison with the Fourier Transform Spectrometer ($I_{\mathrm{FTS}}(\lambda)$ or FTS, Neckel & Labs, 1984) atlas. This atlas has a very high quality, no spectral stray light, and very accurate continuum level. Following Allende Prieto et al. (2004) and Franz et al. (2016), the $I_{\mathrm{FTS}}(\lambda)$ is modified to be comparable to our spectrum $I_{QS}(\lambda)$, generating a "new" intensity profile $I_{\mathrm{NFTS}}(\lambda)$:

$$I_{QS}(\lambda) \simeq I_{\mathrm{NFTS}}(\lambda) = \alpha\langle G(\sigma) * I_{\mathrm{FTS}}(\lambda)\rangle + (1-\alpha)G(\sigma) * I_{\mathrm{FTS}}(\lambda)\ . \tag{2.20}$$

As we see from the previous equation, in order to take into account the different spectral resolution of our instrument, $I_{\mathrm{FTS}}(\lambda)$ is convolved with a Gaussian $G(\sigma)$ with a standard deviation σ. Then, we add another term $\langle G(\sigma) * I_{\mathrm{FTS}}(\lambda)\rangle$ which is the average of the convolved spectrum and it does not depend on the wavelength. This allows us to characterize the amount of non-dispersed spectrum (light that reaches the detector without passing through the grating) by the stray light factor α.

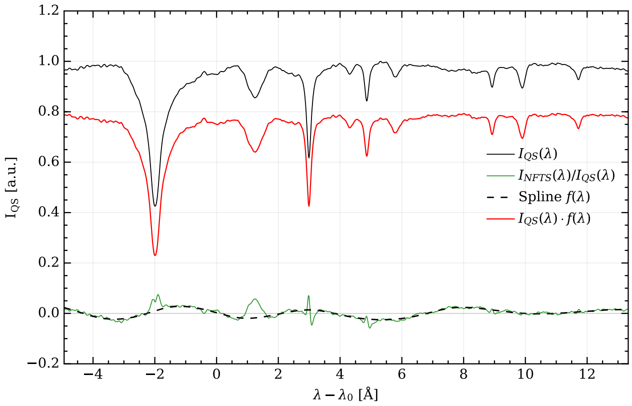

Figure 2.13 – Long-term fringes correction. The different parts of the correction process are shifted in the vertical axis to improve their visualization.

We create our I_{QS} spectrum as an average of the quiet areas available in our observations to mimic the atlas. To compare both spectra, we performed a wavelength calibration using the photospheric lines of the atlas. Consequently, our wavelength reference (and LOS velocity) is the photospheric average motion. After the calibration, the dispersion obtained is 18.10±0.01 mÅ pixel^{-1}.

The values of α and σ are unknown and can be calculated with a least-square fit of the merit function:

$$\chi^2 = \sum_i [I_{QS}(\lambda_i) - I_{\mathrm{NFTS}}(\lambda_i)]^2 \cdot w_i\ , \tag{2.21}$$

where w_i is a parameter to reduce the weight of the wavelengths of the telluric lines. This weight is introduced because the telluric lines vary too much between observations. This weight is also applied to other spectral lines that could be highly dynamic such us the chromospheric He I 10830 Å. Figure 2.13 shows an example of the result when the values of α and σ are calculated, and the fringe pattern is obtained from the ratio $I_{\mathrm{NFTS}}(\lambda)/I_{QS}(\lambda)$. This ratio $f(\lambda)$ is then smoothed or fitted with a spline in our case and used to correct all the pixels of the map and each of the Stokes parameters: $\mathbf{I}\cdot f(\lambda)$. For the data analyzed in Chapter 4, the values are $\alpha \sim 15\%$ and $\sigma \simeq 70$ mÅ.

For short-period fringes we have preferred to use another method. We checked that this component is almost unpolarized and it is mainly seen in Stokes I. A first try to remove this component using Fourier or wavelet decomposition was unsuccessful. The reason is that the period of the fringes change along the spectrum and it is difficult to isolate them by simply using a threshold in the frequency domain. Thus, to remove this component we have used a technique based on the Relevant Vector Machine method[14] (RVM; Tipping, 2000) to decompose the original signal into two components: the clean spectra $I_0(\lambda)$ and the fringes $I_f(\lambda)$:

$$I(\lambda) = I_0(\lambda) + I_f(\lambda) \ . \tag{2.22}$$

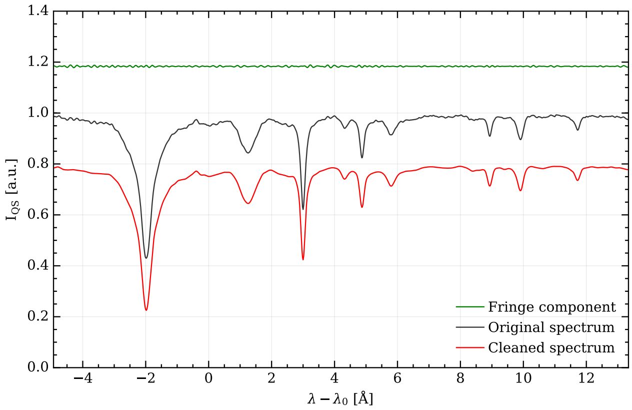

Figure 2.14 – Decomposition of the original signal using the RVM method into two components: the cleaned spectrum and the fringes. Each component was arbitrary shifted for a better visualization.

Fringes have a narrow range of periods, not a very high amplitude and, most importantly, they are present over the entire spectral range, while spectral lines are present only in some parts of the spectrum. With these properties it seems convenient to use two dictionaries with different properties (in general, an overcomplete non-orthogonal basis set) to decompose the two components. The first dictionary is made of Gaussian functions centered at several wavelengths λ_j around the spectral lines with different widths $\Delta\lambda_j$. This dictionary is specially good at fitting the clean spectrum I_0 with just a few active elements. The second dictionary is made of sine and cosine functions of different periods ω_j, similar to those of the fringes I_f. This dictionary is specially suited to fit the fringes with only a few active elements. Then, this problem can be mathematically described as a linear regression problem with N coefficients $\vec{w} = (w_0, w_1, ..., w_G, ..., w_N)$ such that:

$$I(\lambda, \vec{w}) = w_0 + \sum_{j=1}^{G} w_j \exp\left\{ - \left(\frac{\lambda - \lambda_j}{\Delta\lambda_j} \right)^2 \right\} + \sum_{j=G}^{(N-G)/2} w_j \sin(\omega_j \lambda) + \sum_{j=(N-G)/2}^{N} w_j \cos(\omega_j \lambda) \ , \tag{2.23}$$

where G is the number of Gaussian functions. We have generated a dictionary with 3000 Gaussian functions and 400 sinusoidal functions with widths $\Delta\lambda$ between 5 and 10 pixels and periods ω between 0.4 and 0.8 pixels^{-1}. Given that the two dictionaries are very incoherent, it becomes hard to fit the spectral lines with the second dictionary and viceversa. For the continuum level another free parameter is used: w_0. Therefore, the RVM method works by imposing a sparsity constrain on the coefficients of the dictionaries

---

[14] A python implementation of this tool can be found in `https://github.com/aasensio/rvm`.

(forcing many elements of the dictionary to be inactive). With this we managed to fit the spectrum at each position to separate the two contributions. Finally, the clean spectrum is just the spectral line contribution $I_0(\lambda)$, without the fringes (see Fig. 2.14). In this figure, this routine is able to separate fringes with 60 sinus and cosines and 100 Gaussian functions. Moreover, we do not have to worry about the Gaussians far from spectral lines because with the sparsity condition they are only activated if necessary. After this final step the data is ready to be analyzed.

2.5.2 CRISP at SST

The other objective we address in this thesis is to study the dynamic and thermodynamic properties of solar filaments. Arguably, the best telescope for this is the SST, which can achieve a spatial resolution and polarimetric sensitivity in the Ca II line at 8542 Å that is not possible with GREGOR at the time of writing.

Telescope structure and optical design

The *Swedish Solar Telescope* (SST, Scharmer et al., 2003) has a diameter of 1 meter and it is located in the *Observatorio Roque de los Muchachos, La Palma, Spain*. It was built in 2002 and it is operated by the Institute for Solar Physics of the Royal Swedish Academy of science. It replaced the old 50 cm Swedish Vacuum Solar Telescope (SVST) and it shares part of its design.

The SST is a refractor with a unique optical design. With 1 meter of aperture, the diffraction limited resolution at 5000 Å is 0.12″ and around 0.2″ at 8542 Å. The sketch of the telescope is presented in Fig. 2.15. In order to avoid the problems of open telescopes, such as telescope seeing, alignment problems or cleanliness of mirrors, the SST is an evacuated telescope. The Sunlight enters the system through a single lens (L1) with a diameter of $\sim$1 m and a focal length of $\sim$10 m; acting as the vacuum window. Then, there are two flat folding mirrors (M1, M2) with an incidence angle of 45° which send down the light to the underground level. The beam is focused at the bottom of the tube (BT) forming a full disk image used as a second order pointing system. At this point a small field mirror selects the FOV and sends the beam upward and away from the optical axis of the telescope. The image produced by the singlet lens (L1) has chromatic aberration, focusing different wavelengths at different distances from the lens. The SST overcomes this problem by directing the light to a Schupmann corrector (SC) which consist of a negative lens and a mirror, that create an achromatic image focusing all colors together at a single focus (see zoomed area B in Fig. 2.15). The light is then sent to the optical bench. The first two optical elements that the light finds are two mirrors whose purpose is to compensate the inhomogeneities and motions of the wavefront due to atmospheric disturbances. First, a flat mirror (TT) with three actuators compensate the FOV's global movements. Second, a deformable mirror (DM) compensates for high order seeing effects.

Instrumentation

Depending on the type of study and wavelength range, the SST is equipped with some of the following instruments:

- *TRI-Port Polarimetric Echelle-Littrow* (TRIPPLE, Kiselman et al., 2011) is a Littrow spectrograph specially designed to observe three spectral regions simultaneously with a spectral resolution of $R \sim 220000$. It covers a wavelength range within the optical and near-infrared between 3800 Å and 11000 Å and at the time of writing it has no polarimetric capabilities.

- *CRisp Imaging SpectroPolarimeter* (CRISP, Scharmer et al., 2008) is a Fabry-Perot tunable filter with polarimetric capabilities (liquid crystals) in the range 5100-8600 Å (red) allowing spectropolarimetry measurements.
- *CHROMospheric Imaging Spectrometer* (CHROMIS[15]) is a dual-Fabry-Perot filter system, similar to CRISP but without polarimetry. It is designed for wavelengths in the blue range between 3800 Å and 5000 Å. It can work simultaneously with CRISP.

CRISP: Data acquisition and reduction

In the same way we did with GREGOR, we will follow the light path to explain how the CRISP instrument works. A schematic view of the optical setup below the telescope is shown in Fig. 2.16. After the AO system of mirrors (DM & TT), the light is sent through the re-imaging lens (RL) toward the dichroic beamsplitter (DC) that splits the beam at 5000 Å into a red and a blue beam. The dichroic reflects the red light into the CRISP instrument and the blue light is used by the correlation tracker (CT) which measures the image motion and uses the tip-tilt mirror (TT) to keep the image steady. The red light, once reflected by the dichroic, is split again by a first beamsplitter (BS1), sending a fraction of the light to a wavefront sensor (AO WFS on the figure) and the rest is transmitted to the following devices. The wavefront sensor is a Shack-Hartmann with 85 subapertures which measures the phase of the wavefront and tries to keep it flat by controlling the 85-electrode Deformable mirror (DM). The next element in the light path to the instrument is the shutter (chopper). This is a rotation plate with holes that rotates synchronized with the exposure of the three detectors. The chopper is followed by a broadband filter (filter wheel on the figure) which is responsible for eliminating undesired secondary transmission peaks of the etalons, that we will describe later.

After the filter wheel, a second beamsplitter (BS2) reflects a fraction of the light to a broadband camera (WB). The images from this camera are used by the Multi-Object Multi-Frame Blind-Deconvolution code (MOMFBD, van Noort et al., 2005) together with the narrowband images to estimate the blurring induced by seeing and correct for it. The light that is transmitted by the beamsplitter BS2 is sent to two etalons (HRE and LRE on the figure) enclosed in a thermally controlled environment. An etalon consist of two parallel reflecting plates, forming a cavity where the light undergoes multiple reflections. An infinite train of transmission peaks is produced by multiple interference of light inside the cavity.

These two etalons are responsible for the selection of the quasi-monochromatic wavelength observed. Figure 2.17 (left panel) shows the transmission profile of this system. The first etalon is the High spectral Resolution Etalon (HRE) that defines the observed wavelength (ideally monochromatic, dotted gray line in Fig. 2.17). In order to eliminate the nearest undesired transmission peaks generated by the HRE, there is a second etalon whose transmission profile is shown with a dashed gray line. The combined transmission profile is shown with a black line. Despite the combined action of both etalons reduces the number of transmitted wavelengths, there are still periodic transmission peaks at undesired wavelengths. The selection of a single transmission peak is performed by the prefilter located previous to the etalons in the optical path (dash-dotted line in Fig. 2.17). This transmission profile depends on the reflectivity, and narrower profiles correspond to higher values of the reflectivity. The right panel of Fig. 2.17 shows the FWHM of the profiles as a function of wavelength. For the spectral line of Ca II at 8542 Å we have a FWHM of $\sim$ 108 mÅ.

After the etalons, we find the liquid crystals that modulate the incoming light, producing four polarization states that are linear combination of the four Stokes parameters. Finally, a linearly polarizing

---

[15] More information can be found `https://dubshen.astro.su.se/wiki/index.php/CHROMIS`

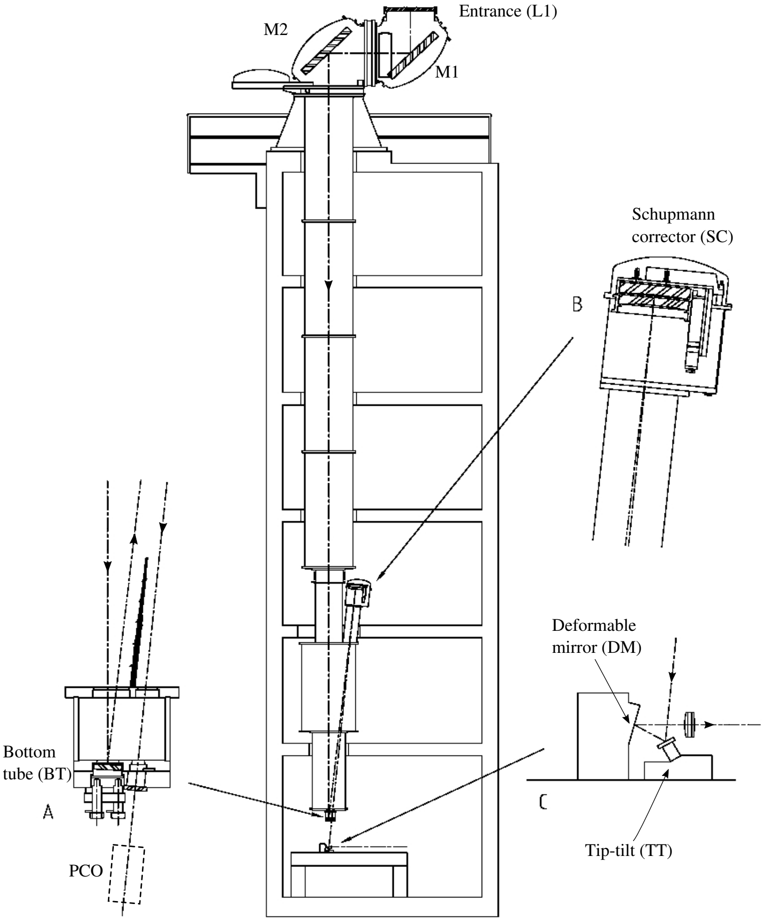

Figure 2.15 – Sketch of the optical layout of the SST telescope from the 1-meter lens via the two alt-az mirrors, the field mirror on the bottom plate (inset A), the Shupmann corrector (inset B), the field lens and exit window (inset A), the tip-tilt mirror, deformable mirror, and re-imaging lens on the optical table (inset C). Image adapted from de la Cruz Rodríguez et al. (2015). The optical path continues in Fig. 2.16. The Polarization Calibration Optics (PCO) is not in the optical path during normal observations.

beamsplitter splits the light into two orthogonal linearly polarized beams (as in GRIS at GREGOR) that are sent to two different narrowband cameras (NB-R and NB-T). This instrument is a tunable imager and hence, each scan is a monochromatic image of a two dimensional area of the solar surface. The various measurements along the spectral line profile are achieved in a sequential manner: at each wavelength position four linear combinations of the Stokes parameters are taken. Then, the etalon separation is

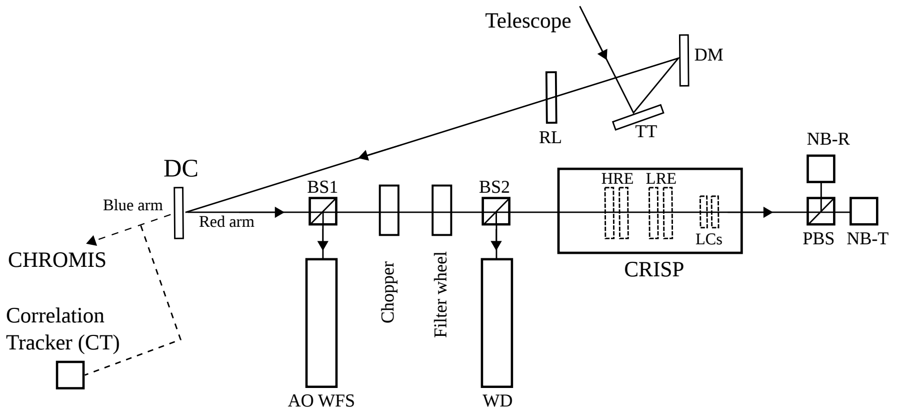

Figure 2.16 – Sketch of the optical layout of the CRISP optical bench. Image adapted from de la Cruz Rodríguez et al. (2015).

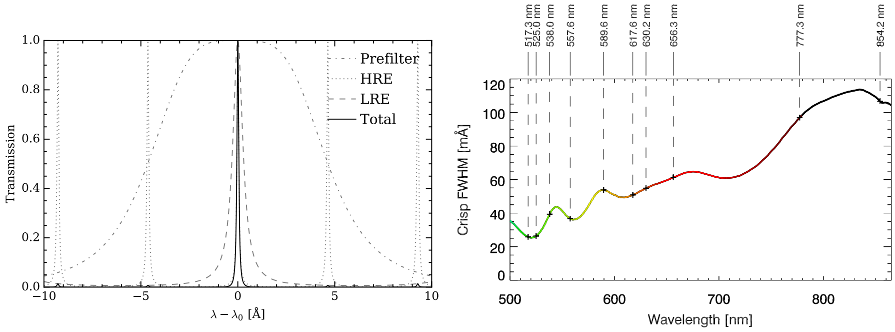

Figure 2.17 – Left panel: Approximate CRISP transmission profile at 8540 Å, computed theoretically assuming perpendicular incidence of the beam with the surface of both etalons. The individual contributions from the high-resolution etalon, the low-resolution etalon, and the prefilter are shown along with the total transmission. All curves are normalized to unity. Right panel: FWHM of the CRISP transmission profile as a function of wavelength. We have indicated those lines that are currently observable. Left panel is reproduced with the values in `https://dubshen.astro.su.se/wiki/index.php/CRISP` and de la Cruz Rodríguez et al. (2013a). Right panel is extracted from de la Cruz Rodríguez et al. (2015).

changed shifting in wavelength the transmission peak to the next wavelength position. Doing this, it is possible to cover a full spectral line and recover the Stokes parameters by means of the demodulation process in the same way as with GREGOR.

Exposure time in solar observations is limited by the evolution time of the Sun. Exposures longer than the evolution time scale can produce smearing of the data. Additionally, FPI instruments can only observe one wavelength at a time, a limiting factor for the wavelength coverage given that all acquisitions within one line scan should be as simultaneous as possible. Therefore, observing the chromosphere involves a difficult trade-off between wavelength coverage and exposure time (de la Cruz Rodríguez et al., 2012). There are ways to ameliorate the sampling. The broad Ca II infrared lines have a wide formation range: the fast-moving features observed in the cores contrast with the slow evolution of photospheric granulation present in the wings of the lines. Additionally, the amplitude of Stokes Q, U, and V rapidly decreases toward the wings of the line. A strategy to optimize the polarization measurements and achieve proper time sampling would be to have a fine grid of points in the chromospheric core and a thiner grid in the wings, where slower variations are expected. Because the photosphere evolves on a longer time scale than the chromosphere, exposures in the wings do not have to be recorded as frequently as in the core. Figure 2.18 illustrates the scheme of the observations, with a fine grid of points (gray circles) distributed in the core every 70 mÅ, being increased up to 800 mÅ in the wings: [0, ±0.07, ±0.14, ±0.21, ±0.28, ±0.35, ±0.455, ±0.595, ±0.735, ±0.945, ±1.75] Å.

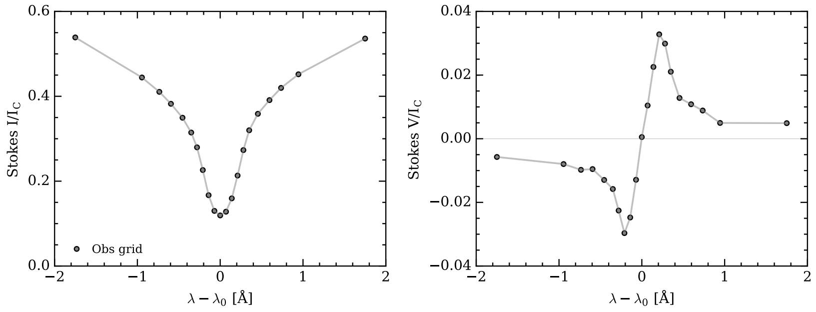

Figure 2.18 – The wavelength sampling used in the observations (shown with gray circles) is thiner in the core as the chromosphere evolves rapidly.

The reduction of CRISP data was carried out using the CRISPRED pipeline (de la Cruz Rodríguez et al., 2015). This software takes into account the dark current subtraction, flat-field correction, and demodulation process. CRISP data is usually handled using the MOMFBD code, that tries to reduce the perturbing effect of the atmosphere. Standard reduction also deals with small imperfections of the reflecting surfaces of the etalons, which are translated onto a field dependent wavelength offset. This is taken into account with the so called *cavity maps*. These maps are a product of the standard reduction routines that compute the wavelength offset for each pixel of the FOV.

Yet, a final inspection of the reduced data showed some residual artifacts that required to be corrected. The first one is the presence of polarimetric interference fringes. These fringes are seen in the individual monochromatic images (see for instance the left image of Fig. 2.19). The shape of these fringes is different for each polarimetric Stokes parameter and are also wavelength dependent. For their correction, for each polarimetric Stokes parameter, the Fourier transform of the bi-dimensional monochromatic image at each wavelength is used. The frequency amplitude of these fringes is well localized far away from the frequencies involved in the data and a threshold is used to set those peak coefficients to zero. Then, we do the inverse Fourier transform to recover our clean image as it is shown in the right panel of Fig. 2.19. Note that the fringes of Fig. 2.19 are almost at the level of our signals so one has to be careful because a wrong estimation can lead to can lead to generate artificial signals. Though not completely removed, the presence of fringes is strongly alleviated.

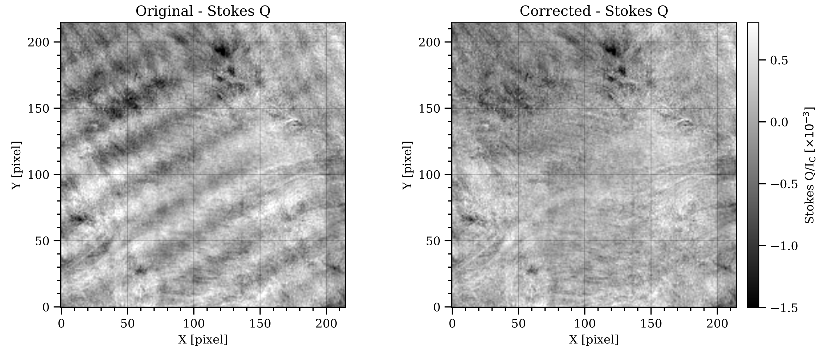

Figure 2.19 – Left panel: monochromatic image close to the core of the line in Stokes Q. Right panel: the same image after the Fourier correction of the fringes. Both panels share the same color scale.

For the correction of very-long period fringes or cross-talk, we have used monochromatic images at continuum wavelengths of each Stokes parameter. The advantage of continuum wavelengths (or very far wings as in this case) is that we do not expect any significant structure in Stokes Q, U, and V. Therefore, the identification of this effect is easier and more accurate (see for instance left panel of Fig. 2.20). To correct for this, we assume that every monochromatic image for each Stokes parameter is composed of the *true* measurement contaminated by a quantity that is proportional to the signal detected in the wing: $X(\lambda) = X_0(\lambda) + C_{\mathrm{X,W},\lambda} X_{\mathrm{W}}$. This coefficient $C_{\mathrm{X,W},\lambda}$ is estimated by minimizing the absolute correlation between the continuum image and each monochromatic image. For the example showed in Fig. 2.20, we estimated $C_{\mathrm{U,W},\lambda_0} \sim 0.2$, which has been removed from the input image (middle panel) obtaining as result the image displayed in the right panel. Since measurements at different wavelengths on the continuum show slightly different patterns (between the blue wing and the red wing), the corrected image changes quite a bit since the artifacts are of the same order or higher than the polarization signals of our region and, therefore, we cannot ensure the accuracy of the signals at these levels.

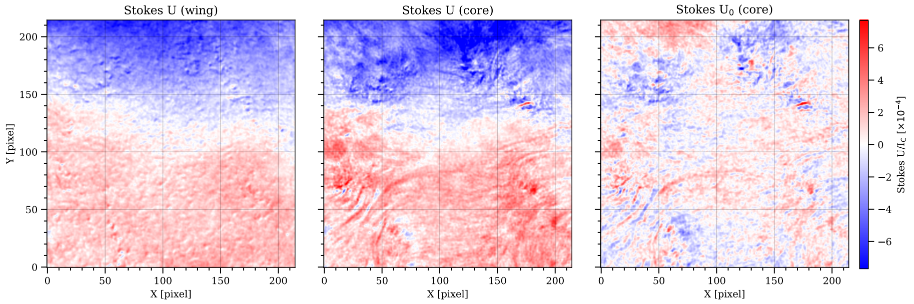

Figure 2.20 – Left panel: monochromatic image at the continuum of Stokes U. Middle panel: monochromatic image at the core of the spectral line in Stokes U. Right panel: previous image corrected from the polarization detected in the wing. All the panels share the same color scale.

Finally, a last step has to be done. To normalize the spectrum by the continuum intensity we have to follow a series of steps since the line sampling strategy does not have points at continuum wavelengths, as can be seen in Fig. 2.18. As in Sec. 2.5.1, we will use the FTS atlas as a reference. Initially, we have a spectrum taken at the disk center on the same day (which we call I_0) but a few hours before the observations we want to analyze (which we call I_1, taken at other disk position, e.g., $\mu = 0.65$). The average of a quiet-Sun region of this spectrum is compared with the FTS atlas (after convolving with the instrument PSF, σ ∼108 mÅ):

$$\langle I_{QS0} \rangle \simeq I_{C0} \cdot [I_{FTS} * G(\sigma)] \,. \tag{2.24}$$

We cannot use yet this value of I_{C0} directly for later observations because the illumination is different due to the Sun position over the horizon. To estimate this difference, we use broadband images obtained during the observations at that positions. Therefore, we calculate the ratio of the broadband images and then divide it by the ideally expected difference, i.e. $R_{\lambda\mu} = I_C(\lambda = 8542.0, \mu = 0.65)/I_C(\lambda = 8542.0, \mu = 1.0)$. This ratio is calculated from the values tabulated in Cox (2000). Therefore the new quiet-Sun continuum is:

$$I_{C1} = I_{C0} \cdot I_{WB1}/(I_{WB0} \cdot R_{\lambda\mu}) \,, \tag{2.25}$$

where I_{WB} are the average intensity of the broadband images of each observation. After this, we only have to divide all the profiles by this new number.

Este documento incorpora firma electrónica, y es copia auténtica de un documento electrónico archivado por la ULL según la Ley 39/2015.
Su autenticidad puede ser contrastada en la siguiente dirección https://sede.ull.es/validacion/

Identificador del documento: 1371210 Código de verificación: HSQ6Lr+z

Firmado por: CARLOS JOSE DIAZ BASO *UNIVERSIDAD DE LA LAGUNA* Fecha: 29/06/2018 11:26:56
ANDRES ASENSIO RAMOS *UNIVERSIDAD DE LA LAGUNA* 29/06/2018 11:56:41
MARIA JESUS MARTINEZ GONZALEZ *UNIVERSIDAD DE LA LAGUNA* 29/06/2018 13:04:01
Basilio Ruiz Cobo *UNIVERSIDAD DE LA LAGUNA* 29/06/2018 18:28:10

62 / 171

3

Interpreting spectropolarimetric signals

In this chapter we synthesize the Stokes parameters for some interesting scenarios (spicules and filaments at different solar positions) and study the signals of the He I 10830 Å triplet to gain some intuition on how the polarization is generated and to do a correct physical interpretation of the observations. Later, we explore the consequences of having several atmospheric components in the same line of sight in off-limb observations where it seems obvious to use multiple components in the line of sight, as well as in on-disk observations where the chromospheric structures are above a background with different properties.

Based on this idea we propose a two component model to explain the absence of scattering polarization signatures measured in recent spectropolarimetric observations of AR filaments. The ensuing scattering polarization signatures of the individual components have opposite signs and its combination along the line of sight reduces the Hanle signatures, giving rise to an apparent only-Zeeman profile. The important conclusion of this numerical experiment is that it suggests that filaments could be quite transparent, with the highest values for the magnetic field being produced by the active chromosphere below, and not from the filament itself, leading to a discussion about the exact magnetic field strength in these structures.

3.1 Introduction

In the previous chapter we showed the importance of the Hanle effect as a diagnostic tool for the chromospheric magnetic field. The Hanle effect, due to its special angular dependence and together with the fact that it acts concurrently with the Zeeman effect, produces Stokes parameters that depend very non-linearly on the physical properties of the atmosphere.

For that reason, it is useful to gain some intuition of how the polarization is generated by means of forward modeling experiments. To this end, we use HAZEL (described in Sect. 2.4.3) to synthesize and study the polarization signals of the He I 10830 Å triplet for some interesting scenarios. HAZEL is able to synthesize this multiplet taking into account the presence of atomic level polarization and the combined impact of the Zeeman and Hanle effects. It is fundamental to clarify the geometrical aspects of the problem, as one of the key properties of the Hanle effect is that it is controlled by the geometry of the scattering event and the magnetic field. This geometry is shown in the left panel of Fig. 3.1 following the same notation as Martínez González et al. (2015). In every scattering event, there are three important reference systems: one defined by the observer, one defined by the symmetry of the radiation field, and one defined by the magnetic field. The Z axis is aligned with the local vertical of the solar atmosphere and the plane $X-Y$ is tangent to the solar surface. The magnetic field vector $\mathbf{B}$ is characterized by its modulus B, the local magnetic inclination θ_B and the local magnetic azimuth ϕ_B. The line-of-sight vector $\mathbf{\Omega}$ is characterized by the inclination θ (known as heliocentric angle) and the azimuth ϕ. For off-limb observations we have $\theta = 90°$, while for observations on the solar disk we have $\theta < 90°$. Without any lack of generality and for simplicity, ϕ is generally taken to be $0°$ so that the LOS vector is contained in the $Z-X$ plane. For example, if $\phi = 0°$ is chosen in an off-limb observation the Ω vector lies along the X axis, while for on-disk observations Ω lies somewhere between the Z and X axis, i.e., the projection of the X axis in the plane perpendicular to the LOS points towards the disk center (see right panel of Fig. 3.1). We have also mentioned in the previous chapter that the definition of Stokes Q and U requires choosing a reference direction for $Q > 0$ in the plane perpendicular to the line of sight. This reference is indicated with the angle γ and it is extracted from the specifications of the polarimeter used for the observations.

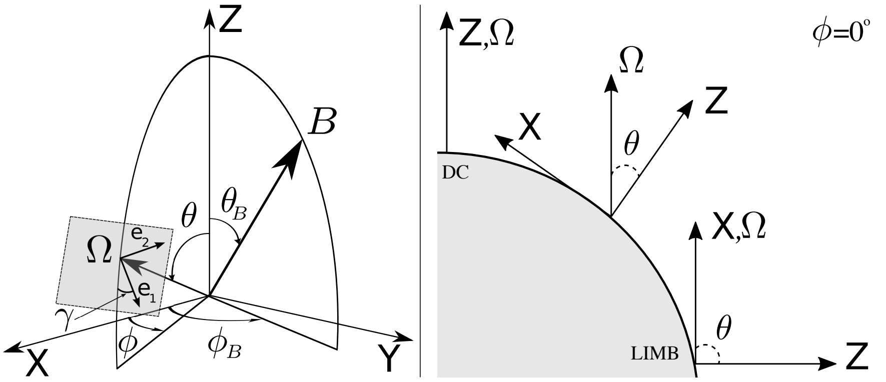

Figure 3.1 – Left panel: The reference system used in this work. The Z axis is placed along the vertical to the solar atmosphere. The magnetic field vector $\mathbf{B}$, is characterized by its modulus B, the inclination angle θ_B and the azimuth ϕ_B. The line-of-sight, indicated by the unit vector $\mathbf{\Omega}$, is characterized by the two angles θ and ϕ. The reference direction for Stokes Q is defined by the vector $\mathbf{e_1}$ on the plane perpendicular to the line of sight. This vector makes an angle γ with respect to the plane formed by the vertical and the line-of-sight. Figure adapted from Asensio Ramos et al. (2008). Right panel: configuration of the system for different heliocentric observations choosing $\phi = 0°$ for different values of θ.

3.2 The generation of polarization

The geometry of the scattering event and its relation with the magnetic field are key for the atomic level polarization and the Hanle effects. We start by computing the expected polarization produced in simple cases. To this end, we assume a plasma layer of constant physical properties (slab model) located at a height of 2000 km above the solar surface (typical of many chromospheric structures), illuminated anisotropically from below (the solar surface) by an unpolarized and limb-darkened photospheric radiation field. The center-to-limb variation $I_0(\nu, \mu)$ at the cosine of the heliocentric angle $\mu = \cos\theta$ and frequency ν is extracted from the tables in Cox (2000).

The optical thickness of the slab is measured along the LOS direction at the line center of the red component represented by τ_R. To calculate the emergent Stokes vector $\mathbf{I} = (I, Q, U, V)^\dagger$ (with † denoting transpose) for a single slab, HAZEL solves the radiative transfer equation (described in Sect. 2.2), which can be written in the following way (Trujillo Bueno, 2003):

$$\frac{d}{d\tau_R}\mathbf{I} = \mathbf{K}^{*}\mathbf{I} - \mathbf{S}, \tag{3.1}$$

where $\mathbf{K}^{*} = \mathbf{K}/\eta_I$ is the propagation matrix normalized to the absorption coefficient for Stokes I, $\mathbf{S} = \boldsymbol{\epsilon}/\eta_I$ is the source function vector, with $\boldsymbol{\epsilon} = (\epsilon_I, \epsilon_Q, \epsilon_U, \epsilon_V)^{\dagger}$ the emissivity vector (see Degl'innocenti & Landolfi, 2004; Asensio Ramos et al., 2008, for more details). For the homogeneous slab case the exact analytical solution is given by (Trujillo Bueno, 2003):

$$\mathbf{I} = e^{-\mathbf{K}^{*}\tau_R}\mathbf{I}_{\rm sun} + (\mathbf{K}^{*})^{-1}\left(\mathbf{1} - e^{-\mathbf{K}^{*}\tau_R}\right)\mathbf{S}, \tag{3.2}$$

where $\mathbf{I}_{\rm sun} = (I_0(\nu,\mu), 0, 0, 0)^{\dagger}$ is the Stokes vector that illuminates the slab boundary. For the He I multiplet we can assume that this is essentially the photospheric continuum for on-disk observations (the He I lines are barely detectable in the quiet solar spectrum) or $\mathbf{I}_{\rm sun} = 0$ for off-limb observations as the scattering geometry is at 90°. We have chosen $\tau_R = 1$ for these experiments. The calculations have been performed with a Doppler width of $\Delta v_D \sim 8{\rm km\ s}^{-1}$ and all Stokes profiles are normalized to the continuum intensity if the profile is in absorption or to the maximum intensity if the triplet is in emission. Also, the reference wavelength used in all the figures $\lambda_0 = 10829.0991$ Å is the central wavelength of the blue component of the He I 10830 Å multiplet.

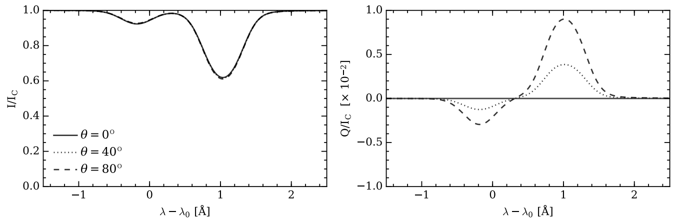

Figure 3.2 – Synthetic Stokes profiles generated without magnetic field at different heliocentric angles θ. The linear polarization generated by the anisotropic illumination increases towards the limb.

For the first case, we assume no magnetic field showing that it is possible to induce atomic polarization (see also Sect. 2.2.3) with the anisotropic illumination of the photosphere below. We choose $\phi = 0°$ and $\gamma = 90°$, so that $Q > 0$ is parallel to the limb. To see the effect of the heliocentric angle we have located the slab at $\theta = 0°$ (disk center), $\theta = 40°$ and $\theta = 80°$ (almost at the limb). Figure 3.2 shows the emergent Stokes profiles for these configurations[1].

In these scattering events, we only get linear polarization signals in Stokes Q with no Stokes U, as the polarization generated is parallel to the limb and no Stokes V can be created as we do not have magnetic field. The height in the atmosphere plus the center-to-limb variations of the photospheric continuum radiation (Trujillo Bueno & Asensio Ramos, 2007) are sufficient to induce population imbalances and quantum coherence among the magnetic sublevels. In the forward scattering case ($\theta = 0°$), there is no

---

[1] We are not really checking what happens to "exactly" the same slab. If we change μ, we also have to change τ_R accordingly, as the opacity is measured in the light of sight direction. However, it is enough to show the general behaviour of the polarization.

polarization signal because the axis of symmetry of the radiation field and the line of sight direction coincide (solid line in Fig. 3.2). In this case, the problem becomes fully symmetric and no polarization can be generated. If the heliocentric angle (θ) is increased (we are looking to a slab closer to the limb), the linear polarization increases (dotted and dashed lines in the same figure), being maximum at $90°$-scattering. From this figure, we can infer that the polarization generated in off-limb structures like spicules or prominences is larger than that from on-disk structures like filaments and theoretically should be easier to observe. As we mentioned in the previous chapter (Sect. 2.2.5) we see the typical one-lobe shape of the scattering polarization, which is very different to the three-lobe shape of the Zeeman effect as the σ and π components are shifted in wavelength.

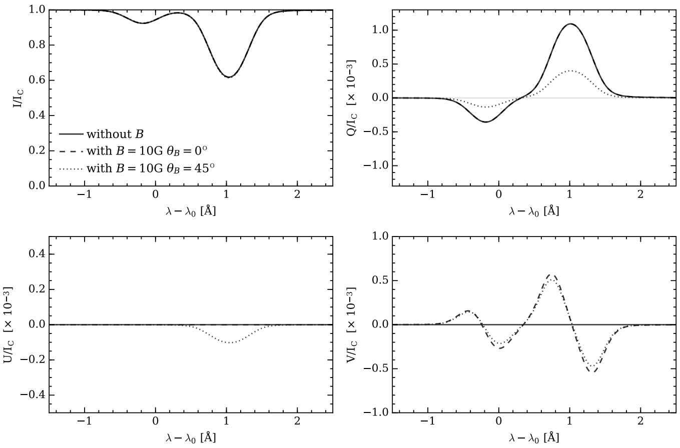

Figure 3.3 – Synthetic Stokes profiles generated with and without magnetic field with different inclinations θ_B. Our slab is located at $\phi = 0°$ and $\theta = 20°$. A magnetic field incline with respect to the vertical is able to modify and create scattering polarization.

As a second example, we introduce a magnetic field of $B = 10$ G which permeates the slab with a local azimuth of $\phi_B = 0°$ (the magnetic field vector is contained the in $X - Z$ plane), with the slab located at $\phi = 0°$ and $\theta = 20°$. If the inclination of the magnetic field is chosen as $\theta_B = 0°$, the magnetic field vector is aligned with the local vertical and the symmetry axis of the radiation (dashed line in Fig. 3.3). As the magnetic field does not introduce any additional symmetry breaking, the linear polarization generated by scattering polarization remains unchanged (solid and dashed lines cannot be distinguished in Stokes Q and U) and a circular polarization signal appears as a consequence of the longitudinal Zeeman effect.

If a local inclination of $\theta_B = 45°$ is chosen, the linear polarization rotates so that Stokes U signals appear and the amplitude of Stokes Q decreases rapidly. This is shown in Fig. 3.3 with a dotted line. Stokes I remains almost the same as the Zeeman splitting is much smaller than the Doppler width of the line and Stokes V decreases because the longitudinal component of the magnetic field vector is smaller. We want to stress that the linear polarization is actually created by the Hanle effect (see Sect. 2.2.5), where the presence of an inclined magnetic field with respect to the symmetry axis of the radiation pumping cause a modification in the atomic-level polarization.

As a third example, we increase the magnetic field strength of our scenario. With this experiment we want to point out when the Zeeman effect starts to have a clear contribution. In order to see that, we

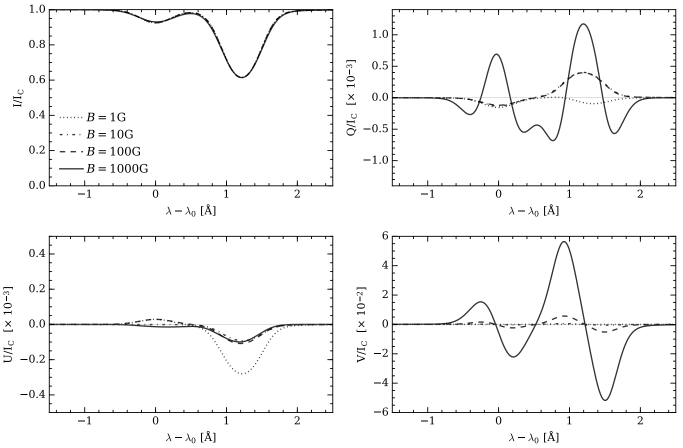

Figure 3.4 – Synthetic Stokes profiles generated under the same conditions of Fig. 3.3 but changing the magnetic field strength. The transverse Zeeman effect starts to appear as we increase the magnetic field strength.

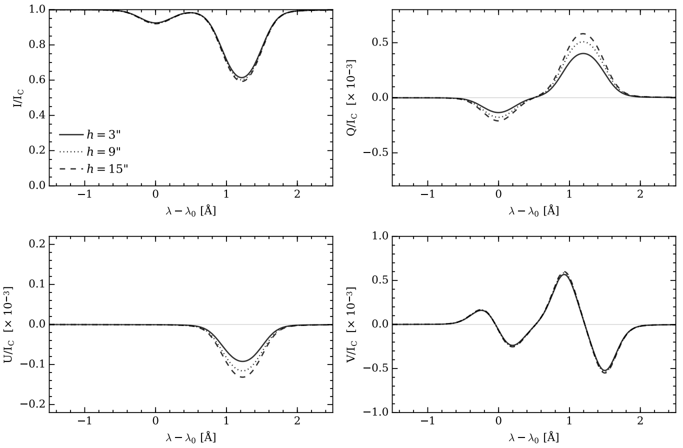

Figure 3.5 – Synthetic Stokes profiles generated from a slab model permeated by a magnetic field of $B = 10\,$G, $\theta_B = 45^\circ$, $\phi_B = 0^\circ$ and located at different heights above the solar surface.

synthesize the same case as the previous Fig. 3.3 but with magnetic fields of increasingly larger strengths. Figure 3.4 shows the Stokes profiles for different magnetic field strength values. From this figure we see: 1) for very weak fields ($\sim 1\,$G) the polarization in the blue and red transitions can have the same sign, 2) for higher fields, between 10 G and 100 G, the linear polarization profiles tend to be similar as they are not sensitive to the magnetic field strength (saturated Hanle regime), and 3) for $B > 100\,$G the transverse Zeeman effect starts to play a significant role in the emergent polarization. Below 100 G we can safely assume that the emergent linear polarization is completely dominated by scattering polarization (and the Hanle effect). With a magnetic field of 1000 G (solid line in the figure) the typical Zeeman pattern of three-lobed profiles is clearly visible. This shape is due to the wavelength shifts between the π and σ components. Although the linear polarization is dominated by the transversal Zeeman effect, the influence of the scattering polarization is still significant for very strong fields ($\sim$1000 G) (Trujillo Bueno & Asensio Ramos, 2007). Note that the longitudinal component of the magnetic field increases and it is detected in Stokes V, and that even for $B=$1000 G we cannot clearly detect the Zeeman splitting in Stokes I although one can see a slight increase in the line broadening.

Lastly, we want to show the consequences of changing the height of the slab. Changing this value affects the degree of anisotropy because larger heights imply smaller solid angles subtended by the solar sphere. Then, as we explained in Sect. 2.2.4, given that the emissivity of the linear polarization is proportional to the anisotropy $\epsilon_{QU} \propto J^2_0$, polarization signals are expected to increase when h increases. This is shown in Fig. 3.5.

3.3 Signatures of structure along the line of sight

The relatively short literature in which He I is used for inferring magnetic fields is full of hints at the presence of structuring along the LOS. These signatures are perhaps easier to see in off-limb observations and, therefore, the difficulty of a correct interpretation of spectropolarimetric observations becomes more visible in such geometry.

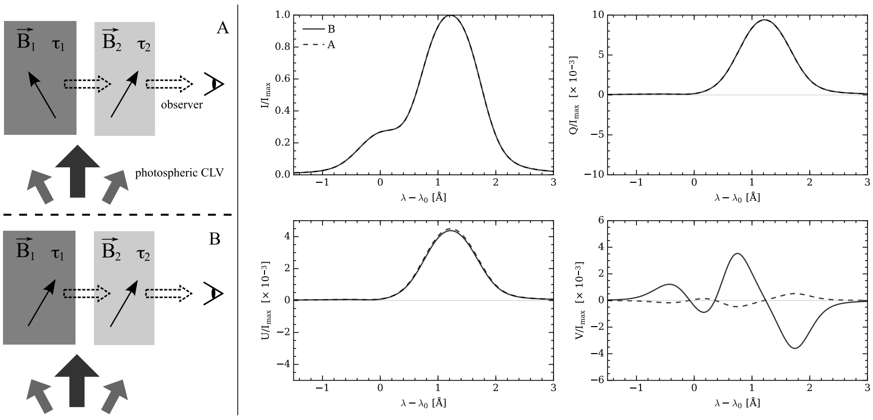

Figure 3.6 – Left panel: Sketch with two possible scenarios of the magnetic field configuration along the line of sight. Right panel: Synthetic Stokes profiles generated in the two slab scenario illustrated in the left panel. Figure adapted from Centeno et al. (2010).

A good example of this is the importance of the line-of-sight cancellation of Stokes V signals in solar spicules. This has lead to a discussion on how strong the magnetic field could actually be in these structures (Centeno et al., 2010). Although a poor temporal and/or spatial resolution observation can mix the signals from nearby pixels, even with perfect atmospheric conditions, several spicules lie in the same LOS. This cancellation effect because of having different magnetic structures along the LOS only allows us to infer a lower limit for the longitudinal component B_{LOS}. An additional problem is that if the circular polarization signal is below the noise level, the full magnetic vector cannot be inferred because we are probably close to the saturation regime of the Hanle effect. To visualize the previous conclusion, we follow Centeno et al. (2010) and use Hazel to generate a numerical experiment with two slabs of constant physical properties at the same height over the solar surface in a 90°-scattering scenario permeated by a magnetic field with different local azimuths as shown in Fig. 3.6. The light emitted from slab 1 is taken as the background radiation for slab 2 and then "re-emitted" to the observer. The left panel of Fig. 3.6 shows two scenarios where A) two slabs have a magnetic field such that the LOS component cancels out and B) a case where they result in a non-cancelling LOS component. The line width of the spicules is very broad, with 13 $\mathrm{km\,s^{-1}}$ being a typical value, and the damping parameter is a =0.2 (Trujillo Bueno et al., 2005; Asensio Ramos et al., 2008). From Fig. 3.6 we see that even a very weak Stokes V signal could imply strong magnetic fields whose circular polarization are almost canceled out. The Stokes parameters were generated with a magnetic field of $75\,\mathrm{G}$ in each slab of optical depth $\tau_R = 0.75$ with magnetic field inclinations of $\theta_B = [45°, 32°]$ and azimuths of $\phi_B = [-160°, -20°]$ for the case A) and $\phi_B = [-160°, -160°]$ for case B). In case A) the observed circular polarization can be reproduced with a single slab with less than $10\,\mathrm{G}$.

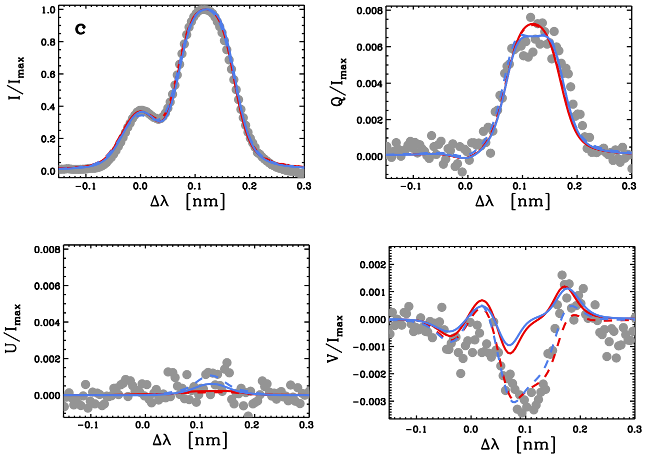

Figure 3.7 – Intensity and polarization (dots) and best-fit profiles from inversions with one (red) or two (blue) components along the LOS, in the absence (solid) or presence (dashed) of atomic orientation. Only when the atomic orientation is considered, the Stokes profiles can be fitted. Figure adapted from Martínez González et al. (2012b).

Another hint of the presence of radiative transfer effects is the detection of "anomalous" circular polarization profiles by Martínez González et al. (2012b). These authors measured the characteristic signatures associated to the Hanle effect in Stokes Q and U, but detected single-lobed Stokes V profiles in spicular material (see Fig. 3.7). This single-lobed profiles were explained as the result of several components along the LOS with different velocities and magnetic fields. As we explained in the previous chapter, the atomic level polarization is not only restricted to the linear polarization with the atomic alignment (ρ_0^2), but there can also be atomic orientation (ρ_0^1) which is able to strongly modify the classical antisymmetric Stokes V profile as each sigma component has a different population. Therefore, these single-lobed profiles can be generated by illuminating with a circularly polarized radiation (e.g. from an underlying magnetized photosphere) a moving structure, or differentially illuminating the $\sigma^{\pm}$ components of a magnetic structure by a relative motion. These results stressed the importance of the illumination from below and the LOS integrations effects (due to several components) to be able to reproduce the observations (dashed lines in Fig. 3.7).

3.4 A model for absorption structures in the He I multiplets

In this section we analyze the case of a solar filament formed above an active region, finding again hints of the presence of structure along the LOS. If the signals are analyzed as generated in a single-component, we infer strong fields in the hG regime, while if we separate the contribution from the underlying magnetized region modeling them with two atmospheric components, we infer weaker fields, more similar to those found in quiet-Sun filaments. The proposed scenario in this section can be extended to other structures seen in absorption towards the solar disk in lines such as the He I multiplets (e.g., filaments, fibrils in emerging flux regions, . . .). Our results raise some doubts on previous analysis and leaves the question on how strong is the magnetic field in these structures still open.

Concerning measurements of magnetic fields, spectro-polarimetric observations of QS filaments and prominences revealed magnetic fields that have strengths of the order of a few tens of G (Trujillo Bueno et al., 2002; Casini et al., 2003; Merenda et al., 2006), where the linear polarization of the He I 10830 Å is dominated by the scattering polarization due to the anisotropic radiation field. Yet, stronger fields are found for the same structures in active regions, in the range of 200-600 G (Wiehr & Stellmacher, 1991; Sasso et al., 2011). Even larger field strengths (up to 800 G) were obtained when large Zeeman-like linear polarization signatures were detected in AR filaments (Kuckein et al., 2009, 2012a; Xu et al., 2012). The work of Kuckein et al. (2009) was the first to show such linear polarization profiles of the He I 10830 Å multiplet with the surprising typical symmetric shape with three lobes of the transverse Zeeman effect.

Trujillo Bueno & Asensio Ramos (2007) and Casini et al. (2009a) soon noted that, even for such strong fields, AR filaments spectropolarimetric observations should show signatures of scattering polarization and Hanle effect. The obvious solution of having a magnetic field inclined by the Van Vleck angle (the angle that fulfills $\cos\theta_B = 1/\sqrt{3}$ and for which the contribution of scattering polarization vanishes, Degl'innocenti & Landolfi 2004) in the whole filament seemed clearly improbable (Kuckein et al., 2009). Trujillo Bueno & Asensio Ramos (2007) pointed out that when the optical thickness of the filament becomes larger than unity, radiative transfer effects start to play a role. In this case, the radiation field inside the filament becomes more horizontal (parallel to the solar surface) and it can compensate to some extent the predominantly vertical (along the radial direction) radiation field that is pumping the He I levels. Therefore, radiative transfer inside the filament produces a reduction of the radiation field anisotropy, that leads to a strong reduction of the scattering polarization and Hanle effect signals. Casini et al. (2009a) invoked the presence of a quasi-random magnetic field coexisting with the organized magnetic field of a filament. The isotropic component of the magnetic field strongly reduces the Hanle signal produced by the deterministic field.

Typically, inversions of spectro-polarimetric observations of absorption features in the He I multiplets have been carried out using a single atmospheric component, as if the observed signal was generated only in the cool plasma overdensities. Even so, these structures (QS and AR filaments, fibrils in emerging flux regions, . . .) usually have optical depths of the order of unity (Kuckein et al., 2009, 2012a; Sasso et al., 2011; Xu et al., 2012). Consequently, it is reasonable to think that the emergent polarization signal can have some contribution from underlying layers outside the structure. This poses no problem in quiet regions because the He I multiplets yield almost no absorption. However, this turns out to be problematic in active regions because, for instance, the He I multiplets produce a significant absorption in the chromosphere of these regions.

We then propose a two-component approach to model the observed Stokes profiles of absorption features above active regions in the He I multiplet. This simplified model is made of two slabs with constant physical properties, one (slab 2) on top of the other (slab 1). Interestingly, this model allows us to naturally reproduce the Zeeman-only Stokes parameters observed by Kuckein et al. (2009) in AR filaments without any additional mechanism to reduce the radiation field anisotropy. In such scenario, the emergent Stokes parameters $\mathbf{I} = (I, Q, U, V)^\dagger$ can be written as:

$$\begin{aligned} \mathbf{I}_1 &= e^{-\mathbf{K}_1^* \tau_1} \mathbf{I}_{\mathrm{sun}} + (\mathbf{K}_1^*)^{-1} \left(\mathbf{1} - e^{-\mathbf{K}_1^* \tau_1} \right) \mathbf{S}_1, \\ \mathbf{I} &= e^{-\mathbf{K}_2^* \tau_2} \mathbf{I}_1 + (\mathbf{K}_2^*)^{-1} \left(\mathbf{1} - e^{-\mathbf{K}_2^* \tau_2} \right) \mathbf{S}_2, \end{aligned} \tag{3.3}$$

where the terms of the equation are essentially the same as the Eq. 3.1, but each component has a different optical depth (τ_1 and τ_2) and magnetic fields.

In some sense, our approach galvanizes from an idea proposed by Judge (2009). This work suggested that the polarization signals observed in the 10830 Å multiplet in filamentary structures in emerging flux regions might not mainly come from the highest part, but from the low-lying chromosphere of the active region. Judge (2009) argues that it is difficult to distinguish the two possibilities because the Stokes profiles would look very similar. Previous observations reinforce this idea because the photospheric and chromospheric magnetic field maps obtained using inversion techniques look astonishingly similar. The chromospheric maps look slightly more fuzzy because of the reduction in the gas pressure with height and the ensuing expansion, but no hint on any filamentary structure is detected (Solanki et al., 2003; Xu et al., 2010; Asensio Ramos & Trujillo Bueno, 2010). We go one step further and stand on the idea suggested by Asensio Ramos & Trujillo Bueno (2010) to propose that what we see is in fact a combination of the two atmospheres. We do not need to distinguish the two options anymore because they are simultaneously present in the Stokes profiles.

In this numerical exercise, similar to Centeno et al. (2010) but in forward scattering geometry, we use the HAZEL code with two different slabs in the same line of sight, so that the emergent Stokes parameters are computed using Eqs. 3.3. Each slab is permeated with a different magnetic field, but the pumping radiation in the two slabs is the same. This simplification is probably not very realistic but this model suffices to make our point. We will address this issue later in Sec. 3.4.2.

To prove our idea, we synthesize the Stokes profiles using the parameters of one of the pixels along the filament displayed in Fig. 2 of Kuckein et al. (2010). The selected magnetic field has a strength of $B = 550\,$G, an inclination of $\theta_B = 95°$, and an azimuth of $\phi_B = 49°$, both angles defined in the local reference system (the quantization axis being the local vertical). Since the geometry of the field was provided in the observer's reference frame, we have transformed the angles to the local reference system taking into account that the heliocentric angle of their observations was $\theta = 23°$ ($\mu = 0.92$). Following Kuckein et al. (2009), our synthetic profile is obtained by artificially reducing the anisotropy of the radiation field by a factor 0.2. We apply this correction to the radiation field anisotropy computed in HAZEL, which is obtained from the solar center-to-limb variation of the continuum at nearby wavelengths and correcting for the geometrical factor due to the height of the filament. The synthesized Stokes profiles are displayed in Fig. 3.8 with dotted lines and are very similar to those published by Kuckein et al. (2009). We note that these profiles are almost indistinguishable from a scenario in which the presence of scattering polarization is neglected. The solid lines show how the profile would look like using the very same physical properties but fully taking into account atomic level polarization (i.e., using the radiation field anisotropy computed by HAZEL). As already pointed out by Trujillo Bueno & Asensio Ramos (2007), clear signatures

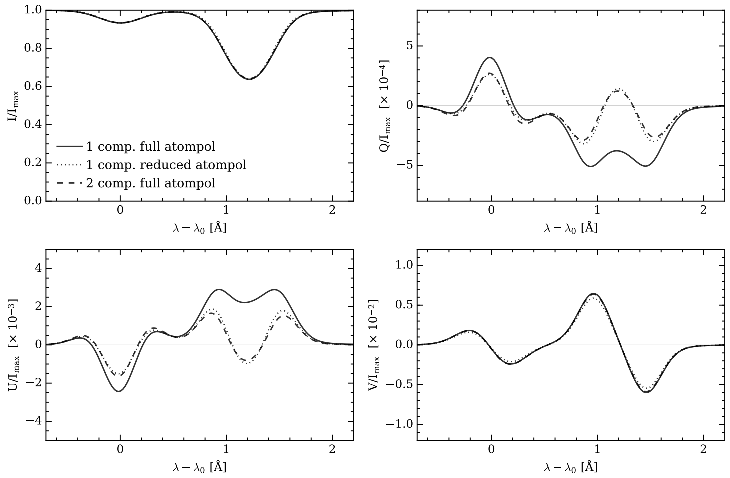

Figure 3.8 – Synthetic Stokes profiles with one component allowing atomic polarization but reducing the anisotropy by a factor of 0.2 (dotted black curve) that reproduces one of the profiles inverted by Kuckein et al. (2010), and taking the full atomic polarization into account (solid curve). The dashed curve is the fit with two components. The reference wavelength $\lambda_0 = 10829.0991$ Å is the central wavelength of the blue component of the He I 10830 Å multiplet.

of atomic level polarization are seen even at fields above 1 kG, especially in the red component of the multiplet.

We carry out an inversion with HAZEL of the dotted profiles shown in Fig. 3.8 with a two-component model. The resulting Stokes parameters are displayed as dashed lines in Fig. 3.8. The inferred values for the low-lying component are $B_1 = 650\,$G, $\theta_1 = 92^\circ$, $\phi_1 = 48^\circ$, and $\tau_1 = 0.6$. The upper component has $B_2 = 10\,$G, $\theta_2 = 85^\circ$, $\phi_2 = 140^\circ$, and $\tau_2 = 0.3$. The fit is almost indistinguishable from the profile with reduced anisotropy. Our inversion indicates that the magnetic field of the low-lying component increases with respect to the single-component inversion but its geometry is not modified much because the Stokes Q, U and, V signals are very strong. The magnetic field in the upper slab turns out to be almost horizontal, with an azimuth that is roughly perpendicular to that of the lower component and to the axis of the filament. We have carried out extensive tests that indicate that the presence of a weak field in the filament is a robust result. We stress the fact that the low-lying component has to have a stronger magnetic field. Otherwise, the profiles cannot be fitted. The magnetic configuration as well as the remaining slab properties were retrieved without imposing such a configuration as starting point of the inversion.

The profiles of the two-component model can be understood by noting that the scattering polarization signatures generated in each individual component have opposite signs because the azimuths of the fields differ by $\sim 90^\circ$. The solution of the radiative transfer equation combines them reducing the Hanle contribution, with the possibility of even fully cancelling it out. We point out that the Hanle contribution to the line profile of both components is similar even though the fields differ by more than an order of magnitude because the He I 10830 Å is already in the Hanle saturation regime for fields above ~ 10 G. In this regime, the Hanle signals are insensitive to the magnetic field strength, so B_2 can still be large and produce the same contribution as a weaker field.

3.4.1 Stability of the solution

It is obvious that the proposed model presents a handicap because a two-component model has a larger number of parameters and the inversion becomes highly degenerate. One of the most obvious degeneracies takes place on the optical depth of each slab. We can only safely obtain the total optical depth $\tau = \tau_1 + \tau_2$ and the optical depth of each slab remains undetermined provided their sum equals τ. This affects the inference of the magnetic field because it is sensitive to the respective value of the optical depth. The only sensible way that we can think of to overcome this degeneracy is to use context information and to take advantage of the whole observed map to introduce constraints (e.g., use extrapolations from the photosphere to the chromosphere).

In spite of the increase in the complexity of the proposed model, we think that it is more physically realistic than any other single-component model used in the past. Considering the increased degeneracy, it is very important to verify the consistency of the model and to check that the space of parameters that is compatible with the observations is not exponentially small. This would give us the idea that our fit is just a coincidence. To this end, we slightly perturb the original profile and inspect whether the inferred parameters do not vary much. The perturbed Stokes profiles are obtained by changing the magnetic field vector but keeping fixed the thermodynamic and dynamic properties of the 1-component model. We consider relative changes of 2, 5, and 10% for the three spherical coordinates of the magnetic field vector. After that, we carry out an inversion with HAZEL and calculate the relative change in the two-component model parameters with respect to the initial configuration.

Table 3.1 – Relative change in the model parameters of the two-component model when the magnetic field vector of the single-component model is modified. The horizontal dashes indicate relative changes below 0.5%, compatible with no change at all.

$\Delta[\%]$	2%			5%			10%		
	B	θ	ϕ	B	θ	ϕ	B	θ	ϕ
B_1	1	-	-	4	-	-	10	-	-
θ_1	-	2	-	-	6	-	-	12	1
ϕ_1	-	-	1	-	-	4	-	-	8
B_2	2	-	-	5	-	-	12	-	-
θ_2	-	2	-	-	4	5	-	14	7
ϕ_2	-	-	1	-	-	3	-	2	6

The results are shown in Table 3.1. The table shows the relative change in the magnetic fields of the upper and lower components when the magnetic field vector in the single-component model is modified with a certain relative change. All horizontal dashes refer to changes below 0.5%, compatible with no change at all. We note that all changes are roughly of the same order than the modification in the original model. Obviously, larger modifications of the model parameters lead to larger modifications of the two-component model parameters. The important point of this table is that our proposed model is very robust to changes in the profile because similar profiles have similar solutions. Of special relevance is the fact that the azimuth difference between the two components is always $\sim 90^\circ$ for every explored perturbation. Converging to the solution with a two-component model is tougher and slower. For that reason, some values of the Table 3.1 are obtained by setting the initial values to the original ones.

3.4.2 Approximations in the radiative transfer problem

In order to solve the radiative transfer problem we are assuming that the spherical tensor components (see also Sect. 2.2.4) of the radiation field J^0_0 (mean intensity) and J^2_0 (radiation anisotropy) that illuminate the top component of the model are the same as those illuminating the lower component. This is a necessary simplification in Hazel to avoid having to solve the full non-LTE problem of the second kind, something that is well beyond our aims. However, in the following, we estimate the possible impact of the presence of the lower component on the illumination of the top component of the model.

The radiation anisotropy of the top slab, $[J^2_0]_2$, for an illumination axially symmetric around the vertical axis is given by:

$$[J^0_2]_2 = \frac{1}{2\sqrt{2}} \int_{-1}^{1} \mathrm{d}\mu \int_0^\infty \mathrm{d}\nu (3\mu^2 - 1)\, [\phi_\nu]_2\, [I_\nu(\mu)]_1 \,, \tag{3.4}$$

where $[\phi_\nu]_2$ is the line absorption profile in the upper component and $[I_\nu(\mu)]_1$ is the specific intensity at frequency ν and heliocentric angle μ that emerges from the lower component. Let us assume a Gaussian line absorption profile with line width $\Delta\nu$ centered at frequency ν_0. For simplicity, we assume that the emergent intensity is an absorption Gaussian line with depression d and that there is no differential Doppler shift between the two slabs (this would generate atomic orientation). Also for simplicity, we assume that only the continuum has center-to-limb variation (d does not depend on μ). Then, the ratio r between the anisotropy of the upper slab illuminated with and without a spectral line is given by:

$$r = 1 - \frac{d}{\sqrt{2}}. \tag{3.5}$$

Assuming values of $d \sim 0.25 - 0.4$ (this value is difficult to estimate because we only observe the total absorption of the two components), the ratio yields values of $\sim 0.71 - 0.82$. Therefore, the influence of the presence of an absorption spectral line on the lower component seems to be negligible given the difficulty in solving the full problem.

The second simplification in Hazel is that the atomic orientation of the upper slab is always zero. However, when the second slab is illuminated by circularly polarized light there is a non-zero orientation of the radiation field $[J^0_1]_2$ which, in turn, produces atomic orientation in the top slab. In order to quantify $[J^1_0]_2$, Martínez González et al. (2012a) showed that it is possible to generate atomic orientation, if there is a relative motion between the lower and upper component. The expression for the orientation of the radiation field is given by:

$$[J^1_0]_2 = \sqrt{\frac{3}{2}} \int_{-1}^{1} \mathrm{d}\mu \int_0^\infty \mathrm{d}\nu \mu\, [\phi_\nu]_2\, [V_\nu(\mu)]_1 \,, \tag{3.6}$$

where $V_\nu(\mu)$ is the emergent Stokes V from the lower component. According to Martínez González et al. (2012a), if the relative velocity between the two components is at least of the order of 10-12 km s^{-1}, some atomic orientation can be generated in the upper component. However, this would produce a visible symmetric Stokes V profile, something that it is not observed (Kuckein et al., 2009, 2012a; Sasso et al., 2011; Xu et al., 2012).

3.5 Summary of the results

After understanding the polarization generated under several different conditions we have showed that the inferred magnetic field is model dependent. In this chapter we have explored the consequences of having several atmospheric components in the same line of sight. In off-limb observations it seems obvious to use multiple components in the line of sight as for example several spicules are seen in the same direction with different motions. Following the same argument, on-disk observations are affected by the same problem as usually structures, such as loops or filaments, are above a background with different properties.

Thus, a two-component model, one on top of the other[2] is a natural way to explain the absence of scattering polarization signatures in some observed AR filaments. This model has been verified with the Stokes profiles of Kuckein et al. (2010) where we can infer a weak magnetic field (around tens of G) in the top component, while the strong hG field is in the bottom one. Both are horizontal and have a magnetic azimuth difference of around 90° between the slabs, the key aspect of the solution that allows the Hanle contributions of both components to be reduced or even being cancelled.

In our opinion, the presence or not of a magnetized lower chromosphere is a natural explanation of why sometimes Hanle-dominated signals are found (e.g., Collados et al., 2003) while Zeeman-dominated profiles are found in other cases. The filament of Kuckein et al. (2009) goes above penumbral regions of an active region, so the field in the lower chromosphere turns out to be much higher than in observations where the filament is above the granulation. In this second case, the magnetic field and the absorption in the quiet-Sun chromosphere are smaller, having a lower impact in the emergent signals through a filament. Therefore, a filament above granulation could in principle be studied with a single component model and retrieve the magnetic field of the filament. However, the problem cannot be overcome easily as we will see in the next chapters.

---

[2] Two atmospheres combined with a filling factor could also be an option but this physical configuration still has to be justified, like other potential scenarios as the one presented by Trujillo Bueno (2010).

4

The magnetism of solar filaments from the He I 10830 Å

In this chapter we address the question about the topology of the magnetic field of solar filaments from spectropolarimetric observations of an active region filament acquired with GRIS@GREGOR. The observations trace simultaneously the chromosphere with the He I 10830 Å multiplet and the photosphere with the Si I 10827 Å line. As it is usual in previous studies, only the one single component model is used to infer the magnetic properties of the filament. However, we have found observational evidences of the need for more complex models to explain the observations. We show the presence of many profiles within the filament with the same sign in the blue and red components in the linear polarization, and numerical experiments that demonstrate that the filament is almost transparent to the circular polarization generated in the active chromosphere below. Finally, in an effort to study the feasibility of two-component inversions, we show that the model contains too much flexibility and it can reproduce the observations with a high number of different magnetic configurations, thus making the interpretation very complex.

4.1 Introduction

During the previous chapters we have discussed the importance of the magnetic field supporting the filament material and how it can be inferred from the He I 10830 Å multiplet. In this chapter we will study the magnetic structure of the filaments from the analysis of the most recent filament observations in terms of polarimetric sensitivity taken at the GREGOR telescope. The necessity of this study is motivated by the lack of knowledge of these structures, the scarce number of studies, the debate about the exact topology of the field lines and, in particular, the debate about the magnetic field strength already mentioned in Chapter 3.

Despite having introduced this topic in Chapter 1, it is important to recall now some of the ideas introduced there. The linear polarization of the He I 10830 Å in QS filaments is dominated by scattering polarization due to the anisotropic illuminating radiation field coming from lower layers of the atmosphere (Trujillo Bueno et al., 2002; Martínez González et al., 2015). However, AR filaments have been found under a higher variety of conditions. For example, the work of Kuckein et al. (2009), which studied the magnetic field vector of an active region filament above a strongly magnetized region, claimed that their signals were dominated by the Zeeman effect without almost any hint of scattering polarization. They found, with a Zeeman-based Milne-Eddington (ME) inversion code, the highest field strengths measured in filaments to date, with values around 600–700 G. After that, Sasso et al. (2011, 2014) studied a complex flaring active region filament during its phase of increased activity, including the Hanle effect, since they detected scattering polarization signatures in the observed profiles. They found values for the magnetic field strength in the range 100–250 G. Another measurement was reported by Xu et al. (2012), who inverted the same filament during the stable phase, before the eruption. They used the Zeeman-based ME inversion (HELIX$^+$; Lagg et al., 2009) because they did not find any clear signatures of scattering polarization nor of Hanle effect. Their observation exhibited a section of the filament above the granulation with weak inferred magnetic fields ($\sim$150 G) and a section above a strongly magnetized area, which returned much higher magnetic field strengths from the inversion ($\sim$750 G). At that time, this non-detection of signatures of scattering polarization was quite surprising. Trujillo Bueno & Asensio Ramos (2007) and Casini et al. (2009a) noted soon that, even for strong fields such as 700 G, spectropolarimetric observations of AR filaments should show signatures of scattering polarization and the Hanle effect. To explain the lack of Hanle signatures, Trujillo Bueno & Asensio Ramos (2007) suggested that a reduction of the radiation field anisotropy due to the horizontal radiation inside the filament could reduce the scattering polarization, while Casini et al. (2009a) suggested that an unresolved isotropic magnetic field could also explain the observations.

From these previous observations, the highest inferred magnetic field values seem to be associated with filaments above highly magnetized areas. Based on this idea, we suggested in Chapter 3 that filaments could be quite transparent, with the highest values for the magnetic field being associated to the active chromosphere below, and not to the filament itself. By adopting a two-component model (one slab for the filament and another for the chromosphere) we reproduced the Zeeman-like profiles of Kuckein et al. (2009) without suppressing the atomic polarization. The lack of scattering polarization found in their study could be due to a cancellation of signatures in the Stokes profiles when combining the scattering polarization features of the Stokes profiles when combining both components.

New recent studies have demonstrated the importance of considering more complex models to understand the physical mechanisms behind the formation of this multiplet. There are observational evidences, for example, of the generation of atomic orientation by the Doppler shifted illumination coming from the underlying magnetized photosphere, which explains the existence of extremely asymmetric Stokes V profiles (Martínez González et al., 2012b). Other studies show, from numerical experiments, the problems of assuming a 1D slab model to infer the magnetic field of complex structures (Milić et al., 2017). They emphasize the multidimensional effects often neglected in optically thick structures, also noted by others (López Ariste & Casini, 2002) from the ratio between the two components of the helium triplet. Finally, new detailed 2D multi-thread radiative transfer codes (Léger & Paletou, 2009) are under development to improve the analysis of spectropolarimetric observations of filaments, and 3D radiation-MHD simulations of a enhanced network are being used to understand and explain the spatial structure of this multiplet in intensity (Leenaarts et al., 2016).

In the light of these results, the magnetic field strength inferred in filaments is still a matter of debate. At present, obtaining high quality polarimetric observations of these structures is a challenge and the inference of the magnetic field vector in the Hanle regime is subject to several potential ambiguities (Orozco Suárez et al., 2014; Martínez González et al., 2015). To shed some light on the problems of the inference, we present the analysis of ground-based spectropolarimetric He I 10830 Å observations in an active region filament located above the granulation adjacent to a sunspot. Despite having the observed polarization less contaminated by the underlying region, a single component model shows some unrealistic and inconsistent results in the inferred magnetic field. In this chapter we show some of the limitations of using a single component model, a common practice in previous studies.

4.2 Observations

The observations were carried out at the GREGOR telescope (Schmidt et al., 2012a) on the 17th of June 2014 using GRIS (GREGOR Infrared Spectrograph, Collados et al., 2012). The slit (0.14″ wide and 65″ long) was placed over the target, an active region filament close to a sunspot in the active region NOAA 12087, at coordinates +187″,–327″, which correspond to an heliocentric angle of $\theta = 23°$ ($\mu = \cos\theta = 0.92$). Six scans of the full sunspot were taken with a scanning step of 0.14″, which provided us with a map of size 65″× 27″. The first scan started at 08:00 UT and the last one finished at 17:30 UT. Each one lasted ∼15 minutes. The rotation compensation of the alt-azimuthal mount in GREGOR was not yet available, so there are some rotation effects in the scans, specially at the borders of the slit. By calculating the power spectrum of the continuum intensity in the quiet Sun we estimated the spatial resolution to be about 0.5–0.6″(see Sec. A.3 for more details about this calculation).

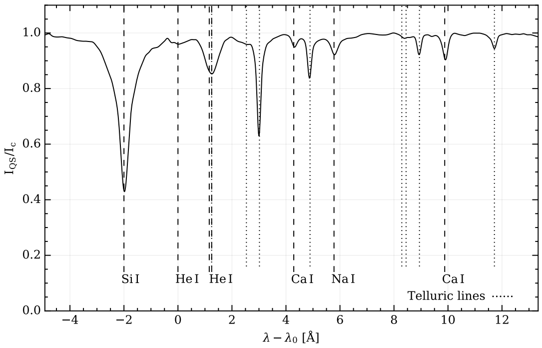

Figure 4.1 – This figure displays the average intensity spectrum of the quiet Sun of our observations showing the GRIS spectral range with the spectral lines mentioned in the text. The reference wavelength ($\lambda_0 = 10829.0911$ Å) is the central wavelength of the blue component of the He I 10830 Å multiplet. The symbol I_c is refers to the average continuum intensity of the quiet-sun.

The observed spectral range spanned from 10824 Å to 10842 Å, with a spectral sampling of 18.1 mÅ/pixel. This spectral region contains the chromospheric He I triplet, some photospheric lines of Si I, Ca I, and Na I, and several telluric lines. The GRIS spectral range with the above-mentioned spectral lines is displayed in Fig. 4.1 together with the average intensity spectrum of the quiet Sun of our observations.

We show the reconstructed maps of the observed active region in Fig. 4.2, where the x-axis represents the position along the slit and the y-axis is the scanning direction. The left panel of the figure shows the Stokes I map of the observed region in the continuum at 10841.3 Å, and the right panel shows the same region in the core of the red component of the helium triplet at 10830.3 Å, normalized to the intensity of the quiet Sun. The filament, visible in the core of the He I line, has a length of about ∼30″(22 Mm) and a width of ∼3″(2 Mm). These images show that the observations were carried out under very good seeing conditions. Both the granulation pattern and the chromospheric absorption features with sub-arcsecond fine structure are prominently visible.

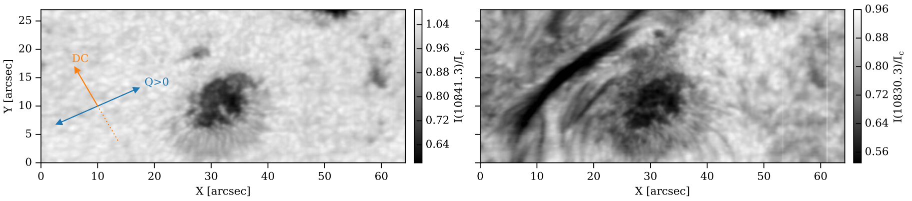

Figure 4.2 – Reconstructed maps of the continuum intensity (left panel) and the He I 10830 Å red core intensity (right panel) taken at 9:45 UT. The orange arrow indicate the direction towards the disk center (DC) and the blue one represents the reference of positive Stokes Q.

The standard data reduction procedure for GRIS was applied to all the data sets, including long-period and short period fringes correction using our novel approach (see Sec. 2.5.1). To improve the signal to noise ratio of the data we averaged 2 spectral pixels and 4×4 spatial pixels, yielding a final spectral and spatial sampling of 36.2 mÅ pix^{-1} and 0.55$''$ pix^{-1}, respectively, and a noise level in Stokes Q, U, and V, estimated from the standard deviation of the continuum, of the order of $(4, 4, 6) \times 10^{-4}$ in units of the continuum intensity, I_c.

The reference direction for $Q > 0$ was not available from the observations metadata. Given that we observed a relatively round sunspot, we make the assumption that the magnetic field is oriented radially from the center of the umbra. We find the reference direction for $Q > 0$ by locating the direction where the integrated Stokes Q profile is maximum, which should coincide with an almost zero Stokes U. For the fifth scan, the $Q > 0$ direction is at $23.7°$ and the disk center is at a direction of $120.3°$, both measured counter-clockwise from the horizontal (slit) axis (see Fig. 4.2). More details about these calculations are given in Sec. 4.3.3 and in the Appendix A.2. The spine of the filament is at $\sim 42°$ from the horizontal axis.

4.2.1 Solar context

In order to put the GRIS observations in context, we have made use of the data provided by some band-pass filters of the Atmospheric Imaging Assembly instrument (AIA; Lemen et al., 2012) and the Helioseismic and Magnetic Imager (HMI; Scherrer et al., 2012) on board NASA's Solar Dynamics Observatory (SDO; Pesnell et al., 2012). The top panel of Fig. 4.3 shows an SDO/HMI image at the continuum of 6173 Å of the NOAA 12087 region which we analyze here. The red box in Fig. 4.3 outlines the GRIS field of view (FOV). In the top right panel, a magnetogram (saturated at ±800 G) shows how the filament is located above the polarity inversion line between the sunspot and the plage of the left side. These maps have a spatial resolution of ∼1.2$''$ (Yeo et al., 2014). Due to the thermal structure of prominences, they can be seen in UV-EUV images. Several studies (Mackay et al., 2010; Parenti et al., 2012; McCauley et al., 2015) have demonstrated the usefulness of UV observations for plasma diagnostic in prominences. For that, the following panels in the second and third row of the figure display the SDO/AIA maps, from top to bottom and left to right: He II 304 Å, Fe IX 171 Å, Fe XIV 211 Å, and Fe XVIII 94 Å. The AIA spatial resolution is between 1.4−1.8$''$ depending on the channel (Boerner et al., 2012).

Figure 4.3 shows a very bright coronal loop linking the first and the third sunspot of the region (counting from left to right) in the AIA images. This brightness is enhanced in the feet and the apex of the loop. Our observed filament as seen in the core of He I is overplotted with a white contour. The He I absorption does not clearly correlate with any of the AIA channels. The reason might be that the filament

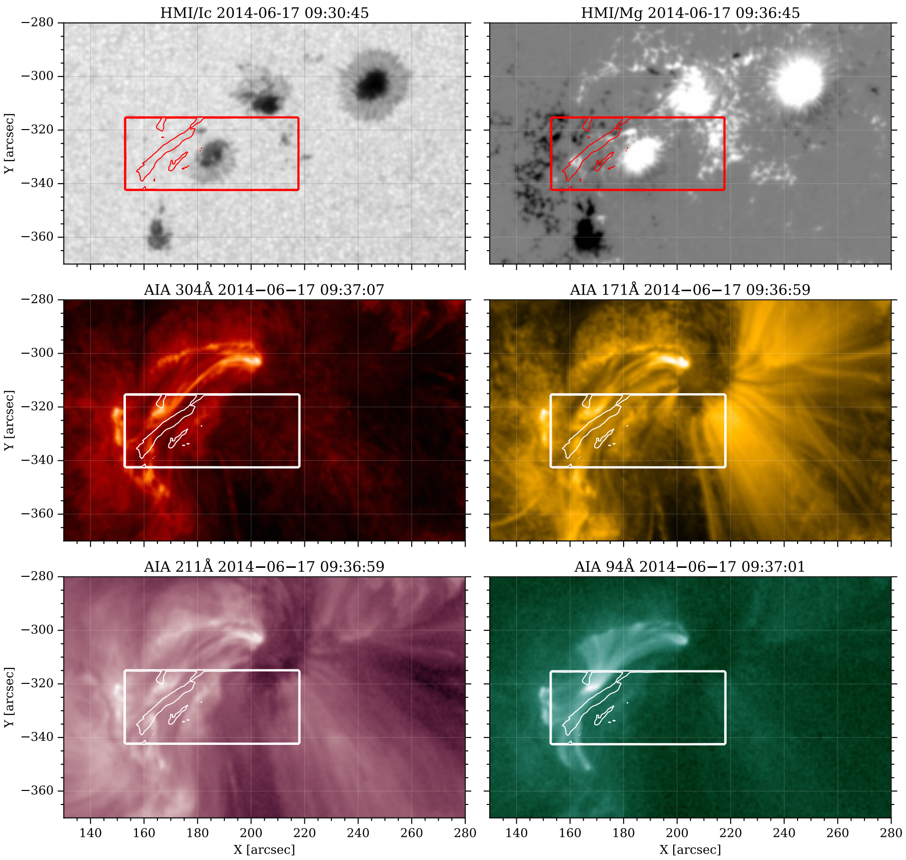

Figure 4.3 – The active region, NOAA 12087, with a contour showing our observed region above some AIA maps in different wavelengths indicated at the top of each panel. Despite the fact that the filament seems to be aligned with the coronal loops that are linking the two sunspots, we do not detected the filament in these maps.

we observed is low-lying, while the emission of higher coronal loops dominates the intensity measured in the AIA channels.

4.2.2 Evolution of the filament

During the same day of the observation several flares occur. In particular, at the same time of our spectropolarimetric measurements, a GOES class B5[1] flare erupted in the central part of the active region inside our field of view, coincident in position with our field of view. Since GOES observes the whole solar disk, we have to verify this, calculating the time evolution of the flux of the active region, which is shown

---

[1] We remind the reader that the class of each flare is chosen according to their X-ray flux detected by the NOAA's GOES satellites in the wavelength range 1 to 8 Å.

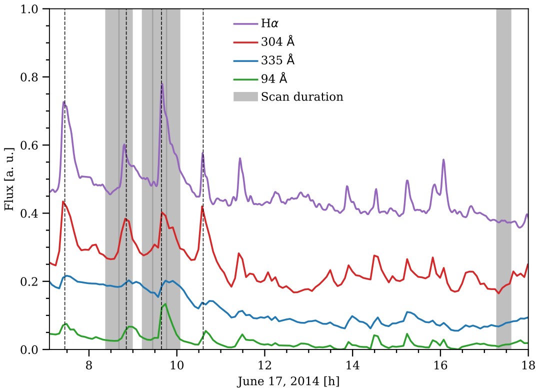

Figure 4.4 – Time evolution of the flux (in arbitrary units) integrated over the active region area for some filters. The six gray areas define the intervals of each scan (∼15 minutes).

in Fig. 4.4. We have used different filters such as the AIA channels at 304 Å, 335 Å, 94 Å, and Hα obtained by the GONG network (Hill et al., 1994).

Figure 4.4 displays a clear peak during the fourth scan. In fact, the energy is released close to the central part of the filament but not exactly above the filament. Figure 4.3 shows this compact bright point at (170″, −320″). We see a sudden and intense variation in brightness from 09:35 to 9:46UT in the 94 Å and 304 Å channels and a weaker brightening in the remaining filters. We do not detect neither emission intensity profiles of the He I observations, nor a significant decrease of the intensity during the flare, in contrast to what have been found in other studies (Sasso et al., 2011; Kuckein et al., 2015; Judge et al., 2015b), possibly because our flare is one or two orders of magnitude less energetic than theirs in X-rays (see Sec. A.4 for more details about the event). Another possibility is that the flare occurs at higher layers above the filament and the energy is redirected towards both feet of the big loop, as some brightening at (200″, −300″) and (150″, −320″) seem to indicate.

We have also analyzed how the filament shape changes during its lifetime. Figure 4.5 shows monochromatic images of the core of the He I line reconstructed from all the observed scans. In the first two scans, the filament is made of several thin threads. At 9:15 UT during the third scan, the filament has a compact body with the largest width of the time series. Later, it changes its shape again and we argue that the two flares at 8:45 UT and 9:30 UT are correlated with the time steps in which the filament is more diffuse. The energy released could evaporate or destabilize the filament structure seen in the He I triplet. After seven B-class flares, at 17:15 UT the filament has almost vanished. Although we do not see a very clear relation between the filament and the flares, if reconnection events are taking place, a reconfiguration of the magnetic field of the environment could be the reason why the evolution of the filament is so fast.

4.3 Analysis of the polarization signals

4.3.1 Polarization maps

We start by analyzing the spatial distribution of the polarization signals. Since all the scans have similar polarization properties and our aim is the study of the filament itself, we have focused our study on the

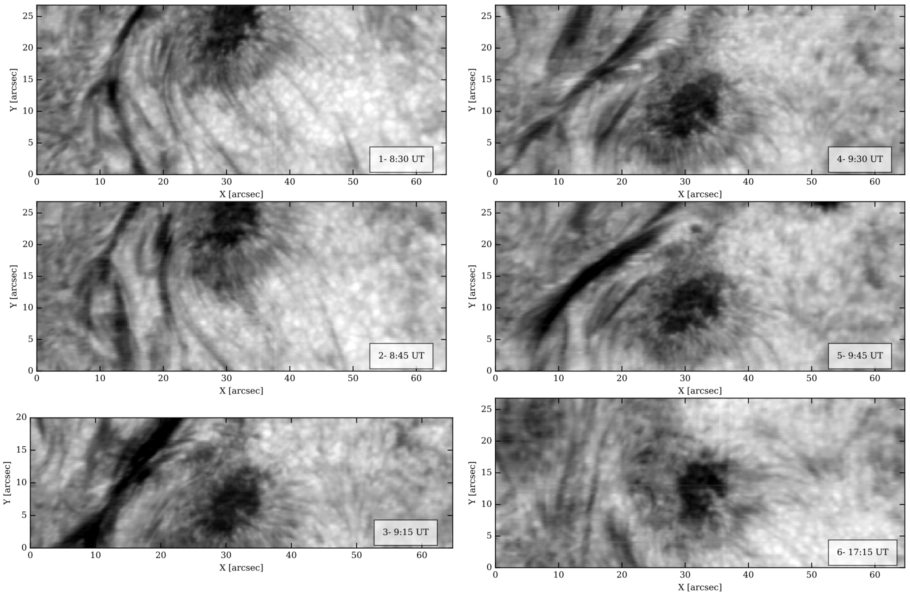

Figure 4.5 – This figure displays six reconstructed maps of the filament between 8:00 and 17:00 UT. The last scan was taken seven hours later showing how the filament has disappeared. These images are built with the intensity of the red component of the He I multiplet at 10830.3 Å.

fifth scan, where the longest and most compact structure is seen (see Sec. A.11 for other scans). Figure 4.6 displays the Stokes $Q(\lambda_0)/I_c$, $U(\lambda_0)/I_c$ at the center of line λ_0 and the amplitude of the red lobe at λ_R of Stokes $V(\lambda_R)/I_c$ for the Si I line at 10827.1Å and for the red component of the He I triplet at 10830.3Å. White contours show the signal above three times the noise level. Solid line contours indicate positive signals while negative signals are displayed with dashed line contours. Red contours displays the location of the absorption features (i.e., the filament). The linear polarization maps of the silicon line (first column of Fig. 4.6) show strong signals in the penumbra of the sunspot. The linear polarization maps in the helium core are shown in the second column of Fig. 4.6. Although the Stokes Q amplitude of the He I triplet does not exhibit an evident correlation with the filament, we can detect a strong signal coincident with the body of the filament in Stokes U. The average Stokes U signal at the line core within the filament is around $1.5 \times 10^{-3} I_c$. Finally, in the last row of Fig. 4.6 we can compare the Stokes V maps for the Si I and He I lines. The Si I Stokes V map shows the polarity of the magnetic field in the whole area (pointing towards the observer in blue and away in red). Interestingly, the He I Stokes V map is very similar to the photospheric map but more diffuse, and it does not show any correlation with the filament at all. The main difference in the area where the filament is located is that the polarity inversion line of the chromospheric map is much better aligned with the filament than the photospheric one. The polarization maps show how the circular polarization of the He I is mainly dominated by the underlying magnetic field, while the linear polarization is dominated by the filament itself, in agreement with the idea discussed in Chapter 3 that the filament could be transparent to the polarized radiation originated in the underlying magnetized chromosphere.

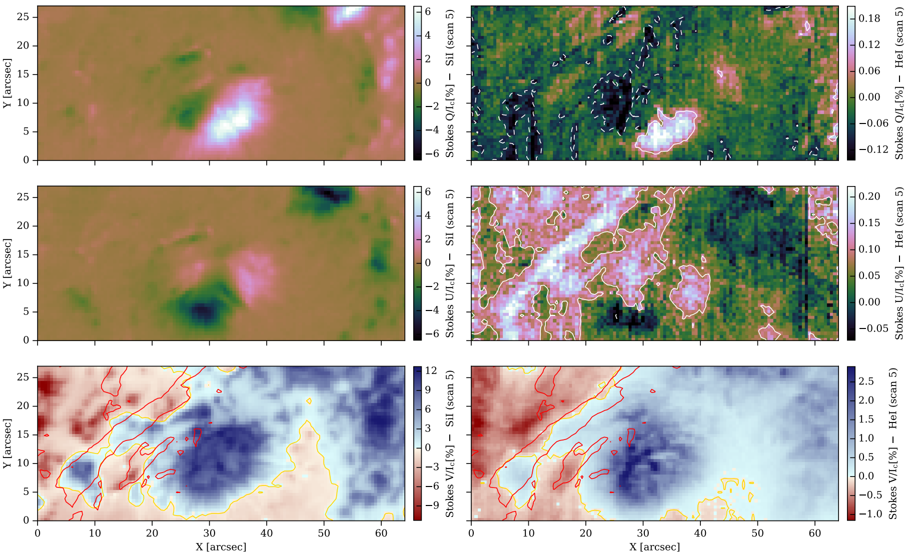

Figure 4.6 – Stokes $Q(\lambda_0)/I_c$, $U(\lambda_0)/I_c$ and the amplitude of the red lobe (λ_R) of Stokes $V(\lambda_R)/I_c$ for the Si I line at 10827.1Å (first row) and the red component of the He I triplet at 10830.3 Å (second row). The white solid (dashed) contour shows the positive (negative) signals above three times the noise level. Red contours at $0.7I_c$ show where the filament is located.

4.3.2 General description of the helium profiles

In this section we describe the morphology of the observed He I Stokes profiles. In general, it is possible to have a quite precise idea of which is the main mechanism dominating the polarization signals in each region by the shape of the Stokes parameters. Anisotropic radiative pumping, the Hanle effect, and the Zeeman effect work together to shape the polarization of the He I triplet (see Sec. 2.1 for a description of each mechanism). Unless specified, when we refer to each Stokes parameter, they will be normalized to their local continuum, I_{LC}, computed in the same pixel and in the nearby spectral continuum region. More details will be given in Sec. 4.3.3.

The strong absorption observed in Fig. 4.2 cause broader and deeper Stokes I profiles as compared to the quiet regions. For a pixel inside the filament we observe signatures of scattering polarization (and likely Hanle effect) in Stokes Q and U. As an example, the lower panel of Fig. 4.7 displays a typical Stokes profile of that area. The He I profiles exhibit the usual single-lobed symmetric shape in linear polarization (Trujillo Bueno et al., 2002). Contrary to the Zeeman effect, the presence of a magnetic field is not necessary in general to produce polarization signals, which are generated by scattering processes. However, the presence of a magnetic field affecting the polarization through the Hanle effect can be inferred from Fig. 4.6. In absence of magnetic fields, due to geometrical considerations we expect all the linear polarization to be parallel to the closest limb[2] (Bommier et al., 1989; Trujillo Bueno et al., 2002; Milić et al., 2017). Since our Stokes $Q > 0$ reference direction is defined almost along this direction

---

[2] This result is strictly true only if the radiative transfer inside the filament can be neglected and the radiation field can be considered axial symmetric.

(parallel to the limb), we would expect the linear polarization of the filament to be observed only in Stokes Q. However, Fig 4.6 shows that the linear polarization signal is fundamentally contained in Stokes U, while Stokes Q is barely detectable. This modification of the polarization is a clear signature of the magnetic field acting via the Hanle effect.

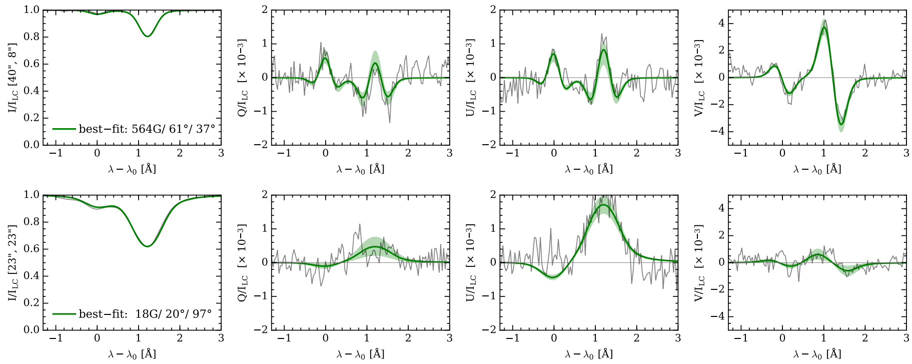

Figure 4.7 – Observed (grey) and best-fitted (green) He I 10830 Å triplet profiles corresponding to different points in the map. In the vertical axis labels of the left column the position in the map is shown. A shadowed green area is displayed indicating the range of solutions compatible with the profiles. In the left column panels the parameters of the best fit are displayed. The symbol I_{LC} is the local continuum intensity.

We also note from the lower row of Fig. 4.7 that both Stokes Q and U profiles extracted from the filament show polarization in the blue component (λ_0 in this figure) of the He I multiplet. Since the upper level of the blue level ($^3P_0$) has angular momentum $J = 0$, it cannot be polarized and the emitted radiation has to be unpolarized. The polarization is then a consequence of dichroism because the lower level ($^3S_1$) has angular momentum $J = 1$ and can be polarized (Trujillo Bueno et al., 2002). We expect the signals in the blue and red components to have opposite signs given their polarizability, which is defined as a factor that depends on the quantum numbers of the transition and accounts for the transformation of the properties of the radiation field into atomic populations. This is not the general behaviour in our observations. We discuss this issue in detail in Sec. 4.6.2. For the moment, and given the small amplitude of the blue component, we neglect its effect on the one-component inversion presented in this first analysis.

Far from the filament and close to the sunspot the linear polarization signals exhibit the typical Zeeman profiles in Stokes Q and U. This profile is characterized by three lobes in the linear polarization as we see from the profiles shown in the upper row of Fig. 4.7 that has been extracted from the penumbra of the sunspot. This region is Zeeman-dominated and, consequently, for this spectral line, the magnetic field strengths are expected to be on the hG–kG regime.

In order to visually localize each profile in the observed FOV and, consequently, which mechanism dominates the polarization signals, we have classified the Stokes Q and U profiles using a *k-means* clustering algorithm (Hartigan & Wong, 1979). Figure 4.8 shows the location of single-lobed profiles in red and three-lobed profiles in blue. The specific value of each pixel is set by the class-value ($+1$ for single-lobed and -1 for three-lobed profiles) multiplied by the absolute value of its linear polarization signal: $C_Q \cdot |Q(\lambda_0)| + C_U \cdot |U(\lambda_0)|$, where $C_Q = \pm 1$ and $C_U = \pm 1$ depending on the shape of the profile in this Stokes parameter. This product enhances those pixels where the classification is reliable and set closer to zero those areas where the profile is very noisy. Finally, the result is normalized to the maximum value of the map.

Concerning Stokes V, the whole map shows the typical antisymmetric circular polarization profile generated by the longitudinal Zeeman effect. We note that the Stokes V signal in the filament is weaker than in the sunspot. Sometimes, the regular shape is hard to distinguish because of the noise, but we can safely say that no orientation-induced signals like those of Martínez González et al. (2012b) are found.

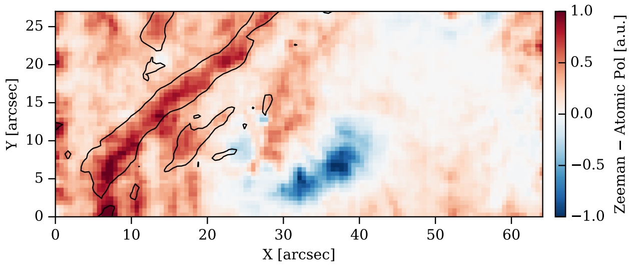

Figure 4.8 – A classification of the Stokes Q and U profiles of the region. Zeeman-like profiles are drawn in blue and Hanle-like profiles in red. Polarization signals are weighted by its strength, with the white color indicating low polarization signals where the shape is unclear. A contour at $0.7I_c$ is drawn to show the filament location.

4.3.3 Thermodynamics and magnetic field inference

In this section we will detail the inference of the thermodynamical and magnetic properties of the filament using the SIR and HAZEL inversion codes. To speed up the inversion of an entire map, we have developed our own *Message Passing Interface* (MPI) implementation by using MPI4py to do several pixels in parallel (Dalcin et al., 2011).

Photospheric inference

The Si I 10827 Å line in the observed spectral range allows us to extract the thermodynamic and magnetic information of the photosphere below the filament. As described before, other photospheric Ca I lines are located a few Angstrom towards the red (Joshi et al., 2016; Felipe et al., 2016), but the Si I 10827 Å is enough to have a rough estimation of the photospheric magnetic field. Some studies have demonstrated that the formation of the Si I line presents some departures from local thermodynamic equilibrium (Bard & Carlsson, 2008; Shchukina et al., 2017), with the core of the silicon line originating in the upper photosphere. Non-LTE effects are certainly non-negligible in the estimation of the temperature stratification, but the impact on the inferred magnetic field is very limited (Kuckein et al., 2012a). For this reason, we use an LTE inversion code which is less accurate but faster than non-LTE inversion codes.

The Si I line has a moderate magnetic sensitivity with an effective Landé factor of $\bar{g} = 1.5$. We have checked with the Stokes V response functions (RFs) to the magnetic field that the highest sensitivity is found close to $\log(\tau) = -2.2$ (Kuckein et al., 2012a; Felipe et al., 2016), where τ corresponds to the continuum optical depth at 5000 Å. Hereafter, we plot every stratification of physical quantities against this optical depth. The Si I 10827 Å line was inverted using SIR (Ruiz Cobo & del Toro Iniesta, 1992), that assumes LTE and hydrostatic equilibrium to solve the radiative transfer equation (see Sec. 2.4.1 for a detailed description). We carried out a pixel-by-pixel inversion with an initialization of the inclination of the magnetic field given by the Stokes V polarity (45° if the blue lobe is positive and 135° if it is negative).

SIR inversions require an initial guess for the atmospheric model. We choose the *Harvard-Smithsonian Reference model Atmosphere* (HSRA, Gingerich et al., 1971), covering the optical depth range $-5.0 < \log(\tau) < 1.4$. We add to the HSRA model a magnetic field strength of 500 G. The inversions were performed in three cycles. The temperature stratification $T(\tau)$ was inverted using $2, 3$, and 5 nodes in each cycle, and two nodes were used for magnetic field strength $B(\tau)$, magnetic field inclination $\Theta_B(\tau)$, and line-of-sight velocity $\mathrm{v}_{LOS}(\tau)$. The magnetic field azimuth Φ_B was set constant with height. The solar abundances were taken from Asplund et al. (2009), while the atomic data for the Si I 10827 Å line was obtained from Borrero et al. (2003). The inversion of the Si I photospheric line has been carried out using the original spectral and spatial resolution given by GRIS because the polarimetric signals of the Si I line have sufficient signal to noise. The results of the inversion will be shown in Sec. 4.4.

Chromospheric inference

To extract the physical information from the chromospheric He I 10830 Å triplet we have used the inversion code HAZEL (Asensio Ramos et al., 2008). This code is able to infer the magnetic field vector from the emergent Stokes profiles considering the scattering polarization and the joint action of the Hanle and Zeeman effects (see Sec. 2.4.3 for a detailed description).

As suggested in Asensio Ramos et al. (2008), we used a two-step procedure in the inversion process. First we obtain the optical depth, the velocity in the LOS, and the Doppler width from Stokes I. Then, we infer the magnetic field vector using all Stokes parameters, keeping the already inverted parameters fixed. To fully characterize the incident radiation field, we need to determine the height h of the filament above the solar surface. In our case, this height cannot be measured since we see the filament from above, as the LOS is almost perpendicular to the solar surface at that point. For this reason, we have used a typical value of $h = 3'' \simeq 2200$ km above the surface (Kuckein et al., 2012a; Yelles Chaouche et al., 2012; Mackay et al., 2010) for the whole FOV, as we do not know a priori if the filament is located much higher above the solar surface than the rest of the FOV. To validate our choice, we have used the projected distance between the polarity inversion line obtained from the Si I and He I lines. Under the assumption that the PIL lies roughly at the same local vertical position, one can use the projected distance in the sky and associate it to a difference in height. In our observation we find a difference of ∼1.5″, which corresponds to ~ 2000 km using Eq. 1 of Joshi et al. (2016). Assuming an average formation height for the Si I line of ~ 300 km (Shchukina et al., 2017), we find that the filament is lying at $h \sim 2300$ km above the surface roughly similar to the height that we use. We extend the discussion about the height of the filament in Sec. 4.5.4.

While the anisotropy of the radiation field is used in HAZEL to compute the density matrix, is computed using the center-to-limb variation of the photospheric continuum (Cox, 2000), the boundary condition used for the formal solution of the radiative transfer equation to get the emergent Stokes profiles can change from pixel to pixel and it has to be provided to HAZEL. Moreover, the data must be normalized to its local continuum I_{LC}. This is sometimes difficult because the nearby Si I line has strong wings. Therefore, we have used the inversion of SIR to model the Si I line profile. We extend the synthetic wing towards the He I line and then normalize the spectrum by the synthetic profile. The nearby telluric lines have been also removed by modeling them wherever they are not blended with the He I triplet. We have modeled its variation with time by fitting a Voigt profile. After this correction we are ready to invert the data. The left panel of Fig. 4.9 displays an example of this normalization procedure showing the important contributions of the silicon and telluric lines. After applying this normalization, the filament absorption remains visible in the core intensity map, while the granulation pattern and the sunspot disappear. The normalized maps can be found in Sec. A.9.

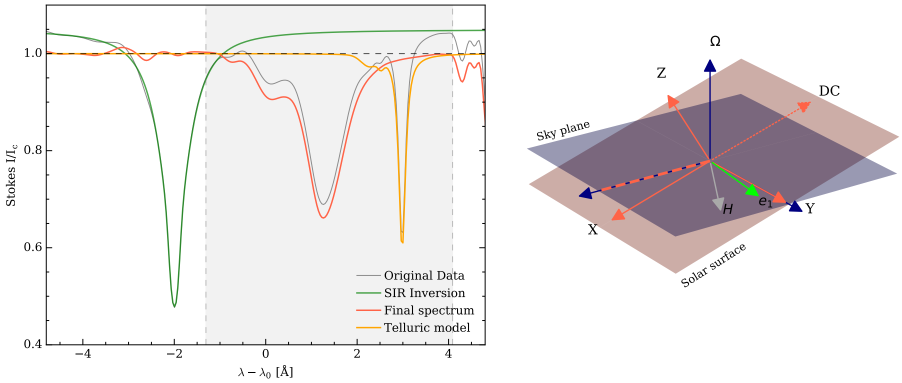

Figure 4.9 – Left panel: example of the normalization procedure of the helium triplet. The shadowed region is the spectral range inverted with Hazel. Right panel: Reference system used for the inversions of the fifth scan with Hazel.

In the previous chapter (Sec. 3.1 and Fig. 3.1) we defined the reference system, and for this observations we have chosen $\phi = 180^\circ$. Under this geometry the projection of X in the plane of the sky is in the radial direction and ,hereafter, the reference system is fixed. The angle between the radial direction (X axis) and the $Q > 0$ reference of the polarimeter (e_1) is $\gamma \sim 83^\circ$ for the fifth scan. This reference system is displayed in Fig. 4.9 (right panel) following the same notation of the previous chapter. The arrow labeled "H" indicates the slit direction. Additional information such as the list of angles[3] and the geometry of each scan is described in Sec. A.2.

A reliable inversion of the He I multiplet required the aforementioned spatial and spectral binning. Even after the rebinning, the polarimetric signals are only few times above the noise. Having a reliable determination of Stokes V turns out to be fundamental to correctly infer the strength of the magnetic field. The reason is that between 10 and 100 G the He I 10830 Å multiplet is in the Hanle saturation regime, where the linear polarization is only sensitive to the direction of the magnetic field and not to its strength. Therefore, the only way to infer the full magnetic field vector is through the full Stokes vector. The results of the inversion will be shown in the next section.

4.4 Inversion results

4.4.1 Magnetic field vector in the LOS reference frame

Figure 4.10 shows the magnetic field strength, inclination, azimuth, and LOS velocity maps for the fifth scan, all of them in the LOS frame (Θ_B, Φ_B). We note that the azimuth and inclination of the He I line have been transformed from the local reference frame, the one used by Hazel, to the LOS reference frame to properly compare the silicon and the helium inversion. The photospheric magnetic field strength map shows a $\sim$2 kG sunspot with only half of the penumbra visible. In the chromosphere, the magnetic field strength of the sunspot reaches values of $\sim$1 kG.

---

[3] We have also updated the manual of Hazel with an explanation of how to carefully calculate these angles: `http://aasensio.github.io/hazel/refsys.html`

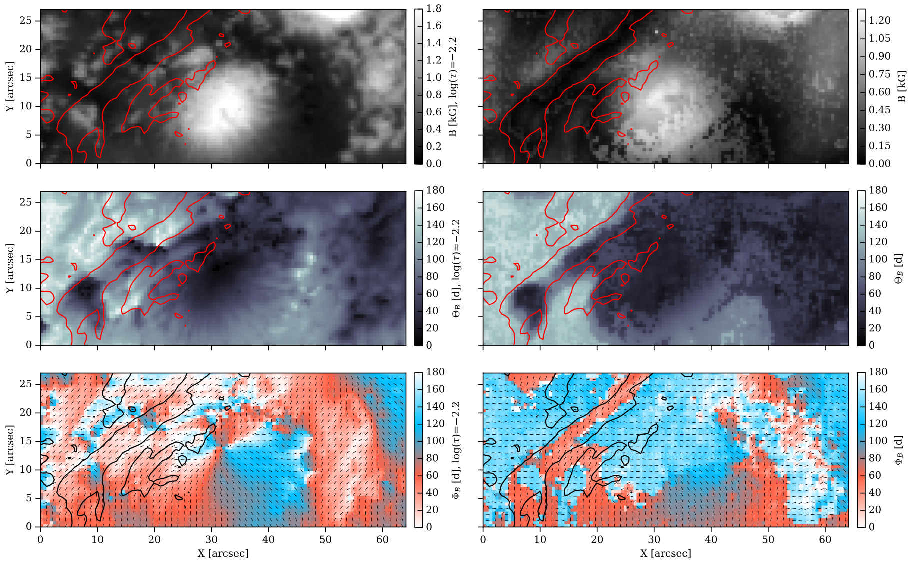

Figure 4.10 – Magnetic field strength (top row), inclination (middle row) and azimuth maps (bottom row) inferred from the inversion of both spectral lines. The left column shows the SIR inversion of the Si I line, while the right column shows the HAZEL inversion of the He I multiplet. Contours are drawn at the filament location. The level has been chosen as all the points with an absorption larger than $0.7I_c$.

The magnetic field strength map shows that the lowest values are associated with the location of the filament, specially in the chromosphere. The magnetic field strength of the area coinciding with the filament shows values around 50–150 G, similar to those quoted by Sasso et al. (2014). The LOS inclination map shows how the FOV is split into two polarities with a very narrow PIL following the filament in the chromosphere, but not so well aligned in the photosphere. Concerning the azimuth, and eluding for the moment the fact that other ambiguous solutions exist, the results show a penumbra with a clearly radial magnetic field. We can affirm this with confidence because we are only affected by the 180° ambiguity in this Zeeman-dominated region. The azimuth in the umbra is not reliably retrieved for He I since the magnetic field is more vertical and Stokes Q and U have lower amplitudes. Given the multiple potential solutions for the azimuth in the chromosphere, one should notice that it is possible to find fields compatible with the observations that are parallel or perpendicular to the filament. We study this problem with more detail in Sec. 4.4.3 and 4.5.

4.4.2 Azimuth in the local frame

Because of the relative simplicity of solving the 180° ambiguity in the interior of the sunspot, we have decided to transform the photospheric azimuths given in the LOS by SIR to the local reference system. To perform this disambiguation we used a simple potential field extrapolation and selected the solution at each pixel that is more aligned with the potential field (also called Acute-Angle-Comparison, Metcalf et al., 2006). The local Si I azimuth map is displayed in the upper part of the Fig. 4.11. As expected, the magnetic field vector in the sunspot is pointing radially outwards from the center of the umbra. In the area where the filament is located the azimuth is apparently aligned with it. However, we note that the potential field extrapolation is probably not the best approximation to the field topology due to the complexity of this region, which might introduce errors in the disambiguation.

The local azimuth map inferred by HAZEL is displayed in the middle part of Fig. 4.11. In this case, the azimuth map is not disambiguated. An interesting observation is that there is a clear correlation between the azimuth and the inclination map displayed in Fig. 4.10. While in the LOS reference frame the longitudinal magnetic field information is purely contained in Stokes V and the transversal information lies in Stokes Q and U, in the local reference frame they are mixed and Stokes V also provides information about the magnetic field perpendicular to the surface. The inferred azimuths seem to be conditioned by Stokes V and its map follows the same pattern than the polarity map.

A crucial conclusion from Fig. 4.11 is that the chromospheric azimuth inside the filament is not smooth, i.e., we witness strong variations between nearby pixels. The PIL clearly marks the regions where we find these sudden (close to 180°) changes in the local azimuth (an indication of the importance of Stokes V in the inference of the azimuth). While Stokes V changes sign in the two sides of the PIL, Stokes Q and U have very similar shapes. Therefore, HAZEL infers that the field changes azimuth by $\sim 180°$. Apart from other compatible solutions, this unphysical situation could arise if the measured Stokes V does not come from the filament itself, but from the active region underneath. In such situation, one is forcing HAZEL to simultaneously interpret circular and linear polarization profiles as coming from the same atmopsheric region in the single component model.

4.4.3 Ambiguous solutions

The main reason why we have not disambiguated the local azimuth map in the chromosphere is that there are many possible ambiguous solutions. In fact, the number of these ambiguous solutions depend on the specific regime of the magnetic field and on the scattering geometry. These ambiguities produce equally good fits to the observed Stokes profiles. They are then impossible to distinguish based on pure spectropolarimetric considerations.

As we mentioned in Sec. 2.2.6, in the plane of the sky the determination of the orientation of the magnetic field vector from the polarization profiles in the Hanle saturated regime suffers from two known ambiguities: the 180° ambiguity (fields with Θ_B and $\Theta_B + 180°$ azimuths give the same signal) and the Van Vleck or 90° ambiguity (fields with Θ_B and $\Theta_B \pm 90°$ give the same signals). One can estimate the other ambiguity solutions of the Hanle effect in the saturation regime with the recipe of Martínez González et al. (2015). They used a two-level atom with $J_u = 0$ and $J_l = 1$ in the optically thin limit. This is a relatively good approximation for the He I 10830 Å blue component, but not for the red component. For that, with this first guess, one have to refine the solution with HAZEL. We apply this procedure for all pixels and display the number of compatible solutions per pixel in the lower panel of Fig. 4.11. In our field of view, similar to what was found by Schad et al. (2015), there is a non-negligible fraction of pixels with only one possible solution. The number of solutions go up to two inside both sunspots (one in the center and another in the upper right corner). They are due to the well-known 180° ambiguity. Away from the sunspot, where the magnetic field is weaker, more than 3 solutions appear. More than 5 solutions are found in regions where the signal is very low, due to the noise (all of them labeled as 5). Finally, in the region of the filament we find between three and four compatible solutions.

The geometry of the observation turns out to be important because it gives us the advantage, in some pixels, of having only one compatible solution. The areas with only one possible solution correspond to regions in which the Hanle and Zeeman effects act together. We defer the detailed study of these signals to Sec. 4.5.2.

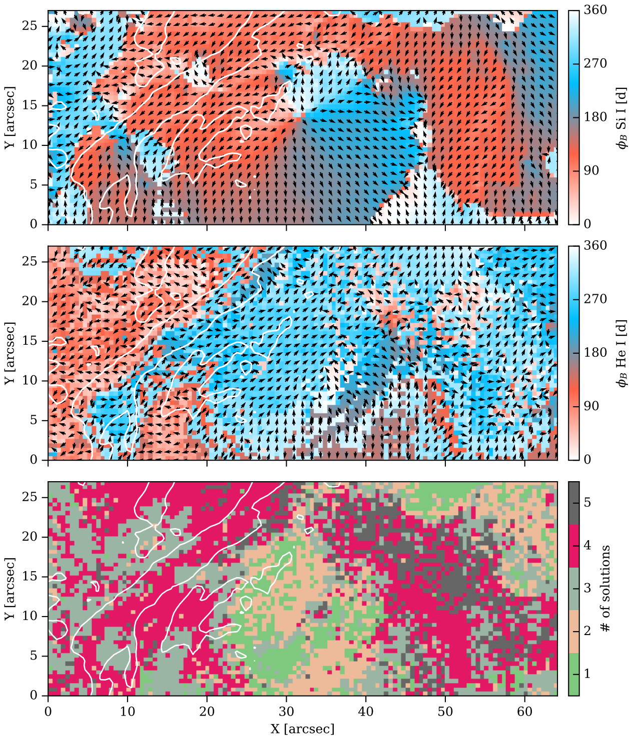

Figure 4.11 – Upper panel: local azimuth map for the Si I inversion obtained after a transformation from the LOS frame using a potential field approximation. Middle panel: local azimuth map for the He I inversion. Lower panel: number of compatible solutions for each pixel.

4.4.4 Line-of-sight velocities

Line-of-sight velocities obtained from the inversions in both atmospheric layers are shown in Fig. 4.12. The wavelength calibration was done using the photospheric spectral lines and comparing the intensity of an average quiet-Sun region in our data with the FTS atlas (Neckel & Labs, 1984). In the photosphere, the umbra is essentially at rest with respect to the velocity of the quiet Sun. At the upper photospheric level ($\log(\tau) = -2.2$) the velocity in the FOV is between 1.5 $\mathrm{km\,s^{-1}}$ and –1.5 $\mathrm{km\,s^{-1}}$.

In the chromosphere, weak upflows are found along the PIL with velocities around 3 $\mathrm{km\,s^{-1}}$. We identify this flow structure as such typical of slowly rising emerging loop-like structures (e.g., Solanki et al., 2003; Xu et al., 2010), suggesting that this is an emerging Ω loop, where cool material rises to chromospheric heights and then drains towards the footpoints of the loops. The only difference between these arch filaments and our active region filament is that the filament material is aligned with the PIL, while their archs are mainly perpendicular. This scenario could be compatible with an emergent flux rope from the active region, presenting similar rising speeds to those of Kuckein et al. (2012b).

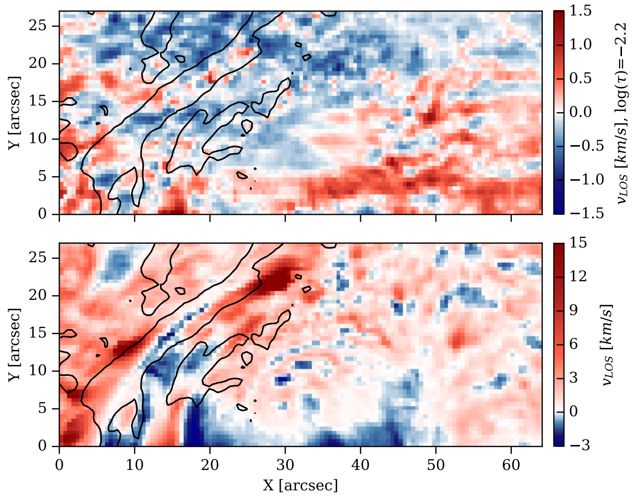

Figure 4.12 – LOS velocity from the inversion of the silicon line (upper panel) and the helium triplet (lower panel). Contours at $0.7I_c$ are drawn to show the filament location. Negative values (blue) indicate motions towards the observer.

The downflows are found at both sides of the filament with velocities larger than 20 km s^{-1} . These pixels show several (at least two) well separated components in Stokes I and V (see Sec. A.8 for an example). Pixels close to them do not show a clear two-component profile, but an extended wing towards red wavelengths. No clear indication of more than two components clearly separated is found, in contrast to Sasso et al. (2011).

Although a clear relation between the photosphere and chromosphere is hard to establish with our observations, it is tantalizing to associate the two small redshifted patches around (25″, 20″) in the photosphere with the chromospheric downflows, produced by material falling to the photosphere. These two patches in the photospheric map are localized to the left of the downflows because of the geometrical projection.

4.4.5 Doppler width and optical depth

Figure 4.13 shows the optical depth τ_R and the Doppler width Δv_D resulting from the inversion of the helium profiles. The mean optical depth in the filament is clearly above 0.7. The maximum value calculated in this scan is 1.9, but it easily goes up to 2.3 for other scans in which the filament is more opaque. Values above $\tau_R = 1$ can be potentially affected by radiative transfer effects (Trujillo Bueno & Asensio Ramos, 2007), not taken into account in the version of HAZEL at the time of writing.

The Doppler width in the filament varies between 10 km s^{-1} and 14 km s^{-1} . Larger values are concentrated in the downflows and they are artificially produced by HAZEL misfits when trying to fit a pixel with two line profiles clearly separated with a single atmospheric component model. Although the Doppler width of the line can also be used as a tool to extract an upper limit to the temperature, we do not consider it to be a good idea. Many effects that produce unresolved velocities (like the fine structure

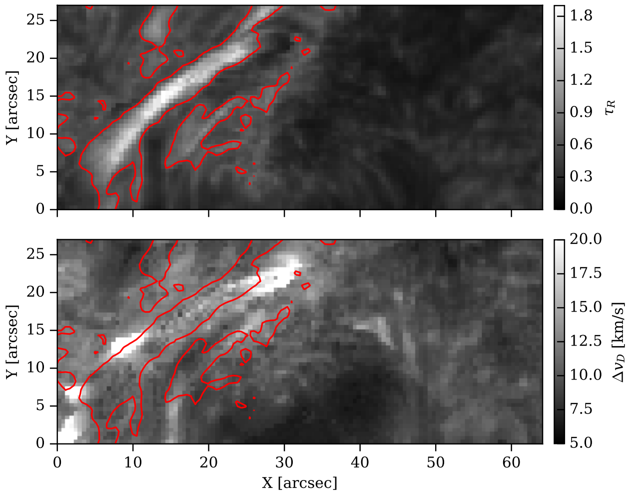

Figure 4.13 – Optical depth measured in the red component of the He I 10830 Å (top panel). Doppler width as a result of fitting a single component (bottom panel). Larger values of Doppler width are obtained in the areas where more than one component appears in the Stokes profiles.

of the filament with small-scale fibrils with potentially different plasma flows) also broaden the profiles and we lack the means to calibrate their importance.

4.5 Bayesian inference

It is clear from Secs. 4.4.1-4.4.3 that the inference of the magnetic field vector in the chromosphere requires a careful identification of all ambiguous solutions. Additionally, it is of paramount importance to capture all the potential degeneracies among the physical parameters and return reliable error bars. For this reason, we carry out a Bayesian analysis to fully exploit the observations.

4.5.1 Bayesian framework

Bayesian inference provides the most complete approach to parameter inference. The inference problem relies on the calculation of the posterior probability distribution function (PDF) $p(\boldsymbol{\theta}|D)$ of a set of M parameters $\boldsymbol{\theta}$ conditioned on the observations D. This posterior distribution describes our updated state of knowledge on the parameters after taking the data D into account. Bayes' theorem allows us to calculate the posterior distribution for $\boldsymbol{\theta}$:

$$p(\boldsymbol{\theta}|D) = \frac{p(\boldsymbol{\theta})p(D|\boldsymbol{\theta})}{p(D)}, \tag{4.1}$$

where $p(\boldsymbol{\theta})$ is the prior and represents our a priori knowledge. In the previous equation, $p(D|\boldsymbol{\theta})$ is the likelihood, that measures the probability that the data D were obtained (measured) assuming given values for the model parameters $\boldsymbol{\theta}$, i.e., gives information about how well the parameters predict the observed data. Under the assumption of uncorrelated Gaussian noise in the data, the likelihood is given by:

$$p(D|\boldsymbol{\theta}) = \prod_{i=0}^{3}\prod_{j=1}^{N} \frac{1}{\sigma_i\sqrt{2\pi}} \exp\left[-\frac{[S_i^{\mathrm{obs}}(\lambda_j) - S_i^{\mathrm{syn}}(\boldsymbol{\theta},\lambda_j)]^2}{2\sigma_i^2(\lambda_j)}\right], \tag{4.2}$$

where $S_i^{\mathrm{obs}}(\lambda_j)$ is the observed Stokes parameter $\boldsymbol{S} = (S_0 = I, S_1 = Q, S_2 = U, S_3 = V)$ at wavelength λ_j, $S_i^{\mathrm{syn}}(\boldsymbol{\theta},\lambda_j)$ is the synthetic Stokes parameter, and $\sigma_i(\lambda_j)$ is the standard deviation for each Stokes parameter and wavelength point.

Finally, the denominator $p(D)$ in Eq. 4.1 is the Bayesian evidence or marginal posterior, which is a normalization factor that has turned out to be important in our analysis, as we will describe later:

$$p(D) = \int p(D|\boldsymbol{\theta})\, p(\boldsymbol{\theta})\, d\boldsymbol{\theta}\,. \tag{4.3}$$

For parameter inference, the information for a single parameter can be obtained from the marginal posterior, obtained from the posterior by integrating over the rest of parameters (marginalization):

$$p(\theta_i|D) = \int p(\boldsymbol{\theta}|D)\; d\theta_1 ... d\theta_{i-1} d\theta_{i+1} ... d\theta_M\,. \tag{4.4}$$

Once the posterior distribution $p(\boldsymbol{\theta}|D)$ is known, the position of the maxima (in case the posterior is multimodal) gives the most probable combination of parameters that reproduce the observational data. Moreover, we can analyze the confidence levels of the parameters, degeneracies, ambiguities, etc.

4.5.2 Multimodal inference

Given that several ambiguous solutions exist, the posterior turns out to be multimodal. Each mode can have its specific model parameter uncertainties, therefore, sampling the posterior distribution turns out to be difficult. The importance of every mode located in the posterior is quantified by its evidence $p(D)$. For two modes having the same peak posterior (or, equivalently, the same likelihood when using flat priors), the evidence is larger the larger the volume of the space of parameters compatible with the observations. In other words, given equally good fits, the evidence is larger for those solutions that require less fine tuning in the parameters. Thus, the evidence may be seen as a quantitative implementation of Occam's Razor.

From all available modes explored during the posterior sampling, we choose the one with the largest evidence. We include in the set of compatible solutions the ones for which the difference between its log-evidence and that of the maximum is smaller than 6, following the Jeffrey's scale (Jeffreys, 1961). We empirically checked that this threshold is ideal to distinguish the compatible solutions.

When the posterior is as corrugated and multimodal as the ones we are dealing with, standard Markov-Chain Monte Carlo (MCMC) techniques can present problems and, for example, the widely-used Metropolis-Hastings algorithm (Metropolis et al., 1953), could get trapped in local minima. To explore the parameter space MCMC standard methods generate new points "close" to the previous one whose probability of acceptance depends on the likelihood ratio between the new and previous point. In this way, if the new point produces a larger likelihood it is accepted, while if it is worse it is accepted with a small probability depending on the ratio of likelihoods. On the other hand, the Nested Sampling method is a Monte Carlo technique in which, after drawing the points (known usually as live or active points in this method) from the prior, they are sorted by their likelihood. The smaller one is removed and replaced by a new point with higher likelihood. In this way, we are continuously sampling layers with larger likelihood independently of the location of the previous points (see Fig. 4.14).

To efficiently draw each new point fulfilling the previous condition while reducing the volume where the solution is located, the ellipsoid technique proposed by Mukherjee et al. (2006) is commonly used. This technique approximates the iso-likelihood contour of the point to be replaced by a D-dimensional ellipsoid determined from the covariance matrix of the current set of live points (red line in Fig. 4.14). New points are then selected from the prior within this ellipsoidal bound until one is obtained that has a likelihood larger than that of the discarded lowest-likelihood point. Ellipsoidal nested sampling as described is efficient for simple unimodal posterior distributions, but is not well suited to multimodal distributions. This problem is solved by identifying distinct clusters of live points that are well separated (Fig. 4.14, panel (e)) and constructing an individual ellipsoid for each cluster (Shaw et al., 2007).

For these reasons, we have used the MultiNest algorithm (Feroz et al., 2009), a Bayesian inference tool tailored to explore multimodal posteriors and estimate the evidence of each mode. MultiNest implements a nested-sampling Monte Carlo algorithm (Skilling, 2004) that is designed to calculate efficiently the evidence (Eq. 4.3) and simultaneously sample the posterior distribution when the later is multimodal and/or has strong degeneracies. Instead of using supervised clustering methods (such as k-means), MultiNest infers the appropriate number of clusters from the set of points. Other details about this procedure are described in the original article (Feroz et al., 2009). By merging together MultiNest and Hazel, we have performed, for the first time, a Bayesian inference for observations in the He I multiplet[4].

One of the few free parameters of MultiNest is the number of live points $N_{\rm live}$, which is directly proportional to the final precision on the estimation of the evidence. A larger number provides a more accurate sampling but increases the computing time. After exhaustive tests, we have verified that $N_{\rm live} = 1000$ gives enough precision for our purposes. Concerning the computing time, the inference for each pixel takes of the order of 20 minutes, although it strongly depends on the number of free physical parameters.

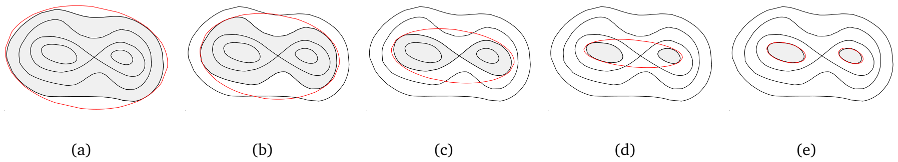
(a) (b) (c) (d) (e)

Figure 4.14 – Cartoon of ellipsoidal nested sampling from a simple bimodal distribution. In (a) we see that the ellipsoid represents a good bound to the active region. In (b)-(d), new points are removed from the exterior and proposed inside the new volume. When some clusters are detected, the sampling is performed in each region separately (e). Image extracted from (Feroz & Hobson, 2008).

4.5.3 Bayesian analysis of magnetic ambiguities

We analyze in detail one set of profiles that are representative of the observations in terms of the number of compatible solutions. We study the ambiguities in the (B, θ_B, ϕ_B) subspace. The rest of thermodynamic

---

[4] We have used MultiNest through the Python wrapper PyMultiNest (Buchner et al., 2014) available on `http://github.com/JohannesBuchner`.

parameters are estimated by a classical least squares fit of Stokes I. We also infer the uncertainties σ_{QU} and σ_V from the observations by including them in the Bayesian analysis. This helps us to absorb any Gaussian-distributed systematic effect in the observations, in these uncertainties.

We have used uninformative flat priors for all the parameters. The priors span the ranges $(0, 2000)$ G, $(0, \pi)$, and $(-\pi, \pi)$ for the modulus, inclination, and azimuth of the magnetic field, respectively. We impose uniform priors in the range $(-7, -8.5)$ for the natural logarithm of the uncertainties, which correspond to a standard deviation in the range $(2, 9) \times 10^{-4}$ in units of the continuum intensity. This range is sufficient to correctly capture the posterior of the uncertainties and narrow enough to reduce the computing time with respect to having a wider range.

In order to gain a better insight about the number of ambiguous solutions and their physical origin, we have found useful to do two inferences: one using only Stokes Q and U, and another one using only Stokes V. The solution compatible with the full Stokes vector lies in the intersection of the posterior distributions of both inferences. Therefore, in the following subsections we will study individual cases where four, three or one solution is compatible with the observed Stokes profiles.

After the inference and before the analysis, it is always a good practice to carry out posterior predictive checks using HAZEL to synthesize the Stokes profiles with the parameters inferred from the posterior. An example of this has been presented in Fig. 4.7, where we have drawn the Stokes profiles of two pixels with their maximum-a-posteriori best-fit and a green shadowed region indicating the range of possible solutions obtained from the posterior distribution.

Four solutions

The pixel at (45″, 47″) is a good example of a posterior with four modes. Figure 4.15 displays the joint (below the diagonal) and marginal (in the diagonal) posterior distributions for the magnetic field strength and, inclination and azimuth in the LOS frame. The green samples and histograms correspond to the inference using only Stokes Q and U, while the grey ones are obtained using only Stokes V. The presence of several modes is clearly seen in the joint posteriors. We have marked with red circles the solutions compatible with the full Stokes vector. The panels above the diagonal show the synthetic Stokes profiles for all the modes, demonstrating that they produce indistinguishable fits to the data.

The posterior distribution of the magnetic field strength and inclination in the LOS frame, $p(B, \Theta_B|D)$, when only Stokes V is used presents a clear degeneracy, showing a hyperbolic-shaped posterior distribution typical of the Zeeman weak field regime, where only the product $B \cos \Theta_B$ can be reliably estimated. In order to facilitate the recognition of the degeneracy, we plot the dashed line $B \cos \Theta_B = c$, where c is a constant.

This pixel is in the saturation regime of the Hanle effect. In this regime, the Hanle effect is not sensitive to the magnetic field strength, being only sensitive to the orientation of the field. In this case, we have the following potential ambiguities: Φ_B, $\Phi_B - \pi/2$,$\Phi_B + \pi/2$,$\Phi_B + \pi$. The green posterior (specially clear in the panel showing the joint posterior $p(B, \Theta_B|D)$) shows the four potential ambiguities in Φ_B as four horizontal lines.

In the joint posterior $p(\Theta_B, \Phi_B|D)$ (the central lower part of Fig. 4.15), we see how each degenerate value of the azimuth is compatible with two potential values for the inclination, generating a maximum of 8 possible ambiguous solutions. All the solutions occupy a similar volume in the parameter space, as it is seen from the green sampling, so the evidence is mainly controlled by the likelihood under our assumption of equal priors. Half of the points are discarded when the polarity of the field is taken into account in the inference through Stokes V. The sign of Stokes V is such that only inclinations in the range $(0°, 90°)$ are favoured by the observations. Therefore, we end up with the final four ambiguous solutions, marked with

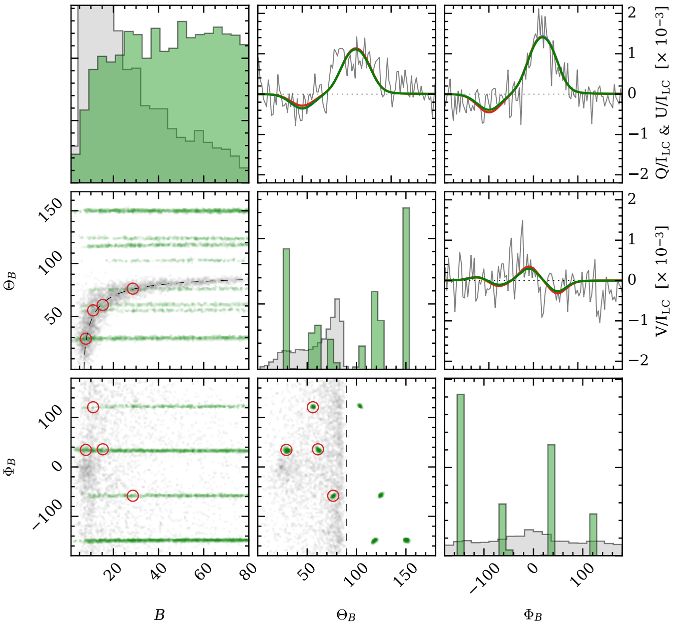

Figure 4.15 – Joint (below the diagonal) and marginal (in the diagonal) posterior distributions for the magnetic field strength, inclination, and azimuth in the LOS frame. The green samples and histograms correspond to the inference using only Stokes Q and U, while the grey ones using only Stokes V. The analysis has been carried out for a pixel with four compatible solutions, drawn in different colors in the upper diagonal panels. The solutions compatible with the full Stokes profiles are indicated with red circles.

red circles. It is important to remember that some of the ambiguous solutions can have the same azimuth in the LOS and are only distinguished by their inclination.

For clarity, we only show the posterior distribution for the magnetic field strength up to 80 G. However, the green posterior goes down to zero as we increase the magnetic field because the shape of Stokes Q and U does not fit the observations anymore. We note that the Hanle saturation regime starts at fields $\sim$10 G and above this we are not sensitive to the strength of the magnetic field anymore and the posteriors are flat.

Three solutions

A pixel representative of a posterior with three modes is the one at ($8''$, $10''$). This pixel has three compatible solutions: two with the same LOS azimuth and one separated by $\pi/2$ to the other pair.

Figure 4.16 displays the same set of quantities as in the previous example, but for this new pixel. In principle this pixel is in the saturation regime of the Hanle effect, but in this case only three of the four solutions (see the joint posterior $p(\Theta_B, \Phi_B|D)$) pass the Bayesian evidence test. The rejected point is very close to $\Theta_B = 90°$, so it is associated with a field almost perpendicular to the LOS. The ensuing magnetic field strength needed to produce the observed Stokes V signal with this orientation of the field is close to 350 G. This field is so strong that this solution is discarded because Stokes Q and U starts to show

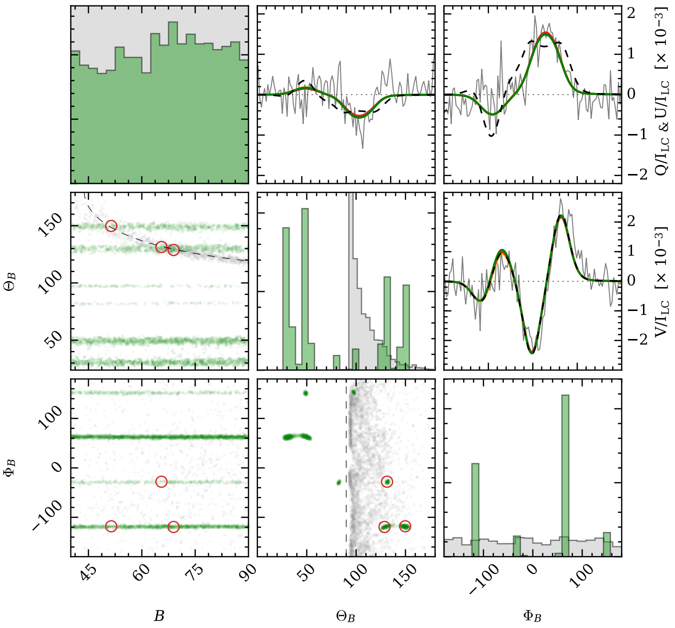

Figure 4.16 – Same as Fig. 4.15 but for a pixel with three compatible solutions. The dashed Stokes profiles come from the rejected solution with the same polarity.

some Zeeman features that are not compatible with the observed profiles. This is clearly seen in the panel for Stokes Q, U, and V. The Stokes profiles of all three compatible solutions are displayed in the upper diagonal panels in solid lines, while the rejected solution is shown with the dashed line.

One solution

One of the most surprising conclusions of this work is the fact that it is possible to find pixels in which only one solution is compatible with the observations. A good example of this is the pixel at (70″, 15″). The joint and marginal posterior distributions of this pixel are displayed in Fig. 4.17. The profiles are clearly close to the pure Zeeman regime for Stokes Q and U, with the typical three-lobed profiles, but some contribution from scattering polarization still exists. In fact, the two effects act together and the $180°$ ambiguity in the azimuth disappears (Schad et al., 2013). The reason is that the Hanle contribution in the core of the Stokes Q and U has opposite sign in both solutions, which produces a misfit in one of them. The Zeeman contribution to Stokes profiles depends on the inclination and azimuth of the magnetic field with respect to the LOS, while for the Hanle contribution, it also depends on the geometry in the local reference frame. For our geometry ($\mu = 0.92$) the two solutions with a difference in the azimuth of 180° lead to a different geometry in the local frame and only one of them is compatible with the Hanle signals. Therefore, the observing geometry plays a key role, allowing us in some cases to reduce the number of compatible solutions to a single one.

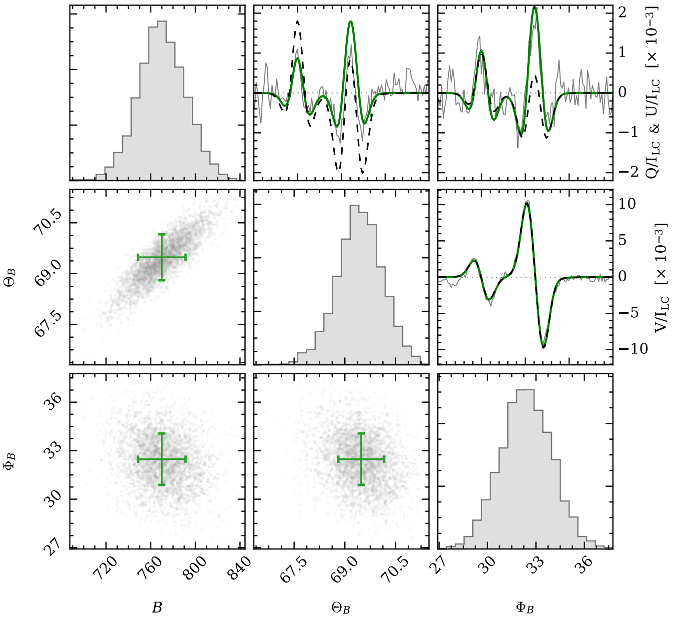

Figure 4.17 – Same as Fig. 4.15 but for a pixel with only one possible solution and using Stokes Q, U, and V for the inference. Observed Stokes profiles (gray), synthetic profiles from the solution (green), and the rejected solution $\Theta_B + \pi$ (dashed) are shown in the upper diagonal panels.

This "self-disambiguation" is only possible in the intermediate regime between the Hanle and the Zeeman effect (∼400–800 G), when the Hanle effect can generate slightly different profiles for the two solutions. The results of Fig. 4.17 show a posterior distribution with only one mode. The dashed lines in the Stokes profiles panels refer to the rejected solution ($\Phi_B + \pi$), being clearly unable to reproduce the profiles.

4.5.4 Height of the filament

When the observed structure is off the limb, imaging techniques can be used to estimate its height (Martínez González et al., 2015; Schad et al., 2016). On the contrary, for on-disk observations it is much more complicated since no straightforward technique for estimating the height is available. Using Bayesian inference we explore the feasibility of the inference of the height of the filament directly from the observations. We showed in Sec. 3.2 the role of the height in the scattering polarization: the larger the height, the larger the anisotropy, which induces a stronger zero-field scattering polarization signal.

Some authors have tried to retrieve the height including it as an inversion parameter (Xu et al., 2010; Merenda et al., 2011), concluding that it can be inferred with high accuracy, solving possible debates in the interpretation (Judge, 2009). Additional arguments based on 3D geometrical reconstructions (Xu et al., 2010; Solanki et al., 2003) have been used to calculate this height. However, it was noted by Asensio Ramos et al. (2008) that the height cannot be easily inferred from the observations unless some information about the topology of the field is fixed a priori (for instance, the inclination). Here, we demonstrate that this is not only the case, but the inference is even more difficult because both the magnetic field and the optical depth are degenerated with the height.

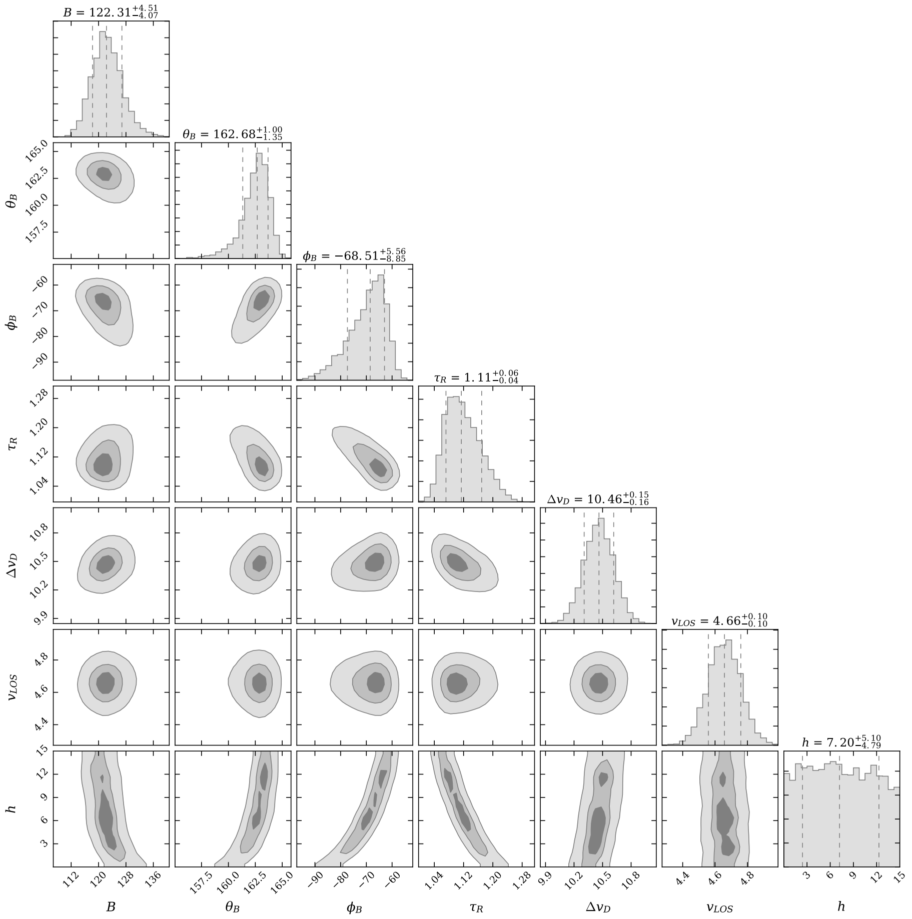

Figure 4.18 – Histograms and correlations of the posterior distributions of the each physical parameter. The label on top of each column provides the median and the uncertainty defined by the percentiles 16 and 84 (equivalent to the standard 1σ uncertainty in the Gaussian case). Also the contours are shown at 0.5, 1, and 2 sigma.

To analyze the reliability of inferring the height from the Stokes parameters, we choose the pixel at (20″, 40″) which lies inside the filament. We include all 10 free variables: B, θ_B, ϕ_B, τ_R, Δv_D, v_{LOS}, h, σ_I, σ_{QU}, and σ_V in our Bayesian analysis. Given that the number of free parameters is large and to decrease the computing time, we use more restrictive priors for the inclination that before, trying to capture only one possible ambiguous solution. The prior for the height is flat and limited to be in the range (0″, 15″). We carried out some tests to check that isolating one mode of the magnetic field does not affect our conclusion. As before, we add the uncertainty of the Stokes parameters as variables and impose a suitable Jeffreys' prior. Sampling the unimodal posterior requires more than 100 minutes on a single CPU (3.4GHz Intel Core i7).

The ensuing posterior distributions (joint and marginal) are displayed in Fig. 4.18[5]. The posterior distribution seems to be quite localized for all variables, except for the height. Its marginal posterior is practically flat, almost indistinguishable from the assumed prior. Concerning the joint posteriors, it displays a very strong correlation with many of the remaining parameters. For instance, changing the height by 15$''$ can be compensated easily by barely modifying the optical depth from 1.2 to 1.04. The same happens with the inclination of the field, where a small change of 4° compensates the change in height. Finally, changes of only 10 G in the magnetic field strength can also compensate for the same change in height, in agreement with Schad et al. (2013).

This experiment clearly states that the information about the height in the Stokes profiles is almost absent because it is degenerated, as it can be compensated with other parameters.

4.6 Limitations of a single component model

In the previous sections we have studied the observations with state-of-the-art inversion codes to recover the physical properties in the filament using a single component model. Stokes profiles outside the filament can be well explained by this simple modeling. However, we find observational features in the filament – mainly the absence of the filament in circular polarization or the same sign in the linear polarization of the blue and red component – that lead to unrealistic and inconsistent results in the inference of the magnetic field vector, such as the abrupt azimuth variations within the filament.

As discussed in Sec. 4.1, recent studies have already demonstrated the need of more complex forward modeling to understand the physical processes behind the formation of this multiplet (López Ariste & Casini, 2002; Trujillo Bueno & Asensio Ramos, 2007; Léger & Paletou, 2009; Martínez González et al., 2012b; Milić et al., 2017). Moreover, we would like to remind the reader that in Chapter 3 we showed that the polarization signals measured in filaments above magnetized regions (Kuckein et al., 2009; Xu et al., 2012) are affected by the illumination from below.

Therefore, in this section we analyze in detail the observed profiles, showing how a single component model is not able to reproduce certain aspects in intensity, linear polarization and circular polarization profiles. For this purpose we make use of the third scan because the filament has the highest absorption and the features are more noticeable.

4.6.1 Analysis of Stokes I

As we have mentioned in Chapter 1, numerous studies of solar prominences have inferred the physical parameters of the plasma, and in particular their temperature by analyzing the shape and intensity of spectral lines when the plasma was optically thin (Parenti, 2014). However, we demonstrate in the following that our observations show signs of the presence of optically thick plasma. To estimate the temperature in these cases, a complex non-LTE radiative transfer treatment would be necessary, in addition to taking into account the cumulative effect of many threads of plasma contributing to the emergent Stokes parameters along the entire line of sight.

The absorption detected on the filament is supposed to be a consequence either of the EUV coronal radiation (Sánchez-Andrade Nuño et al., 2007; Centeno et al., 2008) which populates the levels of the triplet system (see Sec. 2.3.1 for details on its formation), or an increase in density due to the accumulation of cold material that condenses in an area where the magnetic field is able to support it. In principle,

---

[5] We have removed from the figure the distributions of σ_I, σ_{QU}, and σ_V to improve its readability.

we are not able to distinguish between the contribution of these formation mechanisms since the optical depth in the red component of the 10830 Å multiplet is treated as a free parameter to fit the observed intensity profile. From this value of absorption we do not know explicitly how each physical mechanism contributes to produce optical thickness in the spectral line and, therefore, we cannot estimate other physical quantities, such as the height (based on the dependence on coronal EUV).

In the following, we show two consequences of the large absorption in the filament: i) the differential saturation effect between the red and the blue components and ii) misfits when using HAZEL (which could also be explained by transfer effects).

Figure. 4.19 shows the intensity amplitude ratio between the blue and the red components of the He I 10830 Å triplet estimated in the third of our scans (the rest of them are very similar). Given that the lines are in absorption, we have modeled each component with a Gaussian function with the same width. In those cases in which a second absorption profile appears shifted in wavelength, we have fitted two sets of Gaussians. As the width is roughly the same for the two components of the multiplet, the ratio of amplitudes $\mathcal{R} = A_B/A_R$ is also equal to the ratio of areas. The line ratio between the two resolved He I components is around 0.4 inside the filament, whereas it is in the range 0.1–0.2 in the remaining areas (Penn & Kuhn, 1995), the value expected for an optically thin plasma. This means that we find some indication of saturation only in the filament, with a maximum value of $\mathcal{R}$ =0.5. A detailed analysis about the behaviour of the amplitudes with respect to the optical depth is shown in Sec. A.10.

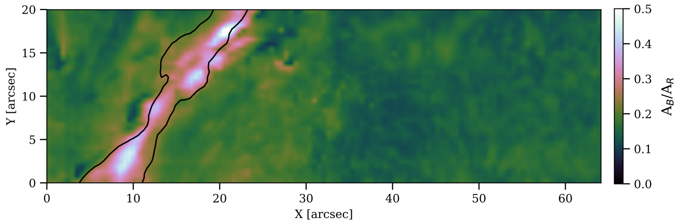

Figure 4.19 – Ratio between the Stokes I amplitudes of the blue A_B and the red A_R component. The contour shows the level 0.4A_R, where the red component starts to saturate.

Another feature that suggests the presence of radiative transfer effects is that the HAZEL code systematically produces misfits in the blue component of the multiplet in Stokes I (see also Sec. A.10 for more information). This indicates that the source function might have some variation along the line of sight. Given that the optical depth of the blue and red components differ, the radiation that we see is emerging from slightly different regions in the slab. For this reason, we have added a new multiplicative parameter β in HAZEL that arbitrarily modifies the source function of the slab $\mathbf{S}$. Consequently, the emergent Stokes profiles are now given by:

$$\mathbf{I} = e^{-\mathbf{K}^*\tau}\mathbf{I}_{\text{sun}} + (\mathbf{K}^*)^{-1}\left(1-e^{-\mathbf{K}^*\tau}\right)\beta\mathbf{S}\,. \tag{4.5}$$

For $\beta < 1$ values we can mimic a slab whose emission properties (new source function) are much smaller than those dictated by the boundary condition. The opposite happens when $\beta > 1$, which can be used to mimic strong emission profiles.

All inversions up to now have been carried out with β=1. We explore here the effect of adding β in the inversion as an additional free parameter. We show in Fig. 4.20 an example of such analysis carried out with MULTINEST to detect possible ambiguities. It is clear that the addition of β results in a much better fit of the blue component of the multiplet. However, β and τ are somehow degenerated and have opposite impacts in the emergent profile: increasing β reduces the absorption, while increasing τ increases the absorption. Therefore, one can compensate (only up to a point) an increase in β with an increase in τ. In spite of this degeneracy, it is possible to find a pair of β and τ that produce a good fit to the Stokes I profile of the multiplet. The general trend is that adding β as a free parameter to produce a better fit of Stokes I leads to a slight increase in β with a larger increase in τ. The figure shows this clear correlation between them.

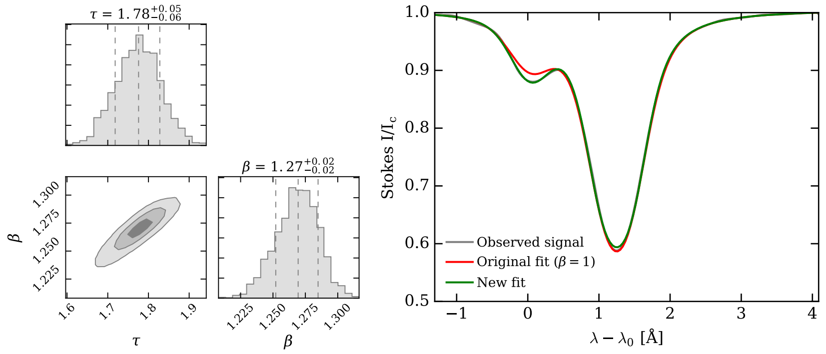

Figure 4.20 – Bayesian estimation of the β parameter. The left panel shows the posterior probability distribution of β and τ, and the correlation between them. The right panel shows the improved fit of the blue component of the He I triplet when going from $\tau = 1.2, \beta = 1.0$ (red line) to $\tau = 1.8, \beta = 1.3$ (green line).

From this experiment, we see that the source function needed to reproduce the profiles is greater than in the case of pure scattering ($S = J^0_0$ and $\beta = 1$). Since HAZEL neglects collisions in the calculation of the source function, one possible explanation of this increase might be the contribution of collisions. This idea seems feasible (also suggested by Casini et al. 2009a) since this term have a larger role for higher densities, that is compatible with the high absorption (optical depths up to 2 in several scans) found in our filament. It seems clear that there are many profiles in the observations for which the approximations used in HAZEL break down.

4.6.2 Linear polarization

As mentioned in Sec. 4.3.1, the observations present signals in Stokes Q and U, with the unexpected same sign in both blue and red components. In this section, we perform a detailed study of such signals. Figure 4.21 displays monochromatic maps of the Stokes parameter U at two different wavelengths: the central wavelength of the blue component, λ_B (upper panel), and at the central wavelength of the red component, λ_R (lower panel). We focus on Stokes U in the third scan because the signals are larger. Similar results can be found for the other scans (see Sec. A.11).

We have carefully checked that the observed signals are not produced by any residual crosstalk from Stokes I to Stokes U. Given that the red component is several times stronger than the blue one, we should have noticed any possible crosstalk first in the red component, and it would have been even more obvious in the silicon line.

The signals outside the filament are generated in a regime where the Hanle and Zeeman effects operate simultaneously. This can be seen in the penumbra of the sunspot, where a very strong and horizontal magnetic field is present. There, two patches are easily observed in the blue component (with opposite

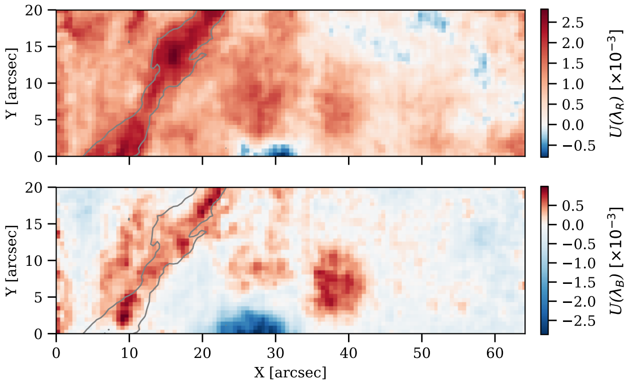

Figure 4.21 – Stokes $U(\lambda_R)$ and $U(\lambda_B)$ of the third scan. A grey contour at $0.6 I_{LC}$ shows the position of the filament.

signs), but no so easily in the red one. The explanation of this lies on the fact that the Hanle effect affects more the red component than the blue one. Moreover, the most striking feature of Fig. 4.21 is that both maps present the same sign inside the filament, and opposite sign outside. In the following, we address this issue and try to find a suitable physical scenario that can produce linear polarization signals with the same sign in the two components.

Lower-level Hanle effect

The lower-level Hanle effect (so called because it is produced by the populations and coherences of the lower level) can potentially create linear polarization with the same sign in the blue and red components of the He I 10830 Å, as is observed. Figure 4.22 shows the ratio $U(\lambda_R)/U(\lambda_B)$ for two different magnetic field strengths and all possible orientations of the magnetic field vector parametrized with the inclination θ_B and the azimuth ϕ_B in the local reference frame. The rest of the parameters are the typical values obtained in the inversion, i.e., $\tau_R = 1$, $\Delta v_D = 10\,\mathrm{km\,s^{-1}}$, $v_{\mathrm{LOS}} = 0\,\mathrm{km\,s^{-1}}$, and $a = 0.1$. The case of $B = 100\,\mathrm{G}$ (lower panel of Fig. 4.22) shows that the ratio is relatively constant and around –3 for all configurations of the magnetic field vector. For this value of the magnetic field strength, we see that the probability to find the two components with the same sign is very close to zero. On the contrary, when the field is decreased to $B = 1\,\mathrm{G}$ (upper panel of Fig. 4.22), we find that 18% of the space of parameters gives profiles with the same sign.

We extended the study to the range [0.01, 1000] G computing the percentage of the space of parameters that produce the same sign in the two lobes. The result is displayed in Fig. 4.23. The behaviour of the variation of the probability of having the red and blue components of the same sign with the magnetic field can be divided in 4 regions: i) below 0.1 G where the atomic polarization is barely changing due to the magnetic field, ii) from 0.1 G up to 10 G the lower-level Hanle effect plays a role creating linear polarization signals with the same sign and one can find $U_R/U_B > 0$ in up to $\sim 20\%$ of the space of parameter; iii) between 10 G and 100 G the curve goes down, and finally, iv) for fields above 100 G the Zeeman effect starts to dominate the sign of the polarization and the ratio becomes always positive again because of the shape of the Zeeman profile.

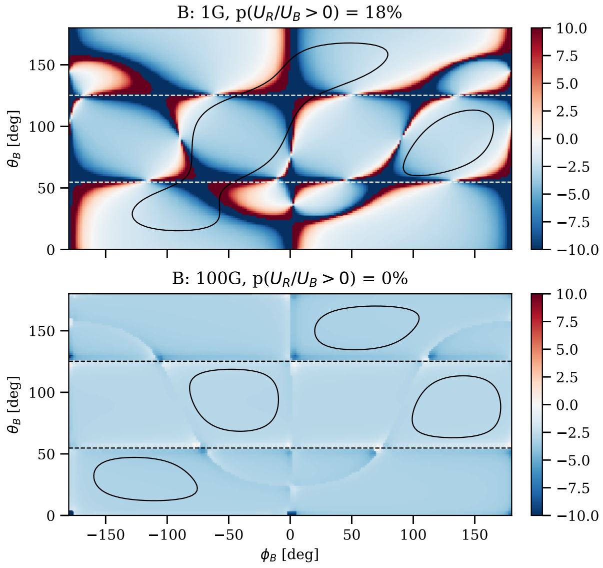

Figure 4.22 – Ratio between the synthetic Stokes U signals at the red component (λ_R) and the blue component (λ_B) for a magnetic field strength of 1 G (upper panel) and 100 G (lower panel). Horizontal dashed lines indicate the two Van Vleck angles at θ_B =54.74° and θ_B =125.26°. The label on top of each panel describes the percentage of area covered by a positive ratio. Contours indicate the areas where Stokes $U(\lambda_R) > 1.5 \times 10^{-3} I_c$.

These conditions would support the idea of filaments with very weak fields in which the lower-level Hanle effect produces linear polarization of the same sign for the red and blue components. However, the amplitudes of the linear polarization signals produced for such weak fields are very small, compared with the observed typical $U(\lambda_R)$ signals of around $1.5 \times 10^{-3} I_c$, marked with contours in Fig. 4.22. Also, the synthetic Stokes Q has larger amplitudes than the observed signals. Therefore, the linear polarization profiles cannot be explained (only) with very weak magnetic fields, with a single component slab model and under the assumptions of the current version of HAZEL.

The anisotropy variation

Another possible option is that the assumptions in HAZEL do not really hold. Specifically, if we allow for radiative transfer effects, we can produce a change in the sign of the linear polarization signals with the variation of the anisotropy of the radiation field along the LOS. This was already observationally noticed some years ago by Judge et al. (2014, 2015b) in the analysis of the impulsive phase of a flare event. They showed that their profiles had the same sign in both components of the linear polarization signals, explaining that an optically thick one-dimensional slab (and a simple two-level atom) generates J^2_0 values that change sign with wavelength, in particular between the blue and red component. The variation of the anisotropy with the optical depth was also proposed several years before by Asensio Ramos et al. (2005) and Trujillo Bueno & Asensio Ramos (2007). They showed that the anisotropy (integrated in frequency) can change sign depending on the optical thickness of the slab, the internal source function, and the illumination from the surface.

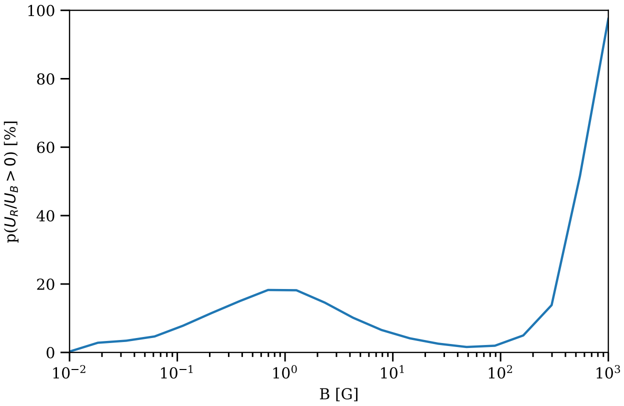

Figure 4.23 – Probability of having $U_R/U_B > 0$ for different magnetic field strengths.

From previous studies we can conclude that using a single value of J_0^2 for the whole multiplet can only lead to polarization with opposite signs in the blue and red components. To generate polarization of the same sign, we need J_0^2 values in the formation region of each component with opposite signs. This seems to be a plausible scenario for active region filaments because they are located at low heights and they have a significant optical thickness. These two ingredients favor a negative contribution to the anisotropy produced by the self-emission of the slab that can compete with the anisotropy produced by the photospheric radiation field. Consequently, changes of sign of J_0^2 with depth are possible.

Although this possibility seems very realistic, both calculations are still simple (and use different assumptions, such as the atomic model or, a specific or integrated anisotropy) compared to a complex multi-slab model where the variation of anisotropy along the slab and the formation of both components are explicitly demonstrated.

4.6.3 Analysis of Stokes V

In Sec. 4.3.1 we showed that the circular polarization chromospheric maps displayed a pattern very similar to the photospheric map without any indication of the presence of the filament. In addition, in Chapter 3 we demonstrated that active region filaments, despite being dense chromospheric structures embedded in the corona, do not have enough optical thickness so as to completely block the light emerging from the underlying chromosphere. In this section, we investigate the presence of more than one magnetic component in the filament region from the observed circular polarization profiles and, in particular, from the amplitude ratio of both components. If both components are formed under similar physical conditions, the circular polarization profiles will have an amplitude ratio that will match the Landé factor ratio of both components. If this ratio changes, it could be an indication that both components are sensitive to different physical conditions.

To this end, we compute the ratio of the Stokes V amplitudes (calculated in one of the lobes) of the red and blue components from the observations (V_R/V_B) which is displayed in the lower panel of Fig. 4.24. To compare with the single component model inferred by HAZEL, we show the same ratio for the synthetic profiles in the top panel of Fig. 4.24. The ratio calculated from the observations showed very small values

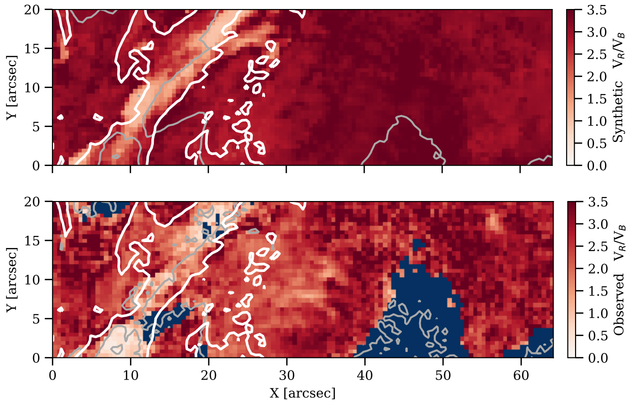

Figure 4.24 – Upper panel: map of the ratio of the amplitudes of the circular polarization between the red and the blue components calculated using the synthetic profiles from the HAZEL fit. Lower panel: the same ratio but calculated from the observed signals, masking the signals below 1.5σ. The gray line indicates the PIL while the white contour indicates the filament location.

in the polarity inversion line (gray line in the figure), which are produced by the presence of noise. To avoid artifacts produced by the noise, we mask all values with signals below a certain threshold. To set this threshold we find that the estimation of the ratio is only reliable when the Stokes V signals are above 1.5 times the standard deviation of the noise (see Sec. A.6 for more details about the procedure). The similarities between both maps in Fig. 4.24 is an indication that the code is able to reproduce the observed asymmetries between the components of the line.

The decrease of this ratio in the filament is a consequence of the saturation due to the high optical depth of the red component (see Sec. A.7 for more information). A single component model seems to be sufficient to reproduce many of the filament profiles. However, we find pixels in the FOV with much smaller ratios than those that can be produced by the saturation effect of the spectral line. One cannot achieve ratios below 1 with a single component atmosphere, but values as low as 0.2 are found in the observations. This indicates that more complex models with magnetic field gradients have to be used to explain such big differences. An example of this case is extracted from the region at $(8'', 3'')$ and displayed in Fig. 4.25. In this figure the Stokes V amplitude of the blue component is almost twice that of the red component.

The question that now arises is whether the rest of the profiles, even if they do not show such clear evidence in the ratio V_R/V_B, can be explained as profiles emerging from a multi-component model. To visualize this and to demonstrate that the saturation effect can be produced by either a single-component or a multi-component model, we show in the following how a single-component model is able to roughly reproduce the emerging profiles synthesized with a two-component atmosphere (one slab on top of the other as we did in Sec. 3.4). In these cases we cannot distinguish between them.

For this numerical experiment, we synthesize the emergent Stokes profiles in a top slab with $\tau_R = 1.2$ (with τ_R as the optical depth of the profile of the red components) placed above an active region at the same heliocentric angle as the observations ($\mu = 0.92$) with a background absorption (bottom slab) of $\tau_R = 0.3$ (value extracted from our observations). The magnetic field in the active region is parallel to the surface ($\theta_B = 90°, \phi = 0°$) and perpendicular to the filament axis (simulating a polarity inversion line)

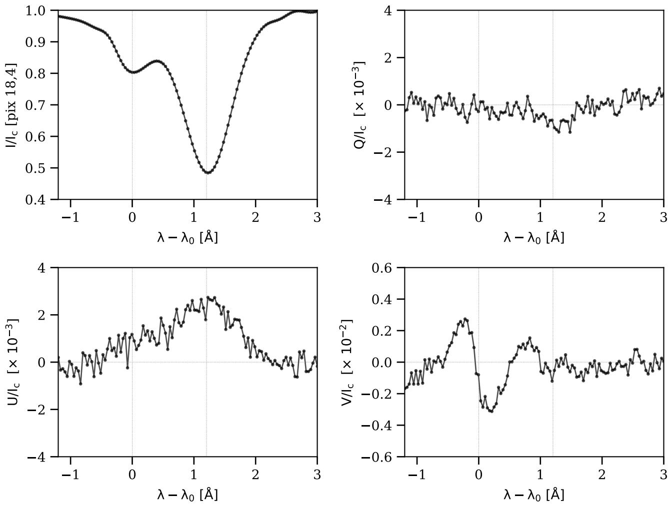

Figure 4.25 – Stokes profiles of the pixel [18,4] with very low ratio V_R/V_B, located in the lower part of Fig. 4.24. The Stokes V amplitude of the blue component of Stokes V is twice the one of the red component and λ_0 is the wavelength of the center of the blue component.

with a strength of $B = 300\,$G. The filament has a field of $B = 10\,$G, with an azimuth of $45°$ with respect to the field underneath ($\theta_B = 90°, \phi = -45°$). This configuration mimics the general trend of what we observe in the Stokes profiles.

The synthetic Stokes profiles are displayed in Fig. 4.26 together with the profiles of the fit to these using a single component model. From the inversion we have extracted the following conclusions: i) the optical depth is roughly equal to the sum of those of the two components $\tau_R \simeq 1.5 = 1.2 + 0.3$. ii) Although the optical depth of the filament is large, the emergent Stokes V from the slab below remains almost unperturbed for the blue component, while its amplitude decreases for the red components (the original Stokes V of the background is drawn in a dashed line). This "transparency" is a consequence of the fact that Stokes V is almost zero in the core of the line where the absorption is very high, while the opacity decreases towards the wings precisely where the Stokes V signals are higher. In the blue component, as a consequence of its lower optical depth, the change is even smaller[6]. iii) A single component inversion is able to reproduce the Stokes signals at a level of $5 - 10 \times 10^{-5} I_c$, including the high asymmetry between the Stokes V of the components. The residuals are well below our noise level of $4 - 6 \times 10^{-4} I_c$ so that it is impossible to detect any difference. iv) From the inversion we have inferred a magnetic field with $B = 250\,$G, $\theta_B = 78°$, and $\phi_B = -45°$ for the filament, which is much stronger and more vertical than the magnetic field in the upper slab (10 G), a fact that has to be kept in mind in the analysis of these structures.

---

[6] This can be easily visualized assuming a Gaussian profile for the absorption with width σ^2. Then, the Stokes V generated in the first slab will be attenuated by $V_2(\lambda_0) = V_1(\lambda_0)e^{-\tau_2(\lambda_0)}$ in the core. At the wavelengths on the Stokes V lobes ($\lambda = \lambda_0 \pm \sigma$) the absorption is $\tau_2(\lambda_0 \pm \sigma) = \tau_2(\lambda_0)e^{-0.5} \sim 0.6\tau_2(\lambda_0)$. If, for example, $\tau_2(\lambda_0) = 1.2$, then $V_2(\lambda_0 \pm \sigma) = V_1(\lambda_0 \pm \sigma)e^{-0.6\tau_2(\lambda_0)} \sim 0.5 V_1(\lambda_0 \pm \sigma)$, that has only reduced to a half. In the blue component, because of its lower optical depth, the change is less important.

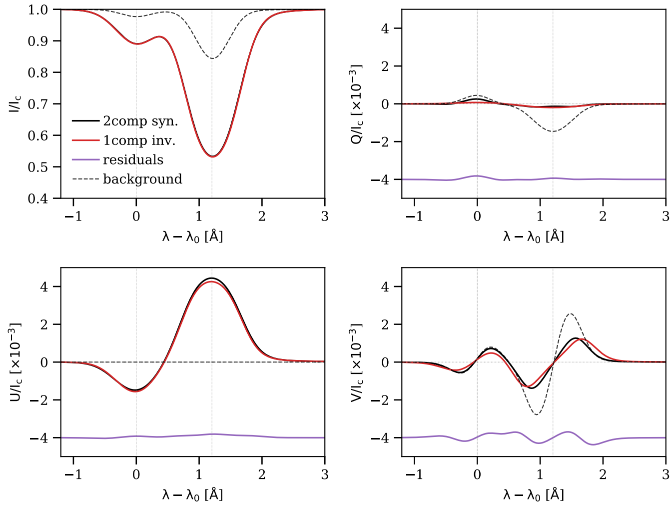

Figure 4.26 – One component model inversion (red) of the synthetic Stokes profiles generated with a two component model (black). The residuals of the best-fit are below each Stokes profile (purple). The dashed line indicates the Stokes signals from the background in absence of the filament.

4.6.4 Abrupt changes in the magnetic field

In Sec. 4.4 we suggested that the local azimuth map obtained from the one component inversion displayed solutions correlated with the polarity of the region, i.e., the solutions were conditioned by the Stokes V information. Moreover, in the PIL, this polarity change produced an azimuth change of up to 180° within the filament. In this section we analyze two contiguous pixels at each side of the PIL (i.e. from the filament axis) only taking into account Stokes Q and U. If this abrupt change in the azimuth is real, it will be retrieved without the information of Stokes V. The Stokes profiles in these pixels are displayed in Fig. 4.27.

Both pixels present very similar linear polarization signals but different polarities in Stokes V. As in previous sections, we have used MultiNest to find the locations of the eight potential ambiguous solutions, which are displayed in Fig. 4.28. These eight combinations of θ_B, ϕ_B generate the same Stokes Q and U profiles. Figure 4.28 is split in two regions of different polarities: the red one with the magnetic vector pointing towards the observer and the blue one in the opposite direction. The red solid line shows the location of $\Theta_B = 90°$ when it is transformed to the local reference frame $\theta = 23°$. This division also splits the eight solutions in two groups of four depending on the polarity of Stokes V. This implies that the local azimuth and inclination inferred would be very different only due to the polarity, even for exactly the same Stokes Q and U profiles.

Given that drastic variations of the azimuth of the field between neighboring pixels are discouraged in the filament, one could try to find whether smooth solutions in the full magnetic field vector can be found. Let us focus on the pair of solutions closest in local azimuth and with different polarities, the pair [4, 6] (Fig. 4.28). In this case, the two solutions differ by $\Delta\theta_B = 120° - 70° = 50°$ in inclination. Consequently, to simultaneously fit similar Stokes V of opposite polarity, one needs to modify the magnetic field strength

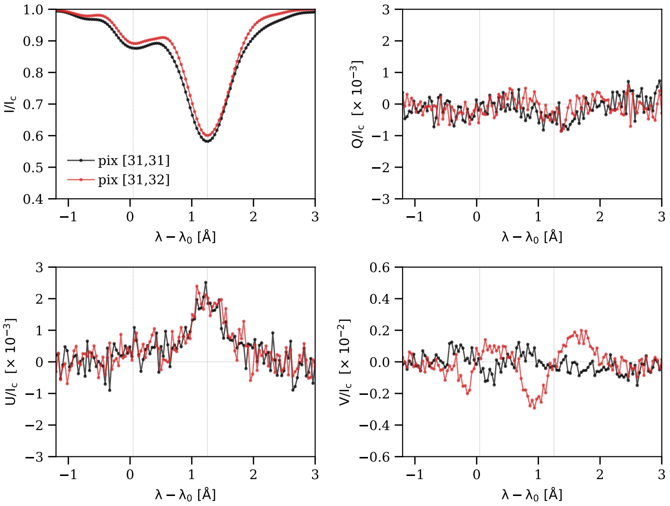

Figure 4.27 – Stokes profiles of the two chosen pixels from the inner part of the filament. They are two contiguous pixels at each side of the PIL. Stokes Q and U are very similar, while each Stokes V have a different polarity.

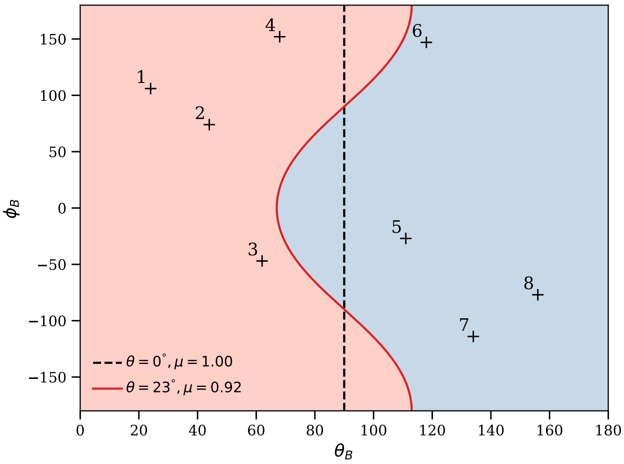

Figure 4.28 – Hanle ambiguities represented with plus symbols, in the space of θ_B and ϕ_B compatible with both Stokes Q and U of the two chosen pixels of Fig. 4.27. The coloured areas correspond to each polarity of the magnetic field, being the vertical lines the division for $\theta = 0°$ and $\theta = 23°$.

from $B = 20\,\mathrm{G}, \theta_B = 70°$ to $B = 200\,\mathrm{G}, \theta_B = 120°$. This increase in magnetic field strength is so large because solution 6 has a magnetic inclination in the plane of the sky close to $\Theta_B \sim 90°$ (near the red line in Fig. 4.28). In conclusion, ensuring smoothness in the azimuth does not ensure smoothness in the inclination and/or the magnetic field strength. This is another indication that these Stokes profiles cannot be analyzed assuming a single component model and we need more than one component to study them.

4.7 Exploring the possibility of a two component inversion

After finding several evidences of the necessity of more complex models to explain the observed signals, in this section we address this problem with a two component inversion. This scenario is based on the assumption of two slabs of constant physical properties, one on top of the other, where the emergent polarized light have to pass through the two of them (as in the example of the Sec. 3.4 or Sec. 4.6.3). In principle, although each slab can have different velocities, absorptions, and line broadenings, we reduce the dimensionality of the problem by only doing the inference over the magnetic field vector of both components: $(B_1, \theta_1, \phi_1, B_2, \theta_2, \phi_2)$. The rest of parameters have been fixed from a single component inversion.

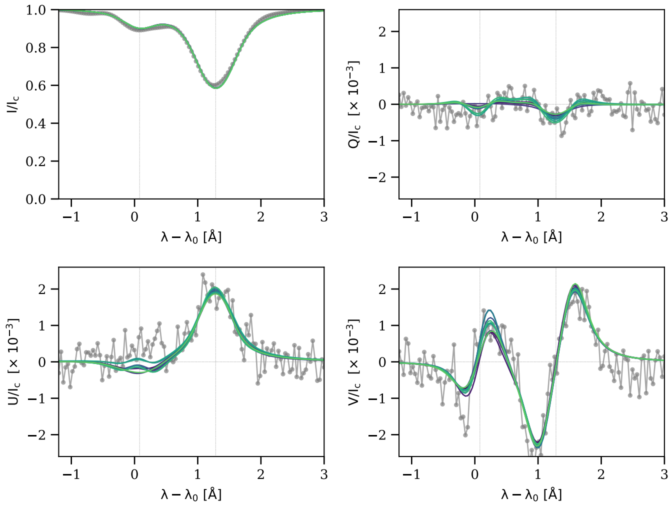

Figure 4.29 – From green to blue colors, 10 of the 30 compatible solutions with the observed profile (grey).

Both slabs have the same thermodynamic properties but different optical depths $\tau_1 = 0.3$ (value estimated from the filament surroundings) and $\tau_2 = 0.9$ (to mimic our average filament absorption). In this exercise we have chosen the same pixel [31, 32] used in Sec. 4.6.4. The observed Stokes profiles and the synthetic ones found for each mode are displayed in Fig. 4.29. We see that it is possible to reproduce more observational features than before, such as the positive Stokes U in the blue component or the complex Stokes Q shape.

However, the inference problem becomes very complex because we find a high number of compatible solutions, all of them with different configurations. In this sampling, we have found up to 30 solutions but only 10 are shown to avoid crowding the figure. These solutions are spread in the space of parameters with an average distance between each one around 10° in the inclination and azimuth and 30 G in the field strength B. The high number of solutions is a consequence of the combination of all possible ambiguities in both components and the flexibility of the two component model to generate the same profiles with different combinations of parameters.

Moreover, because of the potential cancellation of the signals from both components of the model (as showed in Chapter 3), the magnetic field can sometimes be increased (if their signals are opposite) almost arbitrarily, finding cases in which magnetic fields of 500–800 G are required to reproduce the profiles, while with the one component inversion a magnetic field below 100 G was enough to reproduce the same polarimetric signals. Given the multi-parametric nature of this analysis, and after extensive numerical experiments (adding or fixing other parameters such as the Doppler width) we conclude that a two component inversion with all the free parameters is a challenging problem if there is no extra information to constrain them.

4.8 Summary and conclusions

We have presented the analysis of ground-based spectropolarimetric observations acquired with GRIS at GREGOR (at Observatorio del Teide) of the He I 10830 Å multiplet on an active region filament. The active region was located in a flaring area. Although the profiles do not show any relevant signature, the fast evolution of the filament (with, e.g., the absorption strongly changing in consecutive scans, ∼15 min) is a sign of the activity of the area.

The observed polarization signals in the filament show single-lobed linear polarization profiles, which is indicative of optical pumping by an anisotropic illumination and, potentially, the action of the Hanle effect. These linear polarization signatures were close to the noise level ($5 \times 10^{-4} I_c$). We have been able to measure them as a result of our high polarimetric sensitivity and reduction process. Longer integration times than the ones used here are necessary to increase the signal-to-noise ratio and study the weak polarization signals present in these chromospheric structures. The low signal-to-noise ratio of the observations from other studies, such as Xu et al. (2012), might be the reason why they could not detect the linear polarization signals due to scattering, hence neglecting atomic polarization in their analysis.

We have studied the observations with HAZEL, a state-of-the-art inversion code, which includes the Hanle and Zeeman effects, to retrieve the physical properties from the polarimetric signals. Using a one component model, as it is customary in other studies, magnetic field strength values around 50–150 G have been found.

We have also applied the Bayesian framework using HAZEL and MULTINEST to explore the solutions in the parameter space and compute posterior distributions. This Bayesian inversion cannot compete in speed with the standard inversion algorithms but it can be used to investigate in detail the accuracy of the inversions, the sensitivity of the parameters to the noise, and to give confidence intervals to all the parameters. Using this technique, we have studied how many solutions are compatible with the analyzed profiles depending on the geometry of scattering and the magnetic field regime. In addition, we have applied it to the inference of the height, concluding that this parameter cannot be constrained, at least at our noise level.

After this first canonical analysis, we have focused our attention on observational evidences of the necessity of more complex models to explain the observations. First, the intensity profiles points out a very optically thick filament where HAZEL cannot perfectly reproduce the profiles, underestimating the larger absorption of the blue component. We fixed it by using a new parameter which takes into account the extra emission of the slab. This is not enough if radiative transfer effects are present while both components are sensitive to different physical conditions. The second evidence is the ubiquitous presence of profiles with the same sign in the blue and red components in the linear polarization inside the filament. After exhaustive searches with Hazel to reproduce this effect with the magnetic field, we conclude that it is not possible. However, other studies (Asensio Ramos et al., 2005; Trujillo Bueno & Asensio Ramos, 2007; Judge et al., 2015b) stress that a change in the sign in the anisotropy J_0^2 along the LOS can lead to the same sign in both component if each one is sensitive to different regions in the atmosphere. Again, this is another evidence towards an increase in complexity of the models.

Finally, the Stokes V map of He I does not show any clear signature of the presence of the filament, and the inferred azimuth map follows the same pattern than Stokes V, as if the polarity of Stokes V was conditioning the inference. By using simple numerical experiments where we synthesize the emergent Stokes profiles from a two component model we have demonstrated that the filament is almost transparent to the circular polarization generated in the atmosphere below the filament. Its analysis as a signal coming from a unique structure leads to discrepancies, such as assigning large field strengths to the filament. Moreover, some indications of strong gradients of B are also visible in Stokes V. Finally, in an effort to study the feasibility of two-component inversions, we have shown that the model contains too much flexibility and it can reproduce better the observations (better than a single component model), but a large number of compatible solutions with different configurations exist, making the interpretation very complex.

There are other studies that investigate the misinterpretation due to oversimplified models, as the work of Milić et al. (2017), who showed the bias produced when a simple 1D model is used to interpret a 2D inhomogeneous prominence model, retrieving more vertical and weaker magnetic field solutions. In the case where the observed line is optically thin and there is no background (such as in prominence observations using the D_3 at 5876 Å, Casini et al. 2009b), a single component could be a plausible option. However, for optically thick structures close or above the disk (e.g. spicules, filaments, etc.) radiative transfer modeling and extra information about the illumination from the photosphere is needed. For this purpose, stereoscopic observations (to identify the height), magnetic field extrapolations from the photosphere or multi-line observations with for instance the Ca II at 8542 Å (Khomenko et al., 2016; Schwartz et al., 2016), to infer the magnetic field of the active chromosphere, could help constraining the atmospheric stratification below, enabling the analysis of the filaments. Finally, it is also important to add that the presence of noise has a strong impact on the inference process. Very sensitive spectropolarimeters, data corrected for seeing, and precise determinations of telescope PSF are also required.

5

Diagnostic potential of the Ca II 8542 Å line for solar filaments

In this chapter we explore the potential of the chromospheric Ca II line at 8542 Å for the study of the magnetic and dynamic properties of solar filaments. We have used the CRISP instrument at the SST telescope, which obtains images of a large spatial resolution and allows us to carry out spectropolarimetric observations of the Ca II 8542 Å line. We use the NICOLE inversion code to infer the properties of an observed solar filament and discuss the validity of the results due to the assumption of hydrostatic equilibrium. To study the global dynamics of the region and the evolution of the filament, we have used observations from other telescopes such as the CHROTEL and SDO. We show that commonly used methods in the photosphere, such as *Local Correlation Tracking*, may not be suitable for studying plasma motions in the chromosphere. Finally, we show how a solar filament at different heights can generate similar intensity profiles, demonstrating that its height cannot be inferred from spectroscopic inversions.

5.1 Introduction

Solar filaments can also be seen in the Ca II infrared triplet around 8540 Å. One of the advantages of this triplet is that it is a good compromise of modeling efforts, polarimetric sensitivity, and observational requirements (Quintero Noda et al., 2016, 2017a). Although the Ca II 8542 Å is less sensitive (via Zeeman and Hanle effects) to the magnetic field than other chromospheric lines (still being the most sensitive of the IR triplet), it can be observed in the entire solar disk with very high absorption (as opposed to the He I 10830 Å) and can be used to extract information about the plasma temperature. For a more detailed description we redirect the reader to Sec. 2.3.2.

There are only a few studies of prominences (off-limb) in this spectral line (Stellmacher et al., 2003; Park et al., 2013) where they usually calculate the temperature from the line broadening using two lines of different atoms to separate the contribution of the thermal and non-thermal motions, where the most used spectral lines are Ca II 8542 Å, He I 10830 Å, Hα, and Hβ. For filaments (on-disk) the background, which is illuminating the structure, needs also to be taken into account and cloud models are used (Tziotziou, 2007).

This chapter presents, for the first time, the study of a filament using a modern NLTE inversion code such as NICOLE (Socas-Navarro et al., 2000). Since the magnetic field plays a fundamental role in the formation and support of the structure, we will study the full-Stokes vector to retrieve not only the magnetic properties but also the connection with its environment.

5.2 Observations

The observations analyzed in this chapter were carried out at the SST telescope on 22nd of July 2013 using the spectropolarimeter CRISP. A description of this telescope and the instrument is given in Sec. 2.5.2. The telescope was placed over a solar filament situated far from disk center at coordinates x, y = (+653,–305)″, which corresponds to a cosine of the heliocentric angle $\mu = \cos\theta = 0.65$.

The Ca II 8542 Å line was sampled in the range ±1.75 Å from the core in 21 steps of varying size: 70 mÅ close to the core of the line, and up to 800 mÅ in the far wings. This strategy (de la Cruz Rodríguez et al., 2012, 2013a) is used to optimize the sampling in the chromosphere as its evolution time is shorter than in the photosphere. For around 14 minutes, 36 scans were taken (with a cadence of ~23.22 s), which provided us maps of 55″× 58″ with an excellent spatial sampling of ~0.059″pixel^{-1}. The data was processed using the CRISPRED package (de la Cruz Rodríguez et al., 2015) and further applying MOMFBD (van Noort et al., 2005) to improve the spatial resolution down to a value around 0.12″. The resulting noise level is in the range $4 - 6 \cdot 10^{-3}$ in units of the continuum intensity for Stokes Q, U and, V. More details about the reduction process are given in Sec. 2.5.2.

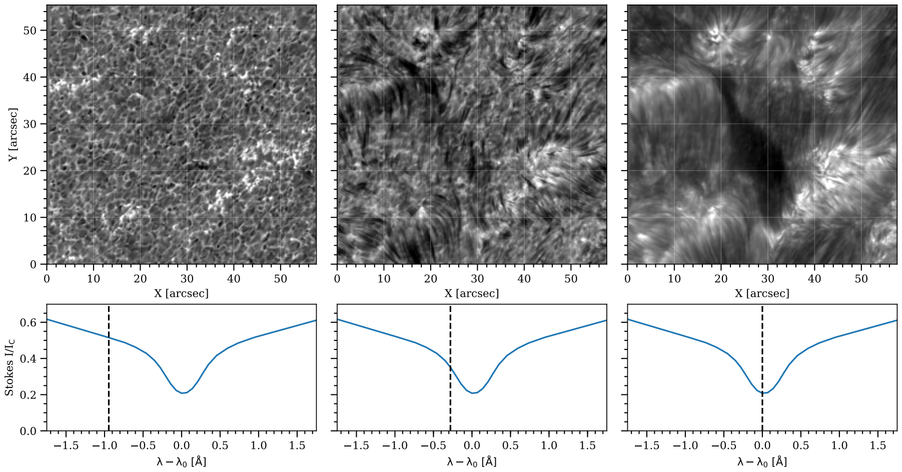

Figure 5.1 – FOV at three different wavelength positions -0.945, -0.28, and 0.0 Å from the line center $\lambda_0 = 8542.1$ Å. The lower panels show an average line profile and a vertical dashed line at the wavelength used to generate the field of view of the upper panel. We see how the spectral line has information from the photosphere (left column) to the chromosphere (right column) where the filament is observed.

Figure 5.1 shows the FOV at different wavelength positions. We have chosen three different $\lambda - \lambda_0$ position -0.945, -0.28, and 0.0 Å from the line center $\lambda_0 = 8542.1$ Å, to visualize how we are mapping different heights while we move across the spectral line. In the left panel we see the reversed granulation at a height around z$\sim$140 km (Cheung et al., 2007) where the intergranular lanes are relatively hotter than the granules, in contrast to what is observed at the lower photosphere. This image gives us an idea how of the deepest layers we can measure given that we do not reach continuum wavelengths. The middle panel shows a filamentary structure that covers the whole FOV. This structure is even more enhanced in the right panel, where bright plage areas are surrounding the dark filament showed in absorption in the core of the Ca II 8542 Å line. This filament will be the focus of this chapter.

5.2.1 Solar context

To put the observations in context, we have made use of data provided by some of the band-pass filters (AIA; Lemen et al., 2012) on board NASA's Solar Dynamics Observatory (SDO; Pesnell et al., 2012) and by the Global Oscillation Network Group (GONG; Hill et al., 1994). We display in Fig. 5.2 images taken at a time in the middle of the observations (around 09:24 UT). The top left panel of Fig. 5.2 shows an SDO/HMI image at the continuum of 6173 Å of the region where we can see the quiet Sun below our filament.

The rest of panels of Fig. 5.2 show wavelengths sensitive to higher temperatures at chromospheric and coronal heights. Despite the low resolution of the images ($\sim$1.2″/pix in HMI, $\sim$1.6″/pix in AIA, and $\sim$5″/pix in GONG) the filament is more visible in the filters sensitive to lower temperatures such as He II 304 Å, while less visible in the coronal filters Fe IX 171 Å, Fe XII 193 Å, and Fe XIV 211 Å. Other filters sensitive to larger temperatures like Fe XVIII 94 Å do not show any hint of the filament. Finally, the filament becomes clearly visible with a high absorption in the Hα filter of GONG (lower right panel).

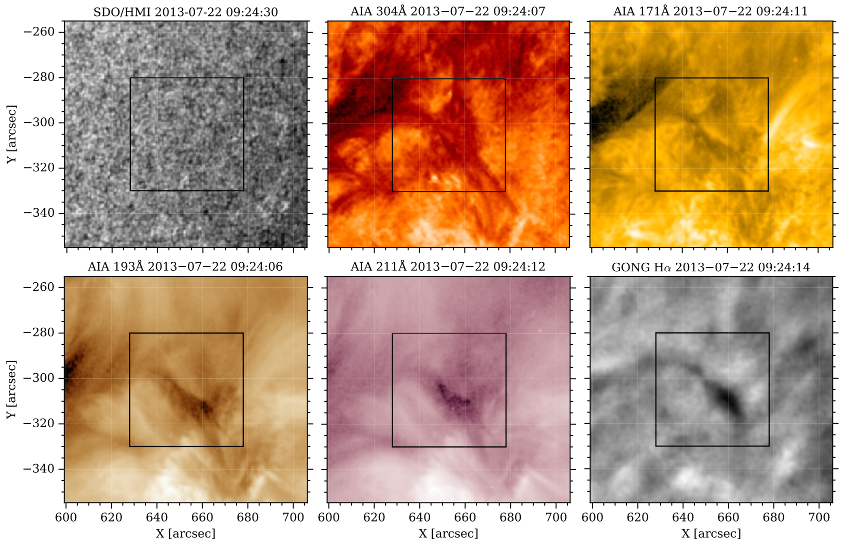

Figure 5.2 – We show an area of 100″×100″, with a square displaying our FOV, tracing the solar photosphere, chromosphere, and corona. The different layers are traced with several filters at different wavelengths, indicated at the top of each panel.

5.2.2 Evolution of the filament

Thanks to the temporal cadence of GONG and SDO, we can trace the evolution of the filament from its birth to its occultation when disappearing at the limb. Figure 5.3 shows the evolution of the filament for more than five days. Throughout the evolution we see how the filament is increasing its absorption (it becomes darker) and its size. The top row shows the filament in Hα taken from the GONG network, where the first four images are from GONG-Teide which has a better resolution, and the last one is from GONG-Mauna Loa. The second row shows the same area in the AIA/171 Å filter. In this filter, large coronal loops in the region mask the filament. Our spectropolarimetric observation was made two days after its birth (third column). Between the third and fourth day something destabilizes the filament and it almost vanishes. A few hours later, the body starts to acquire absorption again. The last column shows the filament at the limb, where a small bright cloud appears to protrude by almost 25″ above the limb. However, due to all the activity of the area, we cannot be sure that the filament seen in this frame is the same as our observation as the properties could have changed a lot. In any case, this filament is at higher altitude than the AR filament presented in Chapter 4, as expected from a filament lying above a quiet-Sun area.

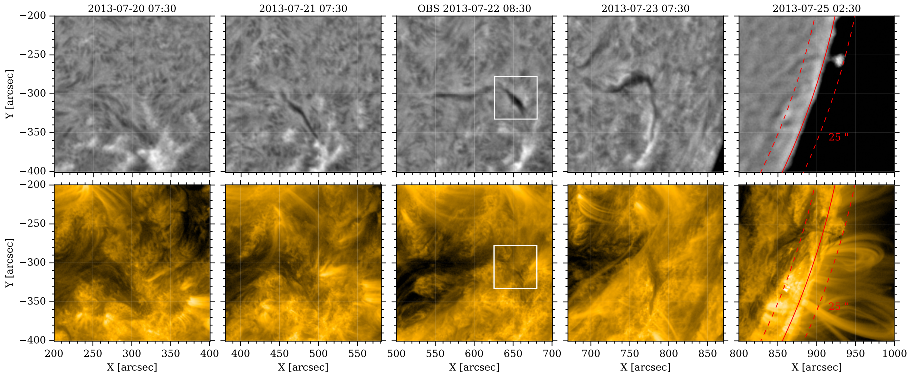

Figure 5.3 – The evolution of the filament during more than five days. We see how the filament is increasing its absorption and its size (up to 100″ long) during its evolution. The top row shows images from GONG and the bottom row the same are but in the channel 171 Å of AIA.

5.3 Data analysis

In this section we proceed to analyze the observations. After the complete reduction process (including fringes and crosstalk correction, explained in Sec. 2.5.2), we prepare the data to be analyzed with the inversion code NICOLE. To increase the signal-to-noise ratio of our observations, we average the entire time series since we do not see any substantial changes in the evolution of the filament. Additionally, we also downsample the image with a binning of 4×4 pixels, yielding a final resolution of 0.24″/pix. We clarify that all this processing is not really needed for Stokes I, but it becomes necessary for the polarization to significantly improve the signal-to-noise ratio. We decrease the photon noise from $4-6\cdot10^{-3}$ to $2-6\cdot10^{-4}$ in units of the continuum intensity for Stokes Q, U, and V. Despite the high polarimetric sensitivity, some systematic artifacts are still present and we discuss them in the next sections.

5.3.1 Inversion process

We use the NICOLE inversion code (Socas-Navarro et al., 2000, 2015) to infer the physical conditions in the formation of the Ca II line at 8542 Å. Like the SIR code, NICOLE iteratively perturbs the physical parameters such as the temperature, line-of-sight velocity, and magnetic field of an initial guess model atmosphere to find the synthetic profiles that best match the observations. The stratifications of density and pressure are computed from the equation of state using the temperature stratification and the upper boundary condition for the pressure under the assumption of hydrostatic equilibrium (HE, more details are given in its description in Sec. 2.4). The stratification of the atmospheric parameters obtained after the inversions is given as a function of the logarithm of the optical depth scale at 5000 Å, with the same notation as in previous chapter, $\log(\tau)$. Finally, to model our spectral line, NICOLE uses a Ca II model atom consisting of five bound levels plus continuum which is synthesized assuming complete frequency redistribution and including the isotope splitting (Leenaarts et al., 2014).

As described in Sec. 2.5.2, CRISP does not have a perfectly monochromatic sampling and the instrumental smearing has to be included in the forward modeling calculation. To this end, we convolve each synthetic profile during the inversion process with the appropriate instrumental profile. According to Fig. 2.17 the FWHM in this spectral range is ∼108 mÅ and the Nyquist–Shannon (NS) sampling theorem establishes that the sampling has to be at least 54 mÅ. As the observations were taken with a minimum sampling of 70 mÅ, we synthesize the profiles with a wavelength axis with a sampling of 35 mÅ (see the red dotted line in Fig. 5.4). This new grid contains exactly all the points of the observed points and fulfills the NS theorem. Moreover some points are added in the border of the wavelength range to avoid artifacts during the convolution. In a last step, our observed profiles are interpolated to the new grid but only the observed points are compared with the synthetic ones. We accomplish that by only weighting these points in the merit function in the same way was shown in Eq. 2.18.

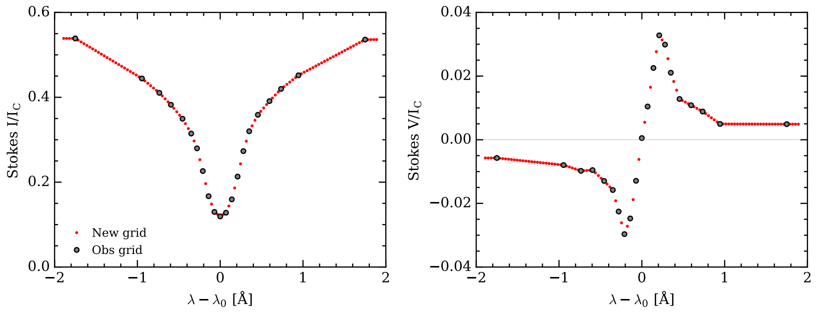

Figure 5.4 – Stokes I (left) and Stokes V (right) with the observation wavelengths (gray circles), coarser in the core as the chromosphere evolves rapidly. To fully take care of the FWHM of CRISP we need to use a finer grid (red dots).

In order to reduce the complexity of the inversion, we have decided to keep the microturbulent velocity fixed. After extensive tests, we estimate a microturbulent velocity of 3 $\mathrm{km\,s^{-1}}$ as the average value needed for a good fit, which might be associated with the broadening produced by unresolved plasma motions. We have verified that the Stokes profiles of the average time series have the same broadening as the individual profiles, meaning that the time scale of the filament evolution is larger than this series.

The inversions are done pixel by pixel, i.e., the NLTE problem is solved for each pixel independently assuming a plane-parallel atmosphere. This approximation is valid for the Ca II 8542 Å line where 3D radiation does not play an important role (de la Cruz Rodríguez et al., 2012, 2013a)[1]. To improve the convergence, the inversions were performed in three cycles. In the first cycle, we have chosen 4 nodes equidistantly located in the $\log(\tau)$ axis for temperature, one in LOS velocity and one more in each one of the three components of the magnetic field. This first cycle is very robust as there are no correlations between the magnitudes: the temperature describes the depth and width of the line, the LOS velocity describes the center of the line, and the magnetic field describes the signal in Stokes Q, U, and V. If a more complex configuration is used, the code tries to compensate the effects between the magnitudes and unrealistic stratifications are obtained. For the involved magnetic fields strengths in our study, the Ca II 8542 Å line is in the weak field Zeeman regime and the Stokes I is weakly affected by the Zeeman broadening. The initial guess model is sampled with 43 points from $\log(\tau)$=–7.2 to $\log(\tau)$=+1.2. We start with a temperature stratification with an almost arbitrary parabolic shape as we do not need a better initial model to fit the spectral line. This robust first cycle is able to capture the main information and model the line profile with excellent convergence. To reduce possible artifacts, a horizontal (in $\log(\tau)$ scale) smooth is applied after each cycle. We use a median filter with a kernel size of 3 pixels to remove bad fits and a Gaussian filter with a FWHM of 3 pixels to smooth the whole FOV. This filter is applied at the same node positions of the inversion and then a Bezier-spline interpolation is applied (de la Cruz Rodríguez & Piskunov, 2013). The output of this smoothing process constitutes the input model for the next cycle. As strong asymmetries are not detected by an inspection of Stokes profiles and the FOV seems to be dynamically quite stable, only a maximum of two nodes are set to the LOS velocity in the second cycle. This is enough to capture the different velocities at the photospheric and chromospheric levels. A similar reasoning is applied to the LOS component of the magnetic field, as some Stokes V profiles show several lobes indicating gradients of magnetic fields along the LOS. A last cycle is needed to improve the model of complex profiles located in the plage region. In this last cycle, the number of nodes in temperature is increased to seven, i.e., we add one node between each pair of nodes from the previous cycle. This inversion strategy used to invert the full FOV is shown in table 5.1.

Table 5.1 – Nodes used to invert each pixel with the inversion code NICOLE. Microturbulent and macroturbulent velocities are not inverted.

Cycle	Temperature	v_{LOS}	B_{LOS}	$B_{\perp}$
1 st	4 nodes	1 node	1 node	1 node
2 nd	4 nodes	2 nodes	2 nodes	1 node
3 rd	7 nodes	2 nodes	2 nodes	1 node

5.3.2 Temperature stratification

To visualize the temperature stratification we have taken two horizontal slices at two different optical depths which are shown in Fig. 5.5: at $\log(\tau) = -1.4$, associated to a photospheric layer, and at $\log(\tau) = -4.8$, which provides a chromospheric view. These values have been chosen to optimize the sensitivity of the line to these two layers (see Sec. B.3 for more information). The left panel of Fig. 5.5 is very similar to the left panel of Fig. 5.1, i.e., the photospheric granulation with temperatures of about 5000 K. The second panel shows a cold filament with an average temperature of 4500 K, surrounded by a hot plage with a temperature more than 6500 K. Again, the temperature is very similar to what we see in the intensity map in the core of the line.

---

[1] See Štěpán & Trujillo Bueno (2016) for conditions in which it is not true

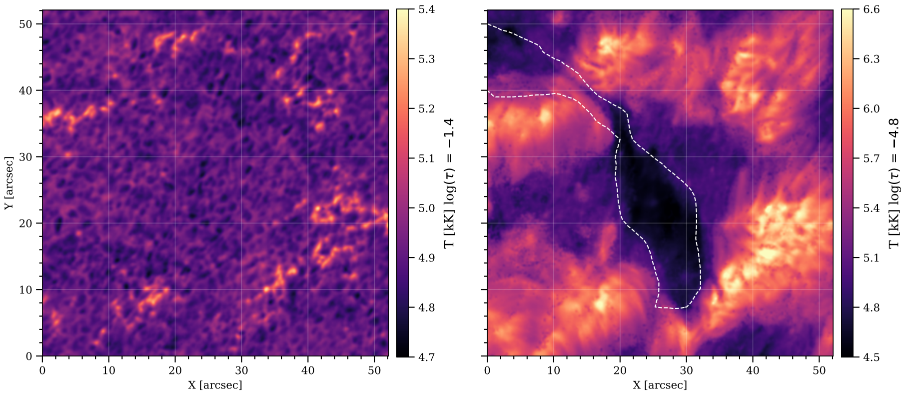

Figure 5.5 – Temperature stratification inferred with NICOLE at $\log(\tau) = -1.4$ (left panel) and $\log(\tau) = -4.8$ (right panel). The white dashed contour draws the shape of the filament seen in Hα by CHROTEL.

To better study the area, we have classified the profiles in the area in three different classes according to the intensity in the core of the line. Filament profiles are those with intensities less than $0.148I_c$[2], plage profiles have intensities higher than $0.22I_c$ and background profiles are those with intensities between the two. The left panel of Fig. 5.6 shows the average temperature stratification of each type of profile, the green line showing the temperature of the plage, the blue line displaying the temperature of the background and the orange line showing the temperature of the filament. We have extended the axis only to $\log(\tau) = -5.5$ because the line becomes insensitive after that point (Quintero Noda et al., 2016). This figure demonstrates that the three curves are overlapping below $\log(\tau) = -3$ and start to separate above. At $\log(\tau) = -5.5$ the difference between the filament and the environment is of around 1000 K. The right panel of Fig. 5.6 displays the average profiles for each type. The coloured bands of each curve indicate the standard deviation of each set of profiles (in both panels).

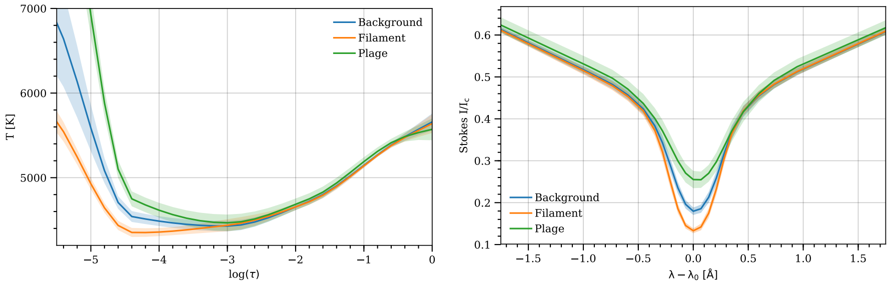

Figure 5.6 – Left panel: temperature stratification calculated from the average of the temperature inferred from profiles of different regions. Right panel: average Stokes I profile of the selected regions. The coloured bands of each curve indicate the standard deviation of each set of profiles.

---

[2] This number has been chosen by inspection to enclose the shape of the filament. The same with the plage threshold.

5.3.3 Longitudinal magnetic field

We focus now on the longitudinal component of the magnetic field as inferred by NICOLE. We show this quantity at two heights in Fig. 5.7. As expected, the Stokes V parameter encodes information from the photosphere to the chromosphere and the inversion process is able to extract gradients of the LOS magnetic field with height.

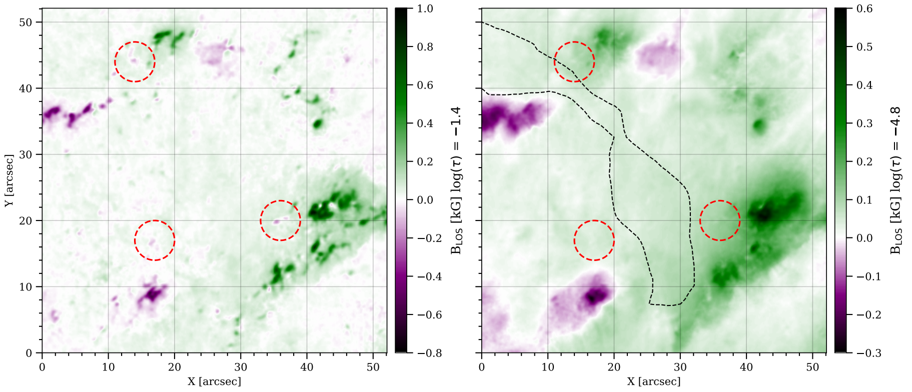

Figure 5.7 – Longitudinal component of the magnetic field inferred with NICOLE at two levels: the $\log(\tau) = -1.4$ (left panel) and $\log(\tau) = -4.8$ (right panel). Some circles are drawn in red indicating pixels gradients which change the polarity of the magnetic field along the LOS.

In the photosphere (left panel of Fig. 5.7) the magnetic field appears more concentrated at small scales, while in the chromosphere (right panel of the same figure) it is more diffuse, though maintains the general topology of the photospheric field. The reason is that as the pressure decreases, the magnetic field expands. Probably, the magnetic field in the filament area appears uniform because we are tracing the upper part of the canopy, while the small loops are closing at lower heights. These small loops could be identified with places where we detect polarity changes between the photosphere and chromosphere. One such event happens at (18″, 18″) where a red circle is drawn. The FOV has a plage of almost 1 kG in the photosphere that decreases up to 500 G in the chromosphere, with a very weak magnetic field in the middle where the filament is. One would expect to see the filament in these maps if the dense filament plasma is modifying the magnetic field lines of the region. However there is not a clear indication of its presence. Although the magnetic field reveals similar values inside and outside the filament, the structure is clearly detected in the temperature. This is somehow equivalent to what we found in Chapter 4 because the filament was not detected in the longitudinal magnetic field. Nevertheless, we do not know if the filament is just embedded in the atmosphere of the region with a similar magnetic field, or with a weaker magnetic field far above the surface.

5.3.4 Transverse magnetic field

We have only used one node to infer the transversal component of the magnetic field. It means that the inferred stratification is constant, the same value at all the heights. The map of $B_{\perp}$ is shown in the left panel of the Fig. 5.8. This map shows higher values in the plage, while the filament is permeated by a very weak transverse magnetic field of less than 200 G.

We point out that in the inversion of a large data set it is always necessary to check if the fit obtained by the code is good or not. Figure 5.9 shows a Stokes profiles from inside the filament at position (30″, 30″), showing that the fit is properly done. However, as Stokes Q and U do not have enough signal, the inversion can fluctuate provided that the profiles produce similar merit functions (see Eq. 2.18). Thus this poses questions on the reliability of the inferred transverse magnetic field.

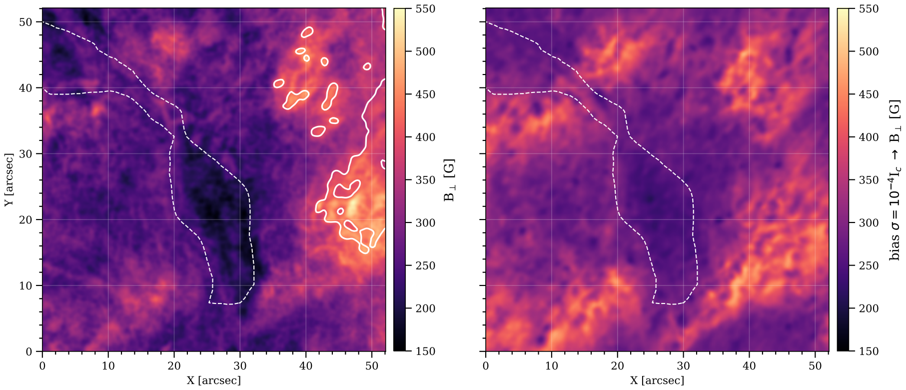

Figure 5.8 – Left panel: transversal magnetic field inferred during the inversion. Right panel: Magnetic field bias generated with a noise of $\sigma = 10^{-4}\, I_c$. Some solid contours have been drawn in the left panel indicating where the inferred value is above the bias. The rest of values are overestimated. The white dashed contour draws the shape of the filament seen in Hα by CHROTEL.

Martínez González et al. (2012a) studied the effect of the noise in the estimation of the azimuth Φ_B, inclination Θ_B, longitudinal magnetic field $B_\parallel$, and transverse magnetic field $B_\perp$ in the weak field approximation. They found that the maximum likelihood estimation of the longitudinal component and the azimuthal angle are unbiased quantities. On the contrary, the transversal component, and hence the inclination angle, presents a non-zero bias. The value of the bias formula was derived by Martínez González et al. (2012a) and it is given by Eq. 5.1. If the inferred $B_\perp$ is similar or smaller than the bias, this value may not be correct and may be strongly affected by the noise of the observations. This bias has the following expression:

$$B_\perp^{\rm bias}(\sigma) = \left(\frac{-2\ln \mathrm{c}}{\sum_j I_j''^{\,2}}\right)^{1/4} \frac{\sqrt{\sigma}}{C}\ , \tag{5.1}$$

where $C = 4.67.10^{-13}\lambda_0^2\sqrt{G}/2$, $G = 1.22$, and $\lambda_0 = 8542$ Å in the case of this line. Using the percentile 50 ($c = 0.5$) and a very conservative value for the photon noise of $\sigma = 10^{-4}\, I_c$, we obtain the map of bias displayed in the right panel of Fig. 5.8. As the noise is in the upper part of the equation, a lower value generates a lower bias and thus more reliable values of $B_\perp$. To compare these values with the original map, we have drawn some contours in the left panel of the same figure indicating where the inferred value is above the bias. The contours show that there are only small patches where the inferred field is well above this bias and almost the rest of the map is below it. Therefore, from the left panel of Fig. 5.8 we see that the inferred value of $B_\perp$ is dominated by the noise in large part of the FOV, something that is expected given that Stokes Q and U have low polarization signals in the area (similar to those profiles showed in Fig. 5.9). The spatial pattern of the bias, with low values in the center of the map and

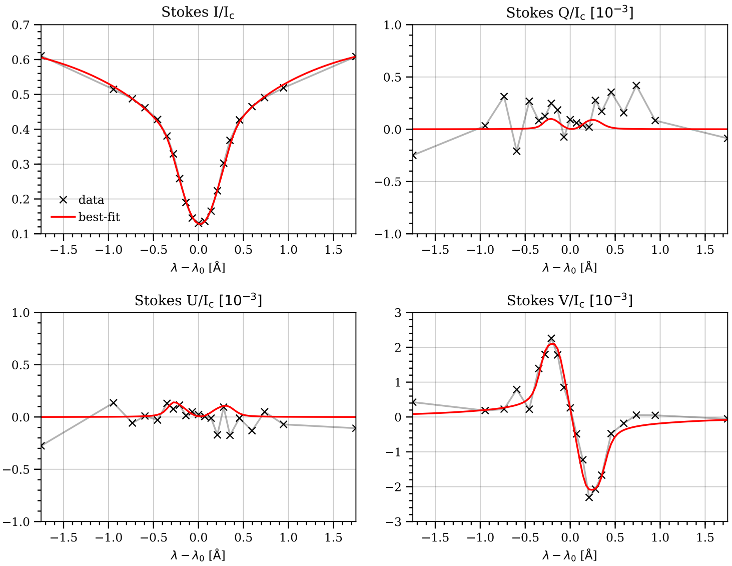

Figure 5.9 – A Stokes profiles sample from inside the filament (30″, 30″) shows how the fit was done properly, but as Stokes Q/I_c and U/I_c do not have enough signal, the inversion code can generate whatever profile with similar merit function values. The magnetic field inferred at $\log(\tau) = -5$ is $B_{\parallel}$ ~60 G and $B_{\perp}$ ~150 G.

higher values in the border of the map coinciding with the plage, is a consequence of the broadening. The dependence of Eq. 5.1 on the second derivative of the intensity profile produces a larger bias for broader lines. Therefore, we can only give an upper limit on the transversal magnetic field of the filament of around 250 G. Using the same formula, we can also estimate the noise required to have a bias below a certain magnetic field. For instance, for a magnetic field of $B_{\perp}$ =200 G, we estimate that one needs a photon noise below $\sigma = 5 \times 10^{-5}\, I_c$ for a proper inference.

5.3.5 LOS velocity

Another quantity inferred in the inversion is the line-of-sight velocity stratification. Figure 5.10 shows the LOS velocity at $\log(\tau) = -1.4$ and $\log(\tau) = -4.8$. After the inversion an offset was added to the whole velocity stratification to have the photosphere with zero mean velocity[3]. The left panel shows small velocities across the FOV, except in the plage region where we find downflows (positive values) with velocities larger than 5 $\mathrm{km\,s^{-1}}$. This map shows the velocity in the upper photosphere and, because of that, it is slightly diffuse and does not show a clear granular pattern.

The right panel of Fig. 5.10 shows the velocity map at the height of the filament. Fast downflows of almost 10 $\mathrm{km\,s^{-1}}$ are found in the plage, while the area of the filament is located is almost at rest (with

---

[3] Due to cavity errors (small imperfections of the reflecting surfaces of the etalons), the velocity map can show an artificial spatial gradient. To fix it, instead of adding a constant offset to the whole map, we have calculated a smooth version of the photospheric velocity map $\log(\tau) = 0$ by convolving the map with a Gaussian of a FWHM of 30 pixels, thus removing the structure of the image. These values oscillate between $-0.8\mathrm{km\,s^{-1}}$ and $+0.4\mathrm{km\,s^{-1}}$.

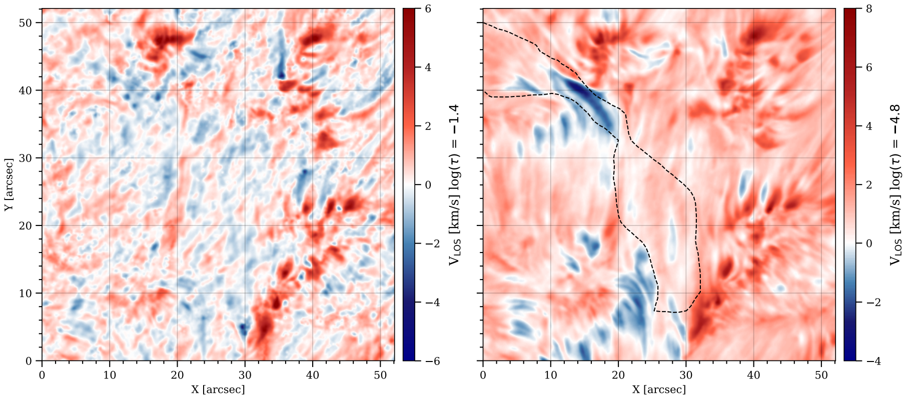

Figure 5.10 – Longitudinal velocity stratification inferred with NICOLE at two atmospheric layers: $\log(\tau) = -1.4$ (left) and $\log(\tau) = -4.8$ (right). The black dashed contour draws the shape of the filament seen in Hα by CHROTEL.

respect to the photosphere). A strong upflow of almost $5\,\mathrm{km\,s^{-1}}$ is found at $(15'', 40'')$, just where the "tail" of the filament is located.

In order to have a better global picture and confirm the veracity of the velocity pattern of the filament, we have used observations from the *Chromospheric Telescope* (CHROTEL; Bethge et al., 2011). It is a robotic telescope for full-disk synoptic observations at the Ca II K, Hα, and He I 10830 Å chromospheric lines. A monochromatic image in the center of the He I line shows us that this filament is also observable in this line (left panel of Fig. 5.11) but less clear than in Hα. A reason for that can be the large difference of drainage timescales between the helium and the hydrogen (Gilbert et al., 2002).

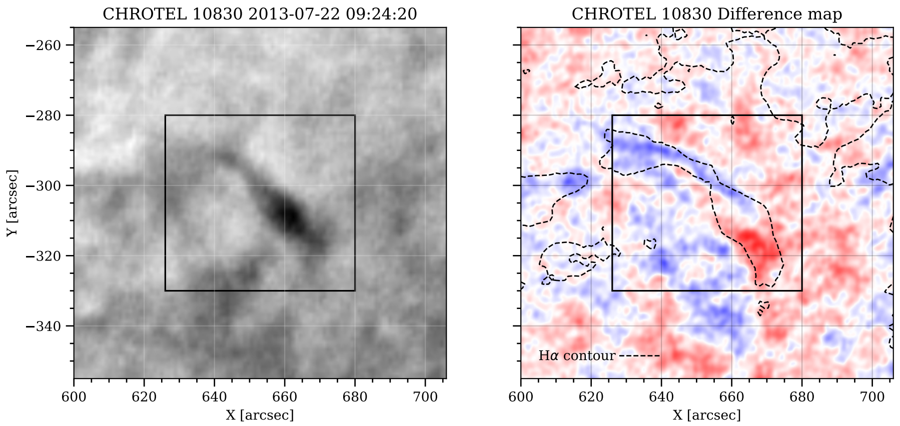

Figure 5.11 – Left panel: intensity in the core of the He I 10830 Å. Right: difference between the blue and red sides (± 0.7 Å) of the He I 10830 Å with contours of Hα taken by CHROTEL. As in the previous figure, the blue represent motions towards the observer. The axes scales have their origin at the disc centre, being the vertical the N-S direction while the horizontal the W-E direction, with negative sign towards the south and the west.

CHROTEL uses a tunable filter for observing the He I line, which allows us to estimate the line-of-sight velocity. Due to the presence of several line components and the weak absorption of the multiplet, the calibration of the LOS velocity in CHROTEL is difficult (Bethge et al., 2011). For this reason, we only show the difference between two filtergrams at ±0.7 Å in arbitrary units (see Fig. 5.11). The velocity pattern detected in this line is very similar to that inferred for the Ca II line, displaying upflows of $\sim 7\,\mathrm{km\,s^{-1}}$ in the border of the filament. Additionally, we also detected redshifted profiles with velocities of up to $\sim 5\,\mathrm{km\,s^{-1}}$ in the lower part of the filament. These value has been calculated from some individual profiles (see Appendix B.1 for more information). This might be a consequence of neutral material (Khomenko et al., 2016) escaping from the structure because this is not detected in Ca II.

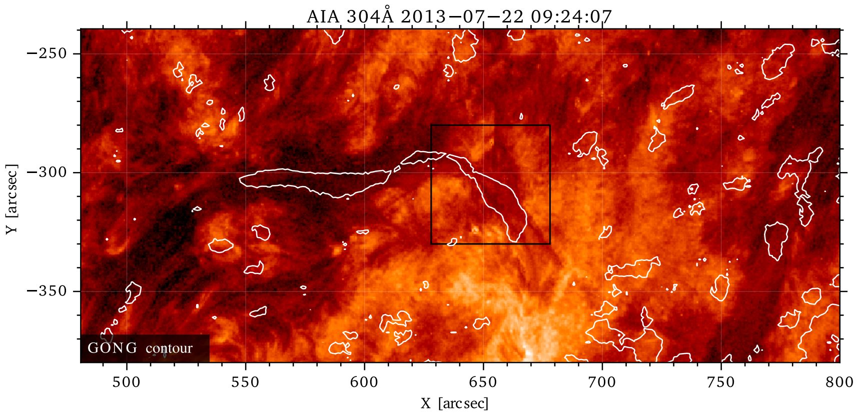

Figure 5.12 – Wider field of view of the area around the filament with AIA/304 Å in the background and with GONG/H_α contours in white. Our filament seems to be the "tail" of a bigger filament which covers the left half of the image and could be feeding the filament with material.

We study the surroundings of the filament to understand the flow of material. Figure 5.12 shows an AIA/304 Å image tracing the upper chromosphere. We mark with white contours the areas with high absorption in the GONG/H_α data[4] In this image, the filament seems to be the "tail" of a larger filament which covers the first half of the figure and could be feeding the filament with material. In fact, the flow of material could be horizontal because it would have component in the LOS direction due to the geometry. This connection is even more clear in the images of the evolution of the filament (see Fig. 5.3).

5.3.6 Transverse velocity

It is not possible to diagnose transverse velocities with spectral lines because they produce no Doppler shift. To measure these velocities, we have used a Local Correlation Tracking algorithm (LCT; Yi & Molowny-Horas, 1995) to analyze the transverse flows in the images. This technique computes the intensity displacement between each two consecutive images and associates the optical flow to plasma velocities. We have used the Python implementation[5] of this technique by Campos Rozo & Vargas Domínguez (2015).

---

[4] Note that these contours are different from the CHROTEL map as not only the threshold is different but also the instrumentation and the width of the filter associated to this line.

[5] The latest version is hosted at `https://github.com/Hypnus1803/FlowMapsGUI`

The applicability of this method to the chromosphere is very delicate. Changes in the intensity due to temperature might be interpreted by the code as something that is moving. In addition, inside the filament, where the contrast is very low, the estimation cannot be properly done. Finally, solar atmospheric changes can strongly affect the estimation of transverse velocities because they deform the solar images.

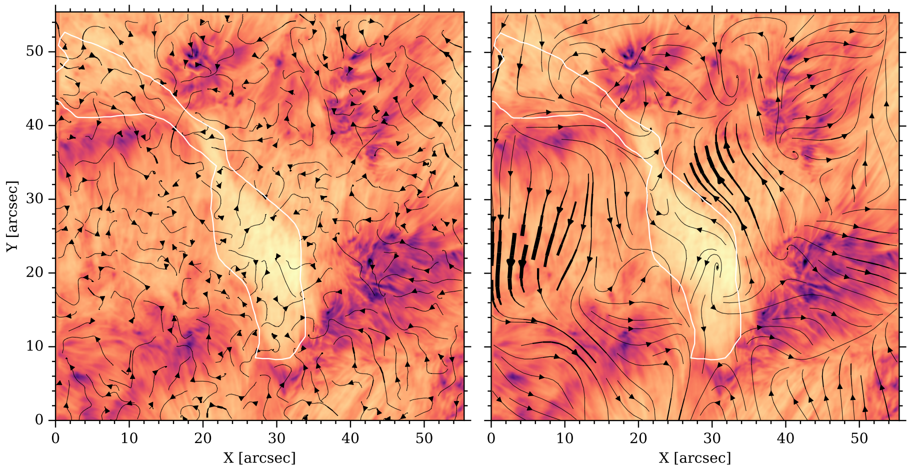

Figure 5.13 – Left panel: Map of the transverse component of the velocity inferred applying LCT to the temporal series at the wing of the Ca II line, tracing photospheric motions. Right panel: The same quantity calculated in the core of the Ca II line, tracing chromospheric layers. The width of the arrows is proportional to the magnitude.

We have applied the LCT method to the core images of the Ca II 8542 Å, where the filament is clearly visible and to the wing images at -1.8 Å from the line center. Since the filament is stable during the 14 minutes of the scan, we have taken the average of the flow estimated in all the frames. This allows us to cancel certain random motions or bad spurious estimations. We have used different spatial windows between 3″and 5″(Diercke et al., 2018), obtaining similar results. The main difference is that with a larger window the map is smoother and the values are a bit smaller.

Figure 5.13 shows the result of the average transversal velocity of the whole temporal series with the width of the arrows being proportional to the magnitude. The velocities at photospheric levels are around $\sim 1\,\mathrm{km\,s^{-1}}$ while the velocity at chromospheric levels reach values of $\sim$2 $\mathrm{km\,s^{-1}}$. The background is the image at the line core of the Ca II line, which helps to locate the position of the filament. The contrast in the central part of the map is very low and the detected velocity is almost zero.

In the core of the line we clearly see groups of fibrils with the same direction, but the arrows are not always aligned with them. Another intriguing fact is that almost no transverse flow is found in the upper tail where we found high upflows of material, which can be explained, for instance, if the flow is constant and does not produce any change of brightness.

Another remarkable fact we want to point out is the opposite motions on both sides of the filament. These horizontal flows reach mean flow speeds of $\sim$1.5 $\mathrm{km\,s^{-1}}$ (averaged over 14 minutes). While other studies such as (Zirker et al., 1998) or Diercke et al. (2018) find counterflows inside the filament and they associate these dynamics with internal motions of the filament itself, our counter-motions are detected mainly outside the filament (like in the case of Yi & Molowny-Horas, 1995) and could be associated, for instance, with the formation of the filament axis through photospheric shearing motions (van Ballegooijen & Martens, 1989). To analyze whether there are shearing motions in the photosphere, we have applied the LCT method also to the photosphere using the far wings of the Ca II line. This result is displayed in the left panel of Fig. 5.13 and it does not show any patterns that indicate these motions, but the granular pattern. A possible explanation for this non-detection could be that such motions have stopped or that our temporal range is not enough to recover these possible small velocities (perhaps below the granulation velocities).

Lastly, we detect that the flows in the bright plage zones are outward, something counter-intuitive since from the NICOLE inversions the material seems to be falling at those points. One possible explanation for this effect could be that the LCT method is also sensitive to changes in brightness produced by wave propagation. Waves moving away from areas of high magnetic field and running along field lines would produce such artifacts. This poses a question whether the opposite motions found in the filament by the LCT method may not be real, but rather changes in the intensity, indicating that the LCT method should not be applied to the chromosphere. Therefore, to differentiate what is actually moving and what are propagating waves we would need to make a more detailed study of the temporal evolution of these oscillations at different heights (Vecchio et al., 2007). Extra material about the oscillations of the FOV can be found in the Appendix B.2.

5.4 Supporting the filament plasma

The general conclusion of the inversions is that we have found a filament with a lower temperature than its environment (approximately 1000 K colder) and a higher density (about 10 times larger). These values may vary slightly depending on the height at which we analyzed the results. Specifically, these values refer to $\log(\tau) \sim -5$. These results are consistent with the observational definition of these structures: *a filament is cool chromospheric plasma overdensity embedded in the hot and low dense solar corona* (Mackay et al., 2010).

With these properties, the filament will persist at chromospheric/coronal heights because of the magnetic field that supports the plasma against the gravitational force. The magnetic field (and in particular its topology) seems to be the main ingredient that allows this sustentation and multiple theoretical models have been proposed to explain the presence of this material for so long (see Chapter 1 for more information about these models).

However, we note that the assumptions made for the inversions are not fully compatible with the description above. NICOLE assumes that the atmospheric models are in hydrostatic equilibrium. This implies that the gas pressure is computed from the temperature by solving, in a plane-parallel atmosphere:

$$F_P + F_g + \cancel{F_L} = 0 \rightarrow \frac{dP(z)}{dz} = -\rho(z) g_\odot(z) \xrightarrow{\text{ideal gas}} \frac{dP(z)}{dz} = -\frac{P(z)}{T(z)} \left(\frac{\mu m_H g_\odot}{k_B} \right) , \quad (5.2)$$

where $g_\odot$ is the solar surface acceleration, k_B the Boltzmann's constant, μ the mean molecular weight and m_H the mass of an hydrogen atom. The equilibrium is obtained between the pressure F_P and gravity F_g forces, neglecting the Lorentz (magnetic) forces F_L. A consequence of the previous equation is that the chromospheric material under this approximation is not supported by the magnetic field and it is only the gas pressure gradient that compensates the gravitational force.

An obvious question is then if the filament is supported against gravity by the hydrostatic equilibrium. This is a sensible question given that the model is capable of reproducing the spectral profile of the Ca II line. First, according to the above equation (and the result of the inversions), one can find a stratification where we have denser material (filament) supported on less dense material (corona). However, the interface between these two layers will become unstable under any disturbance and a Rayleigh-Taylor instability can quickly develop and dilute the body of the prominence (Khomenko et al., 2014). The presence of a magnetic field damps the formation of such instability.

Secondly, to understand how NICOLE is able to find such a solution it is more convenient to discuss it in terms of geometric height. If we transform the stratification from optical depth to geometric height, we would have our filament at a height of 1500 km. At this height, the pressure gradient is still large to support the material, as from the minimum temperature to the chromosphere the pressure decreases by almost 3 orders of magnitude (Judge et al., 2015a). To place it at higher heights, a magnetic force would be necessary since the pressure no longer varies so much.

Concerning this magnetic field, based on the inference from the spectropolarimetric data, the longitudinal component has values around 60 G (see Sec. 5.3.3), while we can only give a maximum value of 250 G to the transverse component due to the noise level in Stokes Q and U (see Sec. 5.3.4). This gives us a maximum value for the magnetic field strength of the order of $\sqrt{B_{\parallel}^2 + B_{\perp}^2}$ ~260 G, a result still quite high compared to the values found in the literature (Gunár & Mackay, 2016).

Checking if the filament is in hydrostatic or magnetic equilibrium from observations is a difficult task. To this end, we have carried out several experiments. In the first numerical experiment, we start from the atmospheric model in HE inferred for the QS and analyze the influence on the emergent profile of modifications in the temperature and the pressure. To this end, we synthesize the profiles with NICOLE without imposing HE and adding some perturbations. The results are shown in Fig. 5.14, where the original stratification is shown as a blue solid line. Since the new material will be not in hydrostatic equilibrium and we want to study only the thermodynamical properties, we assume that a magnetic field is acting to keep the material static, compensating the extra perturbations introduced by us.

The left panel of Fig. 5.14 shows an atmosphere where the pressure has been increased at the lower chromosphere around $\log(\tau) = -5$ (equivalent to a density increase). This scenario shows a dense filament model over a QS atmosphere. The result of the synthesis shows a Stokes I profile with less absorption, drawn as a dashed orange line. The increase in pressure (or density) causes an increase in the source function (see also Sec. B.3 showing the Stokes I response function to pressure), possibly because of the increase in the number of Ca II ions with the new density stratification.

On the other hand, the right panel of Fig. 5.14 shows an atmosphere where we have decreased the temperature also in the lower chromosphere around $\log(\tau) = -5$. In this case, the synthesis gives a deeper profile, similar to the one found inside the filament. As the sensitivity to temperature is higher than that to pressure, one could still increase the pressure (as one would expect for an overdense filament) and the line profile would be still deeper than that of the QS. The resulting stratification is very similar to the solution found in HE. This first experiment shows that an overdensity must be colder than the environment to reproduce the deepest profiles observed. But given the degeneration that exists between temperature and density (although the profile is more sensitive to changes in temperature), we can continue generating the same profile by increasing the density and decreasing the temperature. This does not allow us to ensure a unique solution as the real stratification of our filament.

Now, we investigate the effect of height on the formation of the spectral line to find whether it is the same to have a filament at chromospheric or coronal heights and whether we could somehow infer that height. To do this, we simulate the scenario of a filament of similar characteristics located at a much higher height. Because NICOLE has not been developed to correctly address the external part of the atmosphere (corona) we have used the RH code (Uitenbroek, 2001) which includes the ingredients for that purpose.

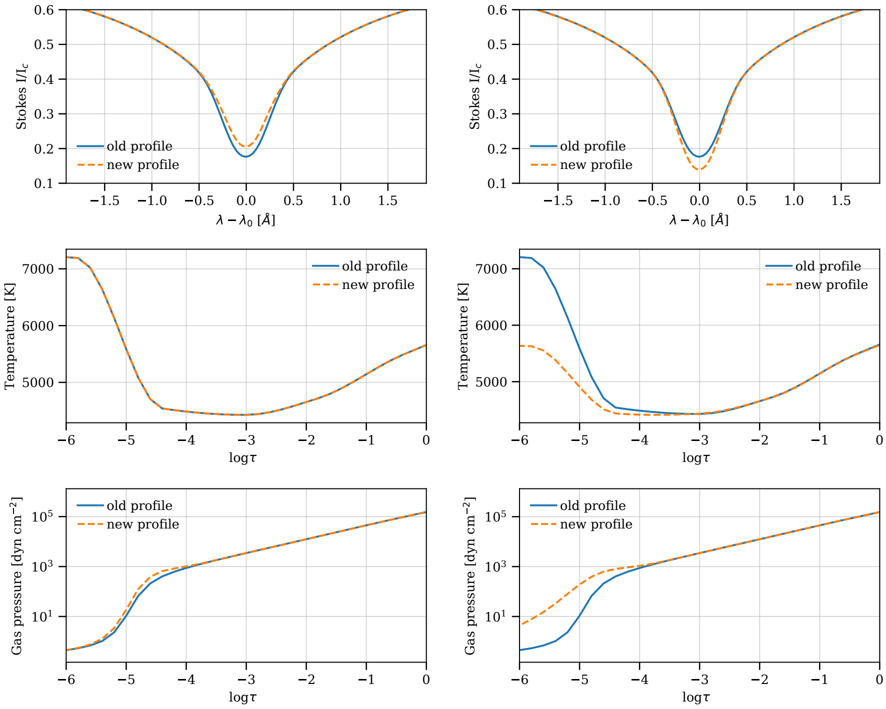

Figure 5.14 – Stokes profiles synthesized under no-HE (called new profile) from the modifications of a HE model of QS (called old profile). Left column: only when the pressure (or density) is increased. Right column: when the temperature is decreased (even with an overdensity).

The disadvantage of this code is that an inversion mode is still not included (although implementations have been developed, see de la Cruz Rodríguez et al. 2016b).

We assume that the filament is embedded in a QS atmosphere that we have taken from a snapshot from a 3D MHD simulation calculated with the BIFROST code (Gudiksen et al., 2011). This simulation (Carlsson et al., 2016) is publicly available as part of the Interface Region Imaging Spectro-graph (IRIS) mission (De Pontieu et al., 2014). To compute the QS model, we horizontally average the snapshot 541 (also used by Quintero Noda et al. 2016 and de la Cruz Rodríguez et al. 2013b). As the simulation provides height (z), gas pressure (P), and temperature (T), we transform them into the quantities required by the RH code, which are: mass column density (ρ), temperature (T), electron density (N_e), LOS velocity (v_{los}), and microturbulent velocity (v_{turb}) (for more details see Uitenbroek 2001). These new quantities are obtained from NICOLE which consistently calculates these variables internally. The synthesis from the original model is shown in Fig. 5.15 in dashed black line. On this QS model we placed a filament of typical parameters (see Chap. 1) with a temperature of 8000 K, pressure of 1 dyn cm^{-2}, and vertical size of 3 Mm at a height of 9 Mm. The resulting Stokes I profile is shown in red in the same figure.

The model shown in Fig. 5.15 has a pressure profile that decreases rapidly to the chromosphere (2 Mm) and then more slowly. The temperature profile includes a smooth transition region, wider than the

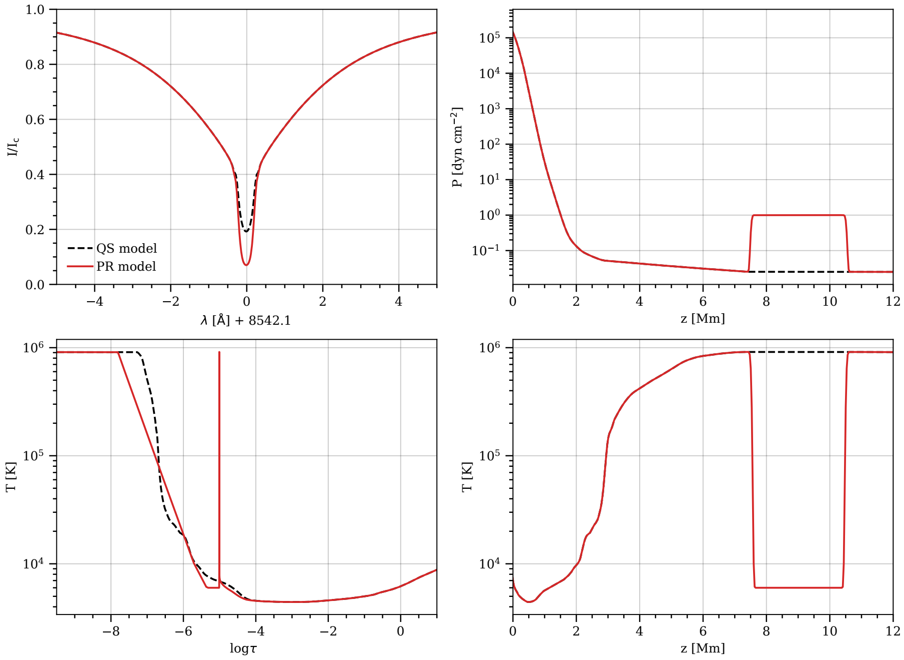

Figure 5.15 – Upper left panel: Stokes I profile generated from two different atmospheres. Upper right panel: gas pressure in geometrical height scale. Lower left panel: temperature in optical depth scale. Lower right panel: temperature in geometrical height scale.

individual stratifications of the model due to the horizontal averaging, finally reaching a corona at 10^6 K. The upper left panel shows the synthesis of Stokes I from both models: the QS model and the filament model. This demonstrates that a deeper Stokes profile (similar to the one observed) can be generated with a filament at coronal heights under no hydrostatic equilibrium conditions. Therefore, we conclude that we cannot infer the height of the filament from spectropolarimetric observations from above and should be done by imaging from another perspective (e.g. in the limb) or by triangulation (e.g. using STEREO).

On the other hand, an important conclusion can be drawn in the transformation from geometric scale to optical depth scale. The lower left panel of Fig. 5.15 shows that the filament, physically located at coronal heights, is at the same optical depths as the original chromosphere, i.e., $\log(\tau) \sim -5$. This is an indication that the line is really sensitive to the filament and its conditions, independently of its height. The latter is reasonable because the filament is clearly visible in the core of the line.

Summarizing, the Ca II 8542 Å spectral line is sensitive to the atmospheric conditions of the filament. However, due to the degeneration that exists among height, temperature, and pressure, we cannot give an accurate estimation of these three parameters. Other chromospheric lines with different sensitivity to temperature and pressure,such as Ca I 4227 Å, may be suitable for restricting the possibilities (see Sec. B.5).

5.5 Summary and conclusions

We have used the NICOLE code to study a solar filament observed on the Ca II 8542 Å line. Through a careful data reduction and inversion we have studied the stratification of temperature, density and magnetic field of a region containing a filament. Thanks to the high sensitivity of the line we have inferred the atmospheric conditions from the photosphere to the chromosphere, i.e., $\log(\tau) \sim [0, -5.5]$. From this inference we have found that the filament appears as an overdensity (10 times greater than the environment) and with colder temperatures (about 1000 K lower than the environment). These results are in concordance with existing literature.

However, NICOLE assumes hydrostatic equilibrium during the inversion process. If this condition is not fulfilled in the real Sun, we have shown that degeneration between the temperature and pressure (or density) in the formation of the intensity profile makes it impossible to estimate these values accurately. We have also shown that we are insensitive to the actual height of the filament, as the small opacity of the material between the filament and the upper chromosphere contributes almost nothing to the optical depth. Therefore, even being sensitive to the "local" filament conditions, it is not possible to only use this spectral line to distinguish between an hydrostatically supported filament at chromospheric heights and a colder and denser filament at coronal heights.

Concerning the magnetic field of the structure, we have detected homogeneous fields with a strength greater than 250 G throughout the region without a clear distinct value on of the filament. Weaker fields exist in the area but we are not able to detect them due to the noise level in the observations. These values indicate that we are in a field regime in which the Hanle effect begins to play an important role and should be taken into account (Carlin et al., 2013; Štěpán & Trujillo Bueno, 2016).

Although a filament is stable during the observations, we also witness abundant dynamics on the region. From a global point of view, the filament appears to be attached to a larger filament, through which material could be transferred. We detect it as a blueshifted flow in the tail of the observed filament. From a local point of view, we have detected using the He I 10830 Å line higher velocities of material falling from the filament than those inferred from the Ca II line. This loss of material due to the neutral nature of He I (not sensitive to the magnetic field) is expected. These differences in velocity reminds us that the filament is not only supported by the gas pressure.

Finally, we have also studied the time series using LCT. As a result, we obtain flows practically aligned with the field lines but with directions opposite to the velocities obtained by the Doppler-shift of the line. One possible explanation would be the propagation of waves emerging in the field concentrations of the plage and could serve as a diagnosis of the field topology. However, more work remains to be done to confirm that.

6

Summary, conclusions and future work

In this thesis, we have addressed one of the most spectacular manifestations of the solar magnetism: solar filaments. To understand its support by the magnetic field, we have analyzed spectropolarimetric observations. The "true" challenge is to understand their magnetic topology through the interpretation of their very weak polarimetric signals, which are very close to the sensitivity limit of the current telescopes and their instrumentation. For this purpose, we have used state-of-art observations and inversion codes and, to approach the data from a statistical point of view, Bayesian inference techniques.

6.1 Summary of the main results

In this work we have presented a detailed observational study of two solar filaments through the analysis of the He I 10830 Å and Ca II 8542 Å lines. These spectral lines have been proven suitable for such purpose because they are a good compromise between magnetic sensitivity and the complexity of the numerical modeling.

In Chapter 3, we have revealed problems and possible uncertainties in the analysis of previous studies for retrieving magnetic fields in solar filaments. While QS filaments have usually similar properties, AR filaments show a very wide range of inferred magnetic field values. Previous studies reveal the following pattern: filaments located above highly magnetized regions (Kuckein et al., 2009; Xu et al., 2012) present Zeeman-like profiles in linear polarization and have a much larger value of the magnetic field (∼700 G) than those above the granulation (∼100 G Sasso et al., 2011; Xu et al., 2012), whose Q and U signals are below the noise level. The lack of scattering polarization signals in their observed Stokes parameters sparked the proposal of new mechanisms to theoretically explain this absence: a reduction of the anisotropy by the horizontal illumination within the filament (Trujillo Bueno & Asensio Ramos, 2007) or the presence of a microturbulent field (Casini et al., 2009a). We have explained the lack of atomic polarization signatures in the Stokes profiles found in Kuckein et al. (2009) using a two component model without the need to reduce the incoming radiation anisotropy. In such a situation, the Hanle contributions of both atmospheric components can be mutually cancelled. From a two components inversion, we have proposed that AR filaments could present weak fields, while the highest inferred values for the magnetic field are produced by the active chromosphere below, and not in the filament itself. This first result shows that the inferred magnetic field is model dependent and opens a debate on the real value of the field of such structures.

In Chapter 4 we have discussed the analysis of GRIS spectropolarimetric observations from the GREGOR telescope in the He I 10830 Å triplet taken in an active region filament. In this chapter we have used a single component inversion (as it was used in the previous studies) to retrieve the physical parameters from the polarimetric signals. This approach is justified by the fact that the observed filament was lying above the granulation so, the expected contamination from below is reduced. In spite of that, we have found again some limitations of using a single component model, obtaining in some cases unrealistic/inconsistent results. By using simple numerical experiments we have demonstrated that the filament is almost transparent to the circular polarization generated below. Therefore, its analysis as a signal coming from a unique structure leads to discrepancies, such as assigning high magnetic field strengths to the filament. We have also found other observational clues clearly pointing towards the necessity of a more complex atmosphere. We have found in the linear polarization signals of the filament the same sign in the blue and red components, which points towards the presence of radiative transfer effects. We have also found clues of the presence of strong gradients in the magnetic field. Finally, in an effort to study the feasibility of two-component inversions, we have shown that the model contains too much flexibility and it can reproduce better the observations (than a single component model), but a high number of compatible solutions are found, making the interpretation very complex.

In the previous analysis we have also applied the Bayesian framework to explore the multiple magnetic field configurations compatible with the Stokes profiles. We have studied the sensitivity/correlation of some physical parameters. In particular, we have found that the filament height cannot be inferred from the observations (at least with our noise level) due to the low sensitivity of the profile to its variations, as well as its degeneracy with other parameters.

In Chapter 5, we have discovered the potential of the Ca II 8542 Å for filament diagnostic, with the unprecedented spatial resolution of the CRISP instrument installed at the SST. In this chapter, the picture inferred from the observations is the presence of a cold and dense plasma similar to the standard picture of a solar filament described in the literature. But since these structures are thought to be held against gravity by the magnetic tension force, the typical approximation of hydrostatic equilibrium (commonly used in the inversion code we use) does not apply anymore. This causes a degeneracy between temperature, density, and geometric height that we cannot solve (using only this spectral line). The inferred magnetic fields are limited to the longitudinal component since we do not detect linear polarization signals above the noise level. We estimate an upper limit for the field strength of $\sim$260 G. For such low field strengths, we expect that the signals would be generated by the joint action of the Hanle and Zeeman effect (Štěpán & Trujillo Bueno, 2016), but still we need a larger signal-to-noise in the observations to detect then and to obtain reliable measurements. In such a case, we should include scattering processes and the Hanle effect to properly understand and interpret future observations.

6.2 Conclusions and future work

The He I 10830 Å and the Ca II 8542 Å spectral lines are good candidates for studying chromospheric structures. However, their diagnostic capabilities (even being better than of other lines) are still limited. Multi-line inversions is the key to bring together the advantages of each spectral line and help breaking the degeneracies of the inverse problem. Multi-layer observations with new space telescopes and future ground based facilities, such as DKIST and EST, will perfectly complement the various available telescopes and substantially improve our understanding of filaments. Recent studies (Casini et al., 2009b; Anan et al., 2014; Schwartz et al., 2016; de la Cruz Rodríguez et al., 2016b; Quintero Noda et al., 2017a) have shown the great utility of including several lines in the same analysis from different telescopes, such as He I 10830 Å, Hα 6563 Å, Ca II 8542 Å, Fe I 6302 Å, Mg II h&k, Mg II UV triplet, H I Paschen Lines, and He I D_3. This would also help overcome insensitivity problems of the chromospheric lines (and in particular for Ca II 8542 Å) to the temperature minimum region in which molecular lines such as H_2, CO, OH or TiO or even ALMA observations are specially sensitive (Wenzel et al., 2010; Avrett, 2003; Leenaarts et al., 2011).

Although multi-line inversions may be a good new strategy, there are other factors to consider in the inversion process. For example, having more spectral lines does not guarantee always a better result (see for example the case of the Fe I 6301 Å and 6302 Å lines in Asensio Ramos et al. 2007). Also, a good inversion strategy is essential to obtain not only a good fit but also to avoid unrealistic or local minimum solutions. We show in this thesis how to properly carry out inversions in chromospheric lines approaching the solution robustly. This is specially more important when the complexity of the models increases.

Stereoscopic observations are also of great help to estimate geometrical properties since, as we have shown, it is not possible to obtain information about the height by a spectropolarimetric analysis of the He I 10830 Å or Ca II 8542 Å signals. Therefore, this work leaves open the question of whether the filaments are isolated structures lying at several Mm above the surface or are otherwise embedded in the chromosphere at lower heights. Multi-layer and multi-point of view observations could serve to estimate the thermodynamic characteristics of solar filaments with much more precision.

We have seen that AR filaments can evolve unexpectedly in a very short period of time. Their short lifetime and constant evolution makes it difficult to increase the cadence of the observations. Another related point that still remains to be analyzed is the identification of transversal motions or oscillations in the filament. Both phenomena have important implications in terms of the stability of the filament itself. All these ingredients make a temporal study difficult but necessary to answer questions about the formation of the filaments and whether the material is lifted from the surface or, on the contrary, is formed by condensation. These and many questions will continue to be of great importance for a good understanding of these structures.

Throughout this thesis we have emphasized the need to include new ingredients in the modeling such as the polarized background illumination when we have absorption structures above the disk, radiative transfer effects, etc. But a more complicated model implies a larger parameter space, so more work needs to be done in order to improve the inversions, e.g., using the full field of view to constrain the model parameters. Moreover, to perform reliable inversions we need high precision spectropolarimetric observations. A limitation in our study is the presence of a high level of noise in the polarization signals, which made us sacrifice the spatial resolution to improve the signal to noise ratio of the data. In the near future, we foresee more complex models for the inversions and we aim at deciphering the fine structure of the magnetic field in solar filaments/prominences, hence we can no more sacrifice the spatial resolution. Very high polarimetric sensitivity, unprecedented spatial resolution, together with multi-line observations are the foundations of the future EST telescope, which will provide us with a unique ability to solve many of the questions we have opened up during this thesis work.

A

Appendix of Chapter 4

In this Appendix we detail some relevant numerical experiments that are slightly outside the focus of the filament study. Among them, a detailed flare analysis, the calculation of the spatial resolution from the GREGOR images, and the same results for the rest of maps not showed in the chapter 4, such as the polarization maps.

A.1 Location of the observations on the solar disk

To contextualize and invert the data correctly it is necessary to establish the precise location of the observations on the solar surface. For this purpose, we move, rotate, and scale the continuum map of the observations to match a continuum image of the same area taken by SDO/HMI in the middle of the scan. To find the parameters of the image deformation, we optimize a merit function (the difference of the continuum images) using the DIRECT algorithm. The result of this accurate location is shown in the table A.1. The importance of this process lies in the correct configuration of the reference system to interpret the signals measured in the spectral line of He I 10830 Å (see Sec. 4.2). Figure. A.1 outlines the observations perfectly located above the SDO/HMI map.

Table A.1 – Location parameters of each scan obtained by DIRECT. The rotation angle is defined clockwise from the W-E axis.

#	time [UT]	x [″]	y [″]	rot [deg]	μ=cosΘ
I	08:23 - 08:41	175.91	-341.03	21.19	0.92
II	08:41 - 08:59	178.70	-340.29	17.21	0.92
III	09:13 - 09:27	185.87	-324.12	9.61	0.92
IV	09:27 - 09:46	187.95	-324.70	5.54	0.92
V	09:46 - 10:04	190.82	-325.08	-0.10	0.92
VI	17:17 - 17:36	252.15	-327.66	35.90	0.90

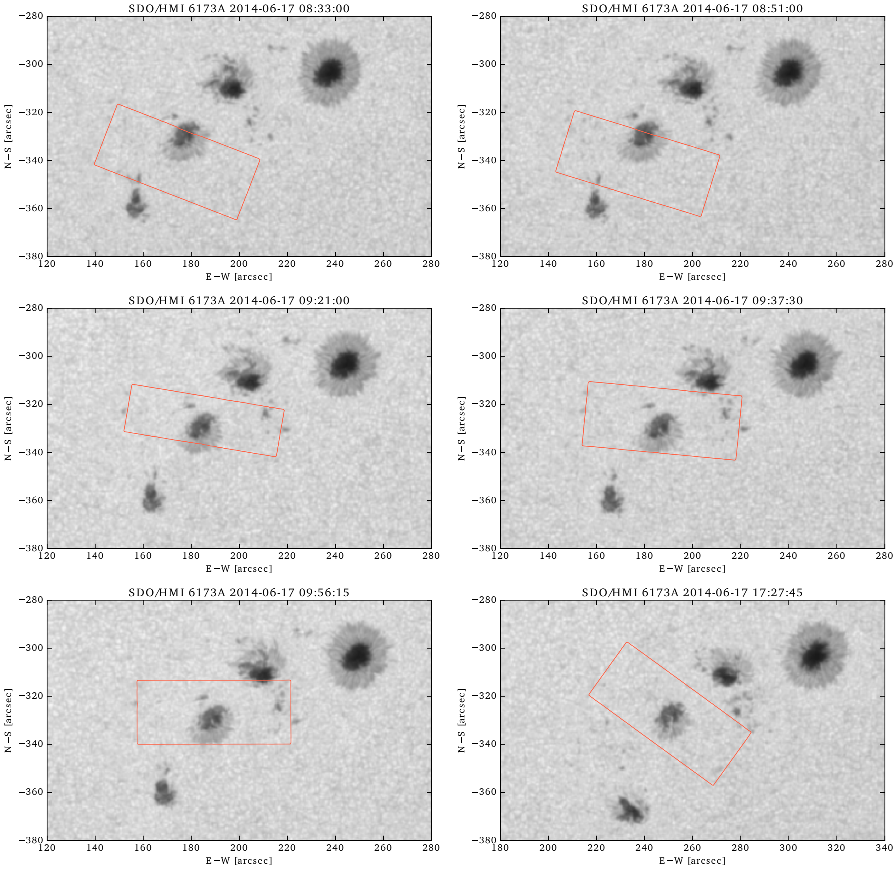

Figure A.1 – All observations are located in the solar disk by comparison with SDO/HMI images. The contours of the observed maps are displayed on the HMI images taken at the middle of each scan.

A.2 The reference for linear polarization

As we have mentioned in Sec. 4.3.3, we need to find the reference direction for positive Stokes Q in the observations. For that, we have calculated the γ angle for all the scans indicated by the direction of e_1 in Fig A.2. In this figure, the title indicates the $Q > 0$ direction from the direction of the slit (H), and DC points to the disk center. As we have chosen the projection in the plane of the sky our X axis in the radial direction, the γ has to be measured from $-$DC. This number is quoted in the bottom part of each panel.

A.3 Image spatial resolution

To calculate the spatial resolution of the images obtained by GREGOR it is usual to use the power spectrum of the continuum image. The power spectrum measures the amount of "energy" of each spatial frequency,

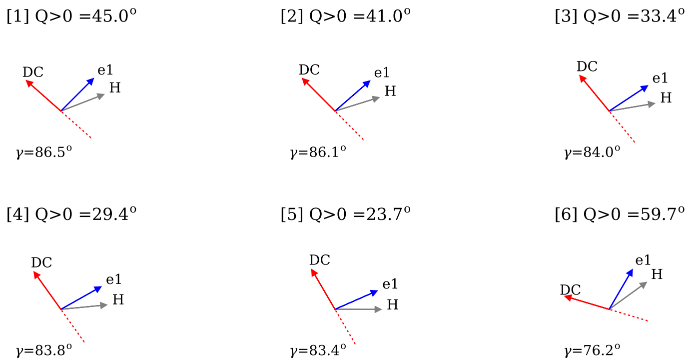

Figure A.2 – Relevant directions for each scan, where H indicates the direction of the slit, DC points to the disk center, and γ angle measured from $-$DC.

which in our images can be expressed as the contribution of each scale in image formation. In case of a noisy randomly generated image it will have a flat spectrum as its power will be spread over all scales. Therefore, we estimate that the spatial resolution of the observations by the intersection of a flat spectrum generated by a noise image and the behaviour at bigger scales. Lower scales than this point are almost noise. This value is marked with a vertical line in Fig. A.3. We estimate that the resolution of the images is around $\sim$4 pixels, which implies a resolution of $\sim$0.56″as the sampling is $\sim$0.14″/pix.

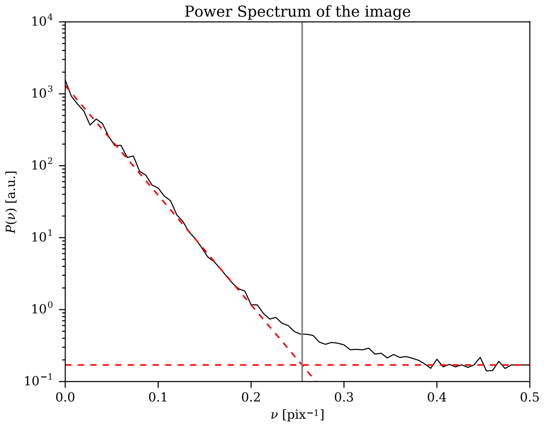

Figure A.3 – Power spectrum of the observations at the continuum intensity. We estimate the resolution of the images by the intersection of a flat spectrum (of an image generated with only noise) and the behaviour at big scales, around $\sim$4 pixels which implies a resolution of $\sim$6″.

This value looks reasonable as the image has a minimum theoretical resolution at this wavelength of 0.2″(see Sec. 2.5.1 for more details) and by visual inspection it can be binned by a factor 2 without losing resolution.

A.4 Flare analysis

Understanding the magnetic field configuration in dynamic solar events such as flares is an unsolved problem in solar physics. Flares are hard-to-predict events (Liu et al., 2017) and are the result of a global change in the magnetic field topology. These changes mainly happen in the chromosphere and corona. Therefore, full-Stokes polarimetric observations of flares, especially including the chromosphere, are essential. They are, however, challenging. Many previous studies have focused on the photospheric magnetic field underneath flare events or their seismic waves if they are stronger (Kosovichev, 1999). It seems clear that changes happen in the photospheric magnetic field during flares. However, it is controversial whether these variations are either associated with an increase or a decrease of the magnetic field strength.

There are several recent studies (see table A.2) on flares in active regions with filaments observed in the same spectral range. For example, Sasso et al. (2007, 2011, 2014) studied an active region filament during a flare of GOES class C2.0 where they found high speeds (upflows up to 60 $\mathrm{km\,s^{-1}}$ and downflows up to 100 $\mathrm{km\,s^{-1}}$). On the other hand, Judge et al. (2014) observed a much more energetic event of class X1.0 estimating that such intense flares can penetrate up to 100 km above the photosphere as they infer from the modeling of the Si I line. They also derive an increase of the photospheric magnetic field comparing the inferred maps before and after the flare. They had a compact filament close to the flare, that erupted after it. Finally, the most recent study of Kuckein et al. (2015) covered the pre-flare, flare, and post-flare phases of an M3.2 class solar flare. Their photospheric Si I inversions revealed that the magnetic field strength in the photosphere decreased during the flare phase, but this decrease was not permanent and, after the flare, the magnetic field recovered its pre-flare configuration (and the same happened with the velocities).

In this section we show the analysis of the FOV before, during and after the development of an B4.5 flare, deriving the magnetic and dynamical conditions at photospheric layers. However, comparing the power of previous studies with the flare of our region it seems difficult to see any impact in our spectral lines. A summary of some important parameters of the observations are detailed in the table A.2 below.

Table A.2 – Summary of flare parameters of several studies and a comparison between their power released in the GOES filter-band. The ratio of the flux measured in the X-ray range is calculated respect to this work.

Study	GOES class	Lines affected	$I(\mathrm{He\,I})/I_c$	X-ray flux [W/m^2]	Ratio
Judge et al. (2014)	X1.0	Si I+He I	2.0	$1.0 \cdot 10^{-4}$	220
Kuckein et al. (2015)	M3.2	He I	1.86	$3.2 \cdot 10^{-5}$	71
Sasso et al. (2011)	C2.0	He I	1.15	$2.0 \cdot 10^{-6}$	4.5
This work	B4.5	–	–	$4.5 \cdot 10^{-7}$	1

In the following sections we will analyze the impact of the flare at different heights, at the photosphere with the silicon line, at the chromosphere with Hα, and finally at the corona with SDO/AIA.

A.4.1 Event at the photospheric level

In this section we tried to identify any signature of the flare in the Si I line. The flare began around 09:39 UT, at about the time the GRIS slit crossed the flare. The photospheric Si I line shows bright points in the flare area. Fig. A.4 shows an image of the core of the silicon line in the third scan with a horizontal line indicating when the flare started.

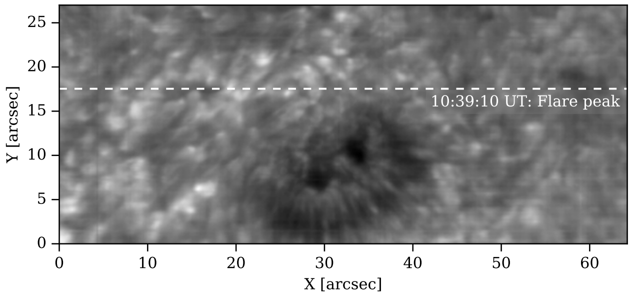

Figure A.4 – Image in the core of the Si I line of the third scan. A horizontal line indicate when the flare started. The time increases in the vertical direction.

From a quick inspection we did not find any correlation with the location of the flare or with the filament. This may be reasonable since a flare as weak as this may not penetrate the photosphere as in Kuckein et al. (2015), where the Si I line never was found in emission.

However, even if we do not find anything clear in the intensity profile we could see the changes in the magnetic field in the photosphere. This line was inverted as it was shown in Sec. 4.3.3. In the following, we focus on the inferred magnetic field strength and the LOS velocity patterns at $\log(\tau) = -2.2$ (Felipe et al., 2016) which is displayed in Fig. A.5.

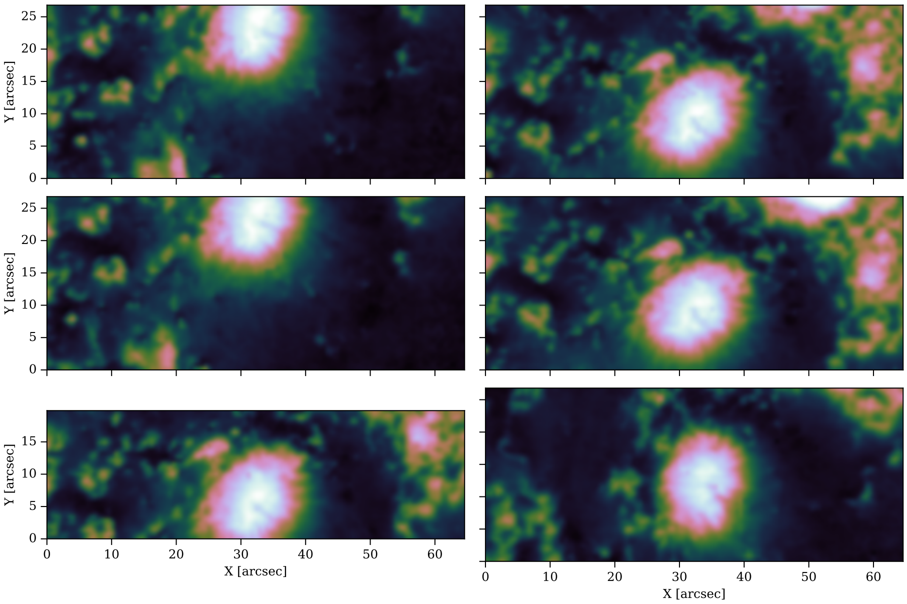

Figure A.5 – Magnetic field inferred from the Si I line at $\log(\tau) = -2.2$. All maps share the same color scale saturated between 1 and 3 kG. See Fig. A.6 for the color scale.

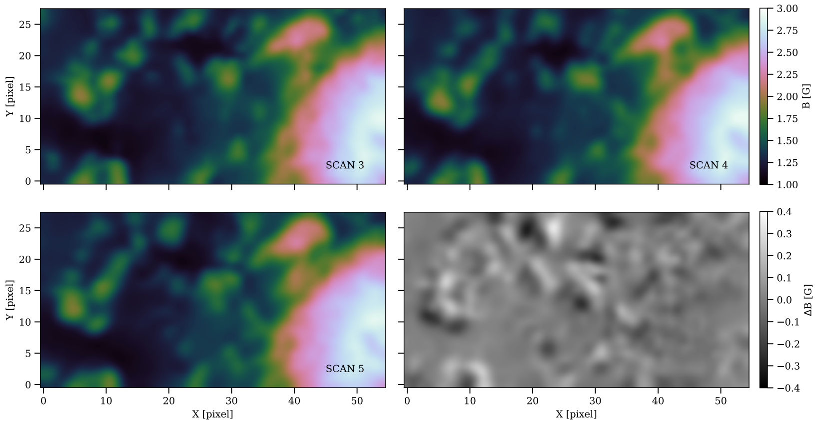

Figure A.6 – Aligned images of the magnetic field inferred at the pre-flare, flare and post-flare state. All maps share the same color scale saturated between 1 and 3 kG. The difference between the pre and post flare state is saturated at ±400 G in the right bottom panel.

Due to the rotation of the field we have to align the images (see Sec. A.1) and calculate the differences between them. The result is shown in Fig. A.6. It displays the three scans aligned and the difference between the pre and post flare state. The figure is saturated at ±400 G, then these values are well below the 1500 G found by Kuckein et al. (2015). We cannot really detect a signature of lower magnetic field strengths due to the flare as these differences could be due to the lack of the derotator in the telescope and the evolution of the active region. Moreover, doing a histogram of the region the distribution is very symmetric, which stresses out our result. Therefore, we do not see any particular pattern or region with a relevant change. In the velocity map it is even more difficult to detect a clear behaviour as other studies have found velocities between 0.1 and 0.3 $\mathrm{km\,s^{-1}}$ and we do not reach this precision (Kuckein et al., 2015; Judge et al., 2014).

A.4.2 Event at the chromospheric level

For studying the event at chromospheric heights, we have used the Hα 6562.8 Å line. To do this, the National Solar Observatory (NSO) telescope of the Global Oscillation Network Group (GONG) provides full-disk observation of the Sun at this line. The spatial sampling of $\sim$1″/pix is very poor but is compensated with the high cadence of 1 minute. This low resolution makes it impossible to accurately study the evolution of the filament with GONG because it is barely visible.

Because our observations are not really monochromatic images at the same time but a slit that moves across the solar surface, we have used the high temporal resolution of the images to make a "GONG raster" simulating what it would have recorded with a slit instrument like GRIS. For each solar coordinate of a GRIS raster step, the GONG reconstructed intensities at that time and location were saved in a new map. Then, we superpose our scans as contour images above the reconstructed Hα map (Fig. A.7).

We have performed this exercise to check that we still see the filament in absorption, since as shown in Fig. 4.3, it was impossible to distinguish it in the SDO/AIA filters. In these images, outside the contours of the filament, the area appears enhanced, possibly due to heating caused by magnetic reconnection events. In fact, the most peculiar aspect is that, during the flare, the brightening occurs confined between the filaments, as if the magnetic structure of the filaments itself was confining the heating region. In other studies we have also seen filaments close to a flare that have not been affected by this released of energy (Kuckein et al., 2015).

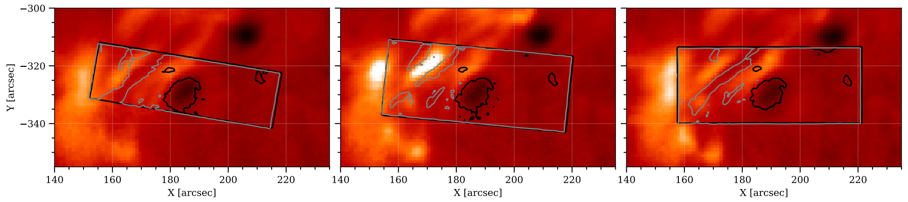

Figure A.7 – Reconstructed Hα maps for the FOV of our filament using data from the NSO/GONG observatory.

Another chromospheric perspective of the area is obtained using information from the HINODE observatory. HINODE takes broadband images on Ca II H line centered at 3968.5 Å with a bandwidth of 3 Å, and spatial sampling of 0.054″/pixel. In Fig. A.8, we still see signs of chromospheric heating, but not of the presence of the filament which may have its formation at higher altitudes above the height of formation of this Ca II line.

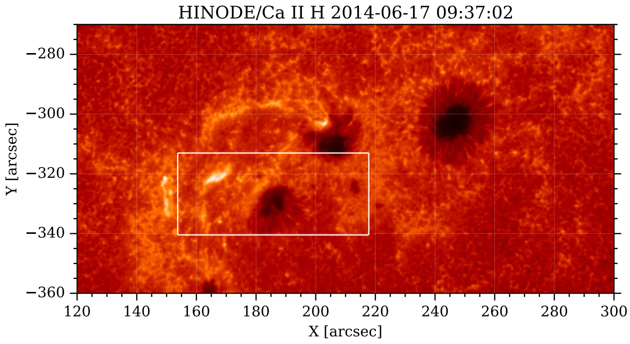

Figure A.8 – Image from the HINODE observatory in the Ca II H line at the same time the flare released.

A.4.3 Event at coronal levels

Finally, we can see the filament evolution with the SDO/AIA filters. Figure A.9 shows pictures of pre-flare, flare, and post-flare phases.

Each image was obtained at the same time that our third, fourth and fifth scan. From the left column, we can see a loop structure linking the first and the third sunspot (left to right). The middle column was obtained at 09:39 UT when the flare began. As we can observe from the evolution, the energetic event released at the middle point of the loop (and probably also the higher) around X=+170″, Y=−320″. Most of the brightening features moved to the outer ribbons. Then, the energy of this localized reconnection event is quickly transported to the outer part of the region. In the right column we still see the bright ribbons because the flare is still there, in its decaying phase.

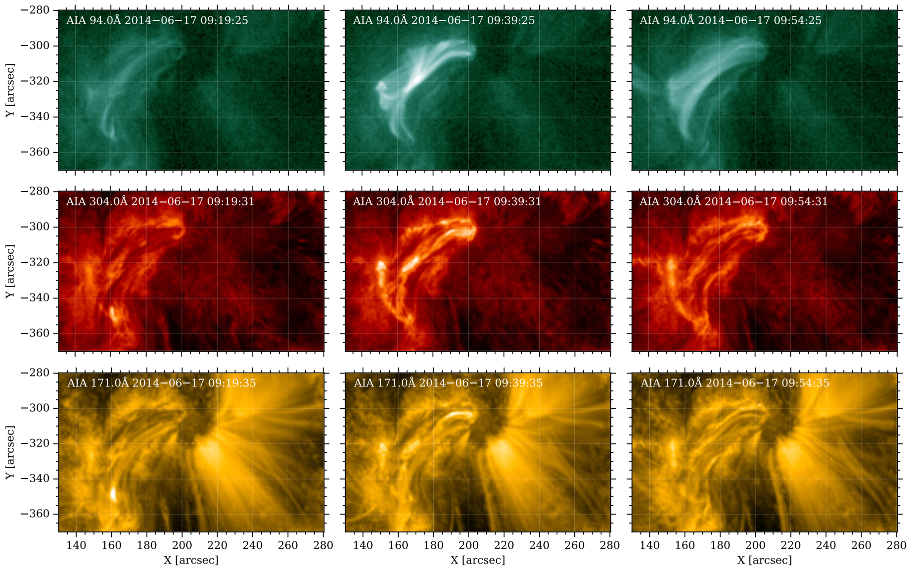

Figure A.9 – SDO/AIA images at 94 Å, 304 Å and 171 Å of the pre-flare, flare, and post-flare phases, from left to right.

A.5 STEREO observation

In this thesis we have dedicated several sections to the importance of filament height (e.g. Sect. 4.5.4) and how to infer it. When the observed structure is off the limb, imaging techniques can be used to estimate the height. On the contrary, the case of on-disk observations we have to used other ways to have an estimation and *Solar Terrestrial Relations Observatory* (STEREO; Kaiser et al., 2008) is one of them. STEREO consists of two space-based observatories designed to get a 3D view of the Sun. For example, Schad et al. (2016) used STEREO observations to stereoscopically triangulate their loop geometry.

To see if it was possible to use a similar technique in our observations, we used the official website `stereo-ssc.nascom.nasa.gov/where.shtml` to calculate the orbit position of each STEREO during the observations[1]. The results form the locations is shown in Fig. A.10. This figure shows that they were in the hidden side of the sun these days. Then, we could not use them to calculate the height of the filament. Anyway, if our filament was located at a lower height, it could be mixed with the spicules and could not be detected.

A.6 Noise effect in the ratio of the Stokes V of the components

When we computed the ratio of the amplitudes (calculated in the red lobe) of the Stokes V of the red and blue components in Sec. 4.6.3, we detected small values in the polarity inversion line. As the amplitude of Stokes V in the PIL is very low, we were thinking whether this effect was real or caused by the noise. To address this question we did a synthetic experiment. In this experiment we generated two quantities

---

[1] Communications with Solar Terrestrial Relations Observatory-B (STEREO-B) were lost on Oct. 1, 2014, due to multiple hardware anomalies affecting control of the spacecraft orientation.

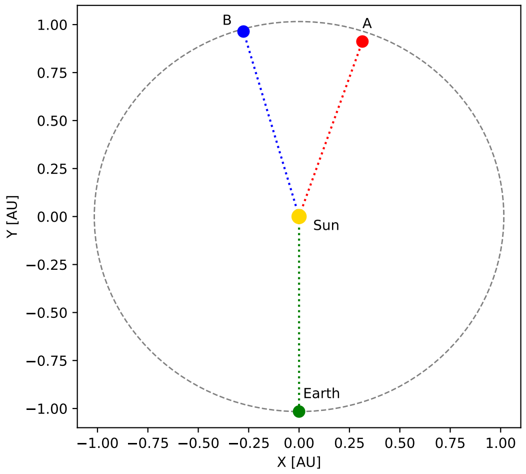

Figure A.10 – Position of each STEREO observatory respect to the Earth at 17th of June of 2014.

whose original ratio was 3 but adding different levels of noise. We calculated the new ratio including this noise and it is showed in Fig. A.11. This figure shows that the ratio is 1 in the limit of noisy signals. Calculating the median value of several realizations, we have delimited our confidence in 1.5σ, that is, the point from which the median and the original value coincide.

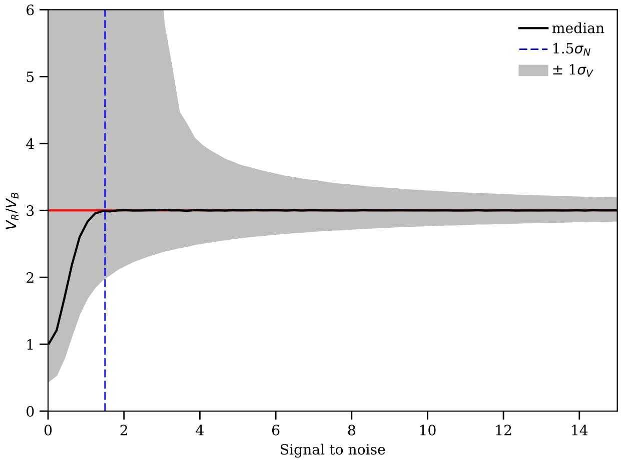

Figure A.11 – This figure shows the result of an experiment to evaluate the influence of the noise in our ratio. In this experiment we have generated two quantities whose original ratio was 3 but adding different levels of noise. We have calculated the ratio including the noise and we have delimited our confidence within 1.5σ

A.7 Saturation in Stokes V

In Sec. 4.6.3, we computed the ratio of Stokes V amplitudes of the red and blue components[2] and detected a decrease of this value inside the filament. We synthesized one profile with HAZEL (displayed in Fig. 4.26) demonstrating that this is due to to the high optical depth of the red component. With the aim of generalizing the previous result, we have partially covered the space of parameters of the previous experiment by modifying the magnetic field strength and the optical depth in different ways and using a single or two component model. We create four cases:

- The first case, referred as $\mathrm{X} = \mathrm{B_T}$, is a one component model with $\theta_B = 90°$, $\phi_B = -45°$, and $\tau = 1.2$ where the magnetic field strength changes between $[0, 1000]$ G.
- The second case, designated as $\mathrm{X} = \mathrm{B_1}$, is a two component model with $\theta_{B1} = 90°$, $\phi_{B1} = 0°$, $\tau_1 = 0.3$, $B_2 = 10$ G, $\theta_{B2} = 90°$, $\phi_{B2} = -45°$, and $\tau_2 = 1.2$, where the magnetic field strength B_1 changes between $[0, 1000]$ G.
- The third case, referred as $\mathrm{X} = \tau_\mathrm{T}$, is a one component model with $B = 300$ G, $\theta_B = 90°$, and $\phi_B = -45°$, where $\tau \in [0, 2.5]$.
- The fourth case, referred as $\mathrm{X} = \tau_2$ is a two component model with $B_1 = 300$ G, $\theta_{B1} = 90°$, $\phi_{B1} = 0°$, $\tau_1 = 0.3$, $B_2 = 10$ G, $\theta_{B2} = 90°$, $\phi_{B2} = -45°$, where $\tau_2 \in [0, 1.7]$.

Figure A.12 shows the amplitude ratio between the Stokes V profiles of the red and blue components, normalized to the maximum value of each case. For simplicity, the same horizontal axis is used for all quantities by normalizing each parameter.

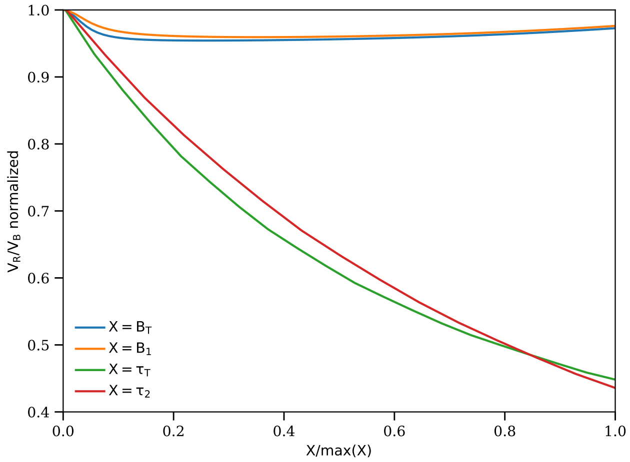

Figure A.12 – Change in the ratio normalized V_R/V_B with the variation of the magnetic field and the optical depth in a single (B_T,τ_T) or in two atmospheric component model. The ratio is almost constant with the variation of the magnetic field, but it decreases with the variation of the optical depth. The behaviour of the lines does not allow to distinguish between a single o two component model.

---

[2] Be careful, we are not referring to the ratio between the amplitudes of both lobes of the same Stokes V profile.

From this figure we can conclude that the ratio does not appreciably change with the magnetic field of the whole slab or only the lower slab in the second case. On the contrary, a significant change occurs when the optical depth changes. Moreover, this change has a similar behaviour for a single or two slabs. This means that Stokes V does not add much information to discern whether we find one or two components along the LOS.

A.8 Inversions of the fast component

In Sec. 4.4.4 we showed the LOS velocities obtained from the inversions. At both sides of the filament downflows are found with velocities larger than 20$\mathrm{km\,s^{-1}}$. These pixels also show several (at least two) components well separated in velocity in Stokes V and Stokes I. For example, in the fifth scan we found redshifts around 25$\mathrm{km\,s^{-1}}$ in the left border (pixel [12, 27]; Fig. A.13) and around 21$\mathrm{km\,s^{-1}}$ in the right border. In the sixth scan, we found stronger velocities values, around 35$\mathrm{km\,s^{-1}}$, at the same points after 15 minutes.

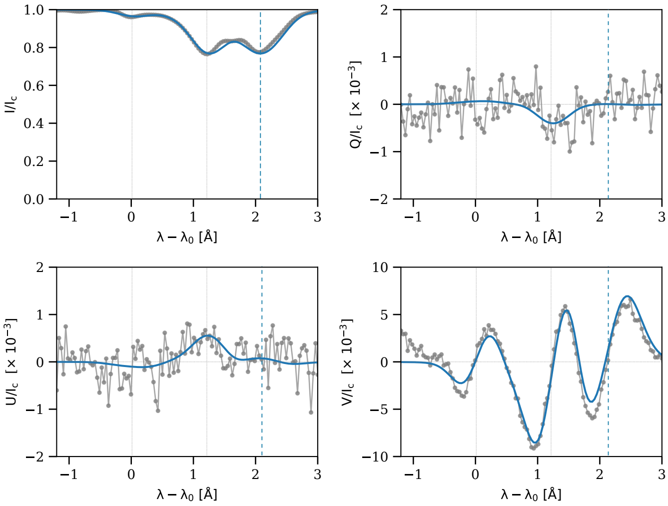

Figure A.13 – Observed and best-fit He I 10830 Å profiles. Two components have been used to fit the second red-shifted spectral line. A blue dashed line indicates the center of the fast component.

To reach these velocities, in free fall ($g_\odot$ ~0.3 km/s^2), the material has to fall during $t = v/g_\odot$=100 s, which corresponds a travelled distance of $x = 0.5 g_\odot t^2$= 1500 km. This velocity is damped in the photosphere because of the increase in density along 1000 km (González Manrique et al., 2017). From that, we could estimate a lower limit for the height of the filament in ~2500 km.

A.9 Helium absorption

In Sec. 4.2.2 we have explained the evolution of the filament during the observations. However, it is interesting to examine the same maps only in terms of the absorption of the He I line. Figure. A.14 displays the same six scans as Fig. 4.5 but after the normalization procedure of Sec. 4.3.3. This figure shows more clearly the complex fine structure of the filament and its surroundings. Probably, the clearest difference with its twin figure (Fig. 4.5) is the absence of the sunspot (located at X = 30″), as this spectral line shows identical absorption. This explains why sunspots are almost invisible in other studies (Penn & Kuhn, 1995).

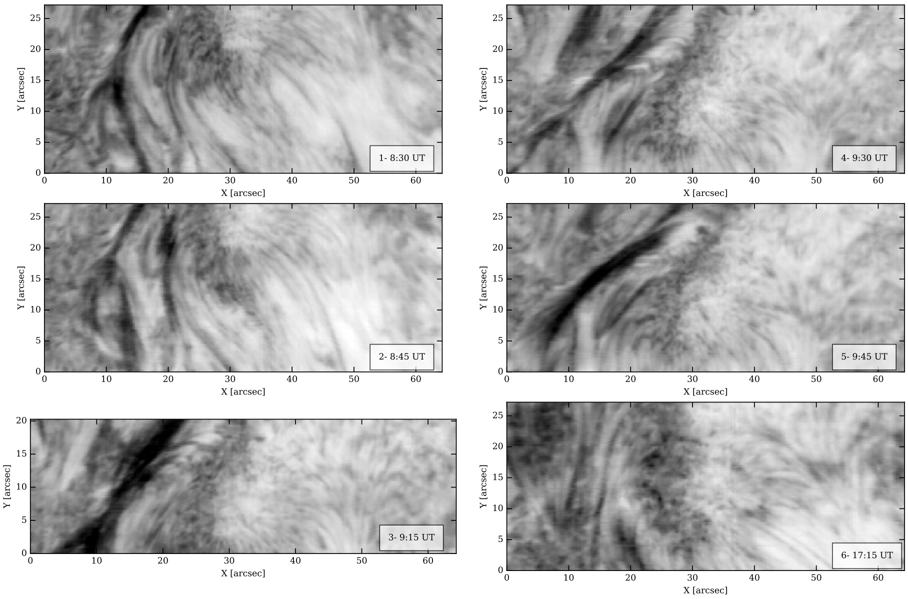

Figure A.14 – Absorption in the red component of the He I multiplet at 10830 Å relative to the local continuum.

A.10 Saturation of the red component

In Sec. 4.6.1 and Sec. 4.6.3 we were studying the consequences of the saturation effect in the red component. To see this in a easier way, we displayed in Fig. A.15 the area amplitudes of the blue versus the red component for all pixels in the field of view. The relation deviates from the linear trend (red line) for sufficiently high optical depths. To have an estimation of where does this transition happen, we made a simulation (shown as a green line) with Hazel (similar to Fig. 8 Centeno et al. (2008) but in absorption). We generate profiles with different optical depths and compute the growth curve (green solid curve). It nicely agrees with our data when the optical depth is below 1.5, and then the synthetic curve describes an "upper limit" for the data. It was mentioned in Sec. 4.6.1 that the blue component is usually deeper than the proposed absorption, and an extra ingredient is necessary to explain these profiles, which obviously coincide with the filament region.

A.11 Extra material

For completeness, we have hosted all the figures which include other scans and their products (such as the inversions, ratios, etc.) in the following link: `https://github.com/cdiazbas/thesis`. We have not

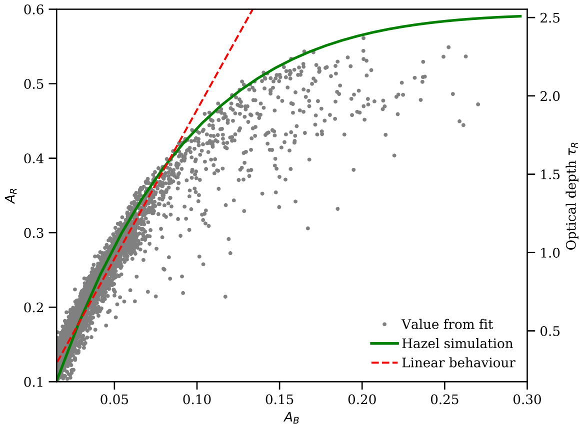

Figure A.15 – Relation between the red component amplitude (A_R) and the blue component amplitude (A_B). A linear trend is drawn with the data, showing how around $0.4A_R$ the profile starts to saturate.

included them in the thesis due to the similarity of those discussed in the main text. An example of this is Fig. A.16 where it is displayed the linear polarization signals in the blue and red component, showing the same behaviour of that shown in Fig. 4.21.

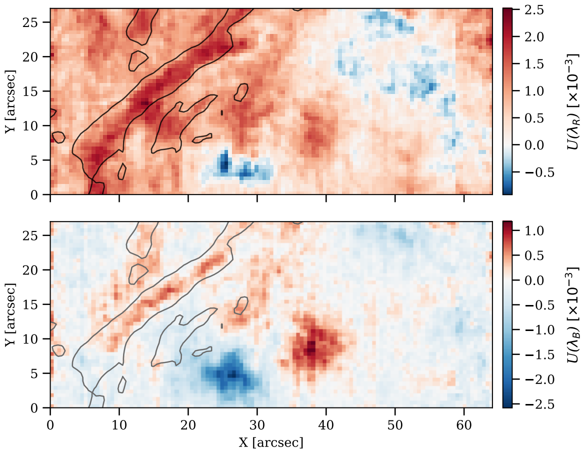

Figure A.16 – Stokes $U(\lambda_R)$ and $U(\lambda_B)$ of the fifth scan. A grey contour at 0.6I I_{LC} shows the position of the filament.

B

Appendix of Chapter 5

In this Appendix we detail some relevant numerical experiments that are slightly outside the focus of the filament study. Here we explore the sensitivity of the line of Ca II 8542 Å to atmospheric parameters, the importance of the location of the nodes in the inversion process and the suggestion of the line of Ca I 4227 Å as a complementary line.

B.1 CHROTEL intensity profiles

In Sec. 5.3.5 we discussed the LOS velocity maps inferred form the He I 10830 Å and Ca II 8542 Å lines and their differences. They indicated the presence of the draining of the neutral material from the filament, as other studies have shown (Khomenko et al., 2016).

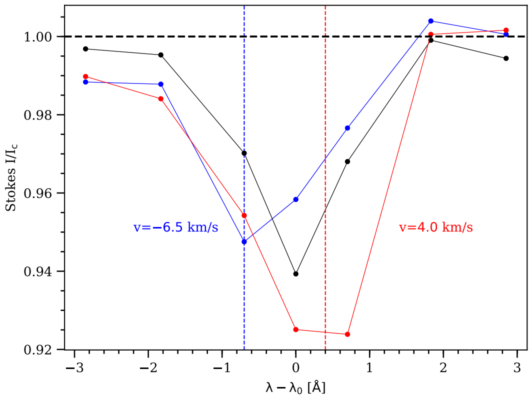

Figure B.1 – Three intensity profiles extracted from the upper left part (blue), center(black) and lower right part (red) of the filament. The reference for λ_0 is the center of the He I red component at 10830.3 Å.

In this section we present some examples of the profiles taken with CHROTEL. The spectral line is only mapped at 7 points, which is enough for a rough estimation of the velocity (Bethge et al., 2011). Figure B.1 displays three profiles extracted from different locations: from the blueshited "tail" (showed in blue), from the center of the filament (in black) and from the redshifted part (showed in red) in Fig. 5.11 of the main text. From these profiles upflows of ∼7 $\mathrm{km\,s^{-1}}$ can be measured (comparing with the ∼4 $\mathrm{km\,s^{-1}}$ measured in the Ca II 8542 Å) and downflows of ∼5 $\mathrm{km\,s^{-1}}$ (comparing with the ∼0 $\mathrm{km\,s^{-1}}$ measured in the Ca II 8542 Å). This is an indication of the nature of the neutral material and its relation with the magnetic field with respect to the ionized calcium material.

B.2 Wave propagation

In Sec. 5.3.6 we discussed the plane of the sky velocity map inferred using the LCT method. In this appendix we present some indications pointing to the presence of wave propagation in the region. To this end, we show in Fig. B.2 the temporal evolution of the intensity fluctuation at the core of the line during the whole scan. These profiles show a oscillatory behaviour with periods between 3 and 4 minutes. This behaviour is not only present near the plage but also at the edges of the filament. Since we only have 36 points in the time axis, it is difficult to carry out a precise study.

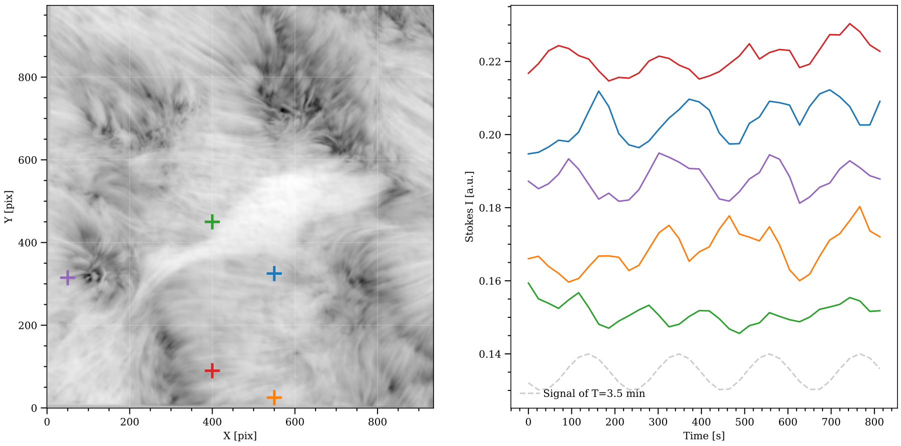

Figure B.2 – Time evolution of the intensity at the core of the line of several points of the region. A example of a signal of period 3.5 minutes is displayed at the bottom of the right panel.

B.3 Response functions of the Ca II 8542 Å line

In this section we want to show the sensitivity of the Ca II 8542 Å line to the changes of some physical parameters via the response functions (Quintero Noda et al., 2016) using the inferred models from the inversion process. The response functions (RF) provide information about the sensitivity of a spectral line to a perturbation in a physical parameter of the solar atmosphere, and it can be written as the derivative of the profile to a physical parameter:

$$R_X(\lambda, \tau) = \frac{\partial I(\lambda)}{\partial X(\tau)} \,. \tag{B.1}$$

These RFs depend on the heliocentric angle and on the model itself, therefore, that the conclusions extracted from this may not be general. Moreover, they can be calculated for each Stokes parameter. We calculate the RF using a finite difference by perturbing to the physical parameters of the model atmosphere.

Given the model, we compute the emergent intensity of a modified version where a perturbation $\delta X(\tau)$ is introduced in the parameter $X(\tau)$. Then, a larger difference in the emergent intensity $\delta I(\lambda)$ indicates a larger sensitivity of this physical parameter to this optical depth range. A small value indicates that the uncertainty in this region is very large, i.e., we cannot retrieve reliable information of the physical parameter from this region.

B.3.1 Temperature

The first physical quantity studied is the temperature. Since we want to isolate the effect of the temperature, we do not update the density through the HE. We have perturbed the initial model with 10 K (which in relative terms is ∼0.14%) at each atmospheric point. The result of this calculation is displayed in Fig. B.3.

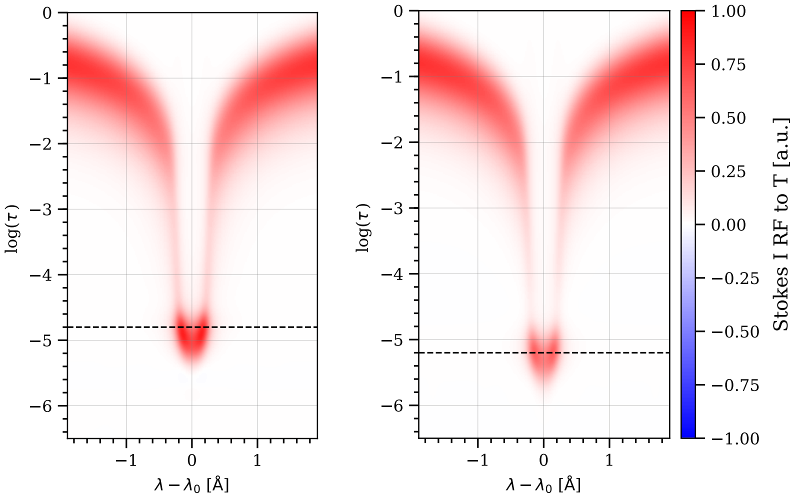

Figure B.3 – Left panel: response function of the Ca II 8542 Å to the temperature from a QS model. Right panel: the same as before but using the average model inferred in the filament. Horizontal dashed lines indicate the position of the maximum of the RFs.

The figure demonstrates that the wings are very sensitive to low heights. On the other hand the core has a peak around $\log(\tau) = -5$ with the well known reduced sensitivity around $\log(\tau) = -4$ (Quintero Noda et al., 2016). The RF falls to zero above $\log(\tau) = -6$ and below $\log(\tau) = 0$ (for wavelengths very close to the continuum). This means that we will not be able to infer accurate information in these layers.

The RF shows that an increase in the temperature produces also an increase in the intensity profile. We also want to note that the filament model has a sensitivity in the core that is 1.2 times lower than the QS model.

B.3.2 Gas Pressure

In this section we show the sensitivity of this line to changes in gas pressure. According to our knowledge, this is the first time that these results are shown, as pressure (or density) is generally not a free parameter of the problem and therefore its sensitivity is coupled to temperature through hydrostatic equilibrium. To decouple this effect, we have calculated the response functions in no-HE. Given its large variation throughout the atmosphere, we use relative perturbations of 10 % for computing the response function. The result is shown in Fig. B.4.

The sensitivity of this line to the gas pressure is concentrated at chromospheric heights around $\log(\tau) = -5$, being 7–8 orders of magnitude more sensitive than to the photospheric conditions ($\log(\tau) = -1$). In order to enhance this photospheric part we have displayed only the changes in intensity (and not the ratio with the perturbation). Since they share the same axis of scales and are normalized to the maximum, we see that the RF of the filament is about 2 times less sensitive to the pressure. This is very important as it indicates that the pressure calculated in the filament has larger uncertainties than that calculated in the surrounding area at the same optical depth.

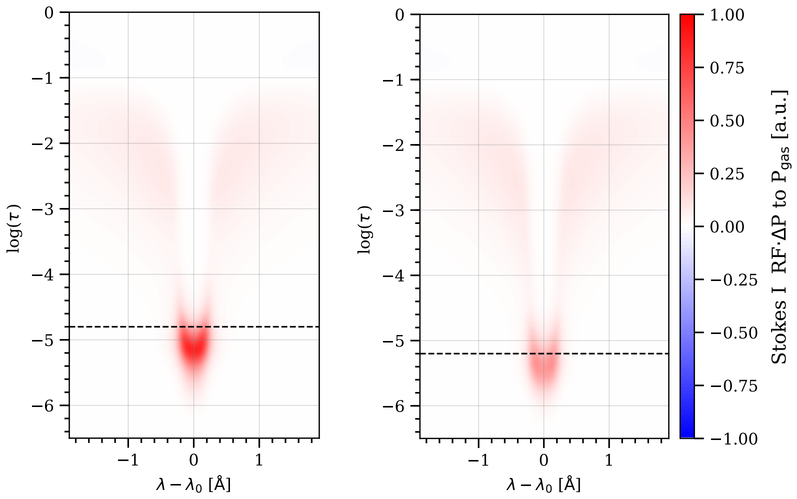

Figure B.4 – Left panel: response function of the Ca II 8542 Å to pressure (density) from a QS model. Right panel: the same as before but using the average model inferred in the filament. As a comparison, an horizontal dashed line indicates the maximum of the sensitivity to the temperature.

Changes in pressure are proportional to the intensity, with the same sign, i.e., if pressure is increased, the intensity profile becomes more positive (less deep). Figs. B.3 and B.4 demonstrate the degeneracy discussed in Sec. 5.4.

B.3.3 Longitudinal magnetic field

Finally, following the same procedure, we have calculated the response function of the Stokes V parameter to the longitudinal magnetic field. We have used a perturbation of 5 G and the result is displayed in Fig. B.5. Other studies such as Quintero Noda et al. (2017b) have shown the high variability of this RF analyzing simulations of the BIFROST code. In our case, a constant field of 60 G is used for both models.

Figure B.5 shows that the sensitivity of this line to the longitudinal magnetic field is concentrated at chromospheric heights, being 5–6 times more sensitive than to the photospheric field. Despite this, we were able to extract the information from both heights without much difficulty, as we have shown in Sec. 5.3.3.

There is a significant difference between the RFs of the two models, with the filament being $\sim$1.75 times less sensitive to the magnetic field. It indicates that the magnetic field calculated in the filament has larger uncertainties than that calculated in the surrounding area at the same optical depth.

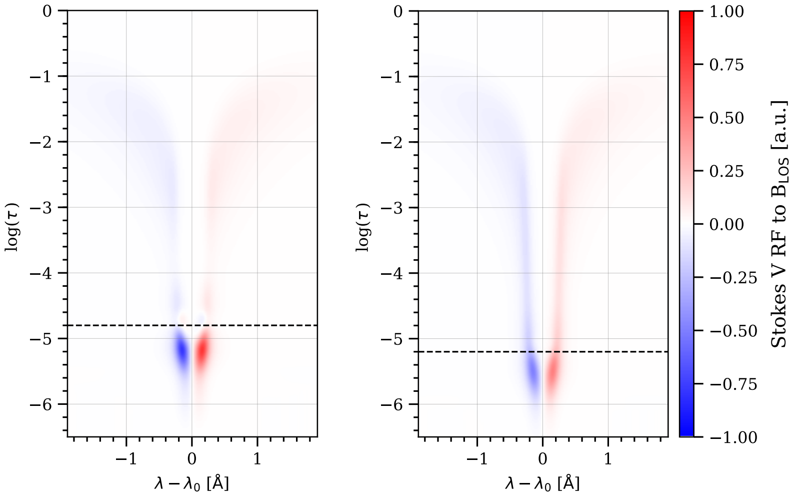

Figure B.5 – Left panel: response function of the Ca II 8542 Å to LOS component of the magnetic field from a QS model. Right panel: the same as before but using the average model inferred in the filament. As a comparison, an horizontal dashed line indicates the maximum of the sensitivity to the temperature.

The other important difference is that although the two models have the same field, their different formation height makes both models sensitive to the magnetic field at different heights. Moreover, the maximum of both distributions is below the horizontal line that indicates the maximum of the Stokes I response to the temperature.

B.4 Node location

Since the atmosphere is discretised in nodes during inversions, the positions of the nodes are considered as hyperparameter of the inversion problem. The default setting of the majority of inversion codes is to set them in an equidistant grid. However, in this section we see how a smarter setting might help improve the convergence and smoothness of the inferred model (without the need of using regularization). If a node is placed in a region of low sensitivity, the parameter can get unphysical values. To illustrate this issue, we have generated a practical example by using the sampling code MULTINEST to study the differences resulting from the node location.

For this example we synthesize the Stokes I profile of the Ca II 8542 Å line, to which we add a random noise following a Gaussian distribution of standard deviation $3\cdot10^{-3}I_c$. The original model (which appears as a black line in Fig. B.6) is chosen to mimic those of the inverted pixels in the QS of our observations. This Stokes profile is then inverted using 7 equidistant nodes in the interval $\log(\tau)=[-7.2,+1.2]$ using linear interpolation. Following the same steps as in Chap. 4, we use the MULTINEST code to explore the parameter space compatible with the observations. As a result, Fig. B.6 shows the distribution of the curves compatible with this profile, where the green shaded area indicates the standard deviation of the solutions at these points.

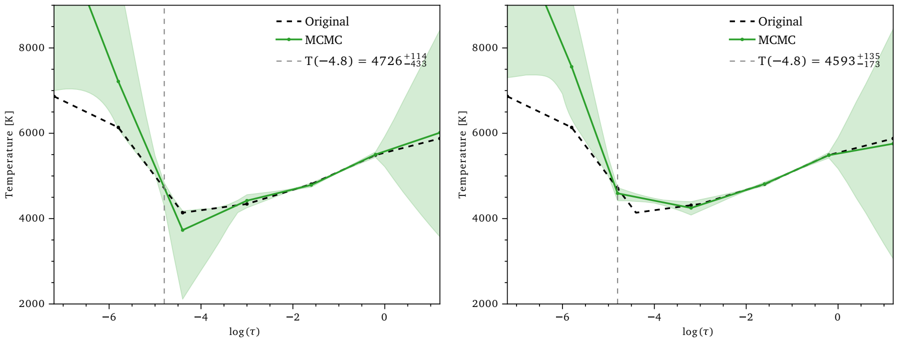

Figure B.6 – Distribution of stratifications compatible with the same Stokes profile using 7 nodes. We change the position of the third node between the panels.

It is easy to see that below $\log(\tau)=0$ the sensitivity of the line is practically zero. The real uncertainty may be higher than the one shown in the figure since we also add a prior to avoid excursions above $|\Delta T|$ =5000 K for each node. Something similar happens for $\log(\tau)=-6$ and above.

Between $\log(\tau)=0$ and $\log(\tau)=-3$, the uncertainties in temperature are quite small, of the order of 50 K. However, the left panel of Fig. B.6 shows that the line becomes less sensitive around $\log(\tau)=-4.5$ as we mentioned in Sec. B.3. At this point, the temperature can have almost any value between 1000 K and 5000 K and can be perfectly compatible with the profile. One possible explanation for this effect is that for such low temperatures the amount of Ca II is very small compared to the amount of Ca I and, therefore, the change in the profile is negligible. This lack of sensitivity is well known in the literature and, for example, Quintero Noda et al. (2018) have investigated and proposed other lines whose sensitivity is greater in these areas and can complement the analysis of this spectral line.

In a second experiment (right panel of Fig. B.6), we distribute the nodes in temperature in the same way as before but shifting the problematic node to a more sensitive area, like $\log(\tau)=-4.8$. Following the same procedure, this time the inversion is much more robust. As we do not have points in $\log(\tau=-4.5)$, the stratification does not show the real uncertainty in this region. This has to be taken into account, as some studies analyzing this line (e.g. Kuridze et al. 2017) usually average the area of the chromosphere between $\log(\tau)=-5.5$ and $\log(\tau)=-3.5$ and may be adding false information from heights where the line has no information.

Finally, we note that a different stratification of the physical parameters produce a different sensitivity since the formation height of the line changes. Consequently, the precise optimal location of the nodes is problem-specific.

B.5 Diagnostics capability of the Ca I 4227 Å

We have discussed throughout this thesis the importance of multi-line inversions as they significantly increase, the ability to infer atmospheric conditions. To complement the analysis of the Ca II 8542 Å line we have considered the Ca I 4227 Å line. This line is also deep and is formed in the chromosphere (see Sect. 2.3 for a detailed description). Because the line Ca I 4227 Å is formed under PRD effects (see Sec. 2.3) we need to use the RH code that does take this effect into account. To verify the synthetic profiles we have shown in Fig. B.7 the solar spectrum obtained by the FTS in black and those generated by RH in a FAL-C model (Fontenla et al., 1993) in red.

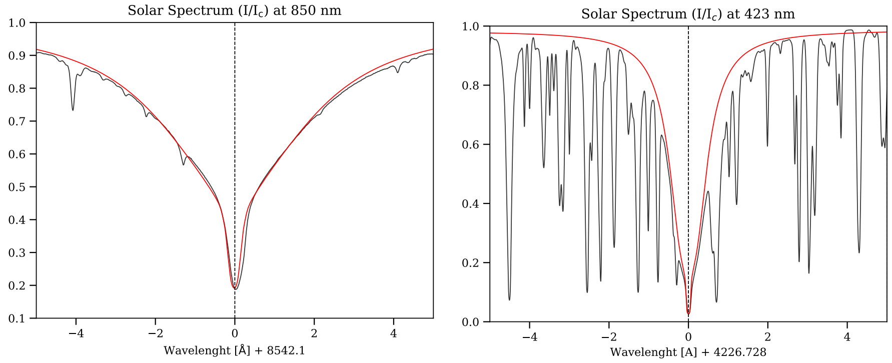

Figure B.7 – Intensity profile of the Ca II 8542 Å and Ca I 4227 Å lines. The red line is the synthetic emergent Stokes I calculated with RH in a QS atmospheric model. The black line is the observed FTS spectrum.

Then, we have calculated the contribution function for the intensity C_I of both lines. The contribution function and the response function have a similar meaning but they are different. While the response function measures the sensibility at different points in the atmosphere to the perturbations of individual physical parameters, the contribution function indicates how each layer of the atmosphere contributes to the formation of the spectral line for a given wavelength, including the effect of all the physical parameters through the source function, the opacity and the optical depth. Then if a line is sensitive to a region,it could be simply because the largest contribution to the emergent intensity comes from this region (see Uitenbroek, 2006, for a detailed comparison). the contribution function for the intensity C_I for a given wavelength is:

$$C_I(\lambda, z) = S(\lambda, z)e^{-\tau(\lambda,z)}\left(\frac{-d\tau(\lambda, z)}{dz}\right) \tag{B.2}$$

where S is the source function, τ the optical depth, and z the geometrical distance. The integral of this equation (in height) is the emergent intensity at a given wavelength. In this case, since the synthesis of a line with PRD effects is computationally more expensive, calculating the response function would take a long time, since we would have to synthesize as many profiles as stratification points. Using this definition, only one synthesis is needed.

After calculating this contribution function for each wavelength (in the range showed in the previous figure), we calculate the envelope, which is the line that connects the points with the maximum contribution at each point in the atmosphere.

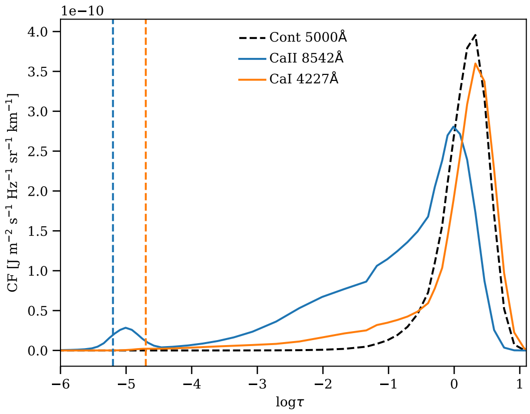

Figure B.8 – Maximum contribution function of each spectral range. The region where the core is formed is drawn with a vertical dashed line.

We also calculated the contribution function for the continuum at 5000 Å to verify that it coincides with optical depth $\log(\tau) = 0$ (dashed black line). The three contribution functions are shown in Fig. B.8. As we have seen in Sec. B.3, the Ca II 8542 Å has a peak around $\log(\tau) = -5$ and a region around the temperature minimum ($\log(\tau) = -4$) with very low values. Concerning the Ca I 4227 line, its curve (orange in the same figure) is much smaller, indicating that it is very influenced by photospheric conditions and that its sensitivity to the chromosphere is less than that of the Ca II 8542 line.

B.6 Cloud model

We have mentioned the difficulty of extracting accurate information on the temperature of filaments using NICOLE (see Sec. 5.4). However, we have tried to use simpler models to check whether some information can be extracted. For this purpose, we have used a "cloud model" to analyze the prominence. In this model, the measured intensity is modeled as:

$$I(\tau) = I_0 e^{-\tau} + S(1 - e^{-\tau}) \tag{B.3}$$

where the value for $I_0(\lambda)$ is obtained as the average intensity of the pixels around the filament, S is the source function and the optical depth of the line is modeled with a Gaussian profile $\tau = \tau_0 \ \exp -(\lambda - \lambda_0)^2/\Delta\lambda_D^2$. With this, we synthesize the emerging Stokes I profile from the above equation.

Figure B.9 shows the background average profile used in green and two synthetic profiles after taking into account the illumination which fit the observed profile almost perfectly in red and yellow. From equation B.3 we see clearly the degeneracy between the absorption of the slab τ and the emission of the slab S. An example of this degeneracy is that we can synthesize a profile only with absorption (τ_0=0.3, S/I$_c$=0, Δ_D=5 $\mathrm{km\,s^{-1}}$) or with higher absorption which can be balanced with the emission (τ_0=2.0, S/I$_c$=0.13, $\Delta_D = 3$ km s^{-1}) and have almost the same shape. Then, an estimation of the temperature from the source function is not possible.

Another possibility to infer the temperature is by using the Doppler width assuming purely thermal broadening[1]. We inferred a width of $\Delta v_D = 5$ km s^{-1} . If we calculate the ionization balance with Saha in LTE (see Fig. B.10) with the electronic density calculated by the model, we see clearly that at this temperature there is not Ca II anymore. To find temperatures such as those inferred with NICOLE of ∼4500 K, we have to increase to the opacity to $\tau_0 = 2.0$ (which broadens the line by saturation) and introduce a microturbulent velocity of ∼3 km s^{-1} . Therefore, the main conclusion is that the physical properties of the optically thick 8542 Å cannot be inferred with the cloud model.

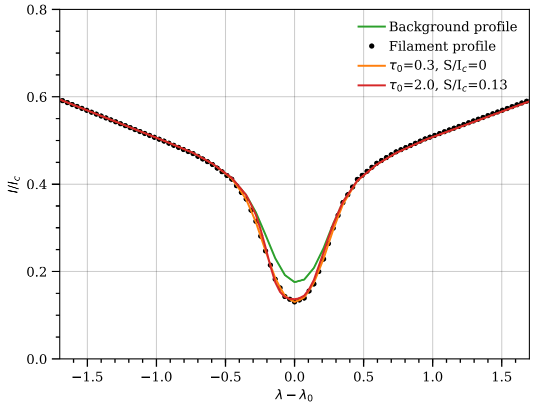

Figure B.9 – The observational profile has been fitted by HAZEL using a "cloud model". The red and the yellow lines show two examples of profiles with different absorption that can fit the same profile with different values of the source function.

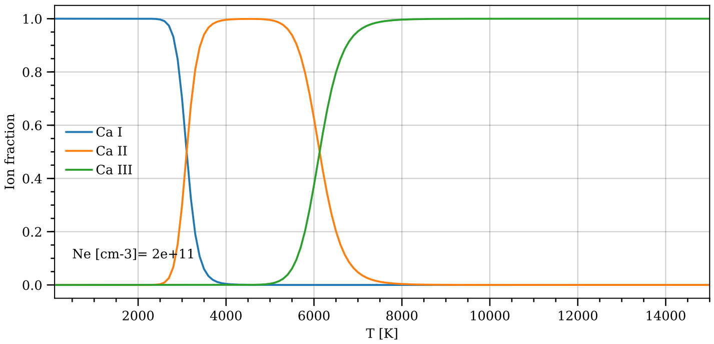

Figure B.10 – Ion fraction calculated by Saha equation showing that for temperatures higher than 10kK there is not Ca II anymore.

---

[1] We have checked that this large width does not change when carrying out spatial averages.

Bibliography

Allende Prieto C., Asplund M., Fabiani Bendicho P., 2004, A&A, 423, 1109

Alsina Ballester E., Belluzzi L., Trujillo Bueno J., 2018, ApJ, 854, 150

Anan T., Casini R., Ichimoto K., 2014, ApJ, 786, 94

Antiochos S. K., Dahlburg R. B., Klimchuk J. A., 1994, ApJ, 420, L41

Anusha L. S., et al., 2011, ApJ, 737, 95

Arregui I., Oliver R., Ballester J. L., 2012, Living Reviews in Solar Physics, 9, 2

Asensio Ramos A., Trujillo Bueno J., 2010, Mem. Soc. Astron. Italiana, 81, 625

Asensio Ramos A., de la Cruz Rodríguez J., 2015, A&A, 577, A140

Asensio Ramos A., Landi Degl'Innocenti E., Trujillo Bueno J., 2005, ApJ, 625, 985

Asensio Ramos A., Martínez González M. J., Rubiño-Martín J. A., 2007, A&A, 476, 959

Asensio Ramos A., Trujillo Bueno J., Landi Degl'Innocenti E., 2008, ApJ, 683, 542

Asensio Ramos A., Manso Sainz R., Martínez González M. J., Viticchié B., Orozco Suárez D., Socas-Navarro H., 2012, ApJ, 748, 83

Asensio Ramos A., de la Cruz Rodríguez J., Martínez González M. J., Socas-Navarro H., 2017, A&A, 599, A133

Asplund M., Grevesse N., Sauval A. J., Scott P., 2009, ARA&A, 47, 481

Auer L. H., House L. L., Heasley J. N., 1977, Sol. Phys., 55, 47

Aulanier G., Démoulin P., 2003, A&A, 402, 769

Aulanier G., DeVore C. R., Antiochos S. K., 2002, ApJ, 567, L97

Avrett E. H., 2003, in Pevtsov A. A., Uitenbroek H., eds, Astronomical Society of the Pacific Conference Series Vol. 286, Current Theoretical Models and Future High Resolution Solar Observations: Preparing for ATST. p. 419, 286, 419

Avrett E. H., Fontenla J. M., Loeser R., 1994, in Rabin D. M., Jefferies J. T., Lindsey C., eds, IAU Symposium Vol. 154, Infrared Solar Physics. p. 35, 154, 35

Bard S., Carlsson M., 2008, ApJ, 682, 1376

Berkefeld T., Schmidt D., Soltau D., von der Lühe O., Heidecke F., 2012, Astronomische Nachrichten, 333, 863

Bethge C., Peter H., Kentischer T. J., Halbgewachs C., Elmore D. F., Beck C., 2011, A&A, 534, A105

Bi Y., Jiang Y., Yang J., Hong J., Li H., Yang D., Yang B., 2014, ApJ, 790, 100

Bianda M., et al., 2011, A&A, 530, L13

Bjørgen J. P., Sukhorukov A. V., Leenaarts J., Carlsson M., de la Cruz Rodríguez J., Scharmer G. B., Hansteen V. H., 2017, preprint, (`arXiv:1712.01045`)

Bobra M. G., Ilonidis S., 2016, ApJ, 821, 127

Boerner P., et al., 2012, Sol. Phys., 275, 41

Bommier V., Sahal-Brechot S., Leroy J. L., 1981, A&A, 100, 231

Bommier V., Landi Degl'Innocenti E., Sahal-Brechot S., 1989, A&A, 211, 230

Borrero J. M., Bellot Rubio L. R., Barklem P. S., del Toro Iniesta J. C., 2003, A&A, 404, 749

Buchner J., et al., 2014, A&A, 564, A125

Campos Rozo J. I., Vargas Domínguez S., 2015, AGU Fall Meeting Abstracts,

Carlin E. S., Bianda M., 2017, ApJ, 843, 64

Carlin E. S., Asensio Ramos A., Trujillo Bueno J., 2013, ApJ, 764, 40

Carlsson M., Hansteen V. H., Gudiksen B. V., Leenaarts J., De Pontieu B., 2016, A&A, 585, A4

Casini R., López Ariste A., Tomczyk S., Lites B. W., 2003, ApJ, 598, L67

Casini R., Manso Sainz R., Low B. C., 2009a, ApJ, 701, L43

Casini R., López Ariste A., Paletou F., Léger L., 2009b, ApJ, 703, 114

Cauzzi G., Reardon K., 2012, IAU Special Session, 6, E5.11

Centeno R., Trujillo Bueno J., Uitenbroek H., Collados M., 2008, ApJ, 677, 742

Centeno R., Collados M., Trujillo Bueno J., 2009, ApJ, 692, 1211

Centeno R., Trujillo Bueno J., Asensio Ramos A., 2010, ApJ, 708, 1579

Chae J., 2003, ApJ, 584, 1084

Charbonneau P., 1995, ApJS, 101, 309

Cheung M. C. M., Schüssler M., Moreno-Insertis F., 2007, A&A, 461, 1163

Collados M., 1999, in Schmieder B., Hofmann A., Staude J., eds, Astronomical Society of the Pacific Conference Series Vol. 184, Third Advances in Solar Physics Euroconference: Magnetic Fields and Oscillations. pp 3–22, 184, 3

Collados M., Trujillo Bueno J., Asensio Ramos A., 2003, in Trujillo-Bueno J., Sanchez Almeida J., eds, Astronomical Society of the Pacific Conference Series Vol. 307, Solar Polarization. p. 468, 307, 468

Collados M., Lagg A., Díaz García A J. J., Hernández Suárez E., López López R., Páez Mañá E., Solanki S. K., 2007, in Heinzel P., Dorotovič I., Rutten R. J., eds, Astronomical Society of the Pacific Conference Series Vol. 368, The Physics of Chromospheric Plasmas. p. Heinzel, 368, Heinzel

Collados M., et al., 2012, Astronomische Nachrichten, 333, 872

Collados M., et al., 2013, in Guirado J. C., Lara L. M., Quilis V., Gorgas J., eds, Highlights of Spanish Astrophysics VII. pp 808–819, pp 808–819

Cox A. N., 2000, Allen's astrophysical quantities, p. 700

Dalcin L. D., Paz R. R., Kler P. A., Cosimo A., 2011, Advances in Water Resources, 34, 1124

De Pontieu B., et al., 2014, Sol. Phys., 289, 2733

Degl'innocenti E. L., Landolfi M., 2004, Polarization in Spectral Lines. Springer Netherlands, Dordrecht, doi:10.1007/1-4020-2415-0

Demoulin P., Priest E. R., Anzer U., 1989, A&A, 221, 326

Denker C., et al., 2018, preprint, (`arXiv:1802.10146`)

Diercke A., Kuckein C., Verma M., Denker C., 2018, A&A, 611, A64

Felipe T., et al., 2016, A&A, 596, A59

Feroz F., Hobson M. P., 2008, MNRAS, 384, 449

Feroz F., Hobson M. P., Bridges M., 2009, MNRAS, 398, 1601

Filippov B. P., Den O. G., 2000, Astronomy Letters, 26, 322

Filippov B. P., Den O. G., 2001, J. Geophys. Res., 106, 25177

Fontenla J. M., Avrett E. H., Loeser R., 1993, ApJ, 406, 319

Franz M., et al., 2016, A&A, 596, A4

Gibson S., 2015, in Vial J.-C., Engvold O., eds, Astrophysics and Space Science Library Vol. 415, Solar Prominences. p. 323 (`arXiv:1702.02214`), doi:10.1007/978-3-319-10416-4_13, 415, 323

Gilbert H. R., Hansteen V. H., Holzer T. E., 2002, ApJ, 577, 464

Gingerich O., Noyes R. W., Kalkofen W., Cuny Y., 1971, Sol. Phys., 18, 347

Golding T. P., Carlsson M., Leenaarts J., 2014, ApJ, 784, 30

González Manrique S. J., et al., 2017, preprint, (`arXiv:1701.02206`)

Gudiksen B. V., Carlsson M., Hansteen V. H., Hayek W., Leenaarts J., Martínez-Sykora J., 2011, A&A, 531, A154

Gunár S., Mackay D. H., 2016, A&A, 592, A60

Guo Y., Schmieder B., Démoulin P., Wiegelmann T., Aulanier G., Török T., Bommier V., 2010, ApJ, 714, 343

Guo Y., Ding M. D., Cheng X., Zhao J., Pariat E., 2013, ApJ, 779, 157

Hartigan J. A., Wong M. A., 1979, Applied Statistics, 28, 100

Harvey J., Hall D., 1971, in Howard R., ed., IAU Symposium Vol. 43, Solar Magnetic Fields. p. 279, 43, 279

Heinzel P., 2007, in Heinzel P., Dorotovič I., Rutten R. J., eds, Astronomical Society of the Pacific Conference Series Vol. 368, The Physics of Chromospheric Plasmas. p. Heinzel (`arXiv:0705.1464`), 368, Heinzel

Heinzel P., Anzer U., 2006, ApJ, 643, L65

Hill F., Fischer G., Grier J., Leibacher J. W., Jones H. B., Jones P. P., Kupke R., Stebbins R. T., 1994, Sol. Phys., 152, 321

Hofmann A., et al., 2012, Astronomische Nachrichten, 333, 854

Jeffreys H., 1961, Theory of Probability, third edn. Oxford, Oxford, England

Jones D. R., Perttunen C. D., Stuckman B. E., 1993, J. Optim. Theory Appl., 79, 157

Joshi J., et al., 2016, A&A, 596, A8

Judge P. G., 2009, A&A, 493, 1121

Judge P. G., Kleint L., Donea A., Sainz Dalda A., Fletcher L., 2014, ApJ, 796, 85

Judge P. G., Kleint L., Uitenbroek H., Rempel M., Suematsu Y., Tsuneta S., 2015a, Sol. Phys., 290, 979

Judge P. G., Kleint L., Sainz Dalda A., 2015b, ApJ, 814, 100

Kaiser M. L., Kucera T. A., Davila J. M., St. Cyr O. C., Guhathakurta M., Christian E., 2008, Space Sci. Rev., 136, 5

Keppens R., Xia C., 2014, ApJ, 789, 22

Khomenko E., Díaz A., de Vicente A., Collados M., Luna M., 2014, A&A, 565, A45

Khomenko E., Collados M., Díaz A. J., 2016, ApJ, 823, 132

Kilper G., Gilbert H., Alexander D., 2009, ApJ, 704, 522

Kippenhahn R., Schlüter A., 1957, ZAp, 43, 36

Kiselman D., Pereira T. M. D., Gustafsson B., Asplund M., Meléndez J., Langhans K., 2011, A&A, 535, A14

Klimchuk J. A., 2015, Philosophical Transactions of the Royal Society of London Series A, 373, 20140256

Kopp G. A., Derks M. J., Elmore D. F., Hassler D. M., Woods J. C., Streete J. L., Blankner J. G., 1997, Appl. Opt., 36, 291

Kosovichev A. G., 1999, in Schmieder B., Hofmann A., Staude J., eds, Astronomical Society of the Pacific Conference Series Vol. 184, Third Advances in Solar Physics Euroconference: Magnetic Fields and Oscillations. pp 151–170, 184, 151

Kubo M., et al., 2014, in Nagendra K. N., Stenflo J. O., Qu Q., Samooprna M., eds, Astronomical Society of the Pacific Conference Series Vol. 489, Solar Polarization 7. p. 307, 489, 307

Kuckein C., Centeno R., Martínez Pillet V., Casini R., Manso Sainz R., Shimizu T., 2009, A&A, 501, 1113

Kuckein C., Centeno R., Martínez Pillet V., 2010, Mem. Soc. Astron. Italiana, 81, 668

Kuckein C., Martínez Pillet V., Centeno R., 2012a, A&A, 539, A131

Kuckein C., Martínez Pillet V., Centeno R., 2012b, A&A, 542, A112

Kuckein C., Collados M., Manso Sainz R., 2015, ApJ, 799, L25

Kuckein C., Verma M., Denker C., 2016, A&A, 589, A84

Kuckein C., Denker C., Verma M., Balthasar H., González Manrique S. J., Louis R. E., Diercke A., 2017a, in Vargas Domínguez S., Kosovichev A. G., Antolin P., Harra L., eds, IAU Symposium Vol. 327, Fine Structure and Dynamics of the Solar Atmosphere. pp 20–24 (`arXiv:1701.01670`), doi:10.1017/S1743921317000114, 327, 20

Kuckein C., et al., 2017b, A&A, 608, A117

Kuperus M., Raadu M. A., 1974, A&A, 31, 189

Kuridze D., Henriques V., Mathioudakis M., Koza J., Zaqarashvili T. V., Rybák J., Hanslmeier A., Keenan F. P., 2017, ApJ, 846, 9

Lagg A., Woch J., Krupp N., Solanki S. K., 2004, A&A, 414, 1109

Lagg A., Ishikawa R., Merenda L., Wiegelmann T., Tsuneta S., Solanki S. K., 2009, in Lites B., Cheung M., Magara T., Mariska J., Reeves K., eds, Astronomical Society of the Pacific Conference Series Vol. 415, The Second Hinode Science Meeting: Beyond Discovery-Toward Understanding. p. 327, 415, 327

Lagg A., Lites B., Harvey J., Gosain S., Centeno R., 2017, Space Sci. Rev., 210, 37

Leenaarts J., Carlsson M., Hansteen V., Gudiksen B. V., 2011, A&A, 530, A124

Leenaarts J., Carlsson M., Rouppe van der Voort L., 2012, ApJ, 749, 136

Leenaarts J., de la Cruz Rodríguez J., Kochukhov O., Carlsson M., 2014, ApJ, 784, L17

Leenaarts J., Golding T., Carlsson M., Libbrecht T., Joshi J., 2016, A&A, 594, A104

Léger L., Paletou F., 2009, A&A, 498, 869

Lemen J. R., et al., 2012, Sol. Phys., 275, 17

Leroy J. L., Ratier G., Bommier V., 1977, A&A, 54, 811

Leroy J. L., Bommier V., Sahal-Brechot S., 1983, Sol. Phys., 83, 135

Levenberg K., 1944, Quarterly of Applied Mathematics, 2, 164

Li X., Morgan H., Leonard D., Jeska L., 2012, ApJ, 752, L22

Lin H., Penn M. J., Kuhn J. R., 1998, ApJ, 493, 978

Lin Y., Engvold O. R., Wiik J. E., 2003, Sol. Phys., 216, 109

Lin Y., Engvold O., Rouppe van der Voort L. H. M., van Noort M., 2007, Sol. Phys., 246, 65

Lites B. W., 2005, ApJ, 622, 1275

Liu W., Berger T. E., Low B. C., 2012, ApJ, 745, L21

Liu C., Deng N., Wang J. T. L., Wang H., 2017, ApJ, 843, 104

López Ariste A., Casini R., 2002, ApJ, 575, 529

López Ariste A., Casini R., 2005, A&A, 436, 325

López Ariste A., Aulanier G., Schmieder B., Sainz Dalda A., 2006, A&A, 456, 725

Luna M., Karpen J., 2012, ApJ, 750, L1

Luna M., Moreno-Insertis F., Priest E., 2015, ApJ, 808, L23

Luna M., Su Y., Schmieder B., Chandra R., Kucera T. A., 2017, ApJ, 850, 143

Mackay D. H., Karpen J. T., Ballester J. L., Schmieder B., Aulanier G., 2010, Space Sci. Rev., 151, 333

Manso Sainz R., Trujillo Bueno J., 2010, ApJ, 722, 1416

Marquardt D. W., 1963, Journal of the Society for Industrial and Applied Mathematics, 11, 431

Martens P. C., Zwaan C., 2001, ApJ, 558, 872

Martínez González M. J., Manso Sainz R., Asensio Ramos A., Belluzzi L., 2012a, MNRAS, 419, 153

Martínez González M. J., Asensio Ramos A., Manso Sainz R., Beck C., Belluzzi L., 2012b, ApJ, 759, 16

Martínez González M. J., Manso Sainz R., Asensio Ramos A., Beck C., de la Cruz Rodríguez J., Díaz A. J., 2015, ApJ, 802, 3

Martínez González M. J., Asensio Ramos A., Arregui I., Collados M., Beck C., de la Cruz Rodríguez J., 2016, ApJ, 825, 119

Martínez Pillet V., et al., 2011, Sol. Phys., 268, 57

Mauas P. J. D., Andretta V., Falchi A., Falciani R., Teriaca L., Cauzzi G., 2005, ApJ, 619, 604

McCauley P. I., Su Y. N., Schanche N., Evans K. E., Su C., McKillop S., Reeves K. K., 2015, Sol. Phys., 290, 1703

Merenda L., Trujillo Bueno J., Landi Degl'Innocenti E., Collados M., 2006, ApJ, 642, 554

Merenda L., Trujillo Bueno J., Collados M., 2007, in Heinzel P., Dorotovič I., Rutten R. J., eds, Astronomical Society of the Pacific Conference Series Vol. 368, The Physics of Chromospheric Plasmas. p. Heinzel, 368, Heinzel

Merenda L., Lagg A., Solanki S. K., 2011, A&A, 532, A63

Metcalf T. R., et al., 2006, Sol. Phys., 237, 267

Metropolis N., Rosenbluth A. W., Rosenbluth M. N., Teller A. H., Teller E., 1953, J. Chem. Phys., 21, 1087

Milić I., Faurobert M., Atanacković O., 2017, A&A, 597, A31

Morgan H., Druckmüller M., 2014, Sol. Phys., 289, 2945

Mukherjee P., Parkinson D., Liddle A. R., 2006, ApJ, 638, L51

Nagy Z., 2015, Field of Fiery Grass a.k.a. Solar Spicules, `spaceplasma.tumblr.com/post/114567942209`

Neckel H., Labs D., 1984, Sol. Phys., 90, 205

Nikol'Skii G. M., Khetsuriani T. S., 1970, Soviet Ast., 13, 815

Nordlund Å., Stein R. F., Asplund M., 2009, Living Reviews in Solar Physics, 6, 2

Okamoto T. J., et al., 2007, Science, 318, 1577

Okamoto T. J., Liu W., Tsuneta S., 2016, ApJ, 831, 126

Oliver R., Ballester J. L., 2002, Sol. Phys., 206, 45

Orozco Suárez D., Asensio Ramos A., Trujillo Bueno J., 2014, A&A, 566, A46

Orozco Suárez D., Asensio Ramos A., Trujillo Bueno J., 2015, ApJ, 803, L18

Paletou F., López Ariste A., Bommier V., Semel M., 2001, A&A, 375, L39

Panesar N. K., 2014, PhD thesis, Georg-August-Universität Göttingen, Institut für Astrophysik, Germany, doi:10.5281/zenodo.581205

Parenti S., 2014, Living Reviews in Solar Physics, 11, 1

Parenti S., Schmieder B., Heinzel P., Golub L., 2012, ApJ, 754, 66

Park H., et al., 2013, Sol. Phys., 288, 105

Parnell C. E., De Moortel I., 2012, Philosophical Transactions of the Royal Society of London Series A, 370, 3217

Penn M. J., Kuhn J. R., 1995, ApJ, 441, L51

Pesnell W. D., Thompson B. J., Chamberlin P. C., 2012, Sol. Phys., 275, 3

Pettit E., 1932, ApJ, 76, 9

Puschmann K. G., et al., 2012, in Rimmele T. R., et al., eds, Astronomical Society of the Pacific Conference Series Vol. 463, Second ATST-EAST Meeting: Magnetic Fields from the Photosphere to the Corona.. p. 423 (`arXiv:1111.5509`), 463, 423

Quintero Noda C., Shimizu T., de la Cruz Rodríguez J., Katsukawa Y., Ichimoto K., Anan T., Suematsu Y., 2016, MNRAS, 459, 3363

Quintero Noda C., et al., 2017a, MNRAS, 464, 4534

Quintero Noda C., et al., 2017b, MNRAS, 472, 727

Quintero Noda C., et al., 2018, preprint, (`arXiv:1801.01655`)

Rees D. E., López Ariste A., Thatcher J., Semel M., 2000, A&A, 355, 759

Ruiz Cobo B., del Toro Iniesta J. C., 1992, ApJ, 398, 375

Rust D. M., Kumar A., 1994, Sol. Phys., 155, 69

Sahal-Brechot S., Bommier V., Leroy J. L., 1977, A&A, 59, 223

Saito K., Tandberg-Hanssen E., 1973, Sol. Phys., 31, 105

Sánchez Almeida J., Martínez González M., 2011, in Kuhn J. R., Harrington D. M., Lin H., Berdyugina S. V., Trujillo-Bueno J., Keil S. L., Rimmele T., eds, Astronomical Society of the Pacific Conference Series Vol. 437, Solar Polarization 6. p. 451 (`arXiv:1105.0387`), 437, 451

Sánchez-Andrade Nuño B., Centeno R., Puschmann K. G., Trujillo Bueno J., Blanco Rodríguez J., Kneer F., 2007, A&A, 472, L51

Sasso C., Lagg A., Solanki S. K., 2006, A&A, 456, 367

Sasso C., Lagg A., Solanki S. K., Aznar Cuadrado R., Collados M., 2007, in Heinzel P., Dorotovič I., Rutten R. J., eds, Astronomical Society of the Pacific Conference Series Vol. 368, The Physics of Chromospheric Plasmas. p. Heinzel, 368, Heinzel

Sasso C., Lagg A., Solanki S. K., 2011, A&A, 526, A42

Sasso C., Lagg A., Solanki S. K., 2014, A&A, 561, A98

Schad T. A., Penn M. J., Lin H., 2013, ApJ, 768, 111

Schad T. A., Penn M. J., Lin H., Tritschler A., 2015, Sol. Phys., 290, 1607

Schad T. A., Penn M. J., Lin H., Judge P. G., 2016, ApJ, 833, 5

Scharmer G. B., Bjelksjo K., Korhonen T. K., Lindberg B., Petterson B., 2003, in Keil S. L., Avakyan S. V., eds, Proc. SPIE Vol. 4853, Innovative Telescopes and Instrumentation for Solar Astrophysics. pp 341–350, doi:10.1117/12.460377, 4853, 341

Scharmer G. B., et al., 2008, ApJ, 689, L69

Scherrer P. H., et al., 2012, Sol. Phys., 275, 207

Schlichenmaier R., Collados M., 2002, A&A, 381, 668

Schmidt W., et al., 2012a. p. 796, doi:10.1002/asna.201211725, 333, 796

Schmidt W., et al., 2012b, in Rimmele T. R., et al., eds, Astronomical Society of the Pacific Conference Series Vol. 463, Second ATST-EAST Meeting: Magnetic Fields from the Photosphere to the Corona.. p. 365 (`arXiv:1202.4289`), 463, 365

Schmieder B., López Ariste A., Levens P., Labrosse N., Dalmasse K., 2015, in Nagendra K. N., Bagnulo S., Centeno R., Jesús Martínez González M., eds, IAU Symposium Vol. 305, Polarimetry. pp 275–281, doi:10.1017/S1743921315004895, 305, 275

Schwartz P., Balthasar H., Kuckein C., Koza J., Gömöry P., Rybák J., Heinzel P., Kučera A., 2016, Astronomische Nachrichten, 337, 1045

Shaw J. R., Bridges M., Hobson M. P., 2007, MNRAS, 378, 1365

Shchukina N. G., Sukhorukov A. V., Trujillo Bueno J., 2017, A&A, 603, A98

Skilling J., 2004, in Fischer R., Preuss R., Toussaint U. V., eds, American Institute of Physics Conference Series Vol. 735, American Institute of Physics Conference Series. pp 395–405, doi:10.1063/1.1835238, 735, 395

Socas-Navarro H., Trujillo Bueno J., Ruiz Cobo B., 2000, ApJ, 530, 977

Socas-Navarro H., Trujillo Bueno J., Landi Degl'Innocenti E., 2004, ApJ, 612, 1175

Socas-Navarro H., de la Cruz Rodríguez J., Asensio Ramos A., Trujillo Bueno J., Ruiz Cobo B., 2015, A&A, 577, A7

Solanki S. K., Lagg A., Woch J., Krupp N., Collados M., 2003, Nature, 425, 692

Solanki S. K., et al., 2006, in Casini R., Lites B. W., eds, Vol. 358, Astronomical Society of the Pacific Conference Series. p. 431, 358, 431

Soler R., Oliver R., Ballester J. L., 2007, Sol. Phys., 246, 73

Soltau D., Volkmer R., von der Lühe O., Berkefeld T., 2012, Astronomische Nachrichten, 333, 847

Stellmacher G., Wiehr E., 2005, A&A, 431, 1069

Stellmacher G., Wiehr E., Dammasch I. E., 2003, Sol. Phys., 217, 133

Stenflo J. O., 1994, Solar Magnetic Fields. Astrophysics and Space Science Library Vol. 189, Springer Netherlands, Dordrecht, doi:10.1007/978-94-015-8246-9, 189

Stenflo J. O., Keller C. U., 1997, A&A, 321, 927

Strong K., Bruner M., Tarbell T., Title A., Wolfson C. J., 1994, Space Sci. Rev., 70, 119

Su Y., Gömöry P., Veronig A., Temmer M., Wang T., Vanninathan K., Gan W., Li Y., 2014, ApJ, 785, L2

Su Y., van Ballegooijen A., McCauley P., Ji H., Reeves K. K., DeLuca E. E., 2015, ApJ, 807, 144

Sukhorukov A. V., Leenaarts J., 2017, A&A, 597, A46

Tandberg-Hanssen E., 1998, in Webb D. F., Schmieder B., Rust D. M., eds, Astronomical Society of the Pacific Conference Series Vol. 150, IAU Colloq. 167: New Perspectives on Solar Prominences. p. 11, 150, 11

Terradas J., Soler R., Oliver R., Ballester J. L., 2015, ApJ, 802, L28

Tipping M. E., 2000, The Relevance Vector Machine

Török T., Kliem B., 2005, ApJ, 630, L97

Tritschler A., et al., 2015, in van Belle G. T., Harris H. C., eds, Cambridge Workshop on Cool Stars, Stellar Systems, and the Sun Vol. 18, 18th Cambridge Workshop on Cool Stars, Stellar Systems, and the Sun. pp 933–944, 18, 933

Trujillo Bueno J., 2001, in Sigwarth M., ed., Astronomical Society of the Pacific Conference Series Vol. 236, Advanced Solar Polarimetry – Theory, Observation, and Instrumentation. p. 161 (`arXiv:astro-ph/0202328`), 236, 161

Trujillo Bueno J., 2003, in Hubeny I., Mihalas D., Werner K., eds, Astronomical Society of the Pacific Conference Series Vol. 288, Stellar Atmosphere Modeling. p. 551, 288, 551

Trujillo Bueno J., 2006, in Ramelli R., Shalabiea O., Saleh I., Stenflo J. O., eds, Solar Physics and Solar Eclipses (SPSE 2006). pp 77–92, pp 77–92

Trujillo Bueno J., 2010, Astrophysics and Space Science Proceedings, 19, 118

Trujillo Bueno J., Asensio Ramos A., 2007, ApJ, 655, 642

Trujillo Bueno J., Landi Degl'Innocenti E., Collados M., Merenda L., Manso Sainz R., 2002, Nature, 415, 403

Trujillo Bueno J., Shchukina N., Asensio Ramos A., 2004, Nature, 430, 326

Trujillo Bueno J., Merenda L., Centeno R., Collados M., Landi Degl'Innocenti E., 2005, ApJ, 619, L191

Tziotziou K., 2007, in Heinzel P., Dorotovič I., Rutten R. J., eds, Astronomical Society of the Pacific Conference Series Vol. 368, The Physics of Chromospheric Plasmas. p. Heinzel (`arXiv:0704.1558`), 368, Heinzel

Tziotziou K., Heinzel P., Mein P., Mein N., 2001, A&A, 366, 686

Uitenbroek H., 1989, A&A, 213, 360

Uitenbroek H., 2001, ApJ, 557, 389

Uitenbroek H., 2006, in Leibacher J., Stein R. F., Uitenbroek H., eds, Astronomical Society of the Pacific Conference Series Vol. 354, Solar MHD Theory and Observations: A High Spatial Resolution Perspective. p. 313, 354, 313

Vecchio A., Cauzzi G., Reardon K. P., Janssen K., Rimmele T., 2007, A&A, 461, L1

Volkmer R., et al., 2010, Astronomische Nachrichten, 331, 624

Wedemeyer-Böhm S., Carlsson M., 2011, A&A, 528, A1

Welsch B. T., DeVore C. R., Antiochos S. K., 2005, ApJ, 634, 1395

Wenzel R., Berdyugina S. V., Fluri D. M., Arnaud J., Sainz-Dalda A., 2010, in Cranmer S. R., Hoeksema J. T., Kohl J. L., eds, Astronomical Society of the Pacific Conference Series Vol. 428, SOHO-23: Understanding a Peculiar Solar Minimum. p. 117 (`arXiv:1003.5114`), 428, 117

Wiehr E., Stellmacher G., 1991, A&A, 247, 379

Xu Z., Lagg A., Solanki S. K., 2010, A&A, 520, A77

Xu Z., Lagg A., Solanki S., Liu Y., 2012, ApJ, 749, 138

Yelles Chaouche L., Kuckein C., Martínez Pillet V., Moreno-Insertis F., 2012, ApJ, 748, 23

Yeo K. L., Feller A., Solanki S. K., Couvidat S., Danilovic S., Krivova N. A., 2014, A&A, 561, A22

Yi Z., Molowny-Horas R., 1995, A&A, 295, 199

Zhang Q. M., Li T., Zheng R. S., Su Y. N., Ji H. S., 2017, ApJ, 842, 27

Zirker J. B., Engvold O., Martin S. F., 1998, Nature, 396, 440

de la Cruz Rodríguez J., Piskunov N., 2013, ApJ, 764, 33

de la Cruz Rodríguez J., van Noort M., 2017, Space Sci. Rev., 210, 109

de la Cruz Rodríguez J., Socas-Navarro H., Carlsson M., Leenaarts J., 2012, A&A, 543, A34

de la Cruz Rodríguez J., Rouppe van der Voort L., Socas-Navarro H., van Noort M., 2013a, A&A, 556, A115

de la Cruz Rodríguez J., De Pontieu B., Carlsson M., Rouppe van der Voort L. H. M., 2013b, ApJ, 764, L11

de la Cruz Rodríguez J., Löfdahl M. G., Sütterlin P., Hillberg T., Rouppe van der Voort L., 2015, A&A, 573, A40

de la Cruz Rodríguez J., Leenaarts J., Asensio Ramos A., 2016a, ApJ, 830, L30

de la Cruz Rodríguez J., Leenaarts J., Asensio Ramos A., 2016b, ApJ, 830, L30

del Pino Alemán 2015, PhD thesis, Universidad de La Laguna

del Toro Iniesta J. C., 2003, Introduction to Spectropolarimetry, p. 244

del Toro Iniesta J. C., Ruiz Cobo B., 2016, Living Reviews in Solar Physics, 13, 4

Štěpán J., Trujillo Bueno J., 2016, ApJ, 826, L10

van Ballegooijen A. A., Cranmer S. R., 2010, ApJ, 711, 164

van Ballegooijen A. A., Martens P. C. H., 1989, ApJ, 343, 971

van Noort M., Rouppe van der Voort L., Löfdahl M. G., 2005, Sol. Phys., 228, 191